



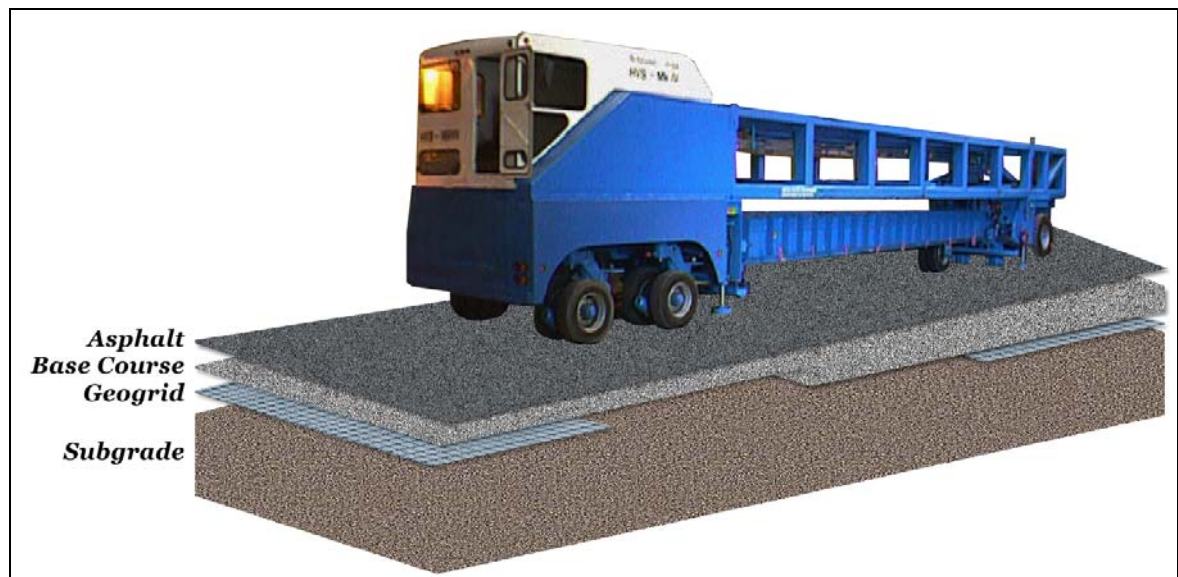
**US Army Corps
of Engineers®**
Engineer Research and
Development Center

Transportation Pooled Fund Program

Structural Improvements of Flexible Pavements Using Geosynthetics for Base Course Reinforcement

Karen S. Henry, Joshua Clapp, William Davids,
Dana Humphrey, and Lynette Barna

October 2009



Structural Improvements of Flexible Pavements Using Geosynthetics for Base Course Reinforcement

Karen Henry, Ph.D., P.E.

*Department of Civil & Environmental Engineering
United States Air Force Academy
USAF Academy, CO 80840-6232*

Joshua Clapp, William Davids, Ph.D., P.E., and Dana Humphrey, Ph.D., P.E.

*Department of Civil & Environmental Engineering
University of Maine
Orono, ME 04469-5711*

Lynette Barna

*Cold Regions Research & Engineering Laboratory
72 Lyme Road
Hanover, NH 03755-1290*

Final report

Approved for public release; distribution is unlimited.

Prepared for Federal Highway Administration
McLean, VA 22101

Under Customer Order Number DTFH6104X30054, Designated as TPF-5(010)

Abstract: A study was conducted on full-scale pavement test sections to assess geogrid/base reinforcement in flexible pavements representative of major highways. The experimental design, trafficking protocol, results and development of rutting models are reported herein. Accelerated trafficking was conducted with a heavy vehicle simulator on eight pavement test sections. Four test sections were reinforced with Geogrid placed at the base/subgrade interface; the other four were matching unreinforced (control) sections. Rut depths in the pavement surface as a function of applied traffic cycles were compared. Except for the thickest base and asphalt combination tested, the grid reinforcement provided benefit compared to unreinforced control sections as indicated by surface rut depth. (Four test sections reached ‘failure’ and four did not—traffic ceased at a set number of load cycles in these cases.) Empirical rutting models presented in NCHRP 1-37A, Guide for Mechanistic-Empirical Design of New and Rehabilitated Pavement Structures (available from <http://www.trb.org/mepdg/>) were extended to account for the reinforcement. Mechanistic finite element models were calibrated using strains measured throughout the test sections. Predicted rut depths using this mechanistic-empirical approach were in reasonable agreement with measured values. For the pavement configurations of this study, Geogrid was predicted to increase the pavement life by 29 to 43 percent.

DISCLAIMER: The contents of this report are not to be used for advertising, publication, or promotional purposes. Citation of trade names does not constitute an official endorsement or approval of the use of such commercial products. All product names and trademarks cited are the property of their respective owners. The findings of this report are not to be construed as an official Department of the Army position unless so designated by other authorized documents.

DESTROY THIS REPORT WHEN NO LONGER NEEDED. DO NOT RETURN IT TO THE ORIGINATOR.

Contents

Figures and Tables	v
Preface	ix
Unit Conversion Factors	x
1 Introduction	1
Purpose and scope of project	1
Project objectives	2
2 Background	4
3 Experimental Design and Test Section Construction	8
<i>Test section construction</i>	9
<i>Soils and geogrid</i>	10
<i>Asphalt</i>	12
<i>Addition of water to subgrade after construction</i>	13
Soil and asphalt instrumentation	14
<i>Temperatures</i>	15
<i>Moisture content</i>	15
<i>Deformation of soil and asphalt</i>	15
Soil stress measurements	16
Geogrid strain gages	17
4 Trafficking	18
<i>Test protocol</i>	19
Permanent surface deformation	21
Level surveys	21
5 Test Results	23
Overview of traffic testing	23
Modulus estimates and water content determinations	26
Surface deformations	34
Deformations of asphalt, base and subgrade	43
Soil and asphalt elastic strains during static load application	52
Geogrid strain gage results	59
<i>Elastic Geogrid strains</i>	59
<i>Permanent Geogrid strains</i>	61
Stress	66
6 Development of Rutting Models	73
FE model development	73
Material properties	74
Validation of FE model using FWD layer moduli	76

Determination of reinforcement parameters.....	79
Development of strain in Geogrid.....	80
Permanent deformation models	82
Modification of NCHRP equations to account for Geogrid.....	83
Calibration results	85
Parametric studies	91
<i>Effect of Geogrid creep and stiffness.....</i>	91
<i>Comprehensive parametric study, constant Geogrid properties.....</i>	92
<i>Parametric study results.....</i>	95
<i>Effect of Geogrid location within base layer – model constraint.....</i>	102
<i>Effect of asphalt modulus on Geogrid performance.....</i>	102
<i>Effect of base layer modulus on Geogrid performance</i>	103
<i>Effect of subgrade layer modulus on Geogrid performance.....</i>	103
<i>Effect of base layer thickness on Geogrid performance.....</i>	103
<i>Effect of AC layer thickness on Geogrid performance</i>	104
<i>Parametric study conclusions</i>	104
7 Discussion	107
8 Conclusions and Recommendations	110
References.....	114
Appendix A – Test Protocol.....	118
Appendix B - Forensics.....	123
Appendix C – Geogrid and Asphalt Viscoelasticity.....	158
Appendix D – Parametric Study Results	173
Report Documentation Page	

Figures and Tables

Figures

Figure 1. Close-up of Geogrid and base aggregate particles during construction.....	4
Figure 2. a) Plan view of the eight test sections indicating grid and non-grid sections; b) profile view of the test sections showing the varying pavement and base thicknesses.....	10
Figure 3. Grain size distribution of subgrade and base course soils.....	11
Figure 4. Tensar® BX1200 geogrid.....	12
Figure 5. Locations of instrumentation of a Geogrid test section.....	14
Figure 6. Mark IV heavy vehicle simulator (HVS) mounted with dual truck tires	18
Figure 7: Surface deformation laser profilometer measurement device.....	22
Figure 8. Plan view showing the test area, test sections, and FWD points	26
Figure 9. Volumetric water content of the subgrade at depths of 840-890 mm from the top of the subgrade in Test Sections 1, 2, 4, 6, 7 & 8 for the duration of the test program.....	28
Figure 10. Estimated subgrade modulus values for Test Sections 1-4, with a base layer thickness of 300 mm.....	28
Figure 11. Estimated subgrade modulus values for Test Sections 5-8, with a base layer thickness of 600 mm.....	29
Figure 12. Estimated base modulus values for Test Sections 1-4, with a base layer thickness of 300 mm.....	29
Figure 13. Estimated base modulus values for Test Sections 5-8, with a base layer thickness of 600 mm.....	30
Figure 14. Estimated subgrade modulus values for Test Sections 1-4 with a base layer thickness of 300 mm for the trafficking phase of the test program.....	31
Figure 15. Estimated subgrade modulus values for Test Sections 5-8 with a base layer thickness of 600 mm for the trafficking phase of the test program.....	31
Figure 16. Estimated base layer modulus values for Test Sections 1-4 with a base layer thickness of 300 mm for the trafficking phase of the test program.....	32
Figure 17. Estimated base modulus values for Test Sections 5-8 with a base layer thickness of 600 mm for the trafficking phase of the test program.....	32
Figure 18. Example of rut depth measurement for the average relative profile in TS 1 after 414,000 cumulative traffic cycles	34
Figure 19. Average relative surface rut depth vs. cumulative traffic cycles	36
Figure 20. Average relative surface rut depth vs. cumulative ESALs.....	36
Figure 21. Average relative surface profiles for all test sections at the time of final static load tests (SLTs).....	37
Figure 22. Relative pavement surface elevation contours for TS 2 (100 mm asphalt, 300 mm base) after 214,000 cumulative traffic cycles.	39
Figure 23. Relative pavement surface elevation contours for TS 4 (100 mm asphalt, 300 mm base, with Geogrid) after 263,000 cumulative traffic cycles.....	39

Figure 24. Relative pavement surface elevation contours for TS 1 (150 mm asphalt, 300 mm base) after 414,000 cumulative traffic cycles.....	40
Figure 25. Relative pavement surface elevation contours for TS 3 (150 mm asphalt, 300 mm base, with Geogrid) after 424,000 cumulative traffic cycles.....	40
Figure 26. Relative pavement surface elevation contours for TS 6 (100 mm asphalt, 600 mm base) after 464,000 cumulative traffic cycles.....	41
Figure 27. Relative pavement surface elevation contours for TS 8 (100 mm asphalt, 600 mm base, with Geogrid) after 464,000 cumulative traffic cycles.....	41
Figure 28. Relative pavement surface elevation contours for TS 5 (150 mm asphalt, 600 mm base) after 464,000 cumulative traffic cycles	42
Figure 29. Relative pavement surface elevation contours for TS 7 (150 mm asphalt, 600 mm base, with Geogrid) after 464,000 cumulative traffic cycles.....	42
Figure 30. Final, unloaded vertical deformations for Test Sections 1-4 with 300 mm base course.....	43
Figure 31. Final, unloaded vertical deformations test Sections 5-8 with 600 mm base course.....	44
Figure 32. Example of deformation measurements for Test Section 2	45
Figure 33. Permanent vertical deformations in the asphalt layer vs. cumulative traffic cycles (data has been adjusted according to the procedure outlined in this section).	47
Figure 34. Permanent vertical deformations in the base layer vs. cumulative traffic cycles (data has been adjusted according to the procedure outlined in this section).....	48
Figure 35. Permanent vertical deformations in the subgrade layer vs. cumulative traffic Cycles	48
Figure 36. Permanent vertical deformations in the asphalt layer vs. cumulative ESALs (data has been adjusted according to the procedure outlined in this section).).	49
Figure 37. Permanent vertical deformations in the base layer vs. cumulative ESALs (data has been adjusted according to the procedure outlined in this section).....	49
Figure 38. Permanent vertical deformations in the subgrade layer vs. cumulative ESALs..	50
Figure 39. Permanent vertical deformations by individual ϵ_{mu} layer for Test Sections 1-4 at the last set of SLTs	51
Figure 40. Permanent vertical deformations by individual ϵ_{mu} layer for Test Sections 5-8 at the last set of SLTs	52
Figure 41. Average of SLT vertical elastic ϵ_{mu} strains by ϵ_{mu} layer for Test Sections 1 through 4 under a 48.9 kN (11 K) wheel load centered over the vertical ϵ_{mu} stack.....	53
Figure 42. Average of SLT vertical elastic ϵ_{mu} strains by ϵ_{mu} layer for Test Sections 5 through 8 under a 48.9 kN (11 K) wheel load centered over the vertical ϵ_{mu} stack.....	54
Figure 43. Average of SLT vertical elastic ϵ_{mu} strains by ϵ_{mu} layer for Test Sections 1 through 4 under a 48.9 kN (11 K) wheel load centered over the longitudinal ϵ_{mu} stack.	54
Figure 44. Average of SLT vertical elastic ϵ_{mu} strains by ϵ_{mu} layer for Test Sections 5 through 8 under a 48.9 kN (11 K) wheel load centered over the longitudinal ϵ_{mu} stack.	55
Figure 45. Average of SLT transverse elastic ϵ_{mu} strains by ϵ_{mu} layer for Test Sections 1 through 4 under a 48.9 kN (11 K) wheel load centered over the vertical ϵ_{mu} stack.....	55
Figure 46. Average of SLT transverse elastic ϵ_{mu} strains by ϵ_{mu} layer for Test Sections 5 through 8 under a 48.9 kN (11 K) wheel load centered over the vertical ϵ_{mu} stack.....	56
Figure 47. Average of SLT longitudinal elastic ϵ_{mu} strains by ϵ_{mu} layer for Test Sections 1 through 4 under a 48.9 kN (11 K) wheel load centered over the vertical ϵ_{mu} stack.....	56

Figure 48. Average of SLT longitudinal elastic ϵ_{mu} strains by ϵ_{mu} layer for Test Sections 5 through 8 under a 48.9 kN (11 K) wheel load centered over the vertical ϵ_{mu} stack.....	57
Figure 49. Elastic Geogrid SLT microstrains for all surviving gages under a 48.9 kN (11 K) wheel load vs. cumulative traffic cycles.....	60
Figure 50. Elastic Geogrid SLT microstrains for all surviving gages under a 48.9 kN (11 K) wheel load vs. cumulative ESALs.....	60
Figure 51. Permanent Geogrid microstrains in TS 3 vs. cumulative traffic cycles.....	62
Figure 52. Permanent Geogrid microstrains in TS 4 vs. cumulative traffic cycles	62
Figure 53. Permanent Geogrid microstrains in TS 7 vs. cumulative traffic cycles	63
Figure 54. Permanent Geogrid microstrains in TS 8 vs. cumulative traffic cycles.	63
Figure 55. Permanent Geogrid microstrains in TS 3 vs. cumulative ESALs	64
Figure 56. Permanent Geogrid microstrains in TS 4 vs. cumulative ESALs	64
Figure 57. Permanent Geogrid microstrains in TS 7 vs. cumulative ESALs.....	65
Figure 58. Permanent Geogrid microstrains in TS 8 vs. cumulative ESALs	65
Figure 59. Transverse Geokon stresses near the top of the base layer as a function of cumulative HVS cycles measured in an unloaded condition.....	66
Figure 60. Transverse Geokon stresses near the top of the subgrade layer as a function of cumulative HVS cycles measured in an unloaded condition.....	67
Figure 61. Vertical Geokon stresses near the top of the base layer as a function of cumulative HVS cycles measured in an unloaded condition.....	67
Figure 62. Vertical Geokon stresses near the top of the subgrade layer as a function of cumulative HVS cycles measured in an unloaded condition.....	68
Figure 63. Vertical Geokon stresses lower in the subgrade layer as a function of cumulative HVS cycles measured in an unloaded condition.....	68
Figure 64. Transverse Geokon stresses near the top of the base layer as a function of cumulative ESALs measured in an unloaded condition.....	69
Figure 65. Transverse Geokon stresses near the top of the subgrade layer as a function of cumulative ESALs measured in an unloaded condition.....	69
Figure 66. Vertical Geokon stresses near the top of the base layer as a function of cumulative ESALs measured in an unloaded condition.....	70
Figure 67. Vertical Geokon stresses near the top of the subgrade layer as a function of cumulative ESALs measured in an unloaded condition.....	70
Figure 68. Vertical Geokon stresses lower in the subgrade layer as a function of cumulative ESALs measured in an unloaded condition.....	71
Figure 69. Relative vertical stresses measured by stress cells when a 48.9 kN (11 K) wheel load was applied.	72
Figure 70. Typical quarter-symmetric FE mesh.....	74
Figure 71. Comparison of microstrains predicted by the FE model and measured by the ϵ_{mu} coils for SLTs in TS 2	79
Figure 72. Rutting model predictions and measured surface rut depths for Test Sections 1 and 3	86
Figure 73. Rutting model predictions and measured surface rut depths for Test Sections 2 and 4	87
Figure 74. Rutting model predictions and measured surface rut depths for Test Sections 5 and 7	87

Figure 75. Rutting model predictions and measured surface rut depths for Test Sections 6 and 8.....	88
Figure 76. Rutting model predictions and measured surface rut depths for test sections 5 and 7	88
Figure 77. Geogrid strains after base layer compaction, after Helstrom et al. (2006).....	95
Figure 78. Effect of increasing the asphalt layer modulus from 2,720 MPa to 4,480 MPa on the EG.....	101
Figure 79. Effect of increasing the base layer modulus from 100 MPa to 300 MPa on the EG.....	101
Figure 80. Effect of increasing the subgrade layer modulus from 35 MPa to 70 MPa on the EG.....	102

Tables

Table 1. Test Section configurations.....	9
Table 2a. Subgrade soil properties. Dry density and optimum moisture content were determined according to AASHTO T-180 (Modified Proctor).	11
Table 2b. Base soil properties. Dry density and optimum moisture content were determined according to AASHTO T-180 (Modified Proctor).	11
Table 3. Properties of geogrids used in test sections.	12
Table 4. Asphalt concrete gradation measured on asphalt cores taken after paving.....	13
Table 5. Static load test intervals.....	20
Table 6. Average change in elevation for each test section away from the trafficking area by level survey.....	22
Table 7. HVS trafficking and FWD test dates	24
Table 8. Validity of ϵ_{mu} readings at the end of trafficking for each test section	25
Table 9. Survivability of Geogrid strain gages in reinforced test sections.....	26
Table 10. Average estimated subgrade modulus values	33
Table 11. Summary of final measured rut depths, surface deformations, and <i>TBR</i> values for each test section.....	38
Table 12. Summary of measured deformations at the location of the ϵ_{mu} coils for each test section.....	45
Table 13. Summary of raw measured and adjusted deformations by material layer for each test section	47
Table 14. Summary of FE model parameters for rutting model calibration	76
Table 15. Summary of calibrated parameters and objective function values	86
Table 16. Predicted number of cycles to failure and <i>TBR</i> values for test section configurations with identical layer moduli	90
Table 17. Summary of parameters varied in parametric study.....	92
Table 18. Summary of parametric study results for 300-mm-thick-base.....	96
Table 19. Summary of parametric study results for 450-mm-thick-base.....	97
Table 20. Summary of parametric study results for 600-mm-thick base.....	98
Table 21. Summary of pavement properties for which the average maximum and minimum benefit that Geogrid provided relative to the unreinforced test section.	99
Table 22. Summary of parameters on EG	105

Preface

This report was prepared by Karen S. Henry of the Department of Civil and Environmental Engineering at the U.S. Air Force Academy, Colorado, Joshua Clapp and William Davids of the University of Maine and Lynette A. Barna of the Force Projection and Sustainment Branch, Cold Regions Research and Engineering Laboratory (CRREL), U.S. Army Engineer Research and Development Center (ERDC), Hanover, NH.

The authors gratefully acknowledge the sponsorship of the Federal Highway Administration (FHWA) and the participating state transportation agencies. In particular, the leadership and encouragement of the Maine Department of Transportation is greatly appreciated. The authors express special gratitude to Mr. Dale Peabody from the Maine Department of Transportation for his advice and support throughout this project. We acknowledge the contribution of Dr. Edel Cortez, who oversaw the construction of the test sections; and Mr. Troy Arnold, who helped construct the test sections and carried out most of the testing that generated the data analyzed in this project.

The report was prepared under the general supervision of Dr. Bradley Guay, Chief, Force Projection and Sustainment Branch; Dr. Justin Berman, Chief, Research and Engineering Division; and Dr. Robert E. Davis, Director, CRREL.

COL Gary E. Johnston was Commander and Executive Director of ERDC. Dr. James R. Houston was Director.

Unit Conversion Factors

Multiply	By	To Obtain
cubic feet	0.02831685	cubic meters
cubic inches	1.6387064 E-05	cubic meters
cubic yards	0.7645549	cubic meters
degrees (angle)	0.01745329	radians
degrees Fahrenheit	(F-32)/1.8	degrees Celsius
feet	0.3048	meters
foot-pounds force	1.355818	joules
gallons (U.S. liquid)	3.785412 E-03	cubic meters
inches	0.0254	meters
inch-pounds (force)	0.1129848	newton meters
miles per hour	0.44704	meters per second
pounds (force)	4.448222	newtons
pounds (force) per foot	14.59390	newtons per meter
pounds (force) per inch	175.1268	newtons per meter
pounds (force) per square foot	47.88026	pascals
pounds (force) per square inch	6.894757	kilopascals
pounds (mass)	0.45359237	kilograms
pounds (mass) per cubic foot	16.01846	kilograms per cubic meter
square feet	0.09290304	square meters
square inches	6.4516 E-04	square meters
square yards	0.8361274	square meters
tons (force)	8,896.443	newtons
tons (force) per square foot	95.76052	kilopascals

1 Introduction

Geogrids are currently being used by many transportation agencies to reinforce pavements, and varying degrees of associated benefit have been reported. Some organizations are considering their use; however, they desire more information on their cost-effectiveness. Investigations of Geogrid reinforcement of pavement have generally been of limited scope, and utilized thin asphalt concrete, thin or moderate base course thickness, and soft subgrades—see, for example, the summary of 15-years of geosynthetic-reinforced base research provided by Perkins and Ismeik (1997), also Vischer (2003) and Perkins and Cortez (2005). In one previous study, Perkins (1999a and 1999b) found that geosynthetic reinforcement of test sections with 75 mm of asphalt overlying 200–375 mm of base provided significant benefit when the subgrade had a California Bearing Ratio (CBR) of 1.5, but no improvement was noted when the subgrade had a CBR of 20.

A national Federal Highway Administration (FHWA), pooled-fund study, TPF-5(010), entitled ‘Structural Improvement of Flexible Pavements Using Geosynthetics for Base Course Reinforcement’ was therefore organized to assess the potential benefits of Geogrid base course reinforcement in flexible pavements that are more representative of state highway projects than most previous research—that is, more representative base and asphalt layer thicknesses in combination with a range of subgrade conditions.

Purpose and scope of project

The purpose of the national pooled-fund study TPF-5(010) was to provide missing data required to help determine whether geosynthetic reinforcement is beneficial at conditions typically encountered in and resulting from state highway construction—specifically, thicker base courses and asphalt layers than most previous research. The original research proposal developed in 2002 in consultation with several state transportation agencies, and requiring a total of over \$2.3 million, called for four phases of research on full-scale test sections failed by trafficking with a heavy vehicle simulator (HVS).

The original overall objectives of TPF-5(010) were:

- To determine whether and under what conditions geosynthetics (geogrids and geotextiles) used to reinforce the base layer increase the structural capacity of pavements typically constructed by state DOTs;
- To determine whether and under what conditions geosynthetic-reinforcement of the base increases the service life of pavements typically constructed by state DOTs;
- To measure in-situ stress and strain response of the pavement sections due to trafficking for use in current or future pavement design processes.

With focus on the typical asphalt and base layer thicknesses required in state highways, the four phases of research proposed in the original proposal were:

- Geogrid used in test sections with constant subgrade moisture content (Phase 1).
- Geogrid used in test sections with varied subgrade moisture content caused by freezing and thawing (Phase 2).
- Geotextile used in test sections with constant subgrade moisture content (Phase 3).
- Effect of subgrade strength on sections reinforced with Geogrid and geotextile (Phase 4).

Funding was provided for Phase 1 (only), and the Phase 1 research effort is the subject of this report.

Project objectives

The Phase 1 research utilized Geogrid reinforced base layers and unreinforced (control) base layers in test sections that were meant to have constant moisture content in the subgrade; and, hence a constant modulus value of the subgrade. As described in the report, the subgrade modulus values varied to some degree; however, great effort was made to hold them as constant as possible, and variations were documented. The research proposal called for an approximate target subgrade modulus value of 35 MPa (CBR value of approximately 3). Hence, the specific objectives of this project were:

- To determine whether geogrids increase the structural capacity of pavements typically constructed by state DOTs when they are used to reinforce the base layer, with the subgrade modulus value being held constant.
- To measure and publish in-situ stress and strain response of the pavement sections as a function of traffic loading for use in current or future pavement design processes.

Test sections were constructed on a relatively soft subgrade (resilient modulus values ranging from 35 to 70 MPa), with and without Geogrid reinforcement. Traffic was applied with a heavy vehicle simulator, while periodic measures of strains and stresses at various depths in the pavement section were made. The stresses and strains were measured in order to conform with requirements for future modifications to the National Cooperative Highway Research Program(NCHRP) 1-37A, Mechanistic-Empirical Design of New and Rehabilitated Pavement Structures (<http://www.trb.org/mepdg/>).

The research effort included the development of a three-dimensional (3D) finite element model that simulates the response of flexible pavements to traffic loading. The model includes Geogrid reinforcement. The results generated by loading the test sections with the heavy vehicle simulator were used to help calibrate the finite element model described in this report (also see Clapp 2007).

2 Background

Geogrid is used to reinforce soils in many applications, including embankments, levees, steep slopes, retaining walls, and roadways. When geogrids reinforce the base layer in flexible asphalt pavement systems, the most benefit is thought to result when there is good interlock of the granular base course and the grid—i.e., larger aggregate particles from the base partly protrude through the grid apertures (Figure 1). When good interlocking is achieved, the grid confines the aggregate so that lateral movement of the base course layer is significantly less during traffic loading than it would be without the grid. This results in improved performance of both the base and the subgrade layers (e.g., Giroud and Han 2004). Other than directly measuring interaction between aggregate and Geogrid in standard pull-out tests, there is presently no measure of the degree or quality of aggregate-grid interlock.



Figure 1. Close-up of Geogrid and base aggregate particles during construction. Aggregate particles protruding partly through the grid apertures suggest good inter-locking.

With lateral confinement of the base layer, there is less surface rutting, increased stiffness due to vertical loading and increased flexural stiffness. By restricting lateral and vertical deformations, the stress imposed by traffic is distributed over a wider area at the bottom of the base resulting

in lower stresses reaching the subgrade-- in both the horizontal and vertical directions. This improves the factor of safety with respect to bearing capacity failure of the subgrade; and, reduces the amount of punching and local shear failure. Hence, there is potentially very significant economic benefit of Geogrid base layer reinforcement, and motivation to better understand reinforcing mechanisms (Giroud and Han 2004).

Kinney et al. (1998a and 1998b) constructed laboratory test sections to examine the effects of Geogrid reinforcement on a model road weakened by spring thaw (CBR 1 from top of subgrade to 0.9 m deep). Two test sections had different geogrids located at the base/subgrade interface, while the third test section was an unreinforced control section. The base thickness tapered from 525 mm to 150 mm over the length of the control section and from 410 mm to 150 mm over the length of each reinforced section. The asphalt thickness was 61 mm in all sections. The test sections were then loaded with a falling weight deflectometer (FWD), and modulus values of the pavement layers were estimated. These estimates were then used to predict tensile strains in the asphalt layer as a function of traffic loading to estimate the benefit of the reinforcement. They found that the traffic benefit ratio (TBR), defined as the ratio of the number of loading cycles to failure that a reinforced section carried to an equivalent unreinforced test section, ranged from greater than 10 at a base layer thickness of about 250 mm to about 2 at a base layer thickness of about 350 mm for the stiffer of the two geogrids tested (modulus of 270 KN m⁻¹). The less-stiff Geogrid (modulus of 197 KN m⁻¹) provided a TBR of 7 to 1.2 for the same range of base thickness compared to the control. They estimated that reinforcement would provide no measurable benefit in base layers thicker than 400 mm.

Perkins (1999a and 1999b) built and tested pavement sections in a large concrete box to compare the performance of two geogrids and a geotextile in reinforcing the base layer. A 40 kN load was applied cyclically to a stationary plate on the pavement surface to simulate a wheel load. Test sections were instrumented with stress and strain cells. Base layer thickness was 200 mm, 300 mm, or 375 mm. Asphalt thickness was about 75-80 mm. Placing a Geogrid 100 mm above the bottom of a 300 mm thick base layer resulted in lower surface ruts than when it was placed at the base-subgrade interface—the reinforcing mechanisms apparently mobilize at a smaller surface rut depth for grid at the shallower depth. In

addition, reinforcing benefit decreased with increased base layer thickness. Maximum TBR values ranged from 8 to 56 for the soft subgrade with CBR of 1.5, and there was little or no improvement for the subgrade with a CBR of 20.

Maine DOT (2006) reported the results observed from geogrid-reinforced paved highway sections. Several sections of highway were reclaimed and Geogrid was placed at the bottom of the new gravel base layer in each one. Base thicknesses ranged from 420 mm to 750 mm and asphalt thicknesses ranged from 95 mm to 165 mm. Construction was performed from 1998 to 1999 and inspections were performed periodically through 2005. Comparing sections with similar asphalt and base layer thicknesses indicated that Geogrid improved the composite pavement stiffness, as determined by falling weight deflectometer (FWD) testing. In general, Geogrid sections had less rutting than control sections, but quantitative conclusions could not be made due to section variability. None-the-less, based on the observed results, Maine DOT recommended that Geogrid be used to provide additional support to roadways that are “susceptible to deformation.” Whether a roadway is susceptible to deformation is based on past performance of a road—e.g., observed severe distortion.

Helstrom et al. (2006) instrumented and then monitored reconstructed highway test sections in Maine for four years. For all test sections, the asphalt layer thickness was 150 mm, while the base layer thickness was either 300 mm or 600 mm. The subgrade soils were considered to be of poor quality. Prior to reconstruction, the studied portion of the existing roadway had suffered several local bearing capacity failures, resulting in substantial rutting and pavement cracking. The subgrade soils were moist and plastic with standard penetration blow counts as low as 10. The subgrade soils for most of the boring samples were classified as American Association of State Highway and Transportation Officials (AASHTO) A4. The location of the Geogrid was either at the bottom or middle of the base layer. Strain gages were mounted to the Geogrid to examine both construction and long-term effects.

Placement and compaction of the base resulted in the development of strain in the Geogrid (Helstrom et al. 2006). During construction, Geogrid located at the base-subgrade interface developed at least as much strain as that located in the middle of the base layer. After construction, strains increased after paving in sections that had a 300 mm thick base layer, but

did not in sections that had a 600 mm thick base layer. Geogrid located at the bottom of base layers developed as much or more strain over the four years that they were monitored (post construction) than when located in the middle of base layers. Geogrid with the thinner base layers developed more strain over time than with the thicker base layers.

Other geosynthetic reinforcement research has focused on finite-element (FE)-model-simulation of geogrid-reinforced pavements. Two-dimensional (2D) FE models were used by Barksdale et al. (1989), Miura et al. (1990), Wathugala et al (1996), Ling and Liu (2003), Park and Lytton (2004), and Perkins et al. (2005). All 2D models are based on simplifications and assumptions to relate the three-dimensional (3D) pavement system to a 2D model. Perkins et al. (2005) presented a rational strategy to account for observed performance improvements with geogrid. The effects of base layer compaction as well as improved performance over the course of trafficking were incorporated into a procedure that predicted the response of a geogrid-reinforced test section. The predictions from this modeling agreed with observations of the test sections reported by Perkins (1999a and 1999b) and demonstrated the general ability of the method to describe reinforcement mechanisms.

Three-dimensional FE models have the potential to more realistically capture the state of stress in pavement structures than 2D FE models, and have seen increasing use in recent years by Dondi (1994), Perkins (2001), and Perkins and Edens (2003). However, the increased computational complexity of 3D FE models poses barriers to their routine use. Perkins (2001) implemented plasticity in a 3D model, but was only able to apply 10 traffic cycles to the reinforced model due to the computational time required.

In conclusion, Geogrid is often beneficial when used to reinforce supporting soil layers in pavement systems. However, field trials have not provided conclusive evidence that Geogrid reinforcement of the base layer results in less surface rutting for relatively thick pavement sections (e.g., 300-mm-thick and greater) nor have they produced quantitative cost-benefits of utilization of geogrid-reinforced base layers.

3 Experimental Design and Test Section Construction

The experimental design of the test sections was based on the assumption that a constant subgrade modulus (resulting from constant moisture content and density) could and would be maintained throughout the lifetime of the project. Although the proposal stated that the subgrade would have an approximate subgrade modulus value of 35 MPa, the pavement design on which the construction of the test sections was based had an assumed subgrade modulus of 41.4 MPa (CBR of approximately 4) and a required design life of 3×10^6 equivalent 80 kN single axle loads (ESALs). According to the 1993 AASHTO Design Guide, the given conditions produce a required structural number of 4.3, and in order to achieve this with a 90% reliability, standard deviation of 0.45 and a terminal serviceability index, p_t , of 2.0, a 600 mm base layer and 127 mm asphalt layer are required. This configuration produces a structural number of 4.5. Eight test sections were constructed for this study based on this design, with asphalt thicknesses slightly less and slightly greater than that required by design and base course thickness of the required design and half that required (Table 1). One of the motivations for this configuration of test sections is the potentially great savings if asphalt thickness can be decreased due to Geogrid reinforcement of the base.

In addition to the requirement of constant subgrade modulus, the location of the Geogrid in the pavement structure was also held ‘constant’ by being placed between the base and subgrade layers. (Also recall that in the field study conducted by Helstrom et al. (2006), Geogrid located at the bottom of base layers developed as much or more strain over the four years that they were monitored than when located in the middle of base layers.) Two asphalt and base thicknesses were used: 102 and 152 mm for the asphalt; and 300 and 600 mm for the base layer. Each combination of asphalt and base thickness was constructed with and without geogrid. The subgrade thicknesses listed in Table 1 indicate the depth to the concrete floor of the test basin in which the test sections were constructed—the total thickness each test section was 2.44 m.

Table 1. Test Section configurations.

Test Section	Layer Thicknesses (mm)			Geogrid
	AC	Base	Subgrade	
1	150	300	1990	No
2	100	300	2040	No
3	150	300	1990	Yes
4	100	300	2040	Yes
5	150	600	1690	No
6	100	600	1740	No
7	150	600	1690	Yes
8	100	600	1740	Yes

Test section construction

The test sections were constructed at ERDC-CRREL in Hanover, New Hampshire, in the Frost Effects Research Facility (FERF). The FERF is a 2,600 m² climate-controlled building dedicated to full-scale infrastructure-related research. Each test section was 7.92 m long in the direction of traffic, 3.20 m wide perpendicular to traffic and 2.44 m deep (X, Y and Z directions, respectively). The area within each test section where traffic loads were applied, referred to as the test window, was 0.91 m wide. Figure 2a and Figure 2b show plan and cross-sectional views of the test sections, respectively. Details of test section construction are provided in Henry et al. (2008).

For the previous research project conducted in the FERF, the test basin was lined with an impermeable membrane to prevent drainage, and a 250 mm layer of gravel was placed in the bottom of the test basin (below the subgrade) to facilitate moisture distribution. The layer of gravel (drainage layer) is separated from the overlying subgrade by a needle-punched geotextile. For this project, the geomembrane was removed from the side walls to a depth of 1.5 m from the asphalt surface, and was left in place below that depth. The subgrade thickness was not considered to be a design variable, although it did vary among sections since the total thickness was equal for all sections. The bottom gravel layer was not considered when performing analyses of the test sections (e.g., back-calculation of modulus values of pavement layers).

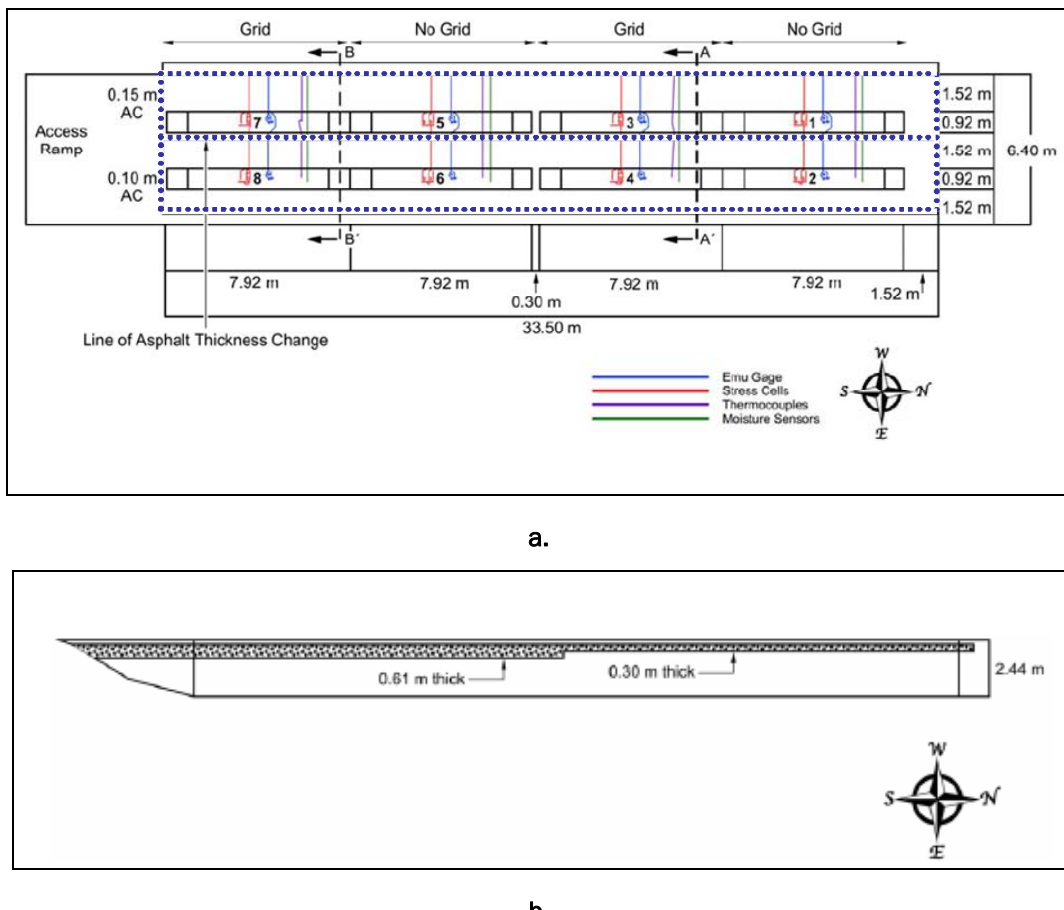


Figure 2. a) Plan view of the eight test sections indicating grid and non-grid sections; b) profile view of the test sections showing the varying pavement and base thicknesses.

Soils and geogrid

The materials used to construct the test sections were obtained locally in the Hanover, NH area (Figure 3). The subgrade material classified as silt (ML under Unified Soil Classification System (USCS) guidance or AASHTO A-4). The base material was an unbound crushed stone USCS classification GP-GM, and AASHTO A-1), and met New Hampshire specifications for base course. Table 2a and 2b provide details about the subgrade and base layers.

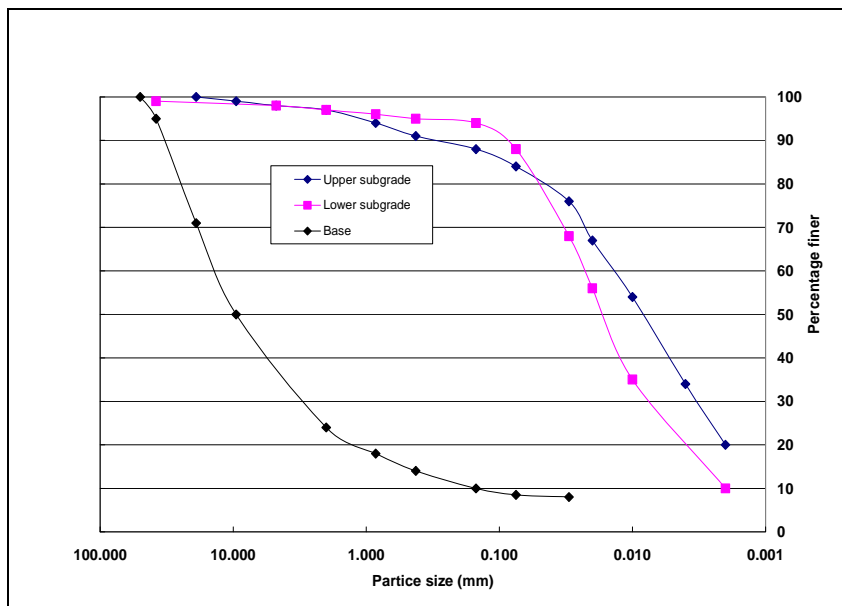


Figure 3. Grain size distribution of subgrade and base course soils. The 'upper subgrade' refers to the material that was placed beginning at a depth of 1.52 m from the top of the asphalt, while the 'lower subgrade' was already in place at the time of construction.

Table 2a. Subgrade soil properties. Dry density and optimum moisture content were determined according to AASHTO T-180 (Modified Proctor).

AASHTO	A-4
USCS	ML
Spec. Gravity	2.72
LL (%)	28
PI	8
Optimum moisture content (%)	13.3
Maximum dry density (kg/m ³)	1922
% passing ¾"	98.6
% passing #200	73.3

Table 2b. Base soil properties. Dry density and optimum moisture content were determined according to AASHTO T-180 (Modified Proctor).

AASHTO	A-1
USCS	GP-GM
Spec. Gravity	2.7
LL (%)	Not applicable, fines non-plastic
PI	
Optimum moisture content (%)	5
Maximum dry density (kg/m ³)	2383
% passing ¾"	82
% passing #200	5.4

The Geogrid installed at the base-subgrade interface was Tensar® BX1200 (Tensar Earth Technologies 2005), a commercially available product (Figure 4; Table 3. Properties of geogrids used in test sections.). It was selected for the ease of affixing instrumentation (strain gages) to it, and because it has been used in previous studies, allowing comparison of the results in this study with others.

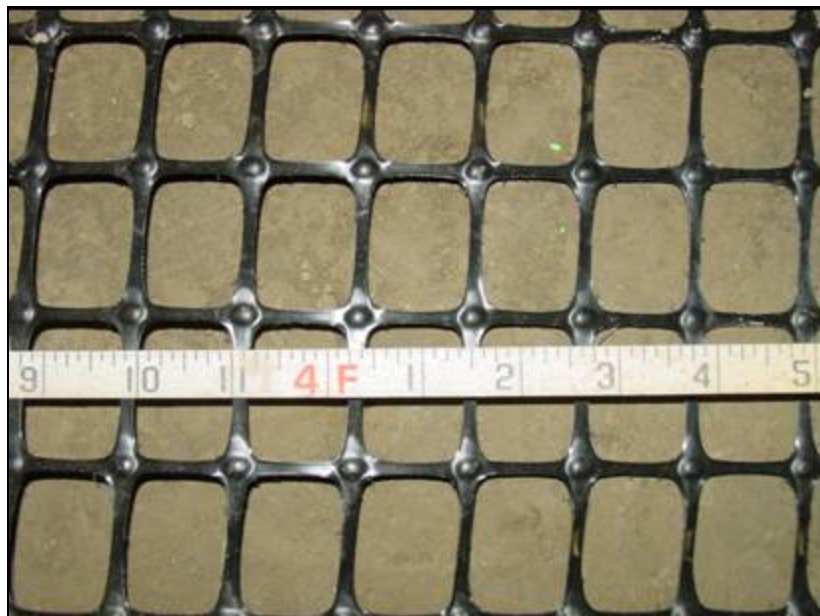


Figure 4. Tensar® BX1200 geogrid.

Table 3. Properties of geogrids used in test sections.

Aperture size mm		Wide-width tensile strength at 2% strain*, kN m ⁻¹	
Machine Direction	Cross-machine direction	Machine Direction	Cross-machine direction
25	33	6.0	9.0

*Determined according to ASTM D6637 (2001).

Asphalt

The asphalt binder grade was PG 64-28. This is commonly used for highway construction by paving contractors in the Hanover, New Hampshire area. The asphalt mix met New Hampshire specifications for a base course and surface course. Measured gradations provided by the Maine DOT, based on tests of an asphalt core, are provided in Table 3. Tests on the asphalt cores also indicated that the asphalt aggregate had a bulk specific gravity of 2.6 and an average air voids content of 2.1 percent.

Table 3. Asphalt concrete gradation measured on asphalt cores taken after paving. (There was no distinction between base and surface course.)

Sieve size	Percentage passing
31.8 mm	
25.4 mm	100
19.1 mm	98
12.2 mm	92
9.5 mm	85
4.75 mm (No. 4)	57
2.36 mm (No. 8)	43
0.60 mm (No. 30)	23
0.35 mm (No. 50)	14
0.152 mm (No. 100)	8
0.075 mm (No. 200)	5
% Asphalt Content	5.8

Addition of water to subgrade after construction

After the test sections were constructed, FWD analyses indicated that the subgrade modulus values ranged from approximately 109 to 138 MPa, whereas the desired value was 34.5 MPa. Water was then added to the subgrade over an extended period to reduce the stiffness to come as close as possible to the original target modulus of approximately 34.5 MPa. To add water, a 150 mm wide strip of asphalt was removed from along the sides of the test basin, to expose the base layer of crushed rock. Short sections of PVC tubing were installed in the center of the test basin area to a depth of 50 mm into the subgrade, to enable monitoring during water addition to assure that it never resulted in saturation of the base aggregate layer. During the time period in which water was being added to the subgrade, the volumetric soil moisture sensors were monitored, and FWD tests were performed periodically on the test sections to obtain back-calculated estimates of the subgrade resilient modulus values. See Henry et al (2008) for details on this procedure. A complete reporting of back-calculated resilient modulus values during this process, as well as throughout the testing program, is provided in Section 5.

Soil and asphalt instrumentation

Each test section was instrumented to measure deformation, stress, temperature and moisture content with depth. The locations of all the sensors are documented in detail in Henry et al. (2008, Appendix A). Figure 5 shows a plan view and cross section of the portion of one Geogrid test section in which instrumentation was installed. A summary of each type of sensor installed follows.

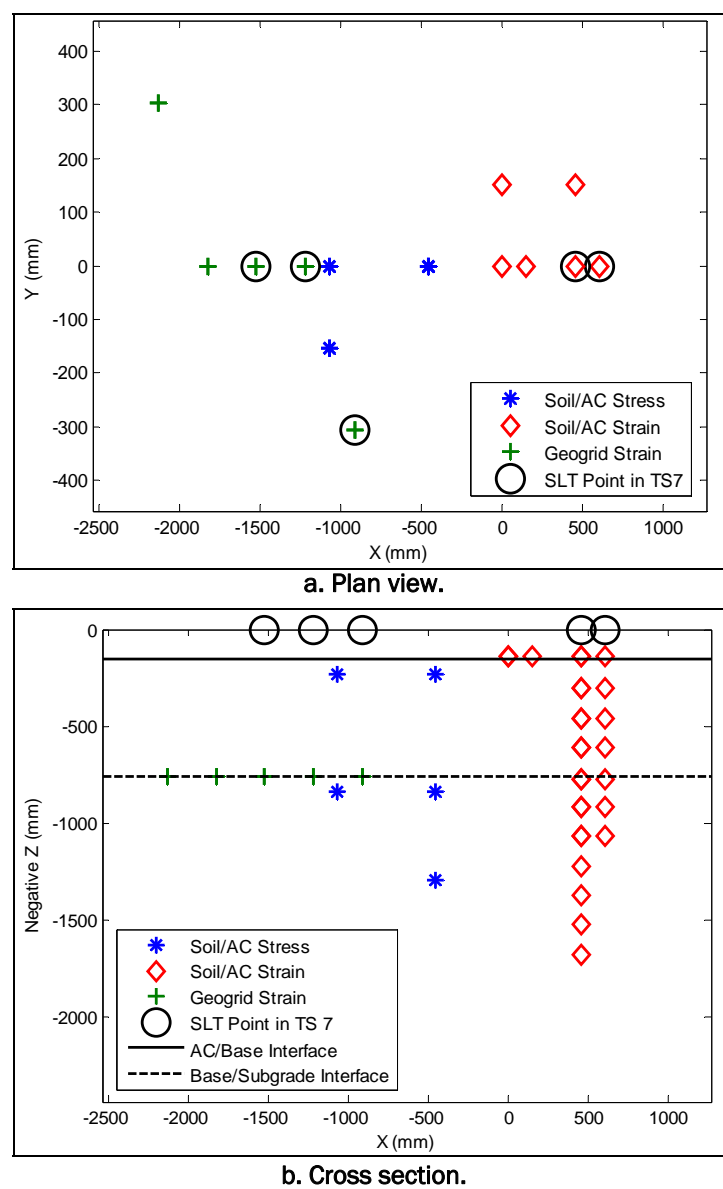


Figure 5. Locations of instrumentation of a Geogrid test section.
 a. Plan view. b. Cross section. The locations of static load tests are also shown.

Temperatures

Temperature sensors (type T, copper-constantan thermocouples, fabricated and installed by ERDC-CRREL) were installed in the test sections to continuously monitor the air, asphalt and soil temperatures throughout the project. Properties of asphalt concrete change with temperature (e.g., Roberts et al. 1996); hence, an effort was made to keep the temperatures constant to minimize temperature-induced distress, and temperature measurements were used to account for temperature changes that did occur.

Moisture content

Moisture content sensors were used to continuously monitor moisture content during the life of the project. ECH₂O™ soil moisture sensors (Echo probes), model EC-20 (200-mm-long), were installed in the test sections to record volumetric soil moisture content in the base course and sub-grade. The accuracy of EC-20 probes in medium-textured soil types is typically $\pm 4\%$, and the resolution is 0.1%. At the conclusion of traffic testing, a forensics investigation was conducted to characterize the soil. Measurements made included soil moisture (by weight) and soil density. These measurements were then used to calculate volumetric soil moisture content. The calculated volumetric soil moisture values were compared to the readings obtained from the moisture sensors embedded in the test sections, and resulted in corrections to two volumetric soil moisture sensors in the mid-base in Test Sections 2 and 5. This is not uncommon given that the properties of the base material are considerably different than ‘medium-textured’ soil. The forensics investigation is described in Appendix B.

In combination with modulus estimates provided via FWD testing, the soil moisture sensors helped determine that moisture needed to be added to the subgrade at the end of construction. They were also used to help track when more water should be added to the test sections to make up for water losses that occurred during the project, and water was added between the trafficking of Test Sections 3 and 1.

Deformation of soil and asphalt

Electromagnetic induction (emu) coils were installed to measure vertical and horizontal deformations. Deformation measurements were made

when the pavement was not loaded and when a static wheel load was applied. The ϵ mu coils were manufactured and calibrated at ERDC-CRREL. The ϵ mu coils do not touch each other, but “float” in the soil, similar to small stones embedded in a fine soil mass. They work in pairs or sets. One coil, called the sender, is energized by an external power supply. The companion coil(s), the receiver(s), are located within the electro-magnetic field of the sender and produce an induced current that is proportional to the distance between the coils. When a layer deforms, the change in inter-coil distance is detected by a change in induced voltage, which increases as the distance between coils decreases. To measure deformation in the asphalt layer, manual measurements were made using a detached individual ϵ mu coil placed on the surface. In addition, the readings were used to determine the permanent and elastic strains in the asphalt and soil layers. The ϵ mu coils and the measurement system used in this project were the same as used in a previous project, described in detail in Janoo et al. (2003), which includes detailed calibration information, see: <http://www.crel.usace.army.mil/library/technicalreports/TR03-5.pdf>.

Soil stress measurements

Geokon[®] Earth soil pressure cells, Model 3500 with a semi-conductor transducer and 0 to 5 Volt output range, were installed in the base course and subgrade of each test section to measure stress. The pressure cells consist of two circular stainless steel plates welded together around the periphery enclosing a fluid connected to a pressure transducer through a high pressure stainless steel tube. The pressure transducer outputs a voltage that is calibrated to produce a stress measurement.

Every test section was instrumented with 7 pressure cells — each cell measured stress in one direction at one location. The location of each cell was tabulated by Henry et al. (2008). The pressure cells were installed in three perpendicular directions at three depths —in the direction of traffic (longitudinal), perpendicular to the direction of traffic (transverse) and vertically. One pressure cell was installed 1,250 mm below the asphalt surface in each test section to measure vertical stress. The pressure cells in the transverse direction were offset 152 mm to avoid measurement directly beneath the wheel load, in which case the transverse component of stress may be negligible.

Geogrid strain gages

Ten electrical resistance strain gages were fastened to the Geogrid in each of the four Geogrid test sections to make longitudinal and transverse strain measurements on the top and bottom of the grid. Five strain gages were fastened on the upper side of the geogrid, and five were fastened at corresponding locations on the lower side of the geogrid. The strain gages were Texas Measurements model FLA-5-23, which are capable of measuring up to 3% strain. Each gage had pre-soldered lead wires that were connected to the ERDC-CRREL data acquisition system. Initial resistance readings on the strain gages verified that the strain gages were operational.

In each reinforced test section, ten strain gages were attached to Geogrid ribs according to the procedure described by Helstrom et al. (2006). (Caution: proper respiratory protection is required to affix the strain gages to the ribs.) These gages were installed in pairs, such that each instrumented rib had one strain gage mounted on the top and one on the bottom. The goal was to measure axial strains, so the effect of bending deformations was minimized by taking the average strain value from a pair, where possible. The central strain gage pair was oriented in the X direction and the other four strain gage pairs were oriented in the Y direction. Two of the pairs oriented in the Y direction were offset 300 mm from the centerline of the wheel path. This provided strain data at a location away from where the maximum rut depth was expected to occur.

4 Trafficking

Traffic was applied to each test section using ERDC-CRREL's heavy vehicle simulator (HVS), Mark IV (manufactured by Dynatest, Inc.) (Figure 6). It is 23 m long, 3.7 m wide, 4.1 m high, and weighs roughly 50,000 kg. The dual truck tires are mounted to the test carriage on the underside of the test beam. The test carriage travels back and forth along the test beam to apply traffic either uni- or bi-directionally. In this project, it was applied in one direction only.



Figure 6. Mark IV heavy vehicle simulator (HVS) mounted with dual truck tires (inset).

During trafficking, the HVS applied the wheel load at a speed of 12.9 km/hr and a tire pressure of 689.5 kPa. Approximately 600 passes per hour were applied for 22 hours per day. During testing, the HVS was shut down about two hours each day, four hours once a week and six hours once a month to perform required maintenance.

The HVS was programmed to simulate wander within the traffic lane. The wander pattern was kept to a 0.9-m-width, with most of the traffic concentrated in the middle. Within the 0.91-m traffic loading window 30% of the wheel loads were applied in the center 200 mm, then 15%, 11% and 9% in 100-mm-wide strips to each side of the center 200 mm. There were no loads applied in the outer 150 mm widths of the test window.

In order to obtain accurate performance information, each test section should be trafficked to ‘failure,’ defined as a 12.5 mm rut depth. The rut depth is measured as the relative difference in surface elevation of the asphalt between the centerline of the wheel load path, where the traffic was concentrated, and 600 mm in a perpendicular offset to the wheel path. Hence, the rut depth also included any surface heave that occurred during trafficking.

Time and financial constraints were considered in establishing the trafficking protocol. The pavement sections were designed for 3 million ESALS (i.e., 3 million cycles with a 40 kN wheel load). This was an unacceptably large number of cycles, so heavier wheel loads were deemed necessary in order to reach 3 million ESALS in a timely manner.

The initial wheel load applied was 49 kN, which represents one wheel in the maximum legal single-axle load allowed on Interstates in several states for vehicles with gross weight under 326 kN of 98 kN. The wheel load was then increased to 71.2 kN after the application of 164,000 cycles, followed by an increase to 93.4 kN at 364,000 cycles. NCHRP (2004a) warns against increasing the axle load to values far above realistic loads because this may initiate failure mechanisms that would never manifest under realistic loads. However, the need to fail the test sections took priority in this accelerated pavement testing.

Test protocol

A test protocol was developed that described the measurements to be collected prior to, during, and at the conclusion of the trafficking program; the test protocol, provided in Appendix A was the initial version, and throughout the testing period the protocol was modified as necessary. A series of baseline measurements were made to record the stress and strain readings of the pavement layers and Geogrid in an unloaded state prior to positioning the HVS on the test section. FWD tests were also conducted to document the subgrade and base modulus values prior to trafficking. A surface level survey was conducted and profilometer readings of the area to be trafficked were also taken prior to trafficking.

The HVS was then positioned on the test section, and another set of unloaded stress and strain measurements were collected. This unloaded data was needed to determine the permanent deformations throughout the trafficking period.

Static load tests (SLTs) in which the wheel load at the appropriate tire pressure was applied to the pavement surface were conducted prior to the start and at fixed intervals during trafficking of each test section (Table 4). These tests were performed with the wheel positioned directly above the vertical and longitudinal stacks of emu coils in each test section, and other points of interest, i.e. directly above a strain gage on a Geogrid rib. Every static load test was preceded by a test in which no load was applied but the emu and/or strain gages were read. In this manner, these tests provided stress and deformation data when the wheel load was applied statically (as opposed to the response under a moving wheel load). This was necessary since the FE model used in this study is based on statically applied loads. Further, it is possible to determine permanent deformation due to prior loading from the unloaded test results.

Table 4. Static load test intervals.

Wheel Load (kN)	Pass Number	Axle Load Equivalency Factor*	Equivalent Single Axle Load
48.9	12	2.322	27.9
	250		581
	12,000		27,900
	24,000		55,700
	74,000		172,000
	134,000		311,000
	164,000		381,000
71.2	214,000	11.5	956,000
	264,000		1,530,000
	364,000		2,680,000
93.4	414,000	38.2	4,590,000
	464,000		6,500,000

*Note: The equivalency factors were determined according to AASHTO (1993), Appendix D (Table D.1).

During the SLTs, the wheel was aligned over stacks of instrumentation and lowered onto the pavement surface. The magnitudes of the load and tire pressure were automatically adjusted via the HVS computer system until 48.93 kN and 690 kPa were reached, respectively, which typically took about 60 to 90 seconds. The operator then manually initiated the applicable gage recording process. All applicable gages (emu coils, stress cells and Geogrid strain gages) were read both before and during the

application of the static wheel loads, allowing the relative effect of the wheel load in the SLTs to be determined.

Permanent surface deformation

Rut depths were recorded periodically as a function of completed passes to satisfy the project objective and to determine when failure occurred. While deformations were measured in the pavement layers using the ε mu coils, rut measurements were also made on the surface along the length of the test section using a laser profilometer.

The laser profilometer used to measure surface deformations of the test section during traffic testing (commercially available from Dynatest, Inc.) comprises an aluminum beam with a stepper motor/cable system that moves a small carriage on the beam. The beam is 3-m-long, rests on three feet, is about 45 cm above the ground, and is connected to a notebook computer (Figure 7). A small infrared laser range finder is mounted on the carriage. The speed of the carriage is controlled as it collects about 530 range data points in 5 mm intervals over the length of the run. A notebook computer automatically logged data related to rut depth measurement whenever the profilometer operated. The beam's feet were placed on the same specifically marked points on the ground when measurements were taken at pass level intervals. At each interval, profilometer measurements were collected at 20 transect locations along the length of the test section.

Level surveys

Level survey measurements were recorded prior to and at the completion of traffic testing. Readings were taken at the specially marked profilometer points located along the edge of each test section and over the ε mu coil. These measurements were used to determine the elevation of each test section and, should they occur, monitor any large movements of the test section. All elevations were measured to the nearest 3 mm.

The average change in elevation of each test section taken at the marked profilometer points (away from the trafficked area) and standard deviations are listed in Table 5. Six consecutive data points in Test Section (TS) 6 indicated unreasonably large (i.e. 24 – 53 mm) changes in elevation. These values may reflect localized damage to the pavement surface that occurred after the completion of trafficking. Thus, the values were removed from the data set. The standard deviations are generally

close to or less than the error tolerance of the measurements. The movements of the test sections were small when the total thickness of test basin is considered. However, these movements have significant implications regarding the deformations measured by the emu coils. Hence, they were used when adjusting the individual layer thickness values when analyzing the behavior of the system.

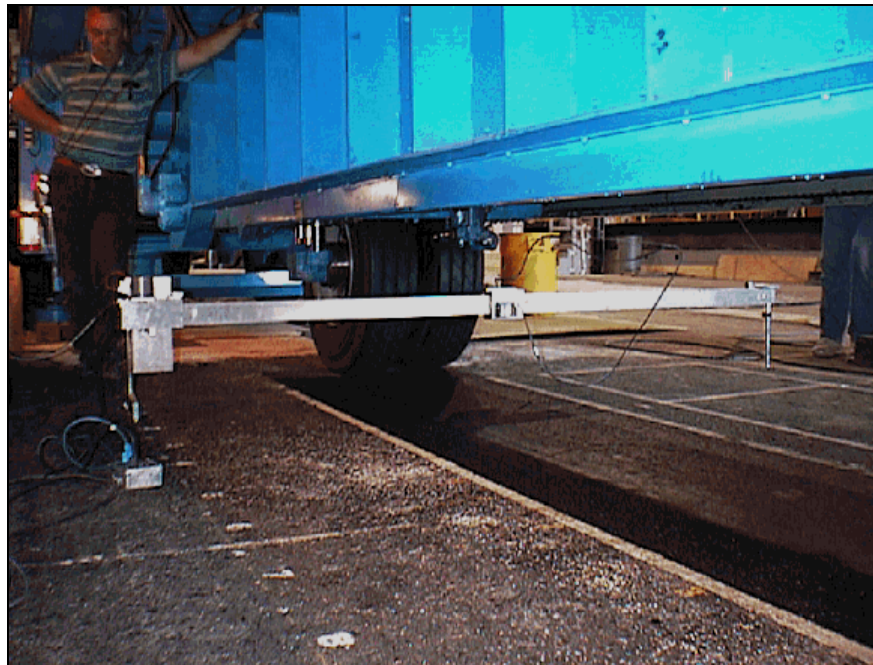


Figure 7: Surface deformation laser profilometer measurement device.

Table 5. Average change in elevation for each test section away from the trafficking area by level survey.

Test Section	Avg. Elev. Change (mm)	Standard Deviation (mm)
1	-4.1	1.2
2	10.5	3.8
3	-20.4	3.7
4	17.9	1.4
5	21.6	1.3
6	-6.0*	0.5*
7	12.5	1.3
8	6.6	1.3

* Invalid data points removed from calculations

5 Test Results

Overview of traffic testing

The trafficking program began upon completion of the moisture conditioning stage. The testing progressed from the thinnest asphalt and base layers without and with grid, respectively, to the thickest asphalt and base layers without and with grid. Hence, Test Section 2, with 100 mm of AC and 300 mm of base, unreinforced, was the first section trafficked. It failed and traffic stopped at 214,000 passes. Test Section 4, identical to Test Section 2, except for the presence of Geogrid at the bottom of the base, was trafficked to failure at a total of 263,000 passes.

Trafficking with the HVS was dogged by several delays from breakdowns requiring maintenance throughout the test program. In addition, there was a four-month-delay between the trafficking of Test Section 4 and Test Section 1, from mid-July to late November 2006, when another project utilized the HVS.

The soil moisture and temperatures were monitored continuously throughout the test program. When the HVS needed repairs during a trafficking phase, causing intermittent delays in traffic loading, profilometer readings were also made immediately prior to the re-start of trafficking.

FWD testing was performed immediately prior to the application of traffic and, as soon as possible after failure of a test section in order to monitor the modulus of the subgrade, the exception occurred following the trafficking of Test Section 4, in which there was a four-month delay after it failed before FWD testing was done. Table 6 lists the trafficking dates and the dates on which FWD tests were performed. In all, the trafficking program required 26 months to complete.

Table 6. HVS trafficking and FWD test dates.

	Description (asphalt/base)					Completed	FWD tests	
Section	mm	Grid	Start Date	Delays	Stop Date	Passes (x1000)	Before	After
2	102 / 300	N	5/17/06	None	7/1/06	214	5/15/06	7/05/06
4	102 / 300	Y	7/07/06	None	7/28/06	263	7/05/06	11/29/06
1	152 / 300	N	12/11/06	12/15/06 - 1/12/07, 1/22/07 - 2/23/07*, 2/23/07 - 3/11/07*	4/6/07	414	12/06/06	4/10/07
3	152 / 300	Y	5/25/07	Delay before testing to add water to subgrade	7/10/07	424	4/16/07	7/11/07
6	102 / 600	N	7/18/07	8/20/07- 9/18/2007	10/9/07	464	7/11/07	10/10/07
8	102 / 600	Y	10/19/07	None	2/12/08	464	10/10/07	2/14/08
5	152 / 600	N	2/19/08	11/20/2007- 1/24/2008	4/14/08	464	2/14/08	4/14/08
7	152 / 600	Y	5/12/08	None	7/3/08	464	5/07/08	7/3/08

*Estimated date based on email records.

As a result of the modulus values and moisture content monitoring, it was deemed necessary to add water after the trafficking of Test Section 1, as the subgrade modulus values were increasing significantly, and these were accompanied by decreasing volumetric moisture contents (see Section 5).

The reference air temperature and pavement and soil temperatures are presented in Appendix B. The average and standard deviation reference air temperatures were 21.6 °C and 1.8 °C, respectively. The minimum reference air temperature recorded was 15.1 °C on 16 November 2007, and the maximum was 28.4 °C on 3 August 2007.

The survivability of the stress and strain gages was generally very good, with the exception of the Geogrid strain gages in TS 4. In this section, the gages were inadvertently wired to a live voltage source that caused all but one gage to fail. The survivability of each gage or reading is presented in Table 7 and Table 8 for the εmu coils and the Geogrid strain gages, respectively. Note that the εmu readings depend on the survival of two gages, so results are based on the validity of the εmu reading for a

particular layer rather than the survivability of a single gage. All of the Geokon stress cells survived through the project, so survivability is not presented.

Table 7. Validity of ϵ_{mu} readings at the end of trafficking for each test section.

	TS 1	TS 2	TS 3	TS 4	TS 5	TS 6	TS 7	TS 8
ϵ_{xx} 1								
ϵ_{xx} 2								
ϵ_{xx} 3	NG							
ϵ_{xx} 4						NG		
ϵ_{xx} 5								
ϵ_{xx} 6					NG			
ϵ_{xx} 7	NG							
ϵ_{yy} 1								
ϵ_{yy} 2								
ϵ_{yy} 3					NG		NG	
ϵ_{yy} 4						NG		NG
ϵ_{yy} 5								
ϵ_{yy} 6					NG		NG	
ϵ_{yy} 7	NG	NG						NG
ϵ_{zz} 1								NG
ϵ_{zz} 2					NG	NG		
ϵ_{zz} 3					NG	NG		
ϵ_{zz} 4						NG		
ϵ_{zz} 5					NG			
ϵ_{zz} 6					NG			NG
ϵ_{zz} 7								NG
ϵ_{zz} 8								
ϵ_{zz} 9								
ϵ_{zz} 10								

* NG: No good (i.e. failed gage)

Table 8. Survivability of Geogrid strain gages in reinforced test sections.

	TS 3	TS 4	TS 7	TS 8
Gage 1	TEMP	NG	TEMP	NG
Gage 2	TEMP	NG	TEMP	TEMP
Gage 3	TEMP	NG		TEMP
Gage 4	NG	NG		TEMP
Gage 5	NG	NG	TEMP	TEMP
Gage 6	TEMP	NG	NG	
Gage 7	NG	NG	NG	NG
Gage 8	NG	NG		NG
Gage 9	NG	TEMP		NG
Gage 10	TEMP	NG		

* NG: No Good (No Valid Data Recorded)

TEMP: Temporarily Functioned during the Trafficking Period

Modulus estimates and water content determinations

As discussed above, the FWD was used to monitor base and subgrade modulus values during the subgrade softening procedure and throughout the test program. The FWD tests were performed at the same locations for the duration of the test program—on the north end of each test section in the transition zones where the wheel load was initially applied (Figure 8).

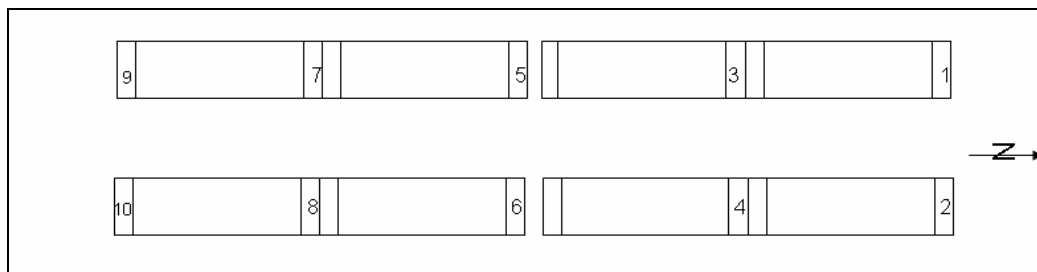


Figure 8. Plan view showing the test area, test sections, and FWD points (labeled 1 through 10). The FWD points 1 through 8 are on the northern transition zone of the test section labeled with the same number.

The modulus values were back-calculated with the commercially-available ELMOD 5 program from Dynatest utilizing the Odemark-Boussinesq method of equivalent thickness, in which the outer geophone readings are used to determine the non-linear characteristics of the subgrade, and the inner geophones are used to determine the upper pavement layer moduli (Dynatest International 2005). The depth to bedrock was fixed at 2.44 m. The asphalt and base layer thicknesses were also fixed at the values

specified in the proposal. The pavement modulus value was held constant at 3,584.6 MPa at 21.1 °C, as measured in the laboratory on a core of asphalt retrieved after construction (Henry et al. 2008). The asphalt temperatures, measured at the base of the asphalt within two hours of the FWD tests, were inserted into the ELMOD data files, and the ELMOD software adjusted the pavement modulus value accordingly.

Figure 9 shows the volumetric moisture content of the subgrade at depths of 840 to 890 mm from the top of the subgrade for each of the eight test sections. The water contents averaged around 30 percent for most of the test program, with a relatively low water content occurring in Test Section 7 of about 23 percent.

Figures 10 through 13 show the modulus values estimated as described above for the subgrade and base layers for the 300 mm base (Figure 10 and 11; Test Sections 1-4) and 600 mm base (Figure 12 and 13; Test Sections 5-8), respectively. The dates on the x-axis were matched, and the correlation of water content to subgrade modulus is apparent. These figures include the moisture conditioning phase immediately after construction but prior to testing, as well as values measured during the trafficking program. (Note that the first traffic was applied to Test Section 2 on 18 May 2006.)

The estimated modulus values of the subgrade correlate strongly with the water content measurements also made in the subgrade. Note that the subgrade modulus during testing of Test Section 1 (300 mm base with 150 mm asphalt, no grid) was approximately twice that of its matching grid-reinforced test section, Test Section 3—about 70 MPa vs. 38 MPa. This is significant when interpreting results.

Since the depth to bedrock was fixed, and the dynamic asphalt modulus value at a specific temperature was also fixed, as were the asphalt and base layer thicknesses in the Elmod analysis program, there was considerable variability in the estimated base layer modulus values among the tests (Figure 11 and 13). However, the modulus values of the reinforced base layers were generally greater than those of the unreinforced control sections that had the same asphalt and base thicknesses. Exceptions occurred immediately after the testing of the grid reinforced test section as all base modulus values decreased immediately after trafficking, as discussed below.

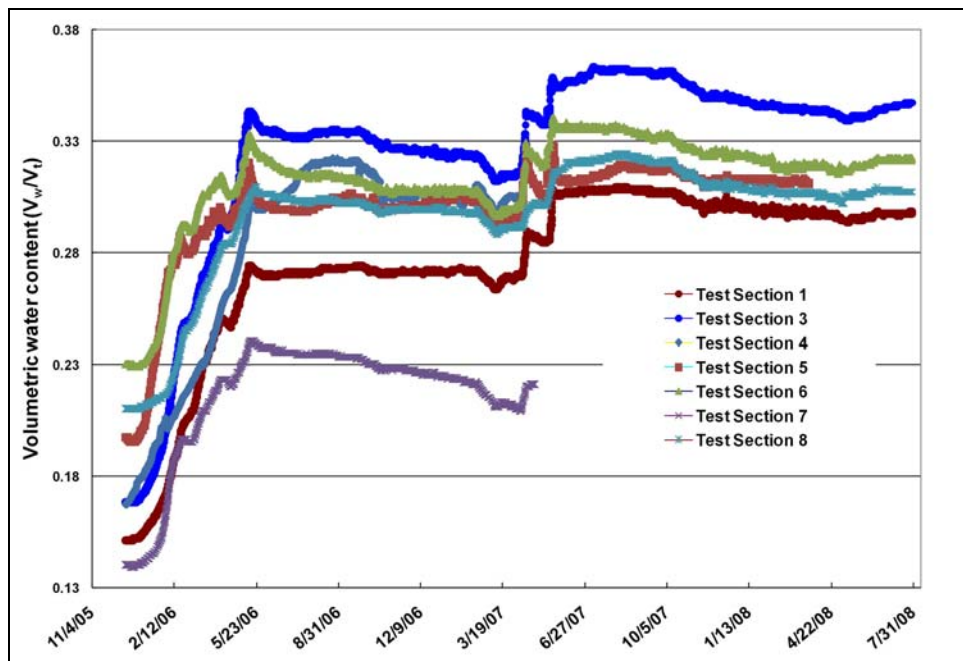


Figure 9. Volumetric water content of the subgrade at depths of 840-890 mm from the top of the subgrade in Test Sections 1, 2, 4, 6, 7 & 8 for the duration of the test program.

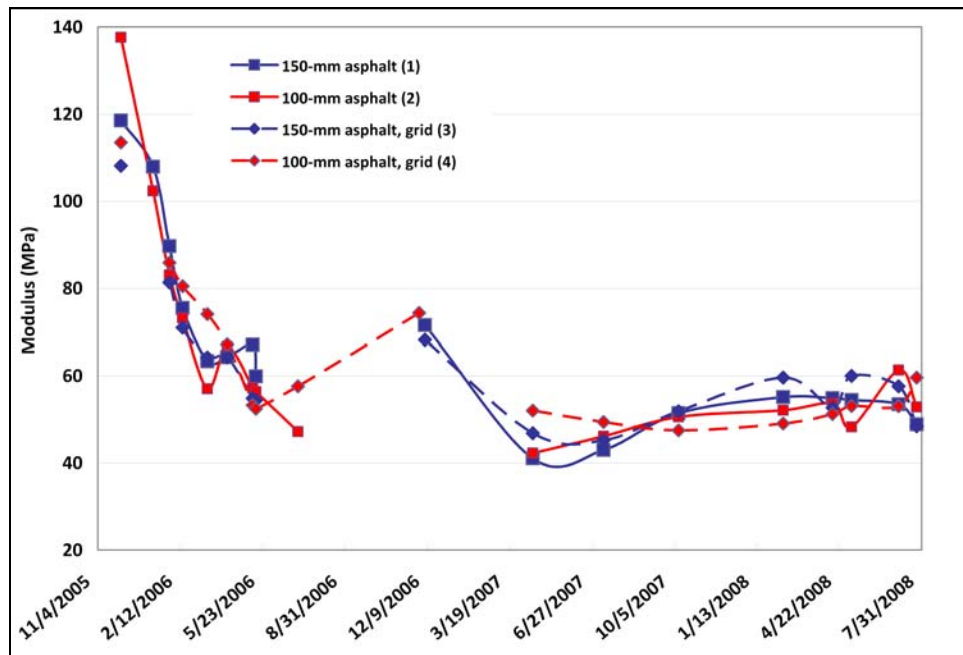


Figure 10. Estimated subgrade modulus values for Test Sections 1-4, with a base layer thickness of 300 mm.

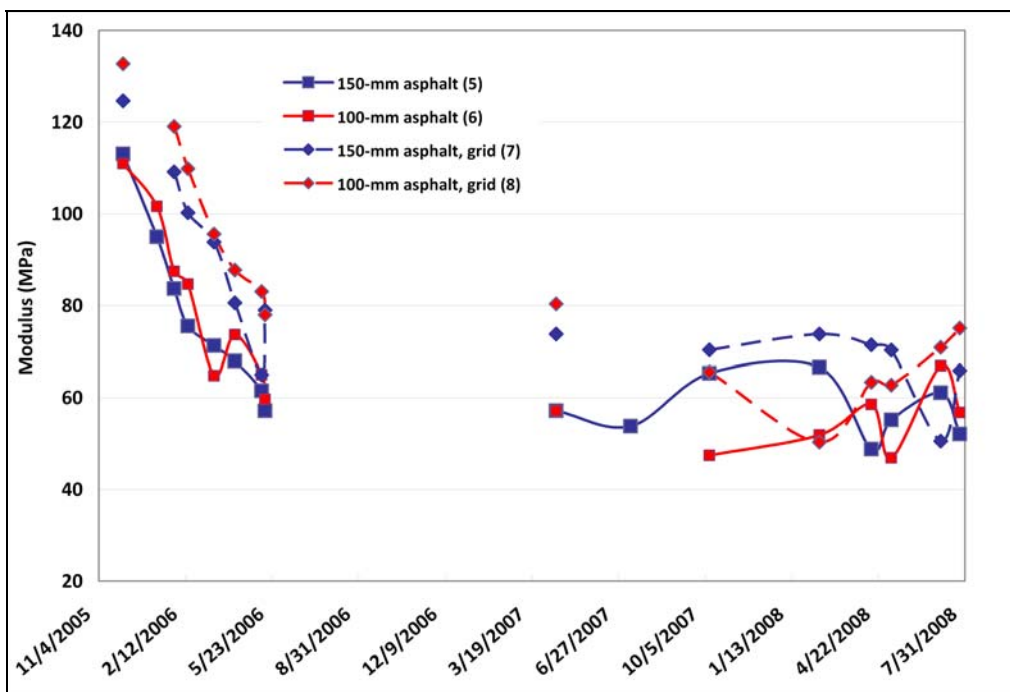


Figure 11. Estimated subgrade modulus values for Test Sections 5-8, with a base layer thickness of 600 mm.

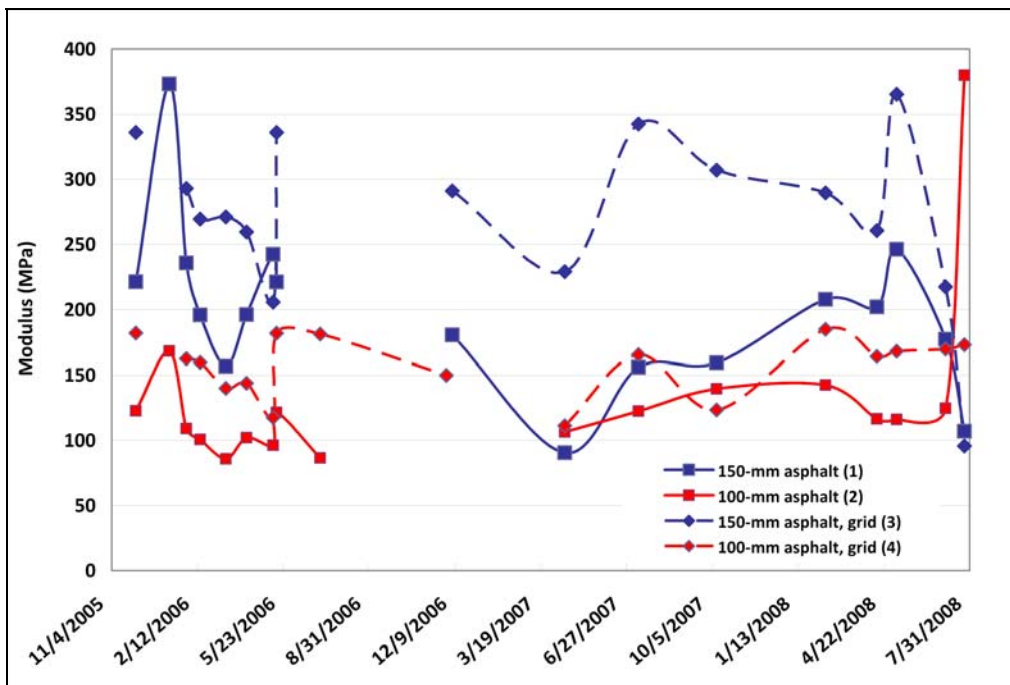


Figure 12. Estimated base modulus values for Test Sections 1-4, with a base layer thickness of 300 mm.

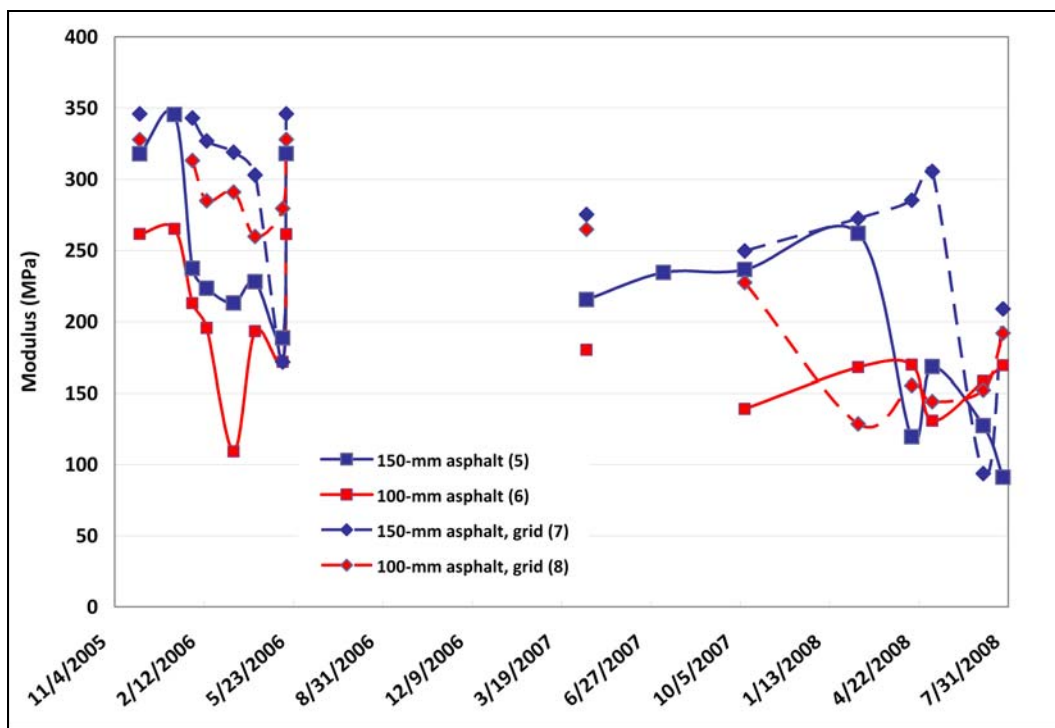


Figure 13. Estimated base modulus values for Test Sections 5-8, with a base layer thickness of 600 mm.

Figure 14 through Figure 17 show the modulus values estimated based solely on back-calculations from FWD data. They contain the same data reported in Figure 10 to Figure 13; however, the axes scales are expanded and the dates during which each test section was trafficked are highlighted on each figure. These figures indicate that, for every test section, both the subgrade modulus value and the base layer modulus value decreased at the conclusion of trafficking from the pre-traffic value. The only exception was Test Section 4, for which the appropriate measurements were not made within a few days of completion of trafficking so that if the modulus did decrease, it was not documented. It is possible that the apparent decrease in base layer modulus after trafficking was affected by the decreased subgrade layer modulus only, versus being a result of trafficking.

The subgrade modulus values also increased with time after the completion of trafficking, indicating time-dependent stiffness (Figure 14 and 15). The base layers also indicated a ‘recovery’ in modulus after trafficking; however, the post-trafficking values varied considerably (Figure 16 and Figure 17).

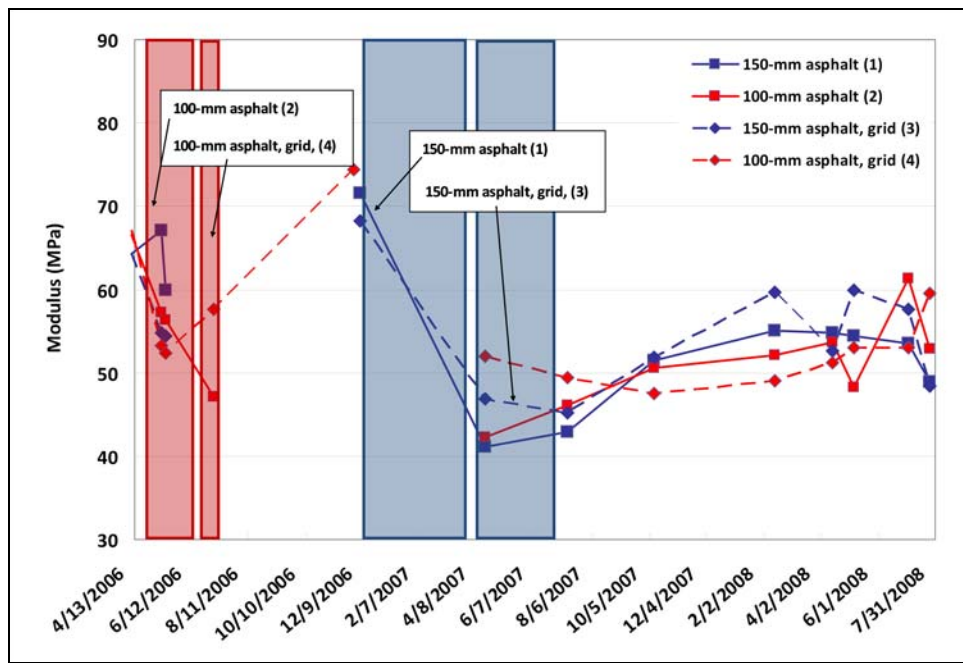


Figure 14. Estimated subgrade modulus values for Test Sections 1-4 with a base layer thickness of 300 mm for the trafficking phase of the test program. The shaded portions of the figure indicate when trafficking was conducted. Labels indicate which test section was trafficked.

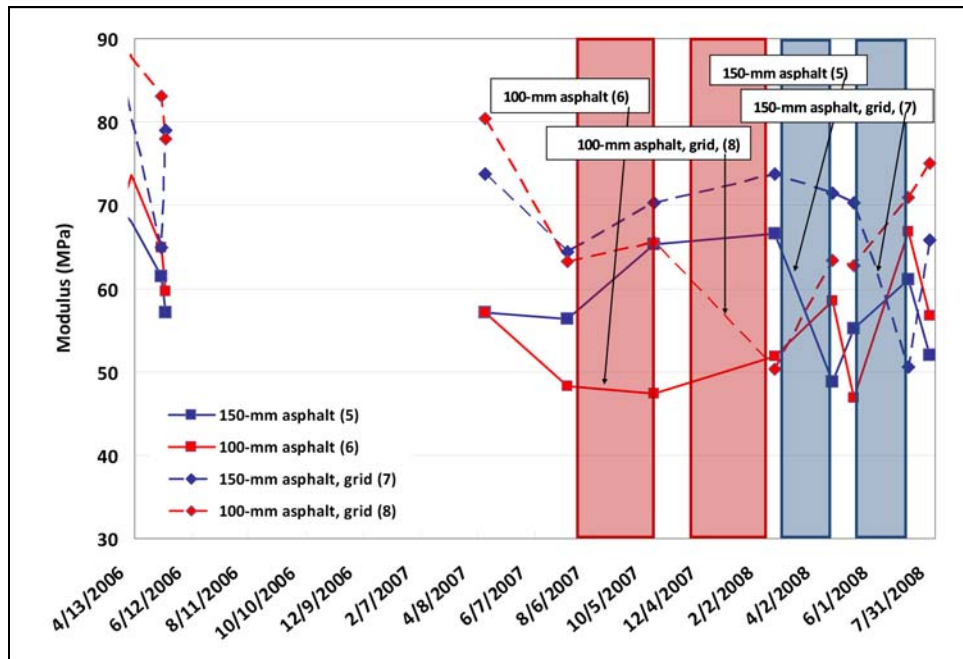


Figure 15. Estimated subgrade modulus values for Test Sections 5-8 with a base layer thickness of 600 mm for the trafficking phase of the test program. The shaded portions of the figure indicate when trafficking was conducted. Labels indicate which test section was trafficked.

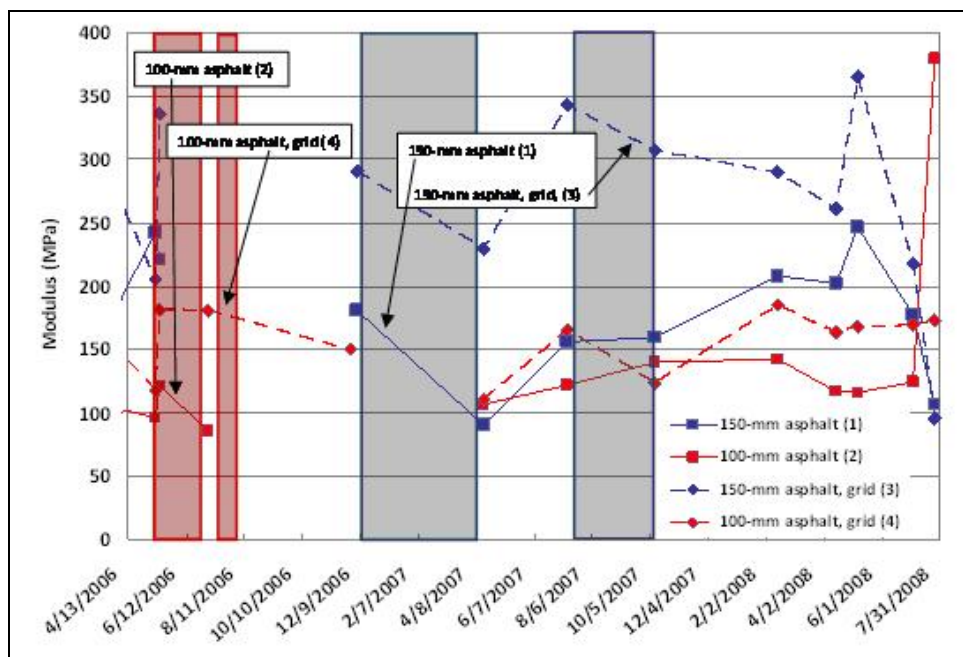


Figure 16. Estimated base layer modulus values for Test Sections 1-4 with a base layer thickness of 300 mm for the trafficking phase of the test program. The shaded portions of the figure indicate when trafficking was conducted. Labels indicate which test section was trafficked.

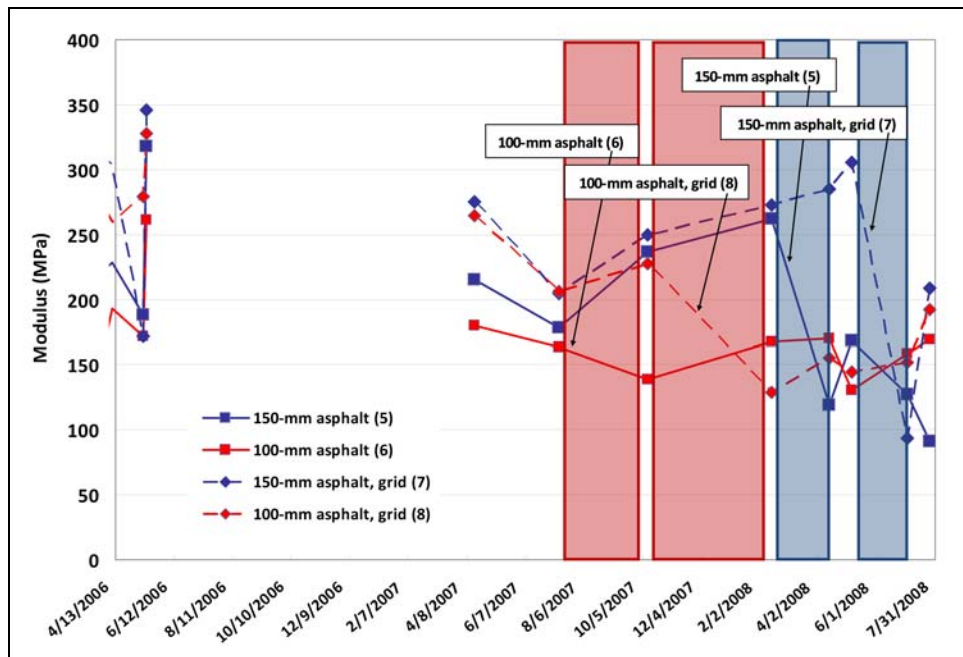


Figure 17. Estimated base modulus values for Test Sections 5-8 with a base layer thickness of 600 mm for the trafficking phase of the test program. The shaded portions of the figure indicate when trafficking was conducted. Labels indicate which test section was trafficked.

The back-calculated subgrade modulus values, based on FWD testing, indicated more variability than had been planned. Table 9 lists the average estimated subgrade modulus values within a few days before testing and immediately after testing, as well as the average of these two modulus values. The average and standard deviations of these values are listed in the bottom two rows and there are three columns indicating whether each value falls within one standard deviation of the average values. Based on the information provided in this table, it would be inappropriate to compare Test Sections 1 and 3 to each other in the field experiment—Test Section 1 had an estimated subgrade modulus value more than one standard deviation higher than the average before testing and Test Section 3 had an estimated subgrade modulus value more than one standard deviation lower than the average before and after testing. Further, the subgrade modulus value for Test Section 7 is apparently high; and, this was considered when interpreting experimental results. This information also has implications for the completion of an Analysis of Variance based on the factorial design of the field; hence, such an analysis was not attempted for this report.

Table 9. Average estimated subgrade modulus values.

Test Section conditions		TS	Before Traffic (MPa)	Within one Std. Dev?	After Traffic (MPa)	Within one Std. Dev?	Average of Before and After traffic (MPa)	Within one Std. Dev?
100 mm AC, 300 mm base	2	56.36	Y		47.14	Y	51.75	Y
	Grid	4	57.65	Y	Did not measure			N.A.
150 mm AC, 300 mm base	1	71.55	N		41.07	Y	56.31	Y
	Grid	3	46.84	N	37.19	N	42.02	N
100 mm AC, 600 mm base	6	52.74	Y		47.73	Y	50.24	Y
	Grid	8	65.53	Y	50.31	Y	57.92	Y
150 mm AC, 600 mm base	5	66.56	Y		48.8	Y	57.68	Y
	Grid	7	70.33	N	50.51	Y	60.42	N
		Ave.	60.95		46.11		53.76	
		Std. Dev.	8.87		5.05		6.30	

Surface deformations

Surface deformations, i.e., rut depths, were used to determine whether the test sections had failed, and were the primary response variable used to compare the performance of test sections with and without geogrid. As shown in Figure 18, the rut depth was defined as the elevation difference between the centerline of the wheel path and fixed points 600 mm away from the wheel path centerline on each side of the wheel path. The elevation differences corresponding to each of the 600 mm offsets were not always equal, so the reported rut depths are the average of the elevation differences. Relative rut depths were determined, meaning that the rut depth was based on the change in surface profile from zero to the number of cycles analyzed, and it also includes any surface heave that occurred outside of the area of compression (see Figure 18). The relative rut depth was used to insure that the only contribution to rutting was the applied traffic cycles (i.e. the small non-zero rut depths that existed prior to trafficking were subtracted from subsequent values). This is the same definition used in the American Association of State Highway Officials (AASHO) road test (Huang 1993), except that the variations in surface elevations that existed prior to trafficking were not quantified in the AASHO road test (i.e. the initial surface was assumed to be level).

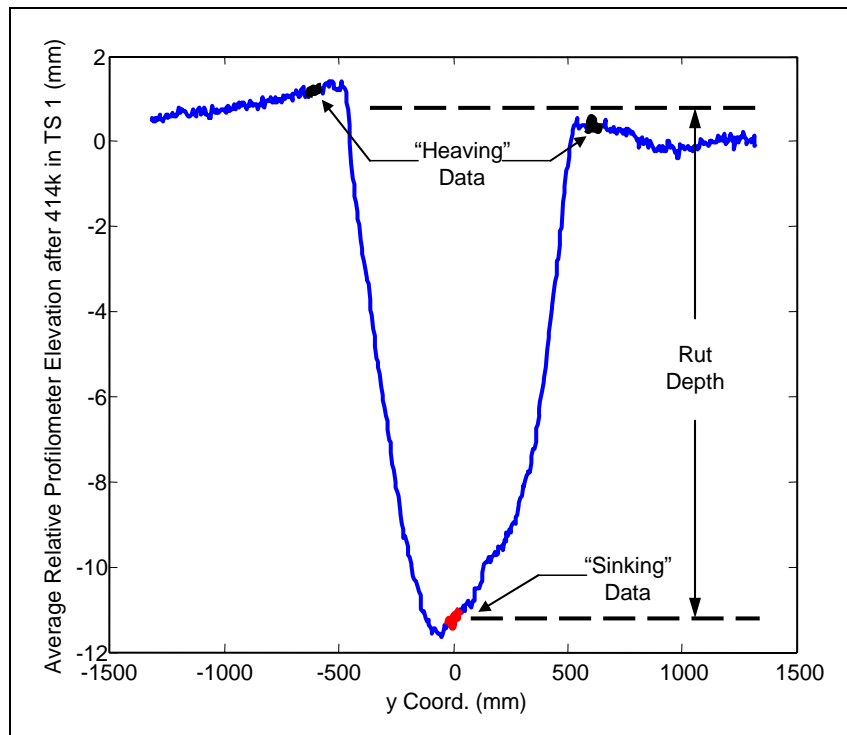


Figure 18. Example of rut depth measurement for the average relative profile in TS 1 after 414,000 cumulative traffic cycles.

Surface rut depths, as a function of the number of wheel loads (traffic cycles) and ESALs applied for all tests, are presented in Figure 19 and Figure 20, respectively. The sections with a 100 mm thick AC layer and a 300 mm thick base layer (Test Sections 2 and 4) reached failure at the lowest number of traffic cycles, and the reinforced section performed better than the unreinforced section. For the sections with a 150 mm thick AC layer and a 300 mm thick base layer, the unreinforced section (Test Section 1) performed “better;” however, recall that water was added to the entire test basin after trafficking Test Section 1 and prior to trafficking the reinforced section, Test Section 3 (i.e., Figure 9). This significantly lowered the subgrade layer modulus of the reinforced section compared to the corresponding unreinforced section, as measured through FWD testing (Figure 14). Thus, it was not possible to draw conclusions about the effectiveness of reinforcement in this pavement configuration based on the experimental data. However, it was addressed via modeling (e.g., Section 6). (Note that these experimental results were used to calibrate the model presented later in this report.)

For the test sections with a 100 mm thick AC layer and a 600 mm thick base layer, the reinforced section performed much better than the unreinforced section throughout most of the trafficking period, but the rut depth of the reinforced test section appeared to be approaching that of the unreinforced section in the latter part of the trafficking. For the sections with a 150 mm thick AC layer and a 600 mm thick base layer, the sections performed similarly over the entire trafficking period, with the unreinforced section exhibiting slightly less rutting at the end of the trafficking period. These results are discussed further in the context of the rutting models in Section 6.

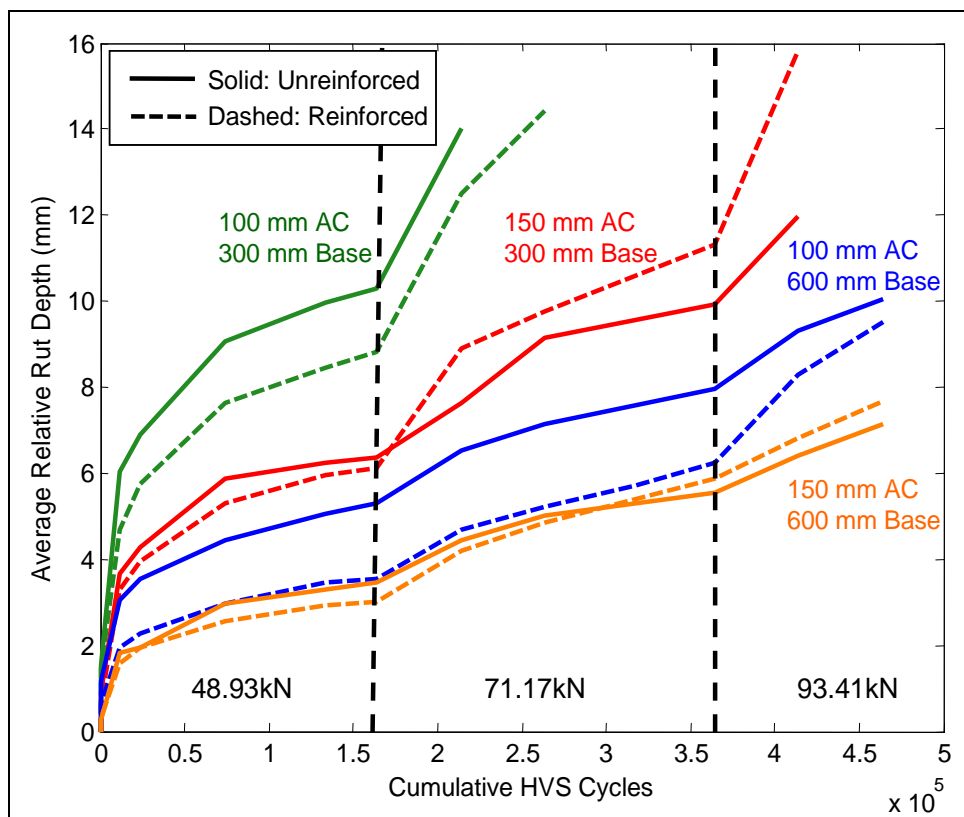


Figure 19. Average relative surface rut depth vs. cumulative traffic cycles.

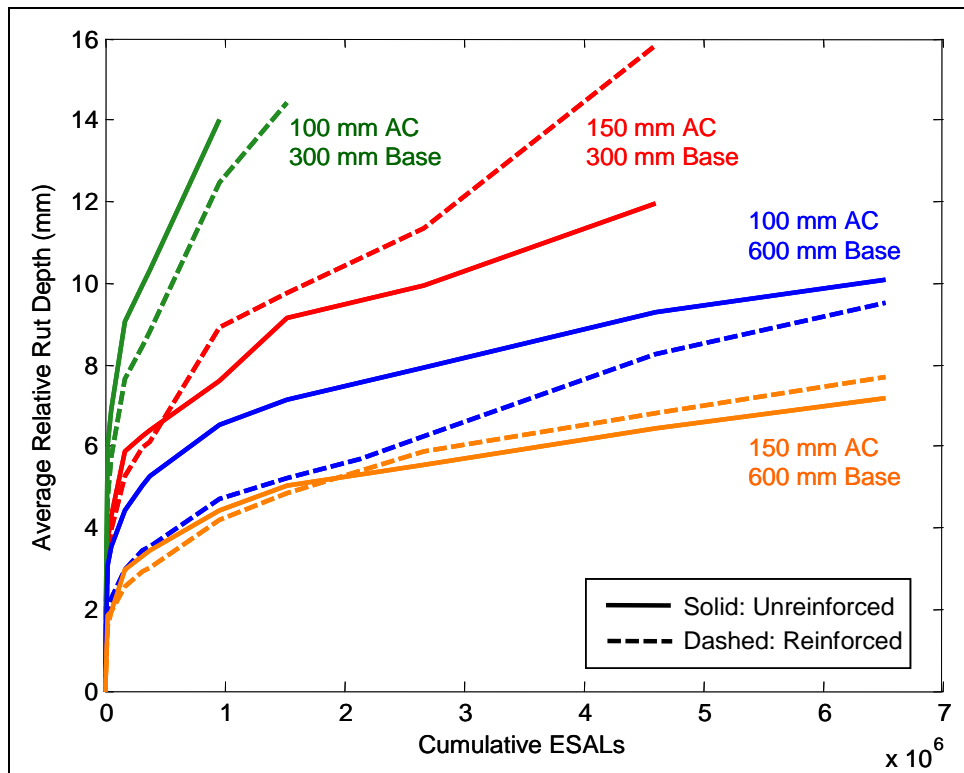


Figure 20. Average relative surface rut depth vs. cumulative ESALs.

The average relative surface profiles for each of the test sections at the last set of SLTs are presented in Figure 21. The profiles do not indicate any significant differences between the reinforced and unreinforced test sections.

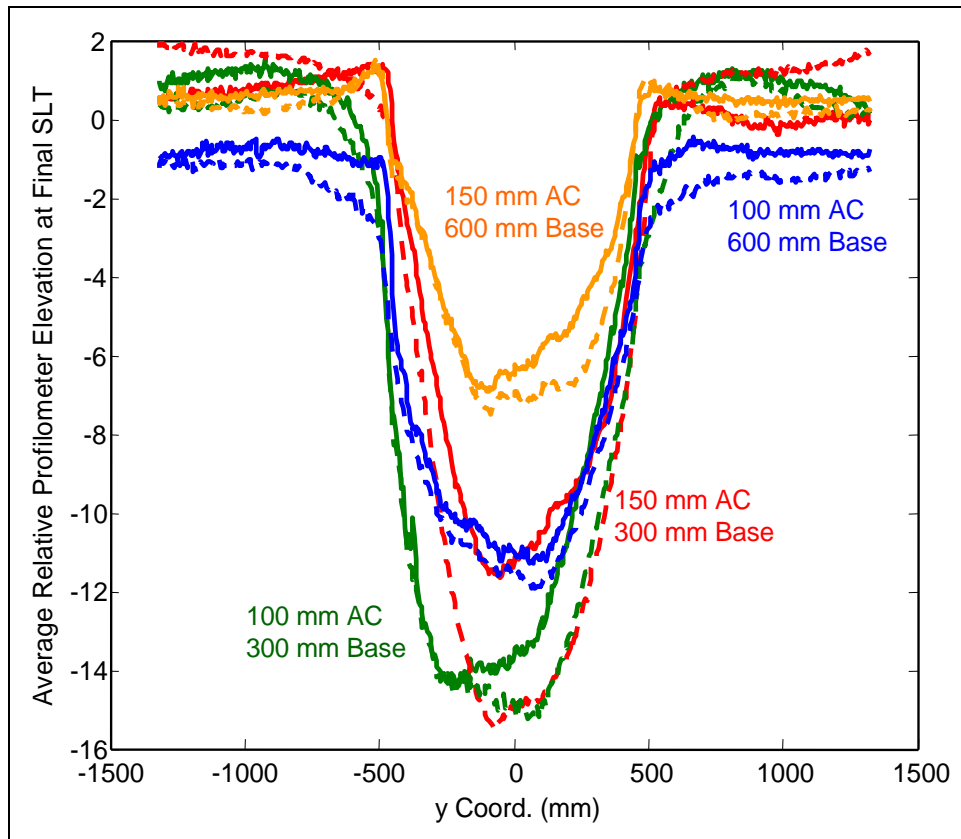


Figure 21. Average relative surface profiles for all test sections at the time of final static load tests (SLTs). The sections with grid are marked with dashed lines.

The final measured relative rut depth and changes in surface elevation that compose the rut depth are summarized in Table 10 for each test section. The elevation change at the centerline of the test section, taken as positive downward (CL Rut), and the average elevation change at the 600 mm offsets (Heave, taken as positive upward) are presented. The sum of these values for a test section is the total rut depth. Note that the smallest heave values, including three negative values, occurred in the test sections with a 100 mm asphalt thickness.

The traffic benefit ratios (*TBRs*), defined as the ratio of the number of ESALs to reach a rut depth of 12.5 mm that a reinforced section carried to an identically-constructed unreinforced test section, are also listed in Table 10. Since four of the test sections did not reach a 12.5 mm rut depth,

smaller rut depths were used as indicated. All ESAL values were linearly interpolated from data, as shown in Figure 20. *TBR* values less than 1.0 indicate that the unreinforced control section performed better than the corresponding reinforced section. A *TBR* was not determined for TS 3 compared to TS1 because these sections had considerably different subgrade modulus values (see Figure 14). The 0.82 value for TS 7 (as compared to TS 5) (reinforced and unreinforced sections with 150 mm asphalt and 600 mm base) was unexpected and may have been due to variability in layer thicknesses or other properties that may have been present in the sections.

Table 10. Summary of final measured rut depths, surface deformations, and *TBR* values for each test section.

Asphalt/base thickness mm	Test Section	CL Rut mm	Heave mm	Total rut Depth mm	<i>TBR</i>
100/ 300	2	13.6	0.4	14.0	1.33
	4	14.9	-0.5	14.4	
150/ 300	1	11.2	0.8	12.0	N.A.
	3	15.0	0.9	15.8	
100/ 600	6	11.0	-1.0	10.1	1.47*
	8	11.5	-2.0	9.5	
150/ 600	5	6.4	0.7	7.2	0.82**
	7	7.0	0.6	7.7	

* Based on the number of ESALs to reach a 9.4 mm rut depth

** Based on the number of ESALs to reach a 6.3 mm rut depth

N.A. = Not applicable because subgrade modulus values are too different.

Relative pavement surface elevation contours were developed, based on the profilometer readings after the completion of trafficking in each section, and results are shown in Figure 22 to Figure 29. No specific trends are noted between reinforced and unreinforced test sections.

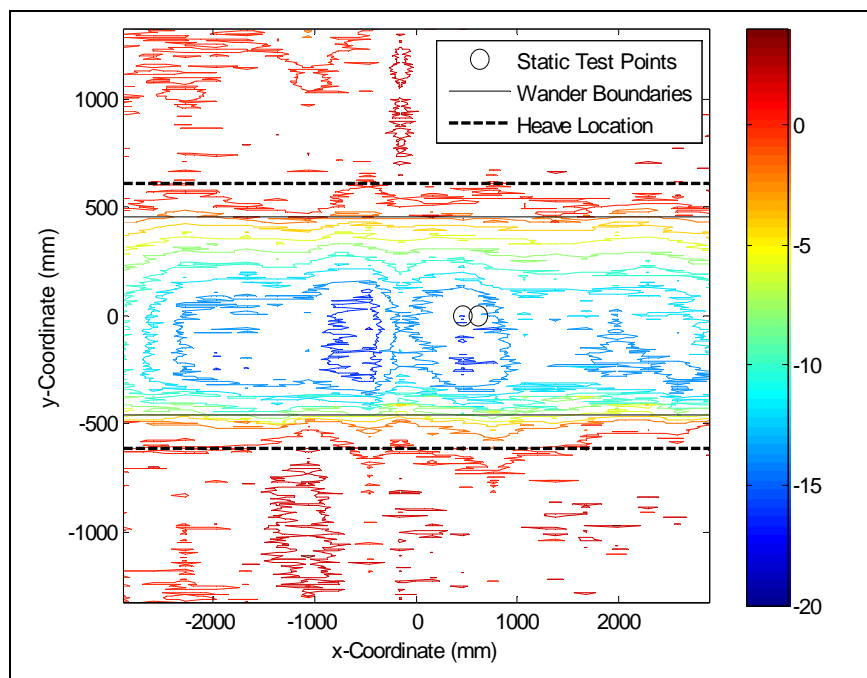


Figure 22. Relative pavement surface elevation contours for TS 2 (100 mm asphalt, 300 mm base) after 214,000 cumulative traffic cycles.

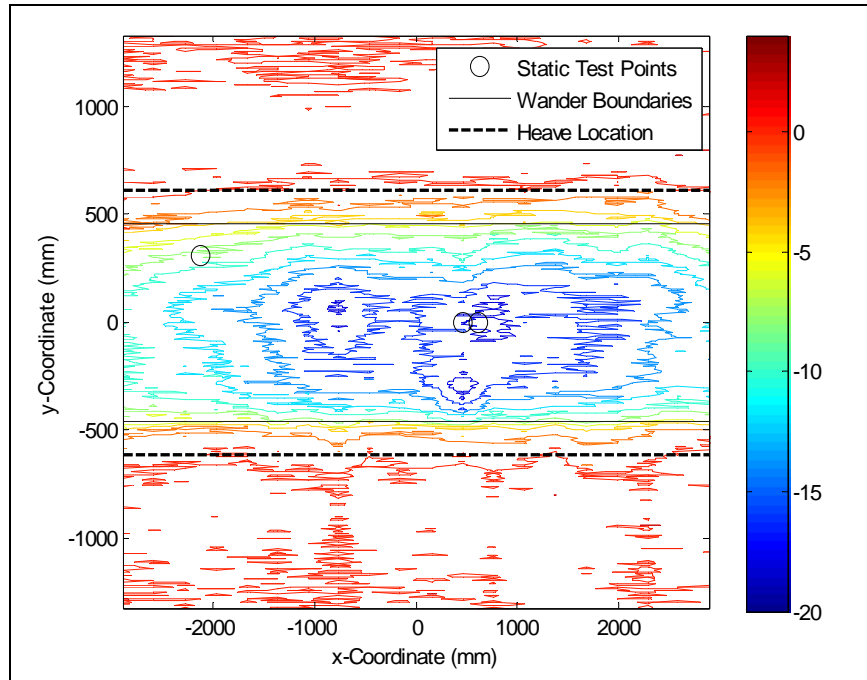


Figure 23. Relative pavement surface elevation contours for TS 4 (100 mm asphalt, 300 mm base, with Geogrid) after 263,000 cumulative traffic cycles.

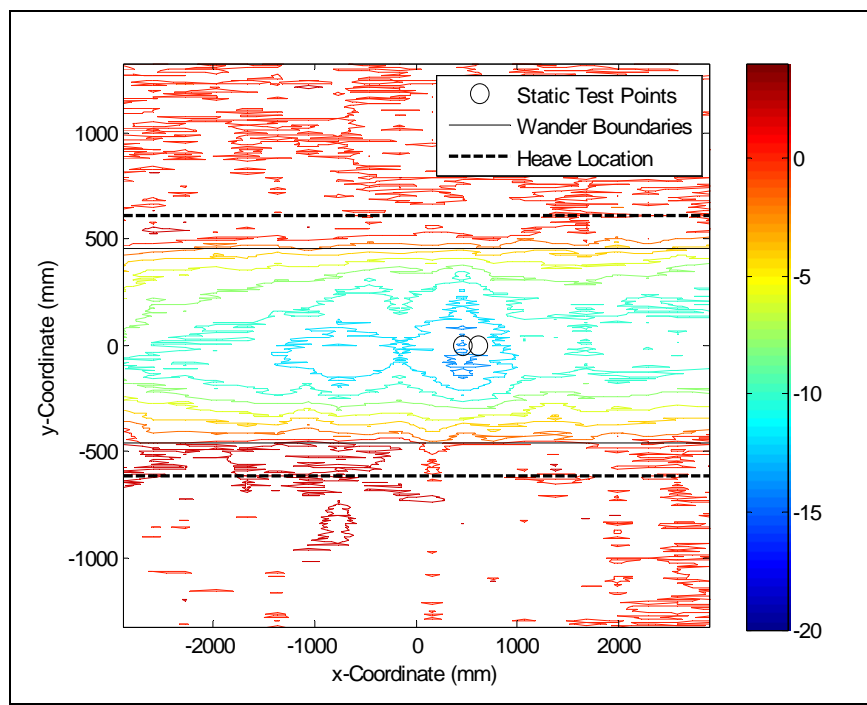


Figure 24. Relative pavement surface elevation contours for TS 1
(150 mm asphalt, 300 mm base) after 414,000 cumulative traffic
cycles.

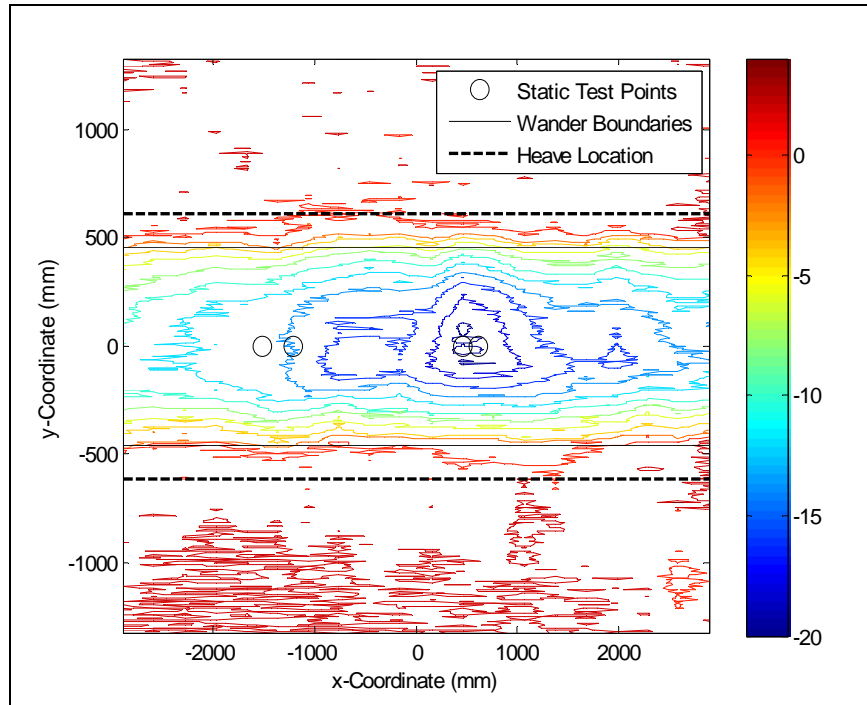


Figure 25. Relative pavement surface elevation contours for TS 3
(150 mm asphalt, 300 mm base, with Geogrid) after 424,000 cumulative
traffic cycles.

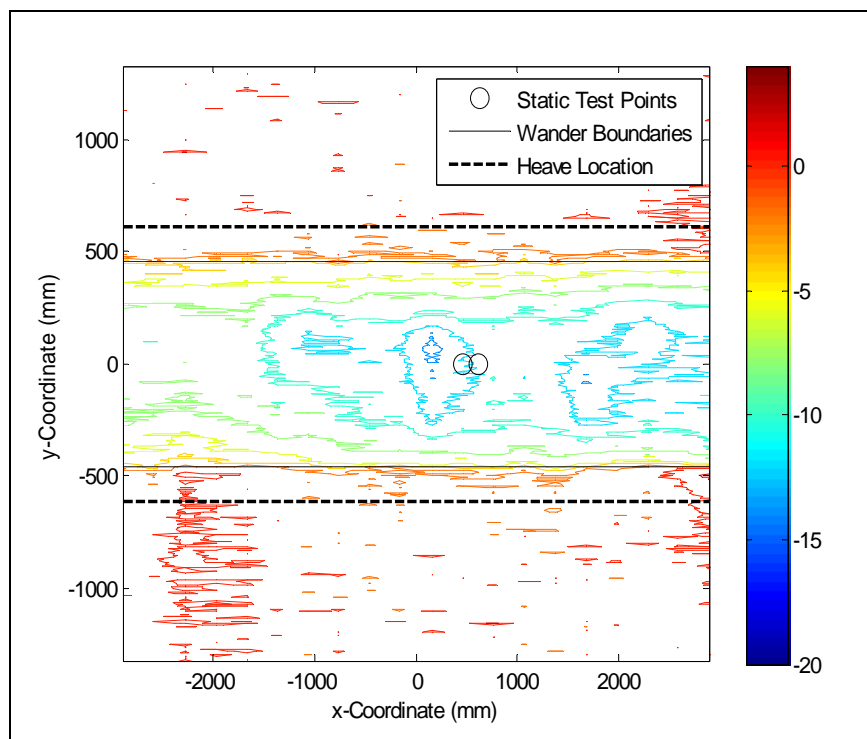


Figure 26. Relative pavement surface elevation contours for TS 6 (100 mm asphalt, 600 mm base) after 464,000 cumulative traffic cycles.

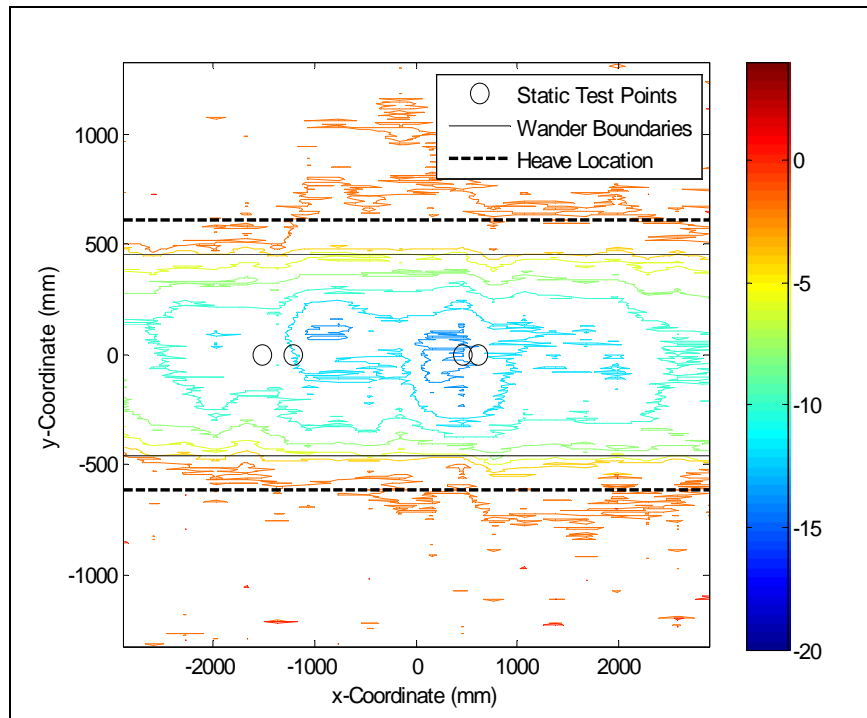


Figure 27. Relative pavement surface elevation contours for TS 8 (100 mm asphalt, 600 mm base, with Geogrid) after 464,000 cumulative traffic cycles.

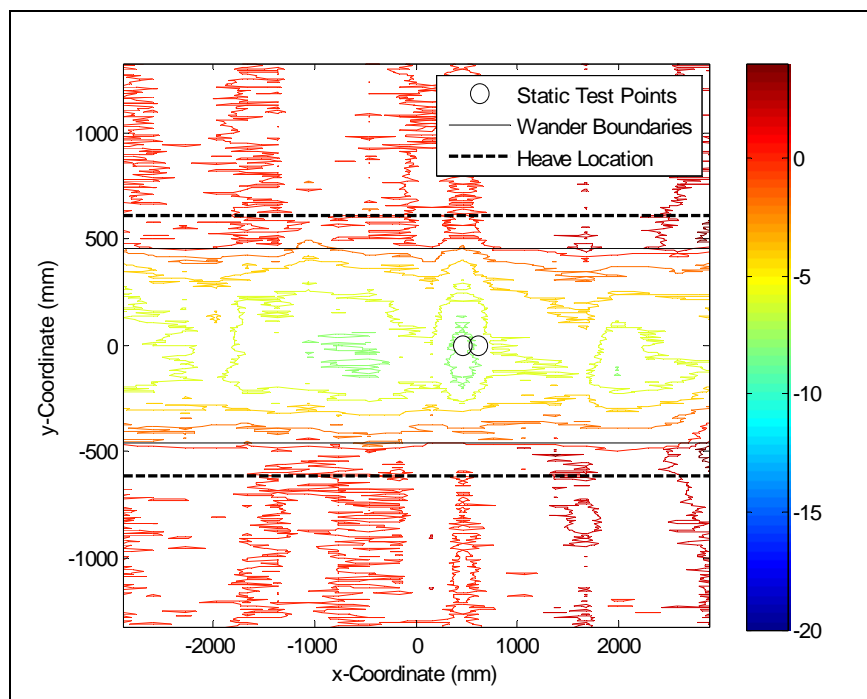


Figure 28. Relative pavement surface elevation contours for TS 5 (150 mm asphalt, 600 mm base) after 464,000 cumulative traffic cycles.

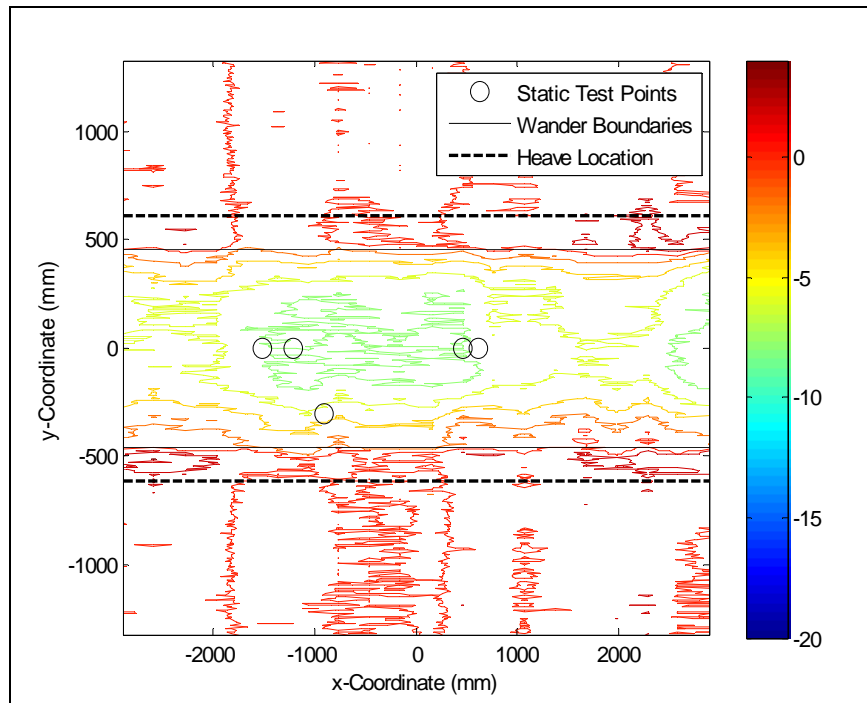


Figure 29. Relative pavement surface elevation contours for TS 7 (150 mm asphalt, 600 mm base, with Geogrid) after 464,000 cumulative traffic cycles.

Deformations of asphalt, base and subgrade

The vertical deformations of the constitutive pavement layers provide insight into the behavior of the reinforced and unreinforced systems. Uncorrected deformations measured by the ϵ mu coils in the unloaded state at the last set of SLTs in TS 1-4 and TS 5-8 are presented in Figure 30 and Figure 31. These deformations are also examined later. Note that for all test sections, 3-5 mm of the total deformation took place in that asphalt layer.

In TS 1-4, the largest deformations typically occurred at the top of the subgrade layer, but significant deformations were also recorded in the base layers. (Recall that when TS 1 was trafficked, the subgrade moisture was lower than usual and the modulus was significantly higher than that of TS 3, the matching grid-reinforced test section.)

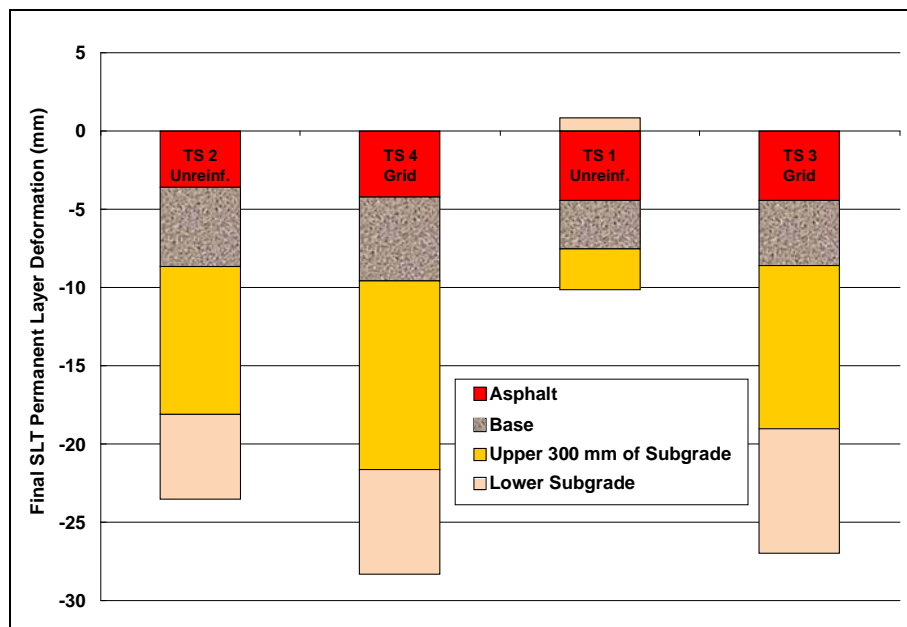


Figure 30. Final, unloaded vertical deformations for Test Sections 1-4 with 300 mm base course.

In TS 5-8, the largest recorded deformations, other than the AC layer, were generally in the upper 300 mm of the base, and were of the same order as those of the base layer in Test Sections 1-4. Several ϵ mu layer readings were invalid for these sections so that the upper subgrade deformations were not available for TS 5 and TS 6, but the available readings indicate that the subgrade deformations were much smaller than those of Test Sections 1-4.

Figures 30 and 31 do not suggest more or less deformation of any layer due to the presence of geogrid.

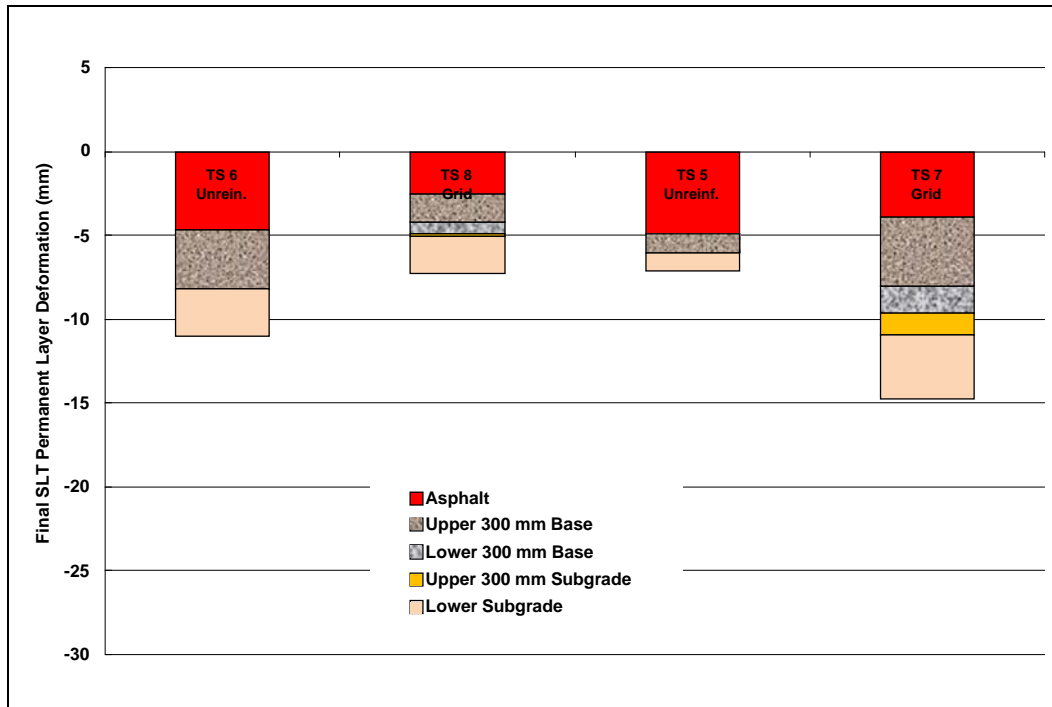


Figure 31. Final, unloaded vertical deformations test Sections 5-8 with 600 mm base course.

Since permanent deformation (rutting) models predict the amount of deformation in each individual material layer, the vertical deformations had to be measured as accurately as possible in order to calibrate the 3D FEM-based permanent deformation models used to predict rutting (see Section 6). The sum of the vertical deformations in all the layers should be equal to the change in surface elevation at the same location.

The permanent layer vertical deformations Δ_{emu} were measured by reading the emu coils in the unloaded state. The deformation of the pavement surface immediately above the emu coils was also quantified as the sum of the profilometer deformation $\Delta_{profilometer}$ and the level survey deformation Δ_{level_survey} . The determination for Test Section 2 is shown in Figure 32. Here, Δ_{level_survey} refers to the average change in elevation of the specific points where the profilometer legs rest when it is collecting data at the longitudinal location of the vertical emu stack. In theory, the sum of the measured permanent layer deformations $\sum \Delta_{emu}$ should be equal to the measured surface deformation $\Delta_{surface}$ assuming that negligible deformations occurred below the deepest emu coils, as described by

Equation 1. However, $\sum \Delta_{emu}$ generally did not agree well with $\Delta_{surface}$ (Table 11.). Furthermore, it was not possible to determine $\sum \Delta_{emu}$ for sections in which some of the emu coils had failed; these values are followed by * in Table 11. and cannot be compared to $\Delta_{surface}$. The number of emu layers missing for the $\sum \Delta_{emu}$ value in each Test Section is given in the last column of Table 11.

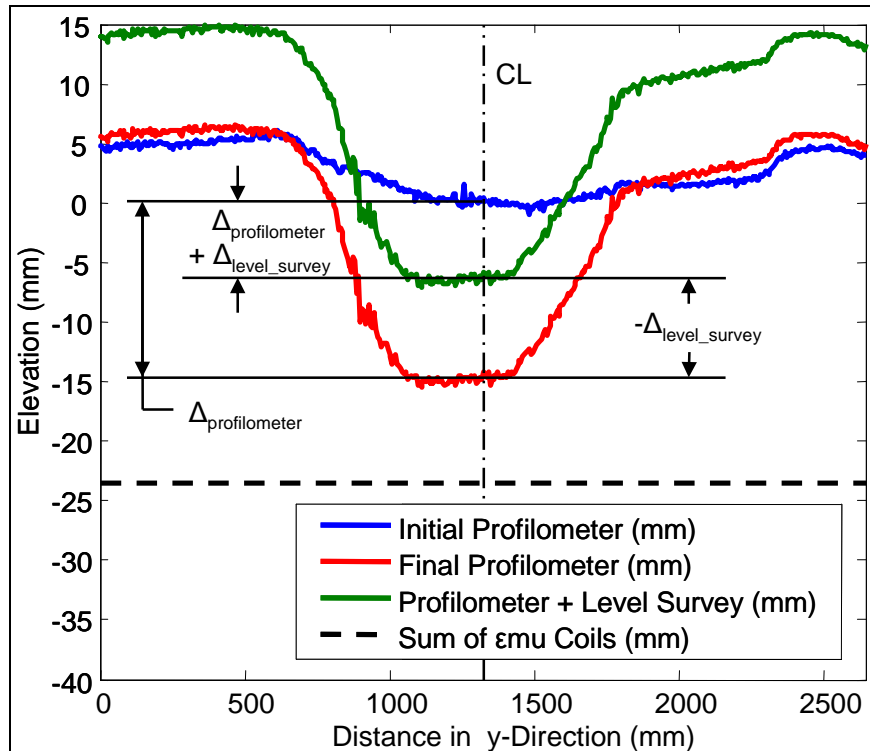


Figure 32. Example of deformation measurements for Test Section 2.

Table 11. Summary of measured deformations at the location of the emu coils for each test section.

TS	Cycles	$\Delta_{profilometer}$ (mm)	Δ_{level_survey} (mm)	$\sum \Delta_{emu}$ (mm)	$\Delta_{profilometer} + \Delta_{level_survey}$ (mm)	Number of Layers Missing
1	414,000	13.1	4.6	9.3	17.7	0
2	214,000	14.8	-8.4	23.5	6.4	0
3	424,000	19.9	20.9	27.0	40.8	0
4	263,000	18.3	-18.3	28.3	0.0	0
5	464,000	7.6	-22.5	7.3*	-14.9	4
6	464,000	11.6	6.1	11.0*	17.7	5
7	464,000	7.3	-12.2	14.7	-4.9	0
8	464,000	13.1	-6.5	7.3*	6.6	3

* Indicates that data from some layers were missing (i.e. $\sum \Delta_{emu}$ is incomplete)

$$\Delta_{surface} = \Delta_{profilometer} + \Delta_{level_survey} \quad (1)$$

The discrepancies presented in Table 11 are well within the tolerance expected when considering all of the potential sources of error. However, the discrepancies could have significant implications on rutting models that define the failure rut depth as 12.5 mm. The permanent layer deformations that comprise the deformations presented in Table 12 were used to calibrate the empirical rutting models of this study. Thus, it was necessary to implement an adjustment procedure to relate the individual layer deformations to measured surface deformations, described below.

The sum of the individual layer deformations was set equal to the measured surface rut depth, which defines pavement performance in this study. The adjustment was accomplished through the following steps:

1. Calculate the difference between the sum of the emu coil deformations and the average measured surface rut depth.
2. For each emu layer, determine the percentage of the layer's thickness with respect to the sum of the emu layer thicknesses.
3. Multiply the difference from Step 1 by the percentage from Step 2 and add this to the recorded deformation value.

Several other adjustment strategies were investigated as well, but this was the only strategy that produced reasonable and consistent results for all test sections. Permanent deformation data was missing for some emu layers in Test Sections 5, 6, and 8, so adjusted individual material layer deformations could not be determined. The total raw measured and adjusted deformations by material layer are presented in Table 12 for the last set of SLT in each test section. The adjustment process clearly affected the subgrade layer the most in terms of deformation difference.

The adjusted permanent deformations in the asphalt, base, and subgrade layers, obtained when the pavement was not loaded are presented for the test sections with complete data sets in Figure 33 through Figure 35, respectively, as a function of cumulative traffic cycles. The same deformations in the asphalt, base, and subgrade layers are presented in Figure 36 through Figure 38 as a function of cumulative ESALs.

These figures present the measured unloaded distances between emu coils. Note that the deformations do not always increase, and sometimes

decrease. The big dip on the solid red line in Figure 33 was measured when the temperature in the test basin was at its lowest, and is not considered to be representative. The other variations in deformations on the curves may correspond to smaller variations in temperature, small debris on the asphalt surface at the time of the reading, etc. The apparent inconsistencies in the data suggest that the measurement precision is in the range of 20-30% of the recorded data.

Table 12. Summary of raw measured and adjusted deformations by material layer for each test section.

	Raw Measurement			Adjusted Value		
	Δ AC (mm)	Δ Base (mm)	Δ Subgrade (mm)	Δ AC (mm)	Δ Base (mm)	Δ Subgrade (mm)
1	4.5	3.1	1.8	4.7	3.6	3.7
2	3.6	5.1	14.8	3	3.3	7.8
3	4.4	4.2	18.4	3.4	2.1	10.3
4	4.3	5.3	18.7	3.4	2.7	8.3
5	4.9	-	-	-	-	-
6	4.7	-	-	-	-	-
7	3.9	5.7	5.1	3.3	3.1	1.3
8	2.5	-	-	-	-	-

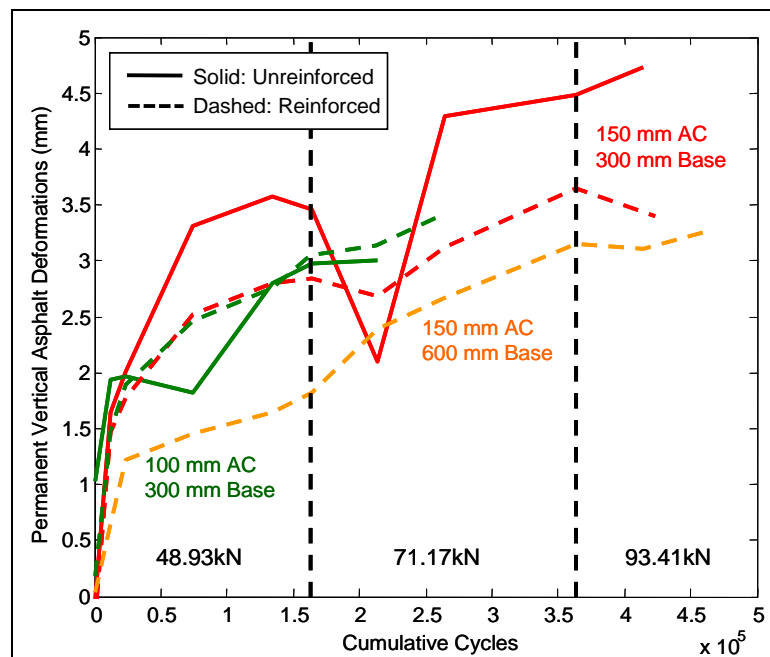


Figure 33. Permanent vertical deformations in the asphalt layer vs. cumulative traffic cycles (data has been adjusted according to the procedure outlined in this section). Matching unreinforced and reinforced test sections are shown in the same color: 100 mm AC/300 mm base is green, 150 mm AC/ 300 mm base is red, and 150 mm AC and 600 mm base is yellow.

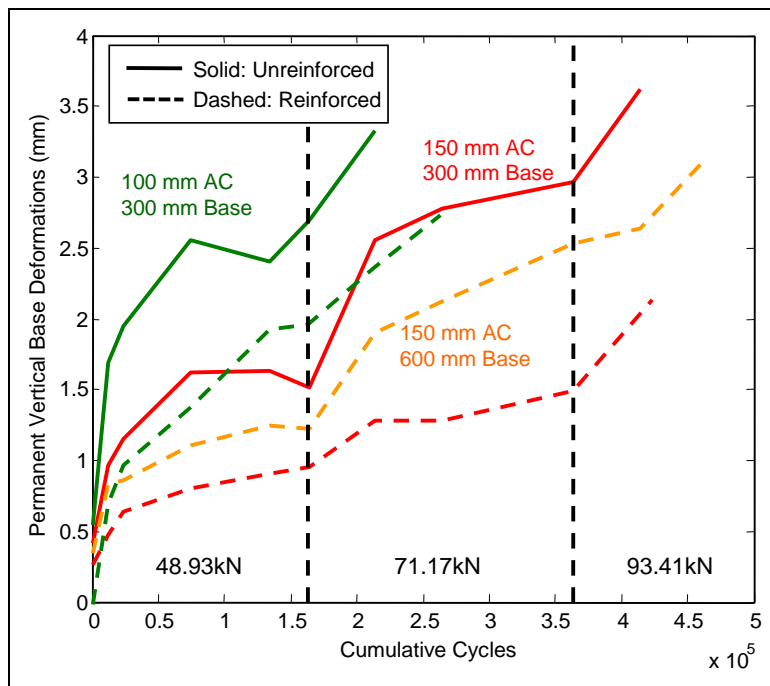


Figure 34. Permanent vertical deformations in the base layer vs. cumulative traffic cycles (data has been adjusted according to the procedure outlined in this section.). Matching unreinforced and reinforced test sections are shown in the same color: 100 mm AC/300 mm base is green, 150 mm AC/ 300 mm base is red, and 150 mm AC and 600 mm base is yellow.

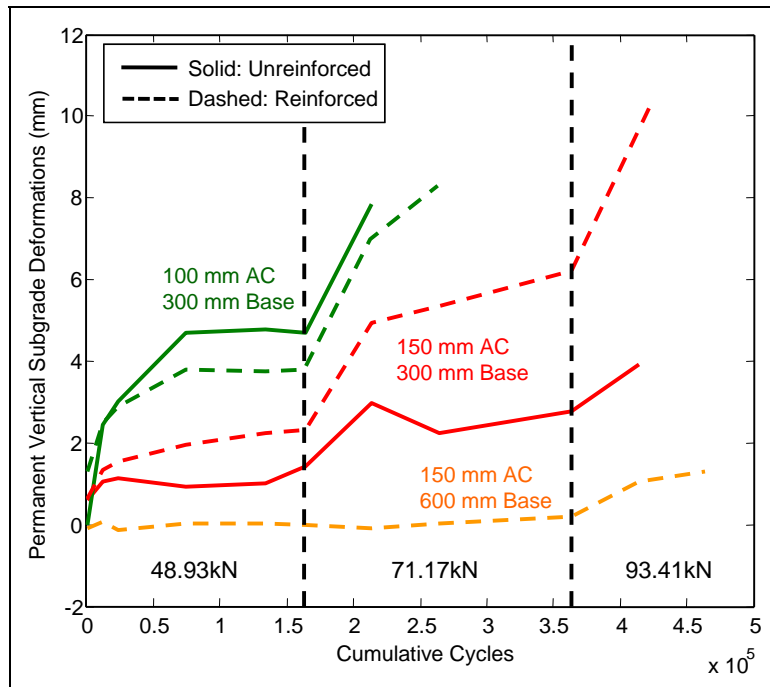


Figure 35. Permanent vertical deformations in the subgrade layer vs. cumulative traffic Cycles (data has been adjusted according to the procedure outlined in this section).

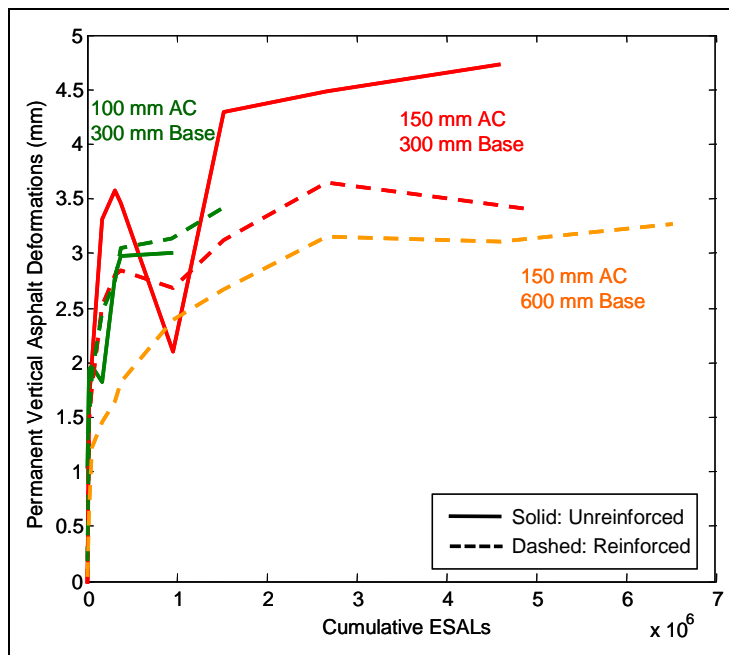


Figure 36. Permanent vertical deformations in the asphalt layer vs. cumulative ESALs (data has been adjusted according to the procedure outlined in this section). Matching unreinforced and reinforced test sections are shown in the same color: 100 mm AC/ 300 mm base is green, 150 mm AC/ 300 mm base is red, and 150 mm AC and 600 mm base is yellow.

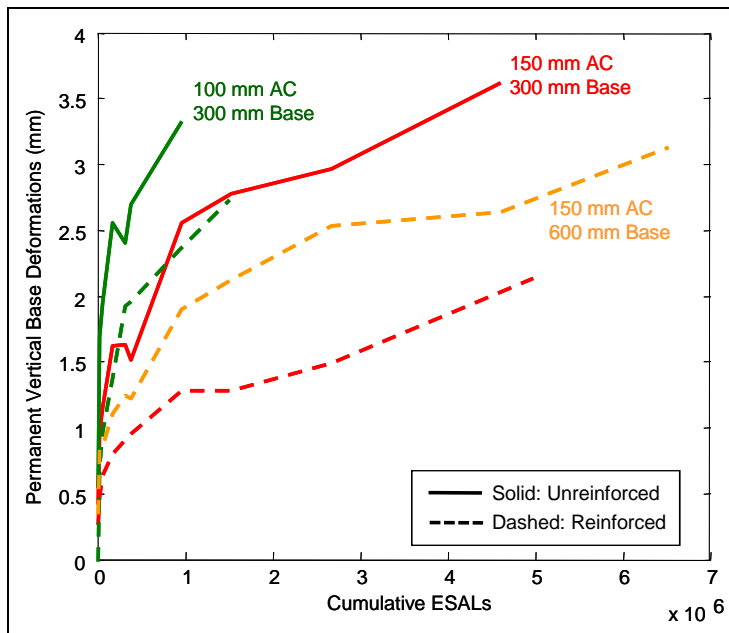


Figure 37. Permanent vertical deformations in the base layer vs. cumulative ESALs (data has been adjusted according to the procedure outlined in this section). Matching unreinforced and reinforced test sections are shown in the same color: 100 mm AC/ 300 mm base is green, 150 mm AC/ 300 mm base is red, and 150 mm AC and 600 mm base is yellow.

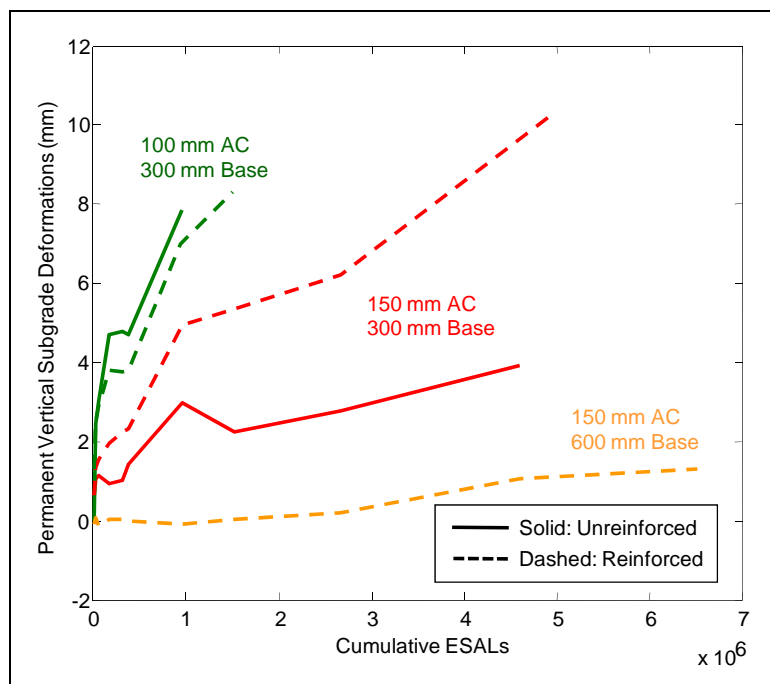


Figure 38. Permanent vertical deformations in the subgrade layer vs. cumulative ESALs (data has been adjusted according to the procedure outlined in this section). Matching unreinforced and reinforced test sections are shown in the same color: 100 mm AC/300 mm base is green, 150 mm AC/300 mm base is red, and 150 mm AC and 600 mm base is yellow.

There are no significant differences in the deformation of the asphalt layers between reinforced and unreinforced control sections (Figure 33); however, using this adjusted data, the reinforced base layers in test sections with 300 mm base experienced only about 40-60% of the deformation of those with the unreinforced control sections (Figure 34). Increasing the asphalt thickness from 100 mm to 150 mm appeared to provide approximately the same benefit as Geogrid reinforcement for sections with a 300 mm-thick base layer (Figure 34).

Compared with the unreinforced section with 150 mm of asphalt and 300 mm thick base, the base layer deformations in the reinforced section with 150 mm of asphalt and 600 mm of base were typically about 0.5 mm less (Figure 34). This is significant, since twice as much base material is subjected to deformations in the section with a 600 mm thick base.

In the test sections with 100 mm of asphalt and 300 mm of base, the deformations in the subgrade layer were slightly smaller in the reinforced test section (Figure 35). For the test sections with 150 mm of asphalt and 300 mm of base, the deformations in the subgrade layer were much larger

in the reinforced test section; however, this is attributed to the water that was added prior to trafficking the reinforced section, resulting in a significantly lower subgrade modulus compared to the unreinforced control section (Figure 14). There were practically no deformations in the subgrade layer for the section with 150 mm of asphalt, 600 mm of base, and Geogrid reinforcement until the wheel load was increased to 93.4 kN, and then the deformations were relatively small.

Deformations are presented for individual pavement system layers for the last set of SLTs in TS 1-4 and TS 5-8 in Figure 39 and Figure 40, respectively. The deformations have been adjusted for the five test sections that had a complete data set according to the procedure described above. Adjustment was not possible for the other sections with incomplete data sets, so the values shown represent those measured directly with functioning emu coils, as also presented in Figure 30 and Figure 31. The deformations in the subgrade with the static load applied are clearly much larger in TS 1, 2, and 4 than in the remaining sections. The permanent strains, taken as a deformation measured within a emu layer divided by the emu layer thickness, were generally concentrated in the upper 900 mm of material in each section. This 900 mm thickness value was used in the rutting model calibration.

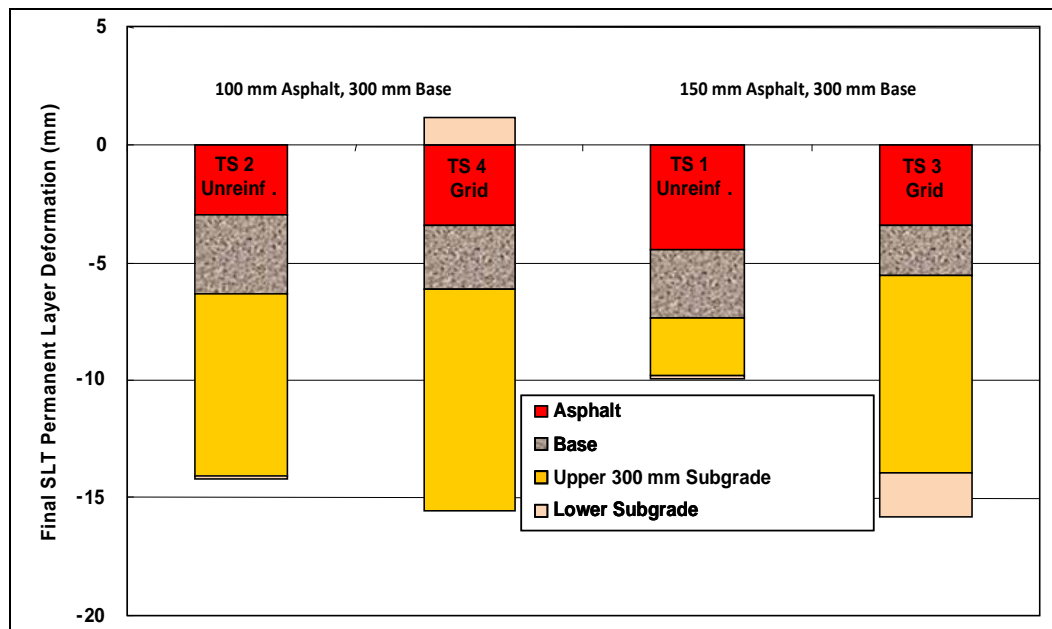


Figure 39. Permanent vertical deformations by individual emu layer for Test Sections 1-4 at the last set of SLTs (data has been adjusted according to the procedure outlined in this section).

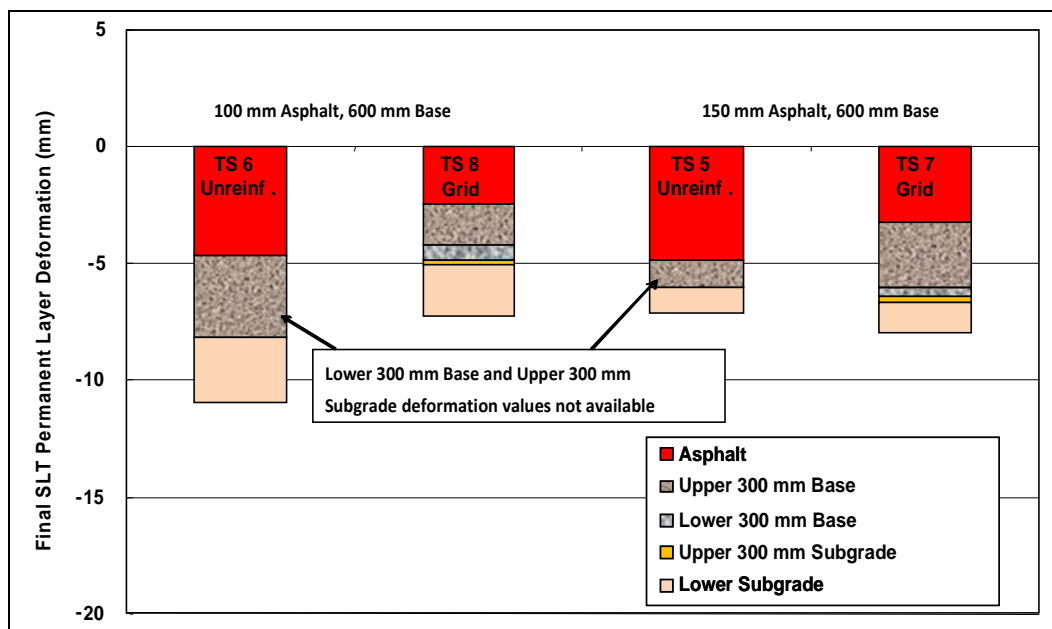


Figure 40. Permanent vertical deformations by individual emu layer for Test Sections 5-8 at the last set of SLTs (data has been adjusted according to the procedure outlined in this section).

Soil and asphalt elastic strains during static load application

The electromagnetic induction coil (emu gage) measurements under static wheel loading also determined the strains (permanent and elastic) for the asphalt, base, and subgrade material layers. For all test sections, the wheel was applied directly over the vertical emu stack with plan view coordinates [457 mm, 0 mm] and the longitudinal emu stack in the X direction (inline with the direction of traffic), with plan view coordinates [600 mm, 0 mm] (Figure 5a). The results of the SLTs with the wheel located over the longitudinal emu stack mainly provided a check on the data. The emu coils in the vertical stack were the transmitters of the signal. The emu coils in the longitudinal stack (and transverse stack—perpendicular to the direction of traffic—in the Y-direction) were the receiver coils. The vertical emu coils were also capable of being a receiver to determine the deformation in the vertical direction.

Thus, the two SLT plan view positions yielded measurements in all three directions, with the only difference being the position of the wheel with respect to the emu coils. The results of the SLTs with the wheel located over the longitudinal emu stack mainly provided a check on the data. The results of the tests with the wheel positioned at each location are presented here, and were used to back-calculate effective layer moduli, as described later in this report.

The average vertical elastic strain measured in each final SLT for each emu layer are presented in Figure 41 and Figure 42 for Test Sections 1 through 4 and 5 through 8, respectively. The average of the vertical elastic strains measured in each SLT with the wheel positioned over the longitudinal emu stack for each emu layer are presented in Figure 43 and Figure 44 for Test Sections 1 through 4 and 5 through 8, respectively. The average of the transverse (Y direction) elastic strains measured in each SLT with the wheel positioned over the vertical emu stack for each emu layer are presented in Figure 45 and Figure 46 for Test Sections 1 through 4 and 5 through 8, respectively. The average longitudinal elastic strains for each emu layer with the wheel load placed over the vertical emu stack are shown in Figure 47 and Figure 48 for Test Section 1 through 4 and 5 through 8, respectively. The elastic strains measured by the static load tests were averaged after removing obvious outliers from the data sets. All of the vertical emu readings in Test Sections 1 through 4 and 7 were valid, but gage failures in Test Sections 5, 6, and 8 caused invalid readings in these sections. Test Section 4 was the only section where all of the transverse emu readings were valid. The invalid readings are not presented.

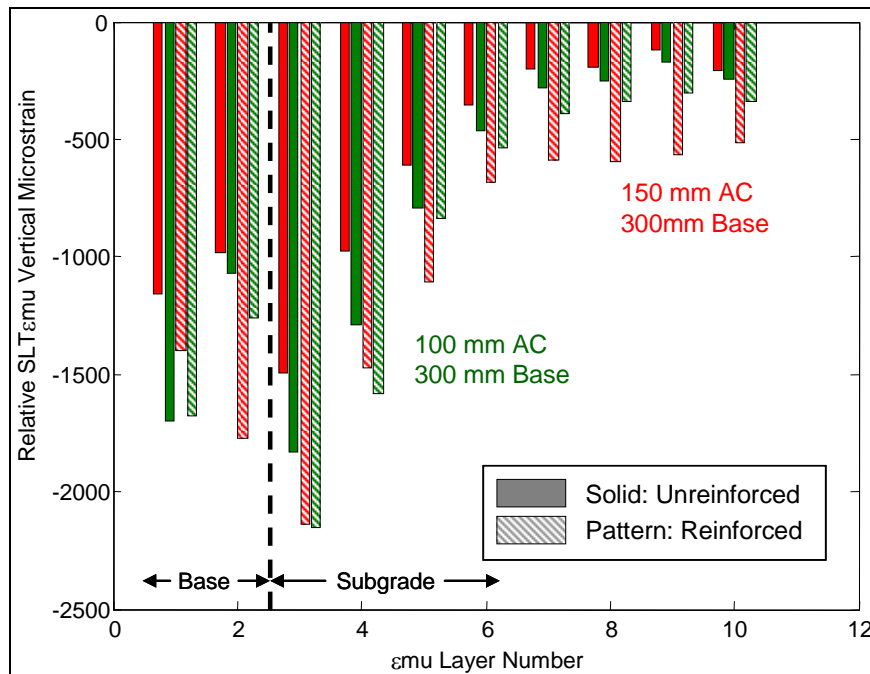


Figure 41. Average of SLT vertical elastic emu strains by emu layer for Test Sections 1 through 4 under a 48.9 kN (11 K) wheel load centered over the vertical emu stack. Matching unreinforced and reinforced test sections are shown in the same color: 100 mm AC/ 300 mm base is green and 150 mm AC/ 300 mm base is red.

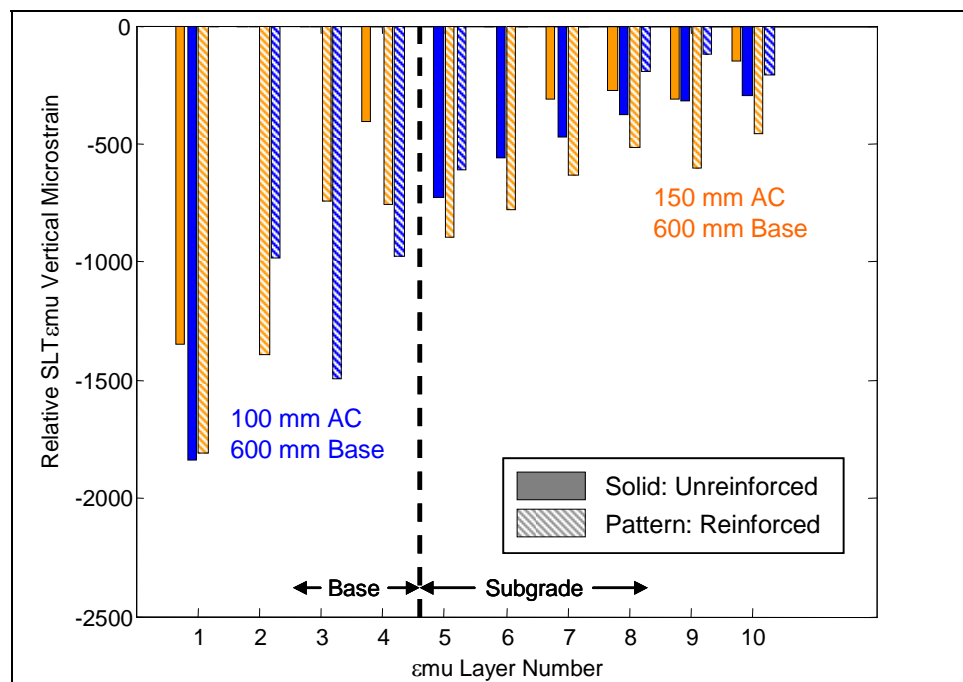


Figure 42. Average of SLT vertical elastic emu strains by emu layer for Test Sections 5 through 8 under a 48.9 kN (11 K) wheel load centered over the vertical emu stack.

Matching unreinforced and reinforced test sections are shown in the same color:

100 mm AC/ 600 mm base is blue and 150 mm AC/ 600 mm base is gold.

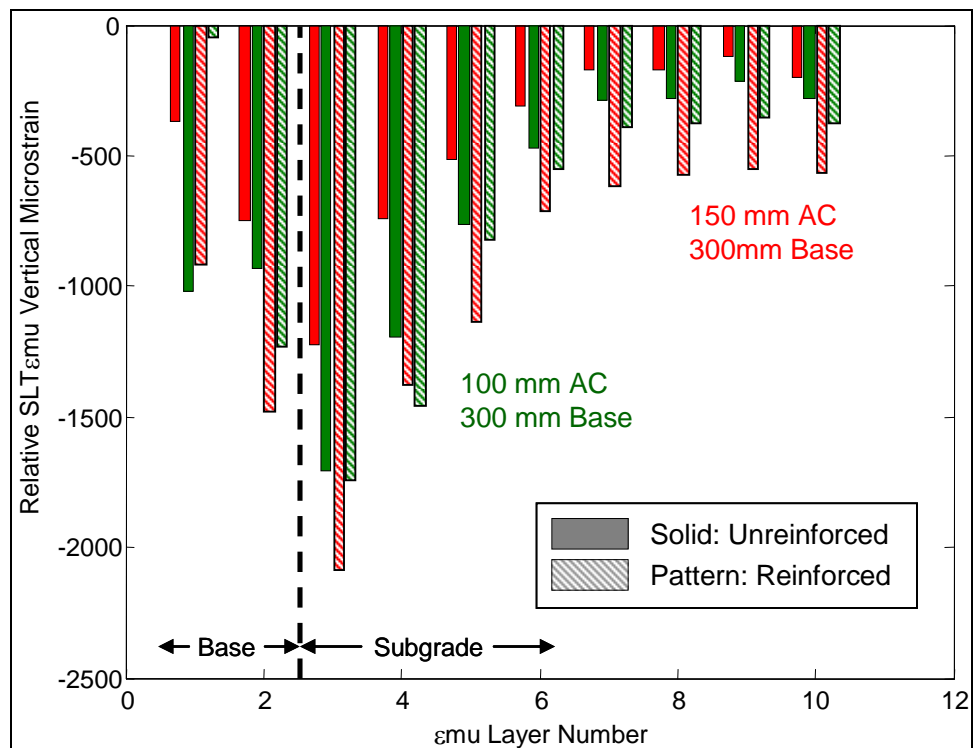


Figure 43. Average of SLT vertical elastic emu strains by emu layer for Test Sections 1 through 4 under a 48.9 kN (11 K) wheel load centered over the longitudinal emu stack. Matching unreinforced and reinforced test sections are shown in the same color: 100 mm AC/ 300 mm base is green and 150 mm AC/ 300 mm base is red.

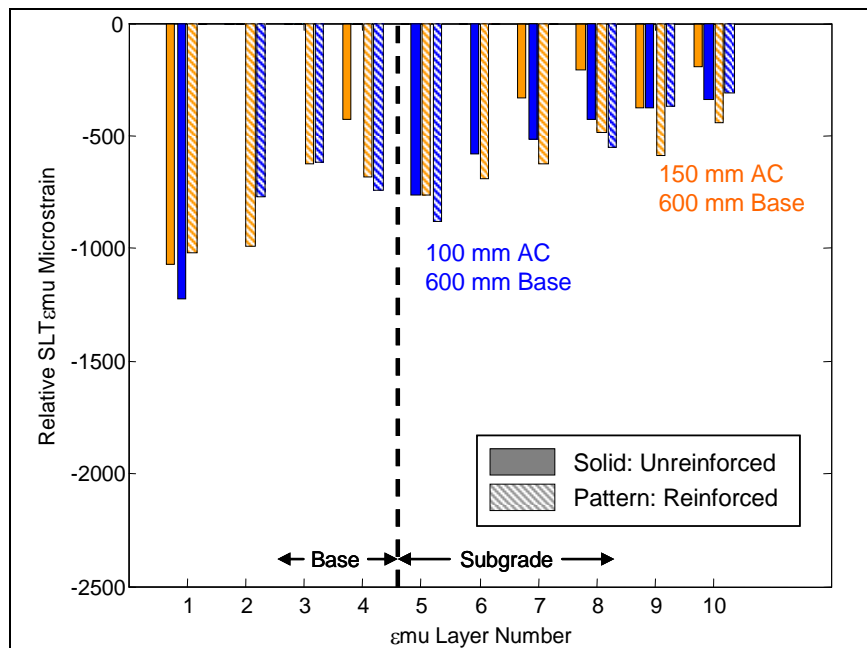


Figure 44. Average of SLT vertical elastic ε_{emu} strains by ε_{emu} layer for Test Sections 5 through 8 under a 48.9 kN (11 K) wheel load centered over the longitudinal ε_{emu} stack. Matching unreinforced and reinforced test sections are shown in the same color: 100 mm AC/ 600 mm base is blue and 150 mm AC/ 600 mm base is gold.

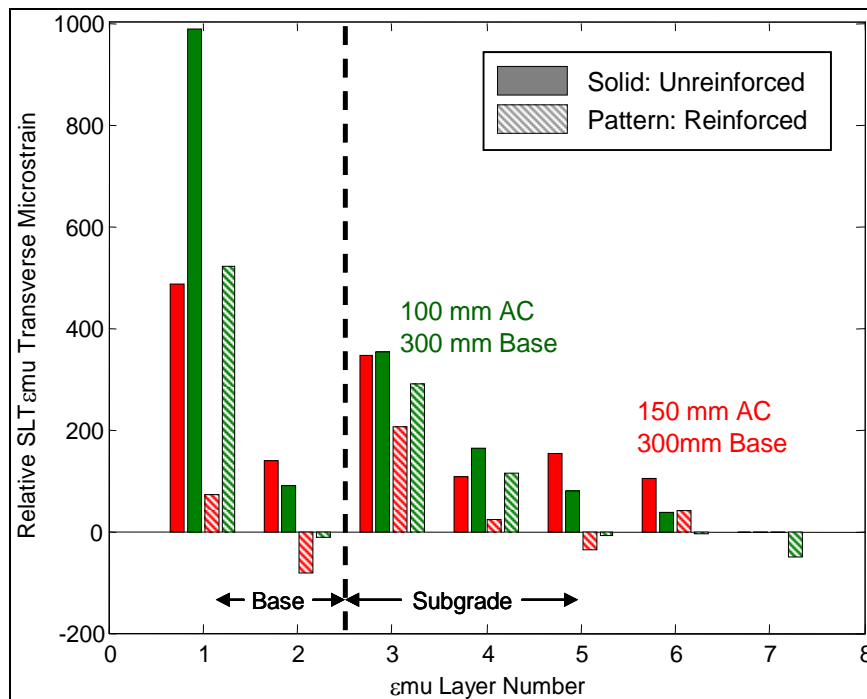


Figure 45. Average of SLT transverse elastic ε_{emu} strains by ε_{emu} layer for Test Sections 1 through 4 under a 48.9 kN (11 K) wheel load centered over the vertical ε_{emu} stack. Matching unreinforced and reinforced test sections are shown in the same color: 100 mm AC/ 300 mm base is green and 150 mm AC/ 300 mm base is red.

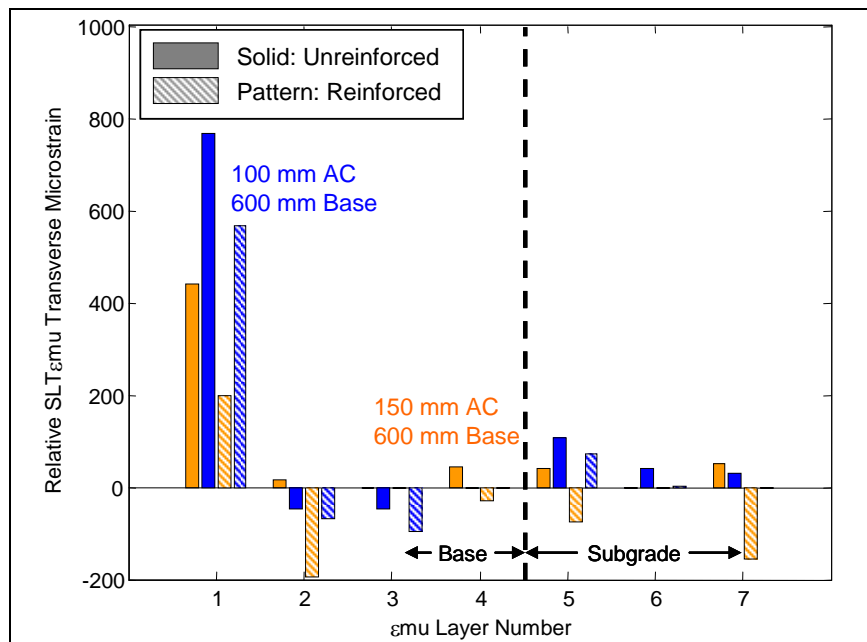


Figure 46. Average of SLT transverse elastic emu strains by emu layer for Test Sections 5 through 8 under a 48.9 kN (11 K) wheel load centered over the vertical emu stack. Matching unreinforced and reinforced test sections are shown in the same color: 100 mm AC/ 600 mm base is blue and 150 mm AC/ 600 mm base is gold.

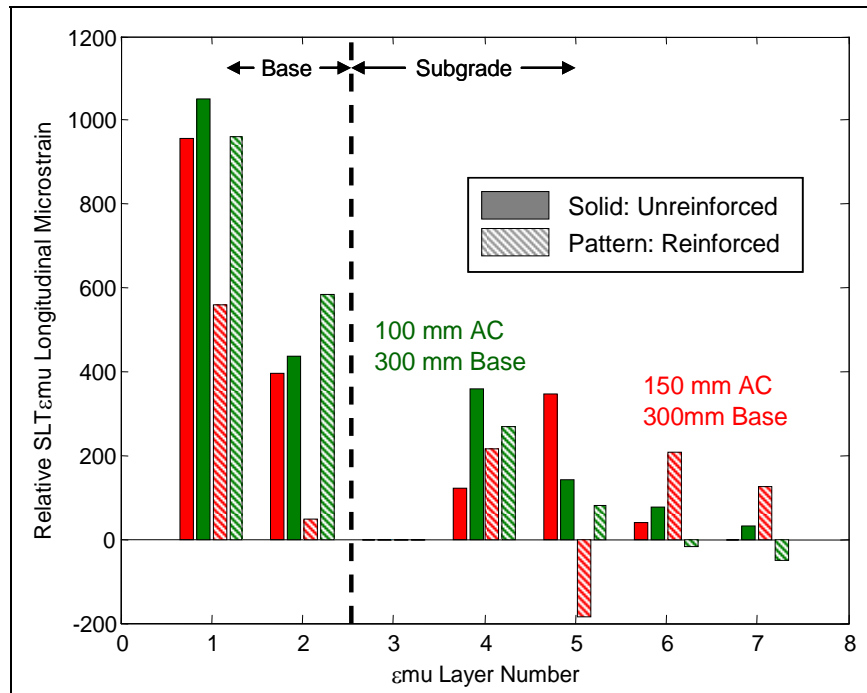


Figure 47. Average of SLT longitudinal elastic emu strains by emu layer for Test Sections 1 through 4 under a 48.9 kN (11 K) wheel load centered over the vertical emu stack. Matching unreinforced and reinforced test sections are shown in the same color: 100 mm AC/ 300 mm base is green and 150 mm AC/ 300 mm base is red.

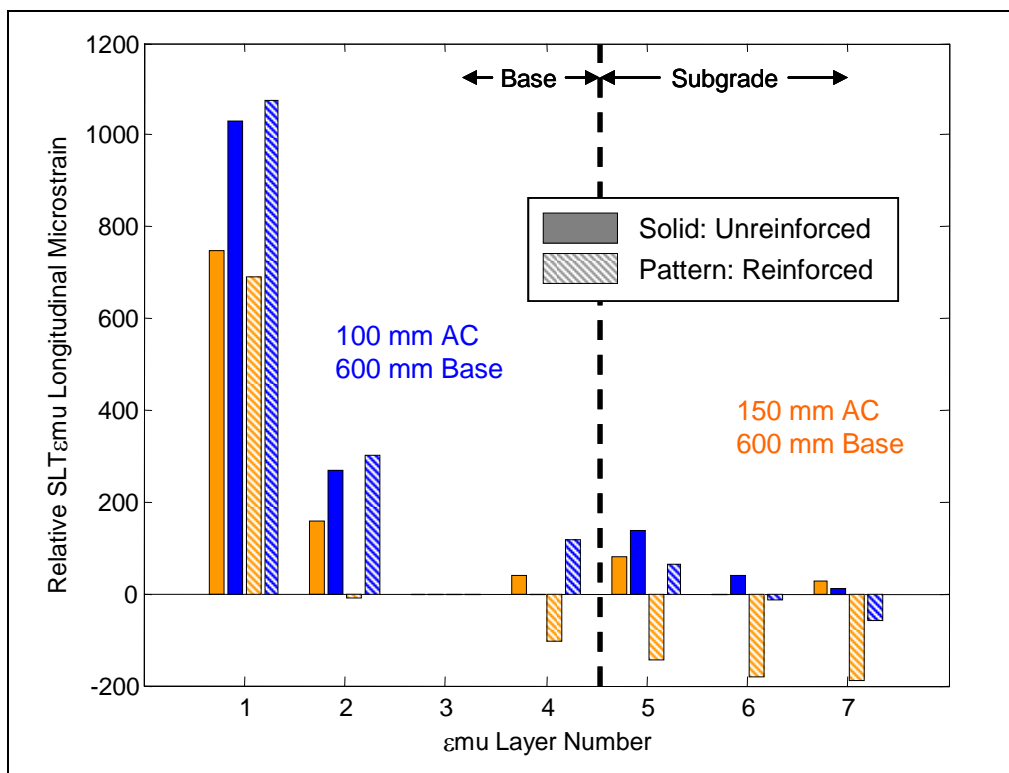


Figure 48. Average of SLT longitudinal elastic emu strains by emu layer for Test Sections 5 through 8 under a 48.9 kN (11 K) wheel load centered over the vertical emu stack. Matching unreinforced and reinforced test sections are shown in the same color: 100 mm AC / 600 mm base is blue and 150 mm AC / 600 mm base is gold.

The elastic strains were generally larger in the upper portions of the base and subgrade layers and decreased with depth in each layer. Vertical elastic strains at the top of the base layer ranged from about 1200 to 1800 microstrains while those at the bottom of the base layer typically ranged from about 500 to 1,000 microstrains. Vertical elastic strains at the top of the subgrade layer generally ranged from 600 to 1,200 microstrains, while the elastic strains at the lower layers in the subgrade ranged from 200 to 500 microstrains.

Transverse elastic strains at the top of the base layer ranged from about 200 to 1,000 microstrains, while those at the bottom of the base layer ranged from immeasurable within the tolerance of the instrumentation to 100 microstrains. Transverse elastic strains at the top of the subgrade layer ranged from immeasurable to about 350 microstrains, while the strains at the bottom of the subgrade layer were immeasurable.

The effect of asphalt thickness could not be established with certainty since variable results were observed and variation in layer thickness was

also observed during the forensic tests (see Appendix B), but it appears that the transverse and longitudinal strains in the base layer may have been reduced with a thicker asphalt layer.

The effect of base layer thickness is more clearly seen with respect to vertical strains. The average vertical elastic strain in the base layer was less with an increased base layer thickness. The average vertical strain in the subgrade layer was generally much less with an increased base layer thickness. However, the vertical strains in emu layers 5 through 10 (representing depths of 710 to 1,680 mm from the surface) appeared to be similar for sections with a 300 mm thick base or a 600 mm thick base. Base layer thickness appeared to have little, if any, effect on the transverse and longitudinal strains, other than reducing the peak strains near the top of the subgrade layer. However, the strains in the subgrade layer were generally comparable at equivalent depths from the surface.

The two reinforced sections (TS 3 and TS 4) experienced larger vertical elastic strains in the base and subgrade layers than the corresponding unreinforced sections (TS 1 and TS 2) (Figure 41). The elastic strains (in the base and subgrade) in reinforced TS 7 were also larger than in its corresponding unreinforced test section (TS 5) for all values that were able to be compared. However, the elastic strains (in the subgrade) in reinforced TS 8 were less than the corresponding unreinforced test section (TS 6) for the four values that were available for comparison.

Horizontal transverse strains in all reinforced sections were less than the transverse strains in the corresponding unreinforced sections at all levels. Horizontal longitudinal strains were reduced in a majority of the possible comparisons of reinforced sections to unreinforced sections, but several comparisons indicated increased longitudinal strains in reinforced sections. The reductions in strain due to reinforcement may have been larger in the transverse direction than the longitudinal direction because pavement rutting tensioned the Geogrid in the transverse direction; but, did not tension the Geogrid in the longitudinal direction. The grid affected transverse and longitudinal strains in a manner consistent with the primary mechanism of improvement being lateral confinement. However, the increased vertical elastic strains for the reinforced test sections were somewhat surprising. The unreinforced sections may have experienced reduced vertical elastic strains with respect to their corresponding

reinforced sections due to increased soil compaction. Greater compaction would result in an increased elastic modulus.

Keep in mind that there are several sources of experimental variability that likely influenced the strain measurements made. These include that compaction of soil around the coils was done by hand to avoid potential instrumentation damage from the heavy equipment used to compact the rest of the soil. It was also unlikely that uniform layer thickness was achieved during construction, as well as an inability to “directly center” the tire over the exact same location--directly above the stack of emu coils--during the SLTs.

Geogrid strain gage results

Elastic Geogrid strains

The wheel was applied directly over surviving Geogrid strain gages during the SLTs. These gages were oriented in the transverse or longitudinal direction. Geogrid strain gages 3 through 8 were located in the centerline of the wheel path, while the others were offset 300 mm from the centerline. Geogrid strain gages 5 and 6 were oriented in the longitudinal direction while the others were oriented in the Y direction. Details on gage locations and numbering are given in Henry et al. (2008). For the remainder of this report, the gages are referred to by number only and the average results are sometimes presented for pairs where both gages were functioning. .

The elastic Geogrid strains obtained during the SLTs are presented as a function of cumulative traffic cycles and ESALs in Figure 49 and Figure 50, respectively, for the reinforced sections. The elastic strain in the Geogrid was larger for the test sections with a 300 mm thick base layer with a range of about 300 to 1,000 microstrains, as compared to about 100 to 300 microstrains for test sections with a 600 mm thick base layer. Some of the gages indicated an increase in elastic strain during the SLTs as traffic cycles were accumulated. Note that the elastic Geogrid strains presented here may be larger than the elastic strains that would be experienced under a moving wheel load because of the dependence of stiffness on strain rate.

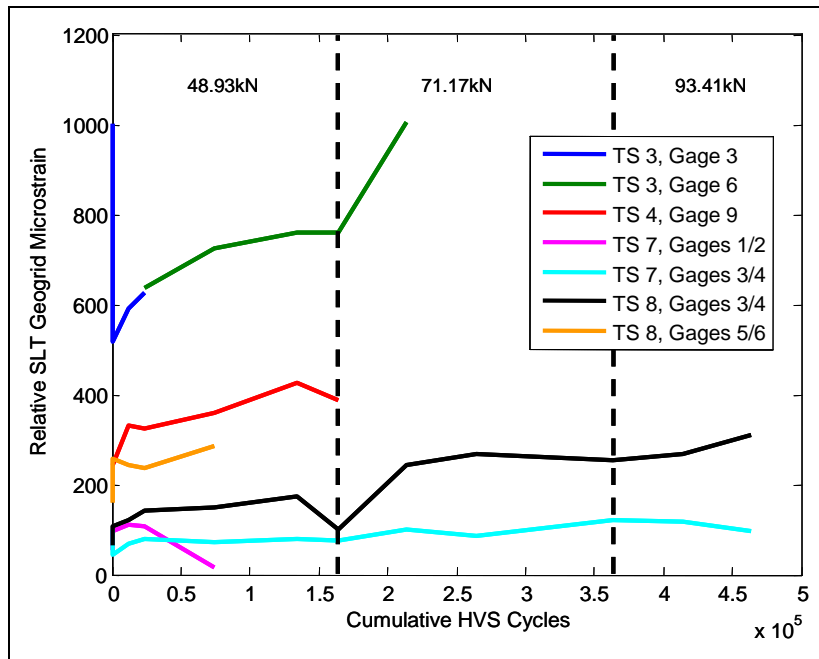


Figure 49. Elastic Geogrid SLT microstrains for all surviving gages under a 48.9 kN (11 K) wheel load vs. cumulative traffic cycles. Gages numbered 3-8 were beneath the center of the wheelpath. Gage 9 was offset 300 mm from the center. Gages 5 and 6 were oriented parallel to the direction of traffic, while the others were oriented perpendicular to the direction of traffic.

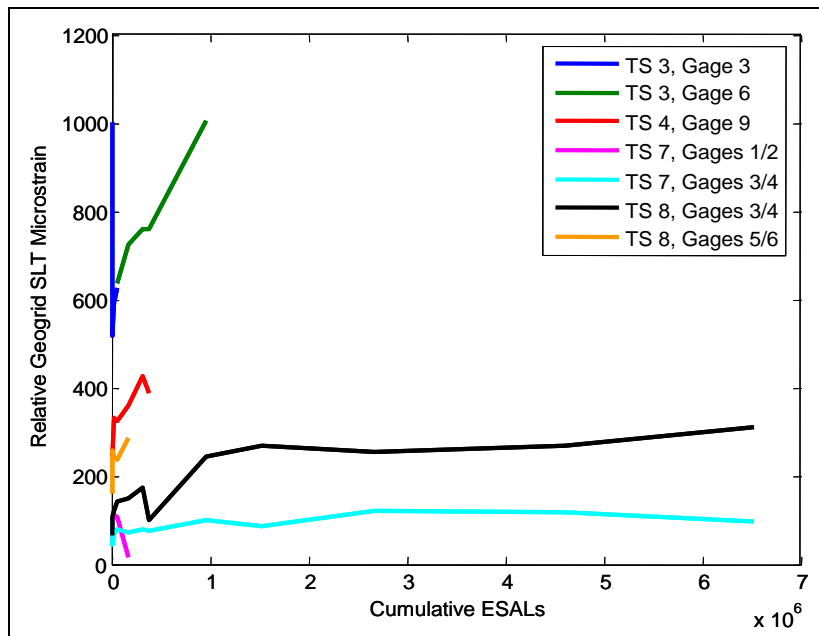


Figure 50. Elastic Geogrid SLT microstrains for all surviving gages under a 48.9 kN (11 K) wheel load vs. cumulative ESALs. Gages numbered 3-8 were beneath the center of the wheelpath. Gage 9 was offset 300 mm from the center. Gages 5 and 6 were oriented parallel to the direction of traffic, while the others were oriented perpendicular to the direction of traffic.

Permanent Geogrid strains

The permanent strain in the Geogrid was monitored by automatically collecting 1200 data points at a frequency of 100 Hz at four-hour intervals. Since this process was completely automated, it was not possible to know ahead of time whether dynamic traffic loads were being applied. Therefore, twelve seconds of data was collected, which corresponds to roughly two complete traffic cycles. This was sufficient to identify the points that corresponded to dynamic loading. A Matlab (MathWorks 2005) routine was implemented to identify these points and subsequently determine the average unloaded strain from 600 points that corresponded to the unloaded state. While this process was automated, the results were visually inspected to ensure that only unloaded strains were used for averaging.

The permanent Geogrid microstrains are presented in Figure 51, Figure 52, Figure 53, and Figure 54 for Test Sections 3, 4, 7, and 8, respectively, as a function of cumulative traffic cycles. The permanent Geogrid microstrains are presented in Figure 55, Figure 56, Figure 57, and Figure 58 for Test Sections 3, 4, 7, and 8, respectively, as a function of cumulative ESALs. All of the data is shown for gages for which times they were operational throughout the trafficking period. Data that exceeds the limits of the y-axis correspond to a gage that was not operating properly. Some gages, such as Gage 10 in TS 3 as shown in Figure 51, operated intermittently as the gage approached failure and the data may not be valid. Other gages, such as Gage 9 in TS 4 as shown in Figure 52, operated consistently and then abruptly failed. Five gages in TS 7 and two gages in TS 8 survived through the entire trafficking period as shown in Figure 53 and Figure 54.

The corresponding average relative rut depth is also shown in Figure 51 through Figure 58 as a comparison. Most of the Geogrid strain gages show a strong correlation between the magnitude of the developed permanent strain and rut depth, as expected.

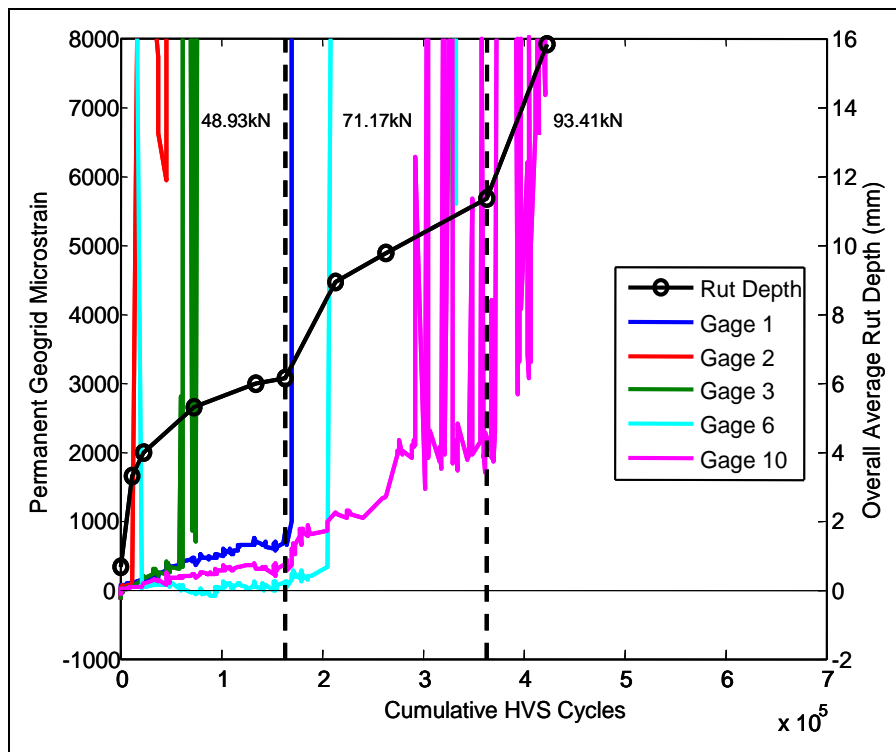


Figure 51. Permanent Geogrid microstrains in TS 3 vs. cumulative traffic cycles.

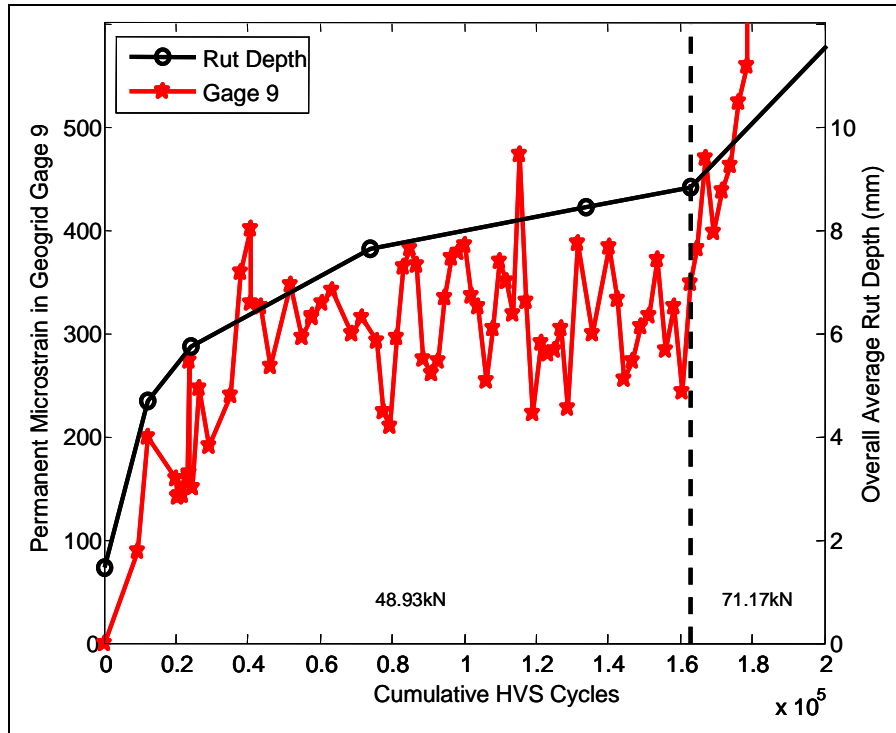


Figure 52. Permanent Geogrid microstrains in TS 4 vs. cumulative traffic cycles.

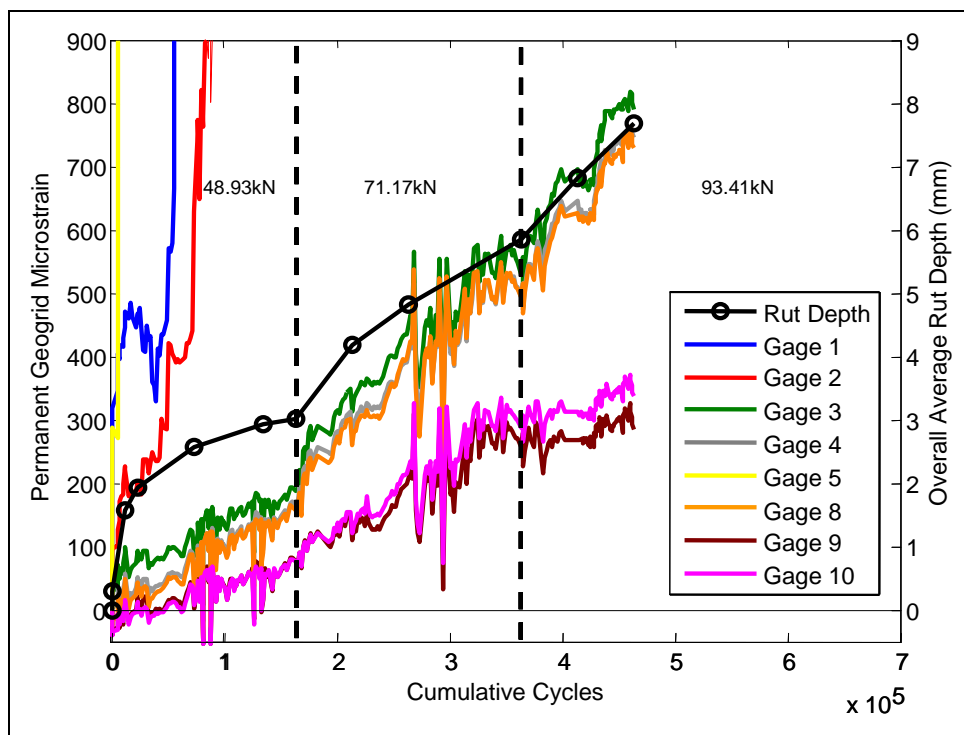


Figure 53. Permanent Geogrid microstrains in TS 7 vs. cumulative traffic cycles.

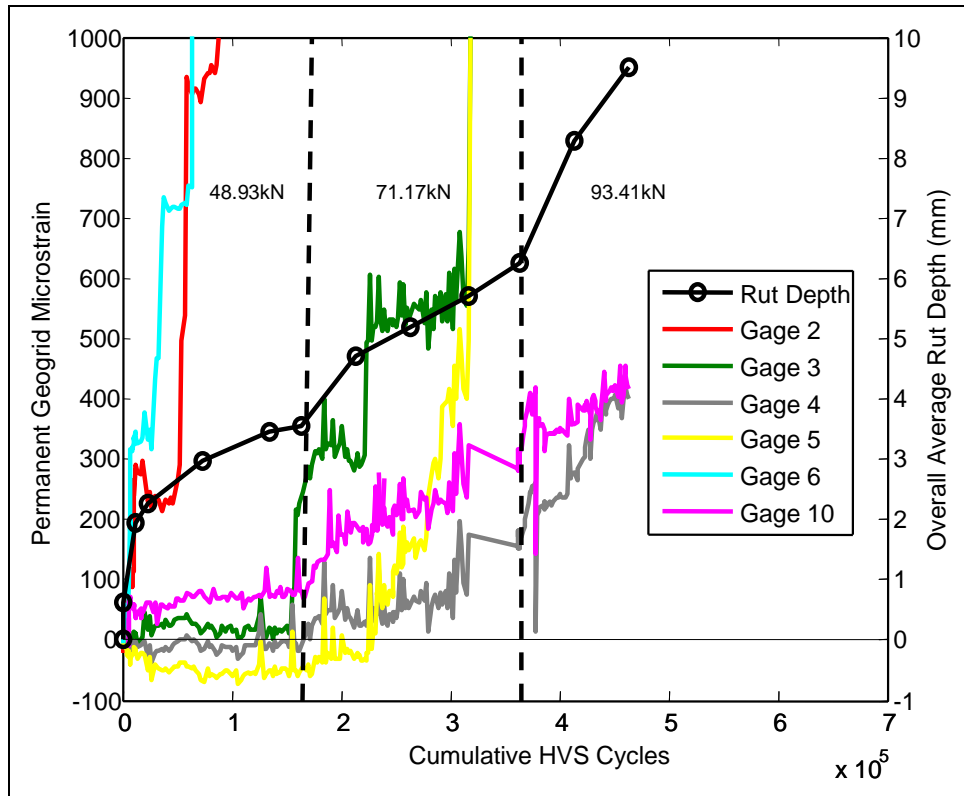


Figure 54. Permanent Geogrid microstrains in TS 8 vs. cumulative traffic cycles.

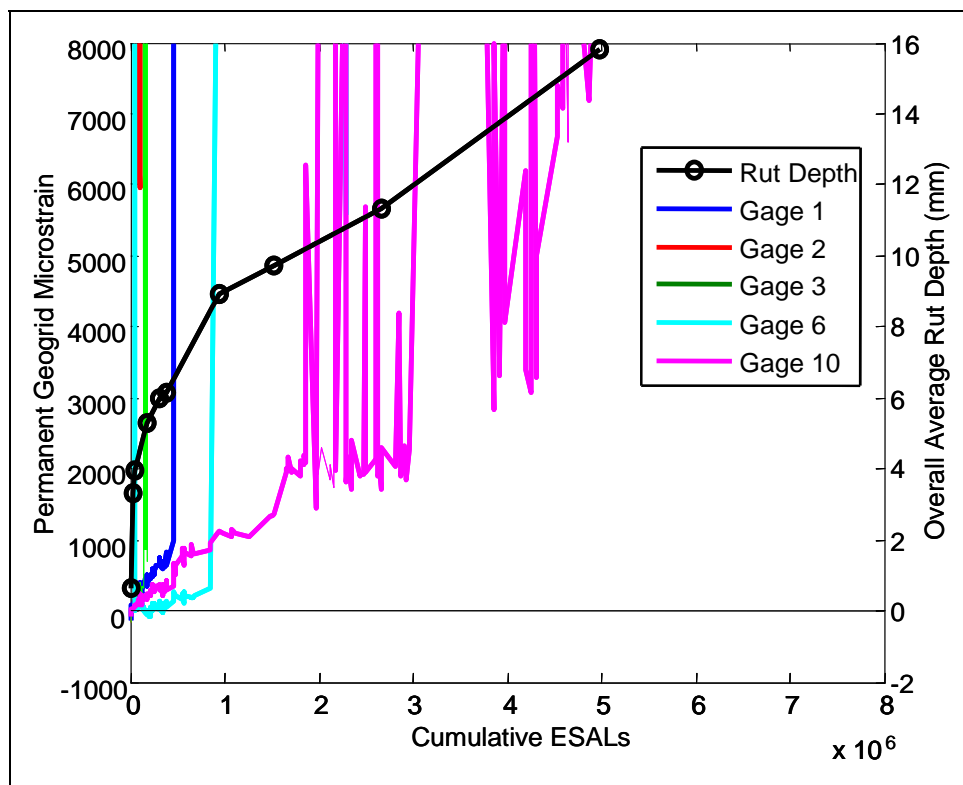


Figure 55. Permanent Geogrid microstrains in TS 3 vs. cumulative ESALs.

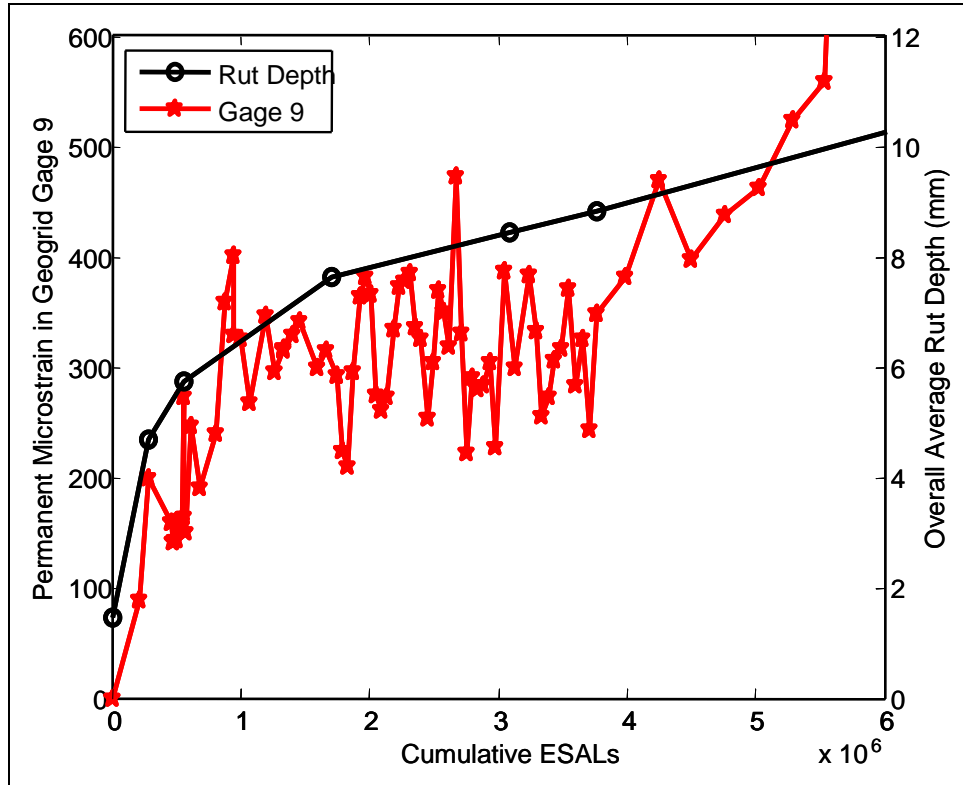


Figure 56. Permanent Geogrid microstrains in TS 4 vs. cumulative ESALs.

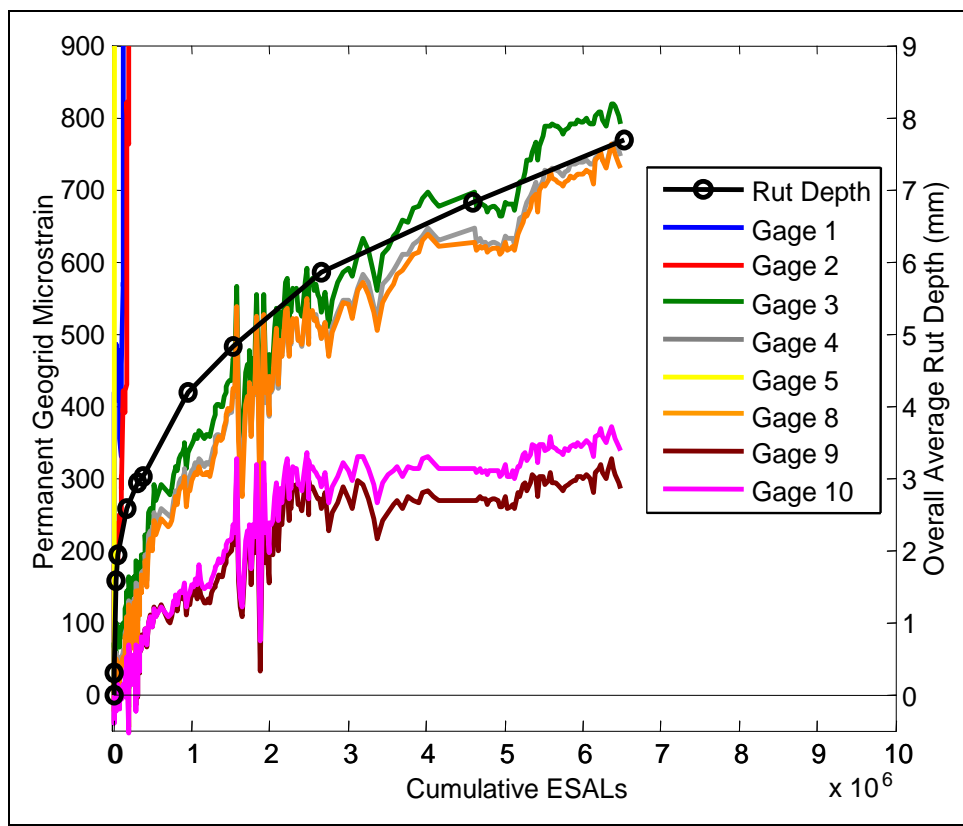


Figure 57. Permanent Geogrid microstrains in TS 7 vs. cumulative ESALs.

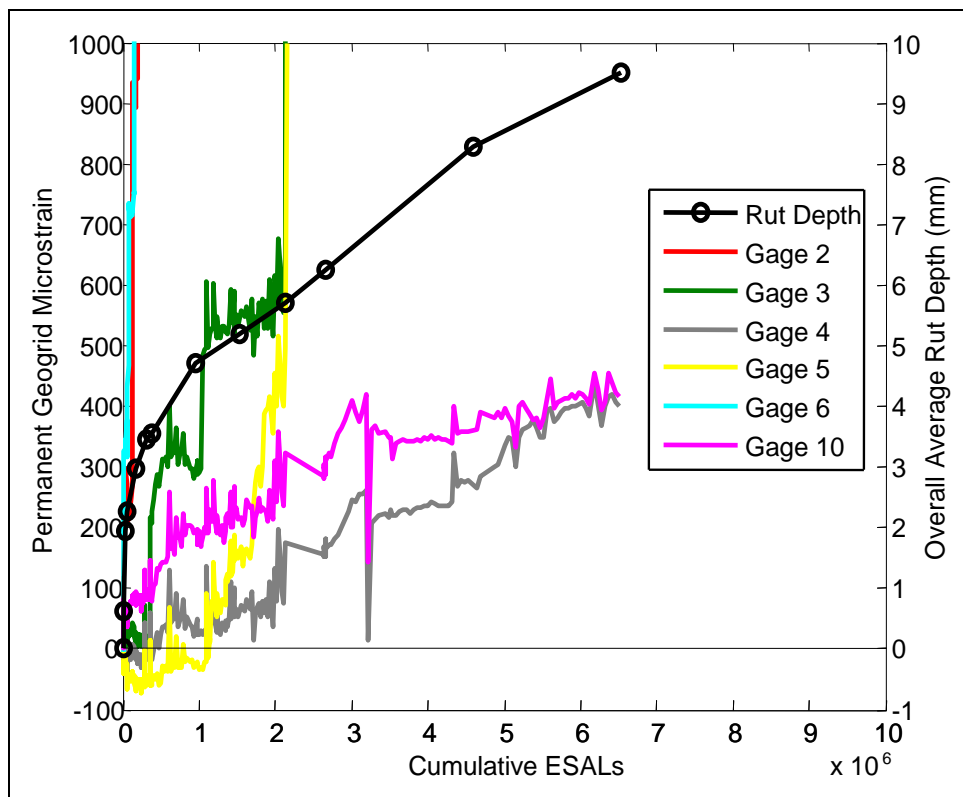


Figure 58. Permanent Geogrid microstrains in TS 8 vs. cumulative ESALs.

Stress

The transverse and vertical stresses that were recorded by the Geokon pressure cells are presented in Figure 59 through Figure 63 as a function of cumulative HVS traffic cycles for all of the unloaded SLTs. The unloaded transverse and vertical stresses that were recorded by the Geokon pressure cells are presented in Figure 64 through Figure 68 as a function of cumulative ESALs for all of the SLTs. There are no distinct trends in the measured stresses as a function of Geogrid reinforcement.

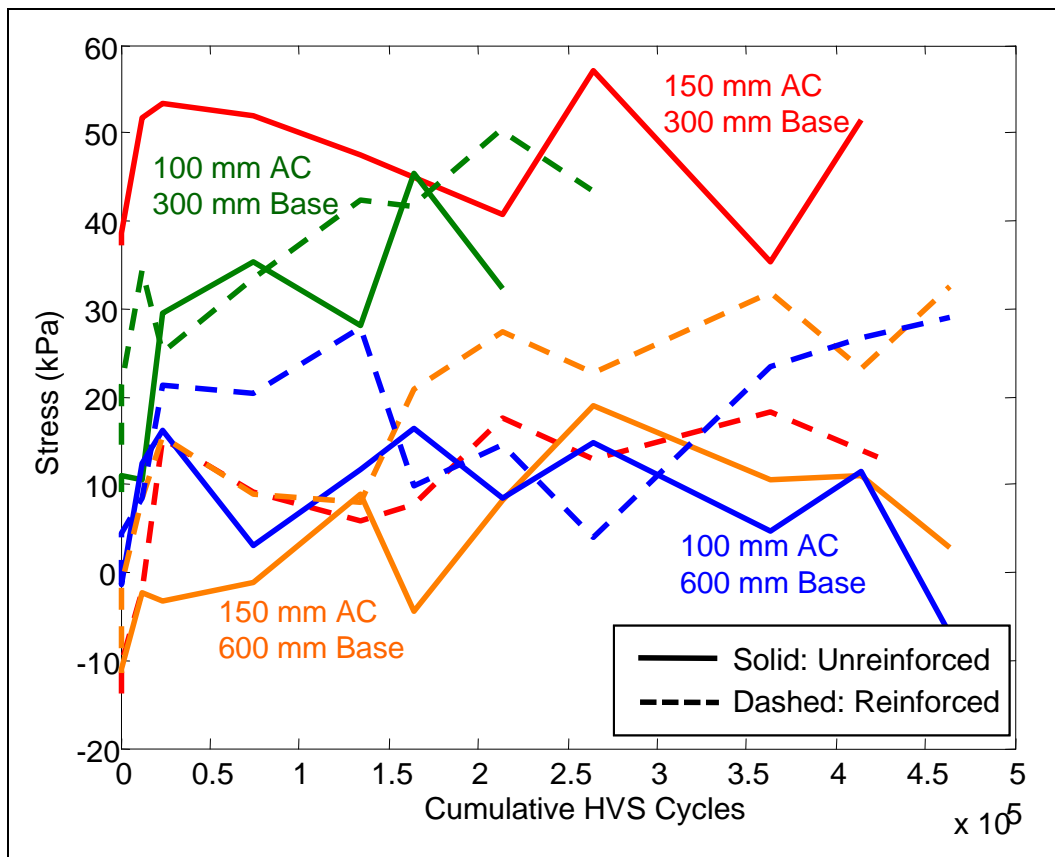


Figure 59. Transverse Geokon stresses near the top of the base layer as a function of cumulative HVS cycles measured in an unloaded condition.

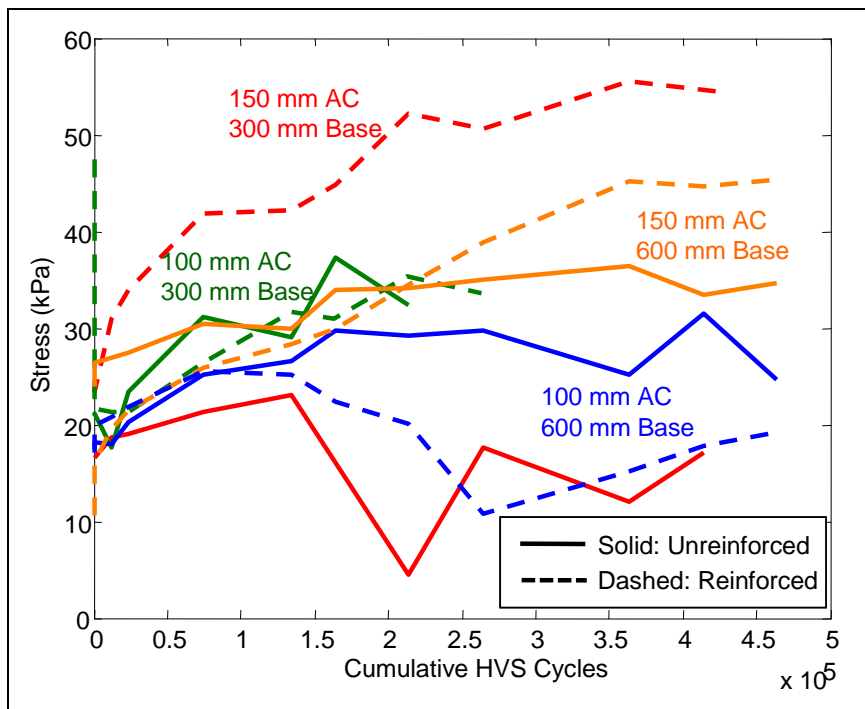


Figure 60. Transverse Geokon stresses near the top of the subgrade layer as a function of cumulative HVS cycles measured in an unloaded condition.

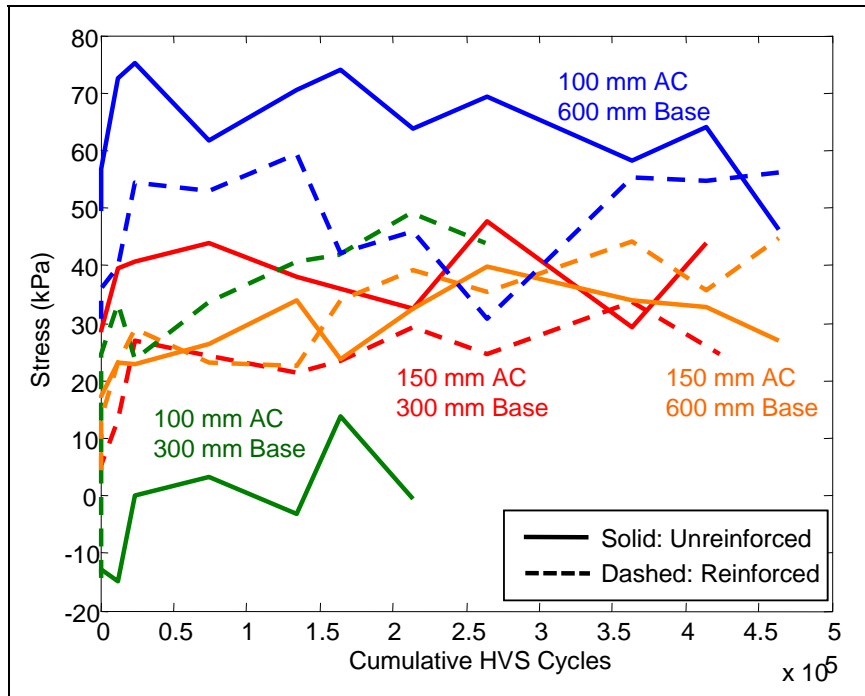


Figure 61. Vertical Geokon stresses near the top of the base layer as a function of cumulative HVS cycles measured in an unloaded condition.

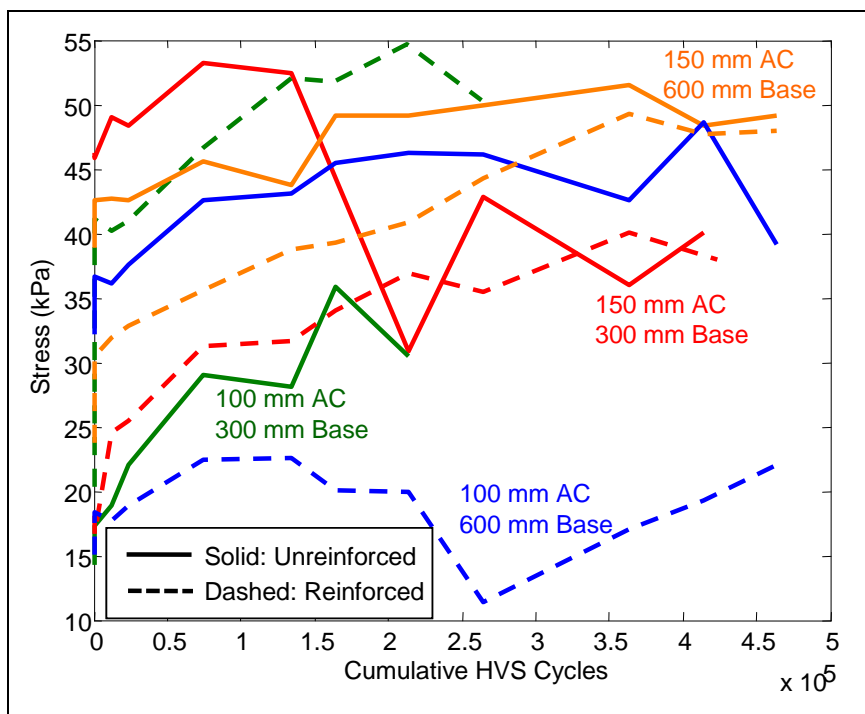


Figure 62. Vertical Geokon stresses near the top of the subgrade layer as a function of cumulative HVS cycles measured in an unloaded condition.

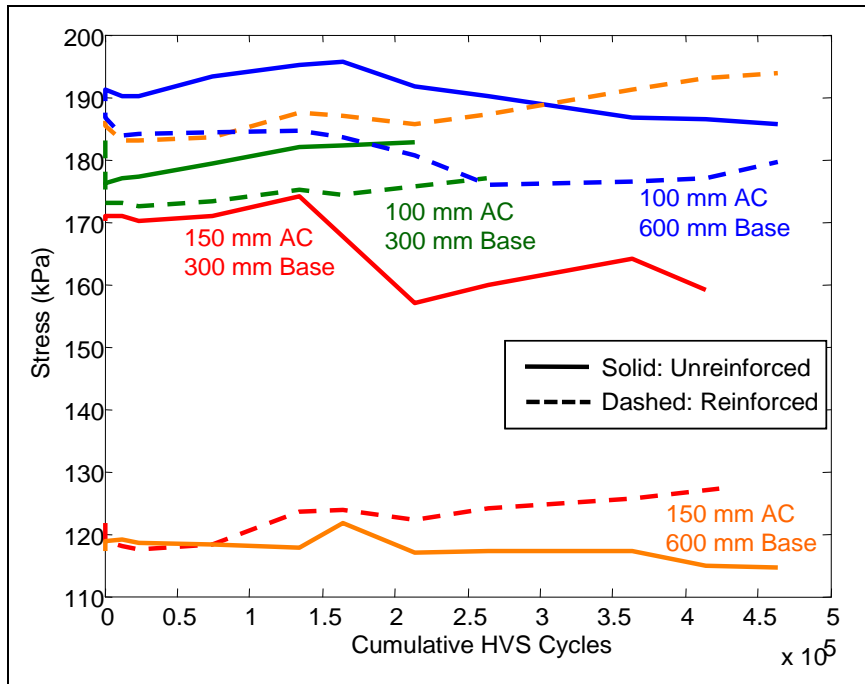


Figure 63. Vertical Geokon stresses lower in the subgrade layer as a function of cumulative HVS cycles measured in an unloaded condition.

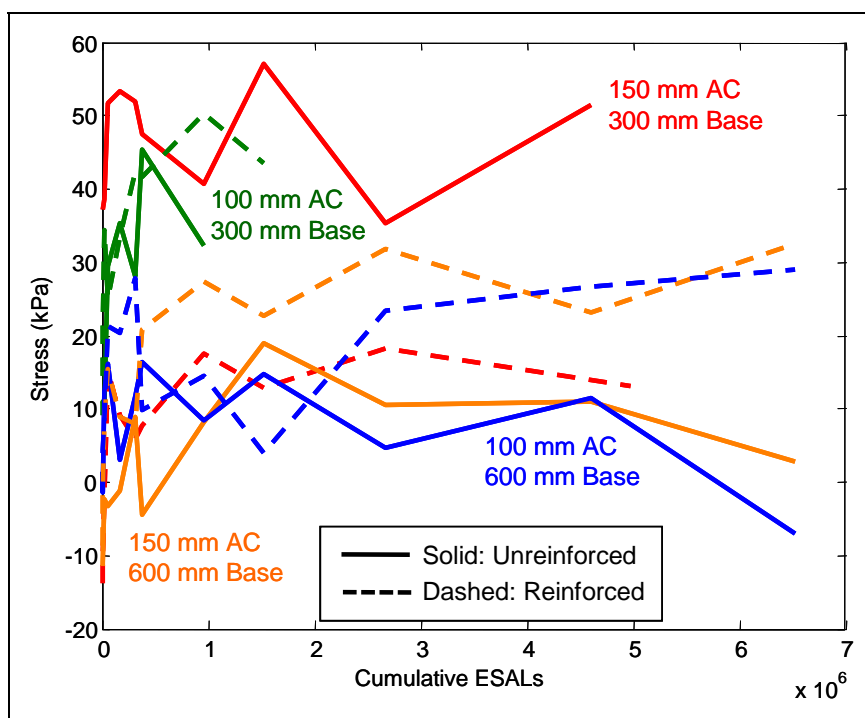


Figure 64. Transverse Geokon stresses near the top of the base layer as a function of cumulative ESALs measured in an unloaded condition.

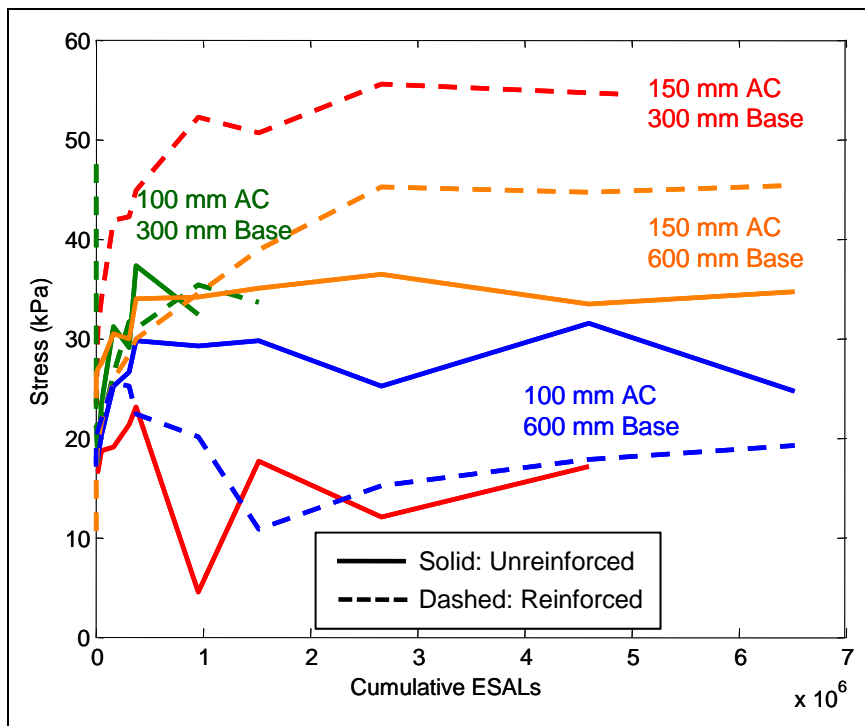


Figure 65. Transverse Geokon stresses near the top of the subgrade layer as a function of cumulative ESALs measured in an unloaded condition.

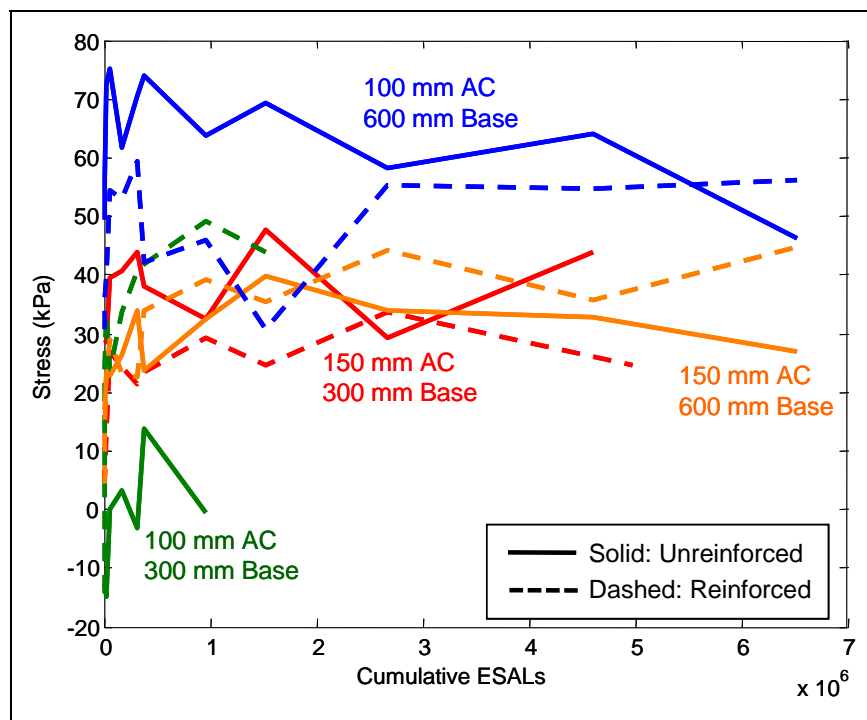


Figure 66. Vertical Geokon stresses near the top of the base layer as a function of cumulative ESALs measured in an unloaded condition.

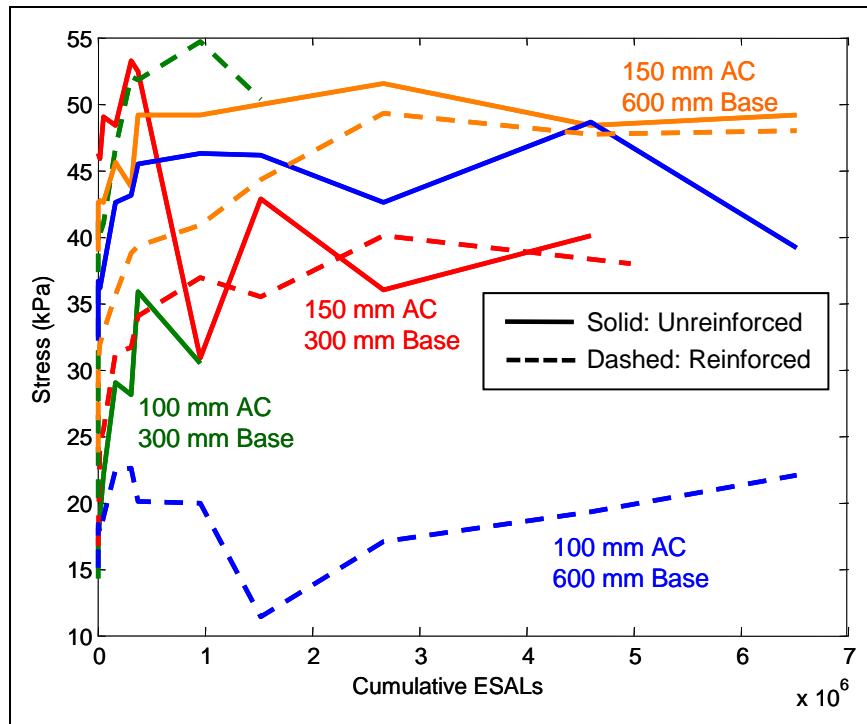


Figure 67. Vertical Geokon stresses near the top of the subgrade layer as a function of cumulative ESALs measured in an unloaded condition.

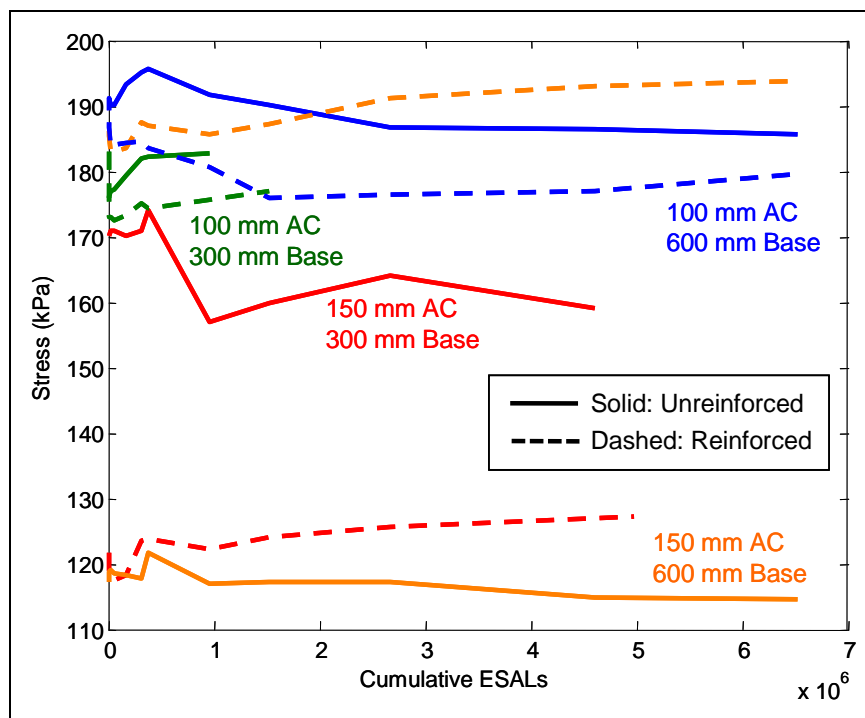


Figure 68. Vertical Geokon stresses lower in the subgrade layer as a function of cumulative ESALs measured in an unloaded condition.

The Geokon pressure cells that measured vertical stresses were also loaded with a 48.9 kN wheel load as part of the SLTs, but only at the first and last sets for any given TS. The relative changes in stress, $\Delta\sigma$, for these SLTs are presented in Figure 69. A data set was not available for the final SLTs in TS 1.

For the vertical stresses in the base layer, the stresses were larger for corresponding reinforced sections in 6 of the 7 possible comparisons, with the exception being the initial SLTs in TS 5 and 7. For the vertical stresses near the top of the subgrade layer, the stresses were larger for corresponding reinforced sections in 5 of the 7 comparisons, with the exceptions being the initial SLTs in TS 1 and 3 and the final SLTs in TS 6 and 8. For the vertical stresses lower in the subgrade, the relative stresses were generally small and no trends were observed.

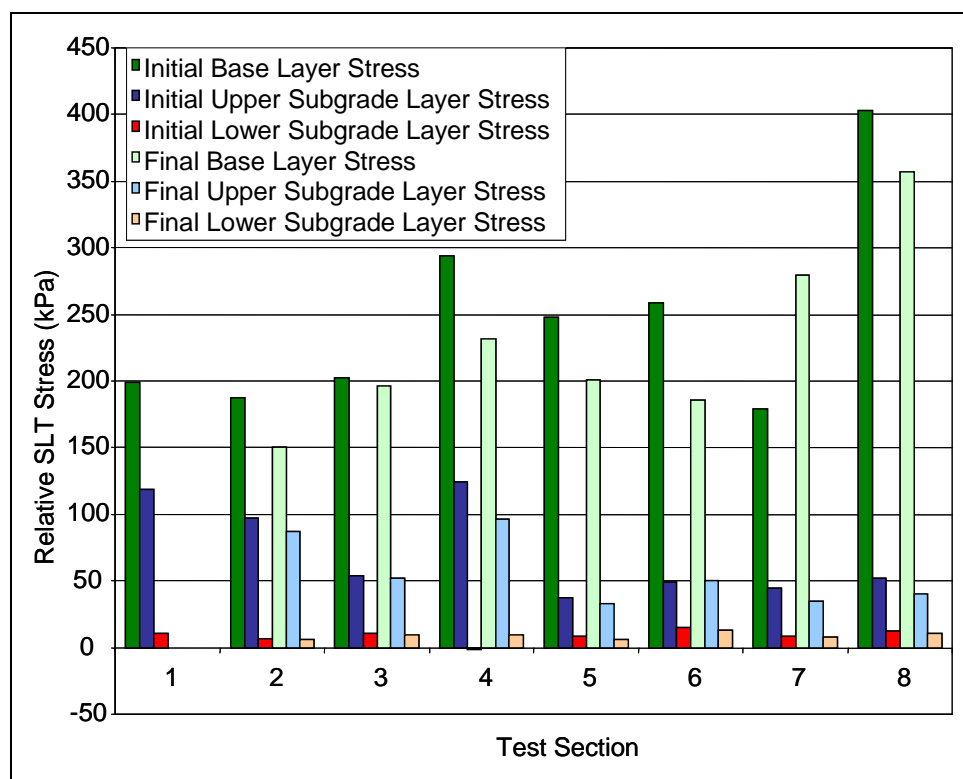


Figure 69. Relative vertical stresses measured by stress cells when a 48.9 kN (11 K) wheel load was applied.

6 Development of Rutting Models

Currently accepted mechanistic-empirical permanent deformation models recommended by NCHRP (2004b) were the starting point for predicting rutting in this study. These models use strains from mechanistic response models to predict long-term pavement rutting response through empirical relationships, which make them well-suited for routine design. For this project, FE models were used to estimate strains in the pavement structure layers due to traffic loads. This chapter describes the development of FE models, the estimation of layer material properties, and the subsequent calibration of permanent deformation equations based on the data obtained in this study.

FE model development

The FE solver used for all analyses in this study was the underlying computational engine for EverFE (www.civil.umaine.edu/everfe) and EverStressFE (www.civil.umaine.edu/everstressfe), freely available 3D FE programs developed for the analysis of rigid and flexible pavements, respectively (Davids et al. 2003). This FE code is applicable to the analysis of geogrid-reinforced flexible pavement systems with the modifications discussed in this section. The numerical computing package Matlab (MathWorks 2005) was used to develop pre- and post-processing routines for the FE models of this study and to calibrate the rutting models that are described later.

The FE mesh was quarter-symmetric with plan-view dimensions corresponding to one quarter of a test section, which avoided modeling the abrupt changes in material properties and thickness in adjacent test sections. Figure 70 shows a typical FE mesh, which had 3636 solid elements and 58914 degrees-of-freedom. The AC, base, and subgrade layers were discretized with 20-node quadratic brick elements. The Geogrid was modeled with orthotropic 8-node membrane elements that only carry in-plane loads. Mesh refinement, size of the refined region, and overall model size were chosen to ensure convergence of strains as detailed by Clapp (2007). Zero displacement boundary conditions were enforced normal to planes of symmetry as well as at the bottom of the subgrade layer. Constraints were used to maintain displacement continuity by fixing relative vertical displacements between pairs of nodes that were not directly bonded, which includes soil layers and the Geogrid layer.

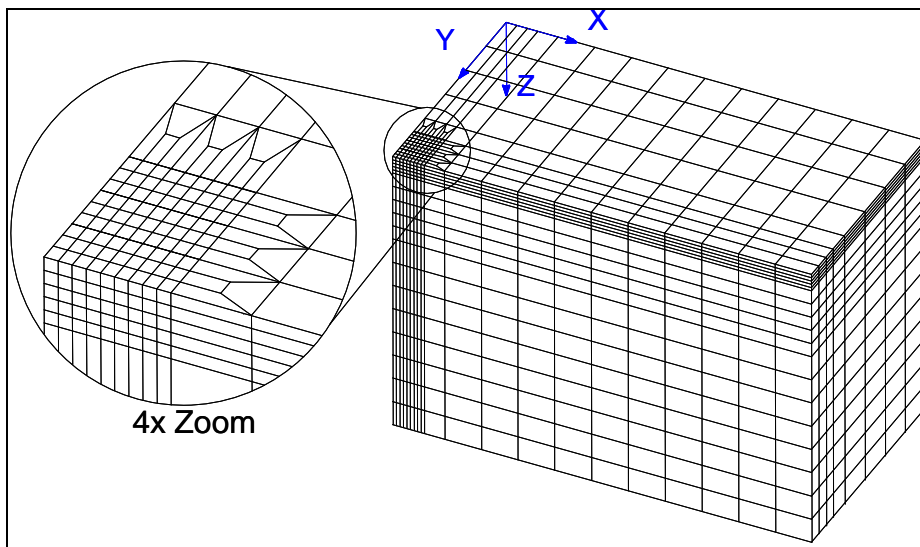


Figure 70. Typical quarter-symmetric FE mesh.

The asphalt and soil were treated as linearly elastic and isotropic; the determination of effective material properties is discussed below. Shear stresses were transferred between the soil and Geogrid through 16-node interface elements (Davids and Mahoney 1999). The interface shear stress (N/mm^2) is the product of interface stiffness (N/mm^3) and the relative displacement (mm) between top and bottom nodes. The interface stiffness was applied independently in orthogonal directions.

The HVS wheel load was applied as a surface load. Each of the dual tires had widths of 223 mm separated by a gap of 112 mm. The tire pressure used in this study was 690 kPa. A constant contact stress equal to the tire pressure was assumed, and the length of the tire contact area was calculated based on the magnitude of the wheel load. As detailed later, the Geogrid was pre-strained to simulate tensile strains that developed in the Geogrid due to construction and trafficking.

Material properties

The effective elastic modulus of the AC layer was determined by dynamic modulus testing according to AASHTO TP 62-03 by Worcester Polytechnic Institute (Henry et al. 2008). However, the loading frequencies utilized in this testing were much greater than the effective loading frequency for the SLTs, so pseudo-static asphalt compression testing was performed by the University of Maine on four asphalt cores taken along the edges of TS 2 and TS 4. The applied compressive stress was ramped up over a time period of 60 sec to a stress equal to the HVS tire pressure. The average

secant modulus after 60 sec was found to be 230 MPa. A detailed description of specimens and testing protocol is described in Appendix C.

FWD testing, as described in Section 5, was performed to obtain an estimate of in-situ layer moduli. Given the large variability in layer moduli among the test sections (especially when caused by adding water during the testing period) it was not appropriate to assume a single set of average effective layer moduli for all test sections. This also meant that measured rutting could not be directly compared without considering the differences in layer moduli. The most comprehensive method for back-calculating layer moduli from the available load response data would be to minimize the error between the FE-predicted strains and the measured emu coil strains by solving for the optimal layer moduli. However, there are several reasons for avoiding this:

- It is a complex and time-consuming process that requires careful oversight, which makes it inefficient in practical applications. Further, the data obtained from instrumentation used in this study is not available in the field.
- The strategy used to account for reinforcing mechanisms does not facilitate direct modeling of reinforced sections.
- Failure of critical gages in some sections would make the results questionable.

For these reasons, the average (before and after trafficking) layer moduli determined through FWD testing and analysis were used as input to the FE model of this study (see Figure 14 - Figure 17). This is shown to be a reasonable assumption in the next section. The layer moduli representing TS 4 were the only exception to this, since FWD test data was not available directly after trafficking. For TS 4, the average FWD layer moduli were taken to be the values from FWD testing of TS 2. Initial FWD layer moduli in TS 4 were 11% and 2% larger for the base and subgrade layers, respectively, compared to TS 2, which was not considered to be significant. Using the same layer modulus values for TS 2 and TS 4 implies that the difference in model-predicted rutting for these two test sections was due only to reinforcement, whereas model-predicted differences during the calibration phase for the other pavement configurations were due to a combination of reinforcement and varying layer moduli. In reality, many factors that are not captured in the models may have contributed to the observed

differences in rutting behavior (e.g. variable layer thicknesses, inaccurate layer moduli assumptions, measurement error, etc.).

A summary of the parameters used in FE models for permanent deformation model calibration is provided in Table 13. During trafficking of TS 1, the heating and ventilation system in the laboratory malfunctioned and the temperature decreased significantly between 164000 cycles to 214000 traffic cycles. This appeared to significantly affect rut development. The corresponding average asphalt temperature of 15.3 °C was used to estimate the asphalt modulus at about 3900 MPa from available laboratory dynamic modulus test results. This value was used in the FE model to represent the range of cycles specified above.

Table 13. Summary of FE model parameters for rutting model calibration.

TS	Cycles ($\times 10^3$)	Layer Modulus (MPa)			Thickness (mm)		Wheel Loads (kN)
		AC	Base	Subgrade	AC	Base	
1	0 - 164, 214 - 414	2720	135.4	56.3	150	300	All
1	164 - 214	3900	135.4	56.3	150	300	71.17
2	0 - 214	2720	87.6	51.6	100	300	48.93, 71.17
3	0 - 424	2720	269.9	38.7	150	300	All
4	0 - 263	2720	87.6	51.6	100	300	48.93, 71.17
5	0 - 464	2720	190.5	57.7	150	600	All
6	0 - 464	2720	151.0	50.3	150	600	All
7	0 - 464	2720	199.6	60.5	150	600	All
8	0 - 464	2720	177.5	57.9	150	600	All

Poisson's ratio for all materials was taken as 0.35, which is in the range of values presented in prior studies. Poisson's ratio and in-plane shear modulus for the Geogrid were estimated as 0.45 and 2.9 MPa, respectively, which are based on values reported by Perkins et al. (2004). The Geogrid moduli in orthogonal directions and interface stiffness are discussed later.

Validation of FE model using FWD layer moduli

The layer moduli of the test sections in this study were estimated by performing FWD testing (see Section 5), which is widely accepted for estimating layer moduli using measured pavement surface deflections. The FE model of this study was also utilized to back-calculate layer moduli

using the average SLT emu strain data measured throughout the pavement thickness. The fact that these two approaches resulted in similar moduli served as a limited validation of the FE model, since the FWD method is widely used and accepted. Details of this process are described in this section.

The layer moduli were back-calculated by minimizing the error between the strains measured by emu coils and those predicted by the FE model for TS 2. Effective average strains were determined from relative displacements and known initial layer thicknesses. The FE model included the applied wheel load and not self-weight, which was consistent with the SLTs. The model calibration parameters were taken as the base and subgrade layer moduli, and the asphalt modulus was fixed at the value of 230 MPa, measured in the laboratory by UMaine to reflect the rate of load application in the SLTs (Appendix C). Three-parameter optimization that included the asphalt modulus as a parameter was also performed, and gave very similar results (see Clapp 2007 for details). The deformation data from SLTs conducted after 0.25, 12, 24, 74, 164, and 214 thousand cumulative cycles were used for calibration. All valid data were averaged and used for back-calculation of layer moduli.

The least squares error (φ) was minimized to determine the optimal set of layer moduli as expressed in Equation (2), where j refers to the direction: x, y, or z, $\varepsilon_{emu,i,j}$ is the laboratory measured strain for emu layer number i in direction j , and $FE_{i,j}$ is the FE-predicted strain for emu layer number i in direction j . If there were no horizontal emu coils within a layer or the emu readings were invalid for a particular layer, the respective error was set to zero.

$$\varphi = \sqrt{\sum_{i=1}^{num_layers} \sum_{j=1}^3 (\varepsilon_{emu,i,j} - FE_{i,j})^2} \quad (2)$$

The process of determining the best set of layer moduli by minimizing φ is a classic optimization problem that has been widely studied in the field of pavement engineering (Uzan et al. 1988, Hossain et al. 1994, Kang 1998). In this study, conventional gradient-based approaches to minimizing φ were found to be largely ineffective due to the presence of multiple local minima, a problem that has been noted by others (Hossain et al. 1994, Kang 1998).

To circumvent this difficulty, a simple genetic algorithm (SGA) with elitism and mutation was used to minimize φ . This method was pioneered by Holland (1975) and has been significantly extended by Goldberg (1989), Goldberg and Deb (1991), and Michalewicz (1992), among others, to mimic the biological process of natural selection. Experience indicated that the SGA was typically able to produce a solution near the global minimum after only a few generations, and that successive generations only improved marginally on the solution. Hence, the final optimization procedure was a hybrid procedure that initially relied on the SGA method to approximately locate the global minimum, and then the Nelder-Mead Simplex search method was used to quickly converge to the global solution. When a certain percentage of the most-fit members of a population were within a certain percentage of the original search space, the genetic algorithm was terminated and the simplex search started. Full details of the SGA used here may be found in Clapp (2007).

The traditional approach for back-calculating layer moduli is to assume perfect bond between all layers in the pavement system. However, models with de-bonded layers sometimes yield more reasonable predictions of layer moduli (Romanoschi and Metcalf 2002). In this study, the effect of the asphalt-base bond condition was investigated by analyzing the two opposite cases: perfectly bonded and completely de-bonded. The two layer modulus values were back-calculated simultaneously for each of these conditions. The bonded case resulted in $\varphi = 2040 \times 10^{-6}$ and the de-bonded case yielded $\varphi = 1580 \times 10^{-6}$. A comparison of the model-predicted and measured strains indicated that de-bonded layers gave better overall results. Figure 71 compares the measured and FE-model predicted strains for the de-bonded case. The back-calculated layer moduli were 81.4 MPa and 50.9 MPa for the base and subgrade layers, respectively. These values compared very well to the average FWD values of 87.6 MPa and 51.6 MPa.

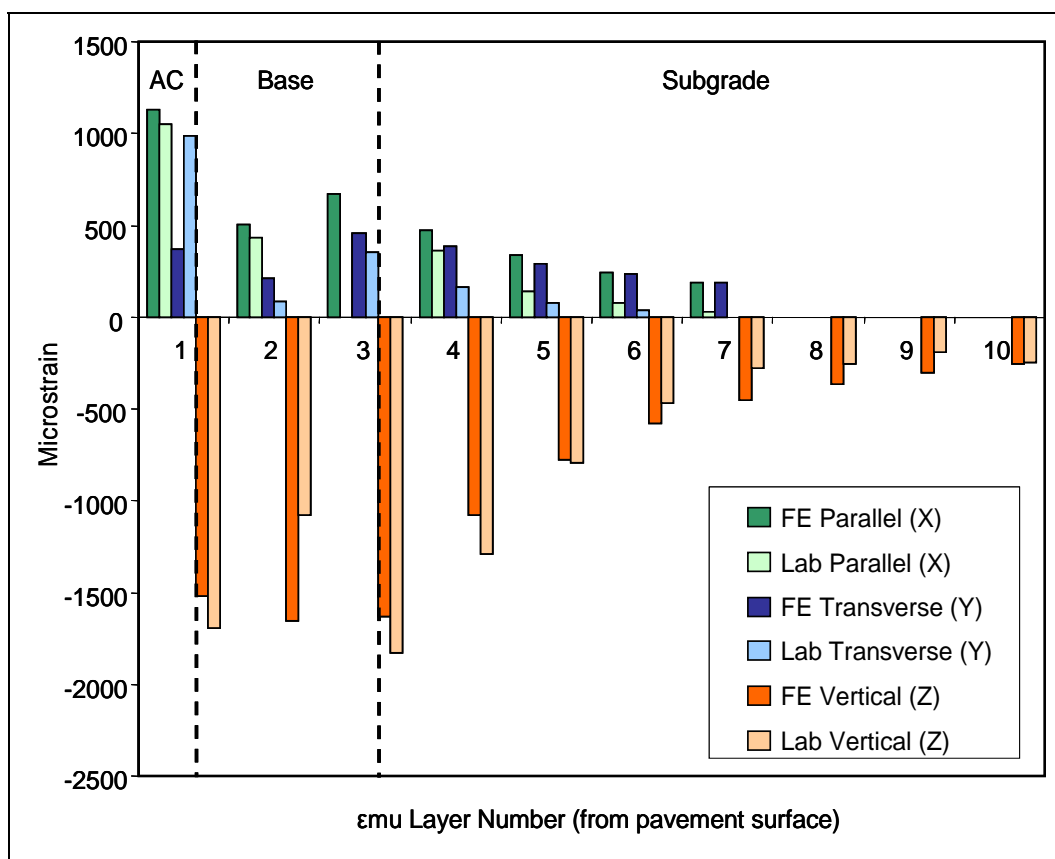


Figure 71. Comparison of microstrains predicted by the FE model and measured by the emu coils for SLTs in TS 2.

It appeared that the vertical strains in the subgrade layer were always under-predicted near the top of the subgrade layer and over-predicted lower in the subgrade layer. Similarly, the horizontal strains were generally over-predicted in the soil layers and under-predicted in the AC layer.

Determination of reinforcement parameters

Laboratory testing was performed to quantify the viscoelastic properties of the Geogrid used in this study. In-air creep tests were performed at two different load levels, each over the course of nine weeks, to examine the effects of stress-dependency. A creep model was calibrated using the commercially available FE package, ABAQUS (HKS, Inc. 2004). The elastic modulus of the Geogrid in the transverse roadway direction with slack removed was also estimated during creep testing at about 900 N/mm. The elastic modulus in the longitudinal roadway dimension was assumed to be 600 N/mm, which maintained the same modular ratio as

the manufacturer's specified values. Details of testing and model calibration are described in Appendix C.

Calibration of the interface stiffness in the FE model, which defines the interaction behavior between the Geogrid reinforcement layer and the soil layers that surround it, was a critical step in modeling reinforced test sections. For simplicity, the interface stiffness values were assumed to be equal in each orthogonal direction as well as for the interfaces above and below the geogrid.

Perkins et al (2004) performed a series of pull-out tests to quantify this interface stiffness at varying levels of confining stress. Although these tests were not conducted with the same soils used in this study, the same Geogrid was used in a granular soil. For the normal stresses expected in TS 4, as a result of self-weight and the applied wheel load (about 100 kPa), the interface stiffness would be about 0.23 N/mm^3 based on the model developed by Perkins et al. (2004). Sugimoto and Alagiyawanna (2003) performed pull-out tests on a Tensar Geogrid that was confined in a sand material. The interface stiffness was calibrated using FE models of the pull-out tests at 0.05 N/mm^3 . The interlocking effect of the Geogrid was considered to be negligible in this situation.

The interface stiffness, used in the models of this study, was calibrated from laboratory data by using a FE model of the SLT in TS 4 where the wheel was positioned over a Geogrid strain gage. The average Geogrid strain for the SLTs in this section (about 460 microstrains) was close to the average Geogrid strain for SLTs in all sections (about 440 microstrains). It was found that an interface stiffness value of about 0.1 N/mm^3 resulted in excellent agreement between the measured and predicted strain in the Geogrid during the SLT. While this value is about half of the 0.23 N/mm^3 estimated with the model by Perkins et al. (2004), the FE model predicted a change in Geogrid strain of about 5% as the stiffness was increased from 0.1 N/mm^3 – 0.23 N/mm^3 .

Development of strain in Geogrid

Elastic and permanent Geogrid strain data was presented in Figure 49 through Figure 58. From these figures, a conservative value of 300 microstrains was chosen to represent the sum of elastic and permanent strain in the Geogrid due to trafficking for all reinforced sections. It was expected that larger strains would develop in sections with thinner AC and base

layers, but there was not enough conclusive evidence to warrant including this in the response models. It is also important to keep in mind that the construction-related strains (discussed later) may be significantly greater than the trafficking strains and would therefore dominate the grid deformation. Some of the gages appeared to develop significantly more strains than others over the course of trafficking or prior to gage failure. Based on the limited amount of valid data available, it was not possible to draw definitive conclusions as to the difference in strain development as a function of test section layer thicknesses.

Data reported by Helstrom et al. (2006) were used to estimate the strains that developed in the Geogrid during construction (construction-related strain information was not collected for this project). For the same geogrid-base configuration as this study, the average Geogrid compaction strains perpendicular and parallel to the centerline of traffic were about 1600 and 1200 microstrains, respectively (Helstrom et al., 2006). These were the values used in this study, and the numbers seem very reasonable based on the strains that were recorded during the forensics process in TS 7 and TS 8 as the asphalt and base layers were removed, the Geogrid was cut free around the gages, and creep recovery was briefly monitored (see Appendix B).

The Geogrid creep model described in Appendix C was used to estimate the stress losses due to relaxation for the observed strains in the geogrid. Constant tensile strains were applied over the respective time periods associated with construction and trafficking. The total time-averaged membrane stresses in the Geogrid over the trafficking period were determined to be 2.27 N/mm in the transverse direction and 1.52 N/mm in the longitudinal direction, which were about 24% below the predicted Geogrid membrane stresses immediately following construction. In other words, the effectiveness of the Geogrid as indicated by the membrane stresses that it carried, was reduced by 24% due to viscoelasticity. A Geogrid that was less susceptible to creep may have provided more benefit to the test sections of this study. The effect of the tensile strains measured was simulated in the model by applying a compressive pre-strain to the geogrid. The pre-strains required to produce these Geogrid membrane stresses in the FE model were equal to -0.001410 and -0.001579 in the Y and X directions, respectively. This caused the Geogrid to shrink, but since the Geogrid was restrained by the soil layers, tensile membrane stresses developed in the geogrid, which consequently subjected the soils to

compressive stresses, and resulted in reduced horizontal tensile strains in the soil layers.

Permanent deformation models

The mechanistic-empirical permanent deformation models recommended by NCHRP (2004b) were simplified slightly in this study by eliminating some terms and expressing equations in terms of deformations where possible as shown in Equations 3 through 10. Here, δ is permanent deformation, t is layer thickness, εr is resilient strain from a response model, $\beta_1 - \beta_8$ are calibration factors, N is the number of applied traffic cycles, ρ and β relate water contents to material properties, w_c is percent water content, εp_{sub0} is the permanent strain at a depth of 0 mm into the subgrade, and εp_{sub6} is the permanent strain at a depth of 150 mm into the subgrade. Temperature was eliminated from the NCHRP (2004b) equation for permanent deformation in the AC layer since it was nominally held constant throughout this study. Because moisture data recorded during the testing was somewhat inconsistent, water contents were taken as unknown.

$$\delta_{AC} = t_{AC} \times \varepsilon r_{AC} \times 10^{(\beta_1 + \beta_2 \times \log(N))} \quad (3)$$

$$\rho(w_c) = 10^{(0.622685 + 0.541524 \times w_c)} \quad (4)$$

$$\beta(w_c) = 10^{(-0.61119 - 0.017638 \times w_c)} \quad (5)$$

$$\delta_{base} = t_{base} \times \varepsilon r_{base} \times \beta_3 \times e^{-\left(\frac{\rho(\beta_4)}{N}\right)\beta(\beta_4)} \quad (6)$$

$$\varepsilon p_{sub0} = \varepsilon r_{sub0} \times \beta_5 \times e^{-\left(\frac{\rho(\beta_6)}{N}\right)\beta(\beta_6)} \quad (7)$$

$$\varepsilon p_{sub6} = \varepsilon r_{sub6} \times \beta_7 \times e^{-\left(\frac{\rho(\beta_8)}{N}\right)\beta(\beta_8)} \quad (8)$$

$$k = \frac{1}{6} \times \ln\left(\frac{\varepsilon p_{sub0}}{\varepsilon p_{sub6}}\right) \quad (9)$$

$$\delta_{sub} = \varepsilon p_{sub0} \times \frac{1 - e^{-k \times h_{bedrock}}}{k} \quad (10)$$

Modification of NCHRP equations to account for Geogrid

A major challenge in this project was simulating the performance improvement mechanisms of Geogrid within the context of the NCHRP (2004b) empirical rutting models. Directly modeling reinforcement in the FE model with the previously described membrane and interface elements as well as the calibrated constitutive properties led to a physically unrealistic response under the applied wheel load (i.e. the vertical compressive strains in the soil layers were larger in reinforced models than in unreinforced models). In the reinforced FE model, the Geogrid provided benefit by carrying tensile stresses (as compared to having an interface layer and no reinforcement), but the net effect was increased vertical strains in the soil layers due to the net loss of composite stiffness at the base-subgrade interface. This problem was also noted by Perkins (2001). This result violates the accepted theory that reinforcement leads to improved performance by laterally confining the soil layers and ultimately reducing the permanent vertical strains in the soil layers. It stemmed from the fact that the base and subgrade layers went from fully-bonded in the unreinforced model to partially-bonded in the reinforced model. NCHRP (2004b) permanent deformation models would therefore have predicted increased rutting with the addition of reinforcement. Thus, a rational strategy for incorporating accepted performance improvement mechanisms in order to capture the observed improvements in rutting performance associated with Geogrid reinforcement was developed as described below.

The modeling approach for incorporating reinforcement was to pre-strain the Geogrid independently of wheel loads in order to represent the improvement in performance with reinforcement. This reinforced model resulted in small vertical tensile strains and horizontal compressive strains of a larger magnitude. Considering this, a form of bulk strain, i.e. the sum of horizontal strains (positive if compressive) and vertical strains (positive if tensile), was chosen to define the improvement due to reinforcement (see Equation 11). This accounts for the fact that Geogrid reinforcement led to decreased vertical compressive strains and, to a greater extent, horizontal tensile strains. This also reduces the complex 3D effect of Geogrid into a single quantity that can be implemented in the rutting models. The vertical design strains (input to the rutting models) corresponding to a reinforced section are then obtained by subtracting the

reinforced model bulk strain (defined above) from the magnitude of vertical compressive strain in the unreinforced FE model with identical layer moduli.

The distance to bedrock from the top of the subgrade, $h_{bedrock}$ in Equation 10, was initially taken as the physical thickness of the subgrade in each respective test section, which followed the recommendation by NCHRP (2004b). However, increased base layer thickness, which implied an equivalent reduction in subgrade layer thickness, resulted in increased total rut depth predictions for some pavement configurations, which was counter to expectations. As a solution, the total section thickness that was considered with respect to rutting models was fixed at 900 mm, which corresponded well to where a majority of the deformations were observed to occur in the test sections of this study, as discussed in Section 5. For example, TS 2 had an AC thickness of 100 mm and a base thickness of 300 mm, so $h_{bedrock}\sqrt{b^2 - 4ac}$ was taken as 500 mm for this section. This resulted in decreased total rut depth predictions as the base layer thickness was increased, which was in line with expectations. This also improved the overall agreement between predicted rut depths and those measured in the test sections.

One final calibration factor, β_9 , was used to multiply the strains from reinforced FE models in order to reflect the improvements observed during trafficking of the test sections. This factor accounted for uncertainties in the permanent Geogrid strains resulting from construction, compaction, and trafficking as well as the elastic Geogrid strains due to traffic loads. Thus, the strain input to the rutting models for reinforced sections (i.e. each of the ε terms in Equation 3 and Equations 6 through 10) was taken as the vertical strain from the corresponding unreinforced model plus β_9 multiplied by the sum of the principal strains in the reinforced model, as shown in Equation 11, where ε_{grid} refers to a strain from a reinforced model and ε_{nogrid} refers to a strain from an unreinforced model.

$$\varepsilon = \varepsilon_{nogrid}_{zz} + \beta_9 \cdot (\varepsilon_{grid}_{zz} + \varepsilon_{grid}_{xx} + \varepsilon_{grid}_{yy}) \quad (11)$$

The overall error was written as shown in Equation 12 or Equation 13, depending on the survivability of gages in the vertical stack of emu coils in the test section. Here, $\varphi_{individual}$ is the least squares measure of error for a

single test section with no failed gages, $\varphi_{surface}$ is the least squares measure of error for a single test section with failed gages, num_{slt} is the number of SLTs (N points), $a\varepsilon$ is the adjusted measured permanent deformation determined from emu coil data in the indicated material layer at N_i , δ_{total} is the sum of the predicted layer deformations at N_i , $surface_rut$ is the measured average relative surface rut depth at N_i , and the other parameters were previously defined. Equation 12 applies for Test Sections 1 through 4 and 7, while Equation 13 applies to the remaining sections.

$$\varphi_{individual} = \sqrt{\sum_{i=1}^{num_{slt}} [(\delta_{ACi} - a\varepsilon_{ACi})^2 + (\delta_{basei} - a\varepsilon_{basei})^2 + (\delta_{subi} - a\varepsilon_{subi})^2]} \quad (12)$$

$$\varphi_{surface} = \sqrt{\sum_{i=1}^{num_{slt}} (\delta_{total} - surface_rut)^2} \quad (13)$$

All nine parameters were calibrated simultaneously for all test sections by minimizing the sum of the error for all of the test sections. The error for each test section was weighted based on the number of SLTs conducted for each test section (i.e. number of SLTs in the section divided by the number of SLTs in TS 2).

Calibration results

The final calibrated rutting model parameters and objective function values are shown in Table 14. The predicted rutting response and measured values for the test sections of this study are also shown in Figure 72 through Figure 75. The table and figures present the results of calibration where the data from all test sections were used, which provided the best overall results. However, it was also possible to use data from a subset of test sections and predict reasonable results for the remaining test sections, as shown in Figure 76, where the responses of TS 5 and TS 7 were predicted after calibrating the rutting models using data from the other test sections. This is a limited validation of the rutting models of this study. It is important to keep in mind that these are empirical equations that may only be valid for the materials used in this study. Future work is needed to establish average values or ranges for a variety of common soil types in order to make the models useful as a design tool.

Table 14. Summary of calibrated parameters and objective function values.

Parameter	Final Model
β_1	0.8304
β_2	0.2396
β_3	43.10
β_4	10.69
β_5	1185
β_6	13.47
β_7	1196
β_8	12.29
β_9	1.739
φ	24.11

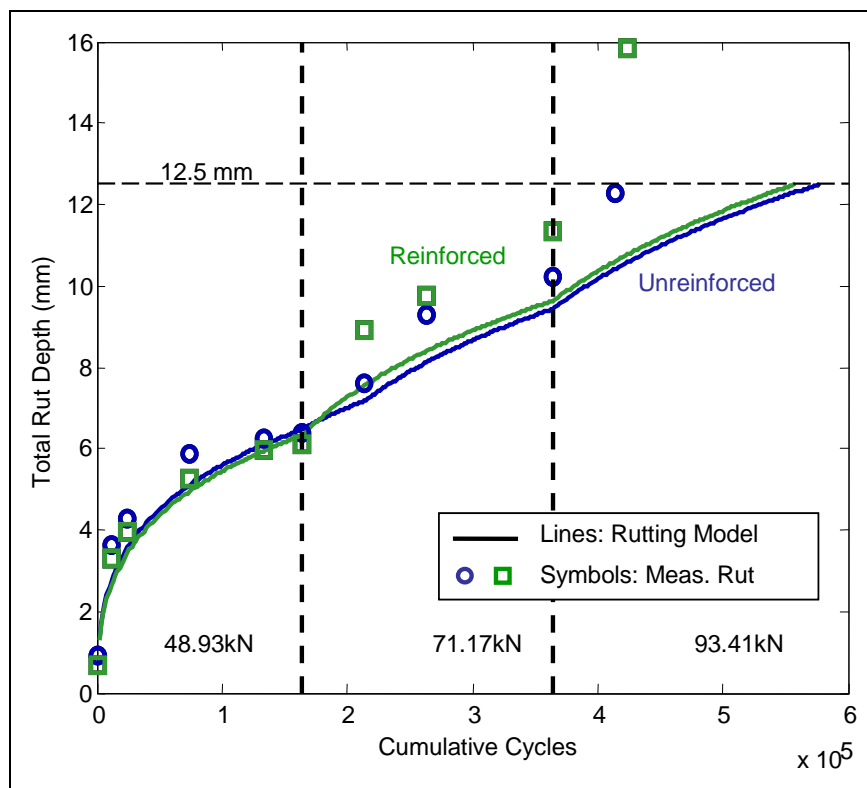


Figure 72. Rutting model predictions and measured surface rut depths for Test Sections 1 and 3.

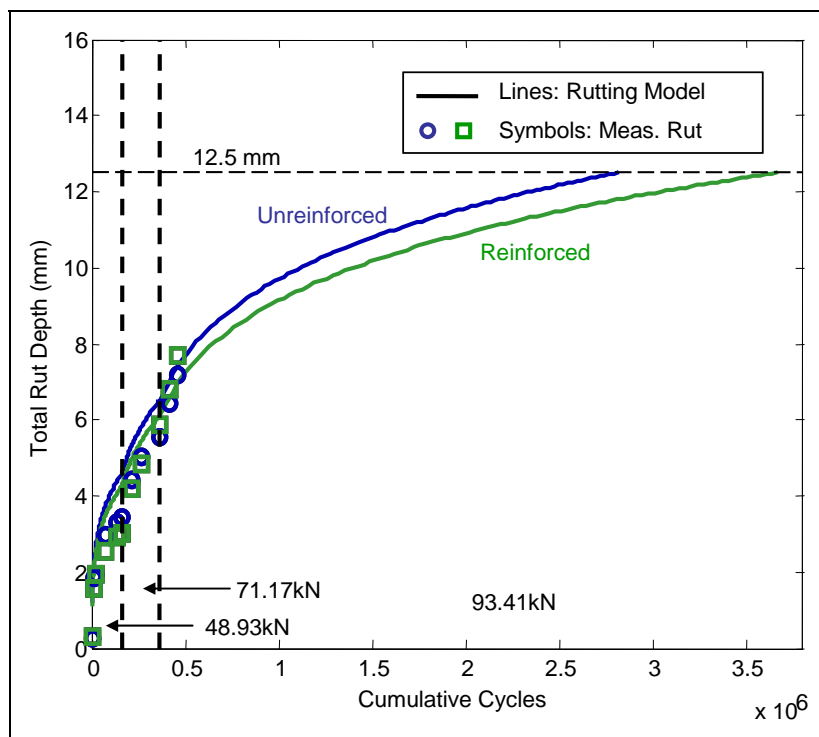


Figure 73. Rutting model predictions and measured surface rut depths for Test Sections 2 and 4.

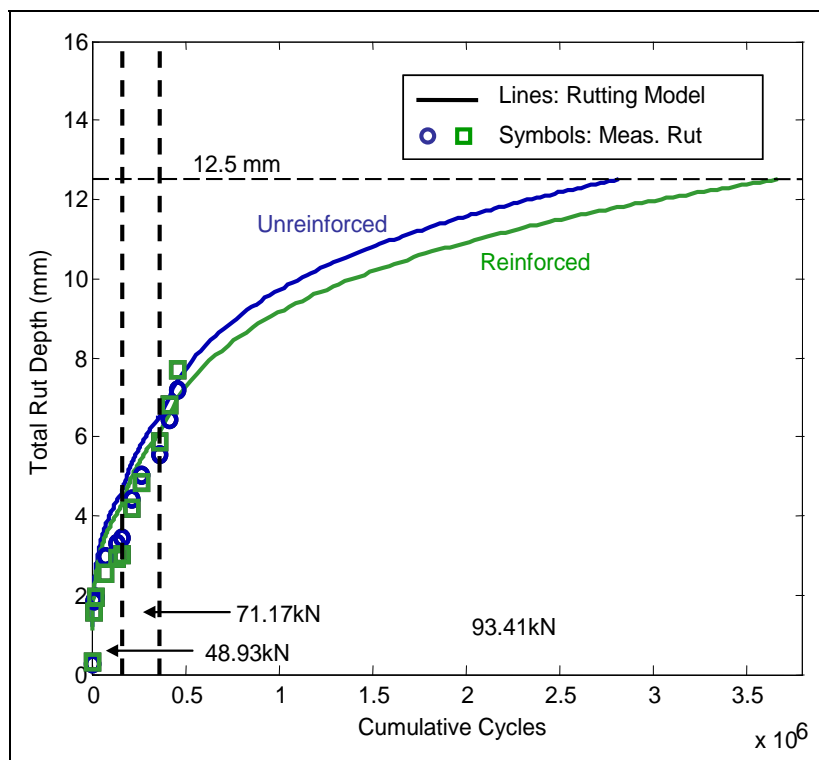


Figure 74. Rutting model predictions and measured surface rut depths for Test Sections 5 and 7.

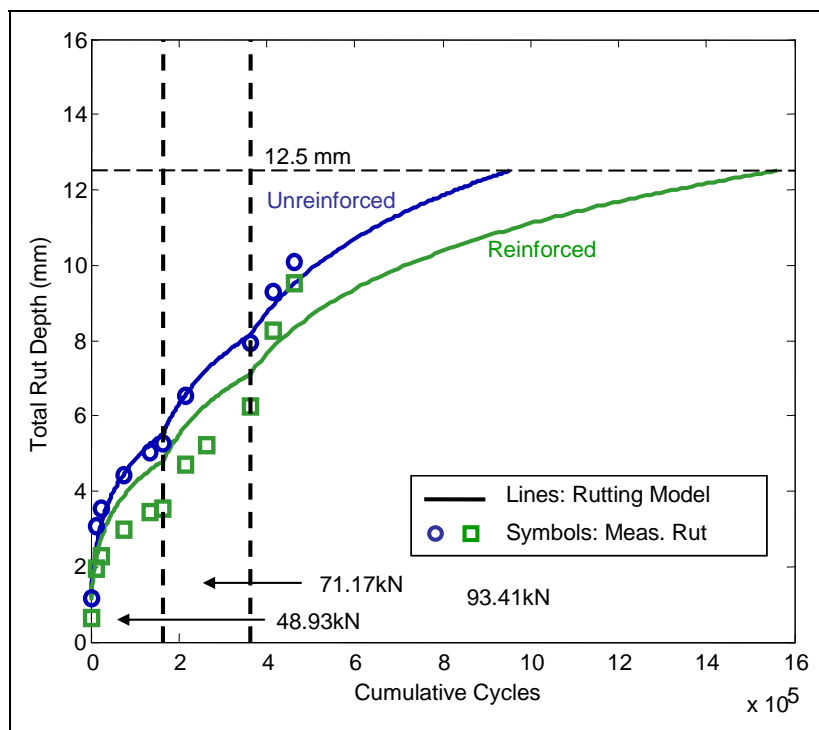


Figure 75. Rutting model predictions and measured surface rut depths for Test Sections 6 and 8.

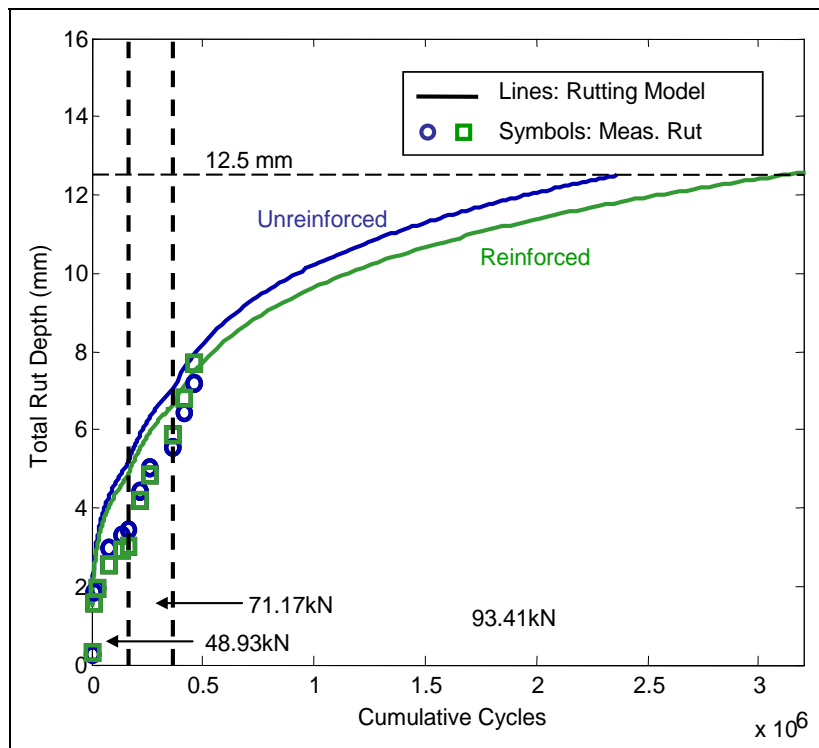


Figure 76. Rutting model predictions and measured surface rut depths for test sections 5 and 7 (data from Test Sections 5 and 7 not used for calibration).

The rutting models reasonably predicted the rutting response of all eight pavement test sections. The rutting models for Test Sections 1 and 3 correctly predicted that the reinforced section would perform slightly better until the cold period in TS 1, and then also correctly predicted that the unreinforced section would perform better after this, as shown in Figure 72. The rutting models for Test Sections 2 and 4 slightly over-predicted the number of cycles to reach the failure rut depth and the relative improvement due to Geogrid was predicted reasonably well, as shown in Figure 73.

The rutting models for Test Sections 5 and 7 generally over-predicted the rut depth at a given number of cycles, as shown in Figure 74. The rutting models did not predict that the unreinforced section would perform better, as observed at the end of the trafficking period. This discrepancy was likely due to uncontrollable variations in the test sections that were not accounted for in the models.

The rutting models for Test Sections 6 and 8 were in good agreement with measured values overall, particularly for TS 6, as shown in Figure 75. The relative improvement due to reinforcement was well predicted, overall. The improvement was over-predicted near the end of the trafficking period and under-predicted when the two lower wheel load magnitudes were used for trafficking.

The rutting models shown in Figure 76 generally over-predict the rut depths for Test Sections 5 and 7 throughout the trafficking period, although the rut depths predicted at the end of trafficking are very close to the measured values. Further, the models shown in Figure 76 are similar to the models shown in Figure 74, despite the fact that a limited data set was used for calibration that did not include measured values from these sections. This provides a limited validation of the mechanistic-empirical approach used here to predict rut depths since it is not necessary to include all of the data in order to reasonably predict rut depths. Overall, the rutting models are capable of predicting the rutting response of the test sections of this study.

Definitive conclusions about the effectiveness of Geogrid reinforcement cannot be drawn based on the test data alone because of the variations in layer moduli that existed among the test sections. Thus, the calibrated models were used to predict the response of the test section thickness

configurations that had identical layer moduli. The AC modulus was taken as 2720 MPa, the base layer modulus was taken as 150 MPa, and the sub-grade modulus was taken as 50 MPa. These represent intermediate values for the soil moduli measured in this study. For simplicity, the wheel load was held constant at 48.9 kN. The predicted number of cycles to reach the failure rut depth and the traffic benefit ratio (*TBR*), defined as the ratio of the number of cycles to failure that a reinforced or thicker section can carry to an unreinforced or thinner test section, were calculated for comparison. These values are presented in Table 15. In addition to the TBR values resulting from the addition of Geogrid to a test section, TBR values were determined for increasing asphalt thickness from 100 to 150 mm and base thickness from 300 to 600 mm for identical test sections (both without and with geogrid). For example, the TBR for increasing asphalt thickness from 100 mm to 150 mm for a 300 mm base, without geogrid, is 3.04.

Table 15. Predicted number of cycles to failure and *TBR* values for test section configurations with identical layer moduli.

Asphalt/base thickness, mm	TS	Predicted Number of Cycles to Reach 12.5 mm Rut Depth ($\times 10^6$)	<i>TBR</i> Geogrid	<i>TBR</i> AC thickness increase	<i>TBR</i> Base thickness increase
100/ 300	2	0.62	--	--	--
	4	0.80	1.29	--	--
150/ 300	1	1.88	--	3.04	--
	3	2.67	1.42	3.35	--
100/ 600	6	6.62	--	--	10.7
	8	9.45	1.43	--	11.8
150/ 600	5	11.1	--	1.68	5.90
	7	15.5	1.40	1.64	5.79

The *TBR* values for Geogrid reinforcement indicate that improvements in the rutting life of pavements of 29 to 43 percent are possible for all pavement thickness configurations of this study if the sections have the identical layer moduli specified above. These predicted improvements may be significant considering that adding Geogrid increased roadway construction cost by only about 17% (Maine DOT 2006), although other failure mechanisms such as asphalt fatigue must also be considered with an extended rutting life.

It is important to recognize that the *TBR* values are based on the number of cycles to failure and not the difference in rut depth after a particular number of cycles. To illustrate the significance of this, using measurements from this study, the *TBR* value for TS 4 compared to TS 2 was 1.35 in terms of the number of cycles to failure, but the rut depth in TS 2 was only 1.14 times greater than that in TS 4 when the failure rut depth of 12.5 mm was reached in TS4. This 14% difference in rut depth relates to a distance of about 1.6 mm, a difference in rut depth within the tolerance of measurements in practical scenarios.

It is hard to make generalized conclusions from only two pavement thickness and two base thickness data points, but the results of this modeling study suggest that adding Geogrid is less effective than adding 50 mm of either asphalt or base course material for the pavement thicknesses considered in this study. The *TBR* values for adding 50 mm of asphalt and doubling the base thickness ranged from 1.64 to 3.35 and 5.90 to 11.80, respectively. To provide a specific example, modeling was performed using a section with 100 mm of asphalt and 300 mm of base course material as the baseline condition. The model predicted that Geogrid is equivalent to increasing the thickness of the asphalt by 11 mm or the base course by 30 mm.

In summary, the rutting model appears to be capable of reasonably predicting the rutting response of the four different pavement configurations of this study with and without reinforcement. It has potential to be used to predict the response of a wide variety of reinforced and unreinforced pavement sections with varying layer thicknesses and layer moduli. However, additional verification is needed.

Parametric studies

Effect of Geogrid creep and stiffness

The effect of Geogrid creep was examined for the section with 100 mm of asphalt and 300 mm of base course material by solving a model that approximated the effect of zero creep in the geogrid. This was accomplished by multiplying the applied Geogrid pre-strain in the model by $100\%/(100\% - 24\%) = 132\%$, since the Geogrid in this study was predicted to lose about 24% of the applied membrane stresses due to relaxation. This change caused the predicted *TBR* value to increase from 1.29 to 1.42, which implies that Geogrid creep affects the rutting response, although the

greatest relative improvement possible by completely eliminating creep is only about 45% (42% more cycles to failure vs. 29% more cycles to failure).

Utilizing the 100 mm of asphalt and 300 mm of base course material configuration, the effect of Geogrid stiffness was examined by looking at two scenarios: 1) doubling the stiffness values in the transverse and longitudinal directions (1800 and 1200 N/mm, respectively) and 2) halving the stiffness values (450 and 300 N/mm, respectively). When the values were doubled, the predicted *TBR* values increased from 1.29 to 1.72, while the predicted *TBR* values decreased from 1.29 to 1.14 when the moduli were halved. These results indicate that the predicted rutting life of the pavements is significantly affected by the stiffness of the geogrid. Hence, halving the stiffness resulted in a 48% loss in number of cycles to failure and doubling it, resulted in a 25% increase in number of cycles to failure.

Comprehensive parametric study, constant Geogrid properties

A parametric study (PS) was conducted with the FE model to further examine the effect of pavement section configuration on pavement performance. This study utilized the documented Geogrid modulus values of 900 N/mm and 600 N/mm in the transverse and longitudinal directions, respectively, and a total of 360 different configurations were analyzed. They were chosen to represent a wide range of pavement sections that may potentially benefit from Geogrid reinforcement, and are similar to those tested in this study, so that there is high confidence in the model calibration for the conditions modeled.

The values selected for the PS are summarized in Table 16. The AC layer thickness, t_{AC} , was selected as 100 mm, 150 mm, and 200 mm. The 100 mm and 150 mm thicknesses correspond to the test sections of this study, and 200 mm was selected as one additional thicker value.

Table 16. Summary of parameters varied in parametric study.

Elastic Modulus (MPa)			Thickness (mm)		Norm. Geogrid Location
E_{AC}	E_{base}	E_{sub}	t_{AC}	t_{base}	<i>LG</i>
2720	100	35	100	300	None
4480	300	70	150	450	0
--	--	--	200	600	0.25
--	--	--	--	--	0.5
--	--	--	--	--	0.75

The base layer thickness, t_{base} , was selected as 300 mm, 450 mm, and 600 mm--the base thicknesses considered in this study, and an intermediate thickness. The normalized location of the Geogrid within the base layer, LG , is defined as the distance from the bottom of the base layer to the geogrid, divided by the total base layer thickness, which was selected at values of 0, 0.25, 0.5, and 0.75. An unreinforced FE model was analyzed for all configurations, so that a TBR could be determined for each configuration that included a grid.

The AC modulus, E_{AC} , was selected as 2720 MPa and 4480 MPa. These values correspond to the dynamic moduli at 21.1°C for the load pulse duration applied by the HVS wheel load and the load pulse duration that FWD applies to the pavement. The base layer modulus, E_{base} , was selected at 100 MPa and 300 MPa, which was representative of the range of values indicated by FWD for the aggregate used in this study. The subgrade layer modulus values, E_{sub} , were 35 MPa and 70 MPa, corresponding to California Bearing Ratio (CBRs) of about 3, and 6. The subgrade moduli measured by FWD in this study ranged from about 38 MPa to 70 MPa. Hence, the subgrade with a modulus value of 35 MPa (CBR of 3) was studied as a representative value of soft subgrade. The magnitude of the pre-strain in the Geogrid was adjusted to account for various locations of Geogrid within the base layer (as described below).

Conclusions from prior studies were considered when determining how to rationally incorporate the effect of different Geogrid positions within the base layer for this study. These are summarized briefly as follows:

For Geogrid located at the bottom of the base layer, Collin et al. (1996) concluded that the benefit from Geogrid increased as the base layer thickness increased to 255 mm, but then decreased as the base layer thickness continued to increase. The AC layer thickness was held constant at 50 mm, while base layer thickness was tapered from 150 mm to 460 mm.

Haas et al. (1988) concluded that the optimum Geogrid location was at the bottom of the base layer for thicknesses up to 250 mm and in the middle of the base layer for greater thicknesses. The AC layer thickness was 75 mm or 100 mm, while base layer thicknesses ranged from 100 mm to 300 mm.

Perkins (1999a and 1999b) concluded that the optimum location for the Geogrid in a 300 mm thick base layer was 100 mm above the bottom of the base layer. The AC layer thickness was 75 mm in all test sections and the base layer thickness ranged from 200 mm to 375 mm. Significant improvements were observed in test sections with a soft subgrade (CBR value of 1.5), but little or no improvements were observed with a stiff subgrade (CBR value of 20).

A more recent study by Helstrom et al. (2006) reported results for sections with an AC layer thickness of 150 mm and base layer thicknesses of 300 mm and 600 mm. It was concluded that Geogrid developed as much or more strain after construction when located at the bottom of base layers than when located in the middle of base layers. According to Perkins et al. (2005), subgrade material is believed to offer relatively little resistance against movement of the aggregate material during compaction, which may explain this observation. Since these test sections had comparable thicknesses to the sections used for this study, the results were weighed more heavily than prior studies where conclusions were based on relatively thin pavement sections.

In this study, Geogrid was considered to improve the performance of test sections by developing strain as a result of base layer compaction followed by rut development due to trafficking. The data reported by Helstrom et al. (2006) indicated that the strains developed in the Geogrid due to compaction of a 300 mm thick base layer were approximately linearly related to the depth of the Geogrid within the base layer, as shown in Figure 77 below. The values of zero compaction strain, which would occur if the Geogrid was not located within the base layer, were added to further illustrate the linear relationship between strain and depth. The lift height in the section with 600 mm thick base layer was 300 mm (vs. 150 mm in sections with a 300 mm thick base). The data indicated that the strain developed in the Geogrid was approximately equal in these sections after placement of the first lift. Thus, the Geogrid strain appeared to be linearly related to the relative position of the Geogrid within the base layer in this specific case where the base layers were placed in two lifts regardless of total thickness.

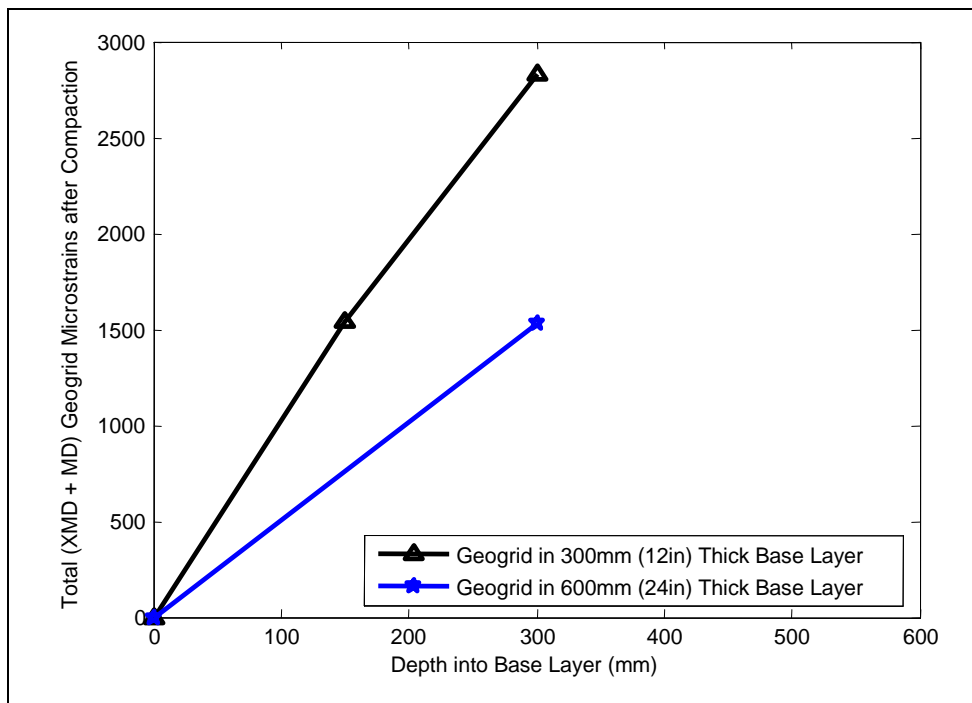


Figure 77. Geogrid strains after base layer compaction, after Helstrom et al. (2006).

Based on the observation described above and lack of additional data, the applied pre-strains were linearly scaled by a factor ranging from zero to one for reinforced FE models used in the PS, which was based on the relative position of the Geogrid from top to bottom of the base layer. Helstrom et al. (2006) also concluded that Geogrid located at the bottom of the base layer developed equal or more strain after construction than when located in the middle of the base layer. Therefore, the linear scaling factor was also used to modify the strains associated with trafficking effects. While this strategy takes advantage of available knowledge, there was still significant uncertainty involved, so for simplicity, the effect of stress relaxation associated with varying initial pre-strains was not considered.

Parametric study results

The results of the PS are presented in terms of the number of 48.9 kN wheel loads that each respective pavement section is predicted to carry before reaching the failure rut depth defined as 12.5 mm, which is designated as N_f .

Comprehensive results are presented in Appendix D in terms of N_f and TBRs. Because pre-strain was assigned to the grid as a function of its height above the base layer, all results indicated decreasing effectiveness

above the bottom of the base, all other things being equal. Hence a summary of the results that includes the average and standard deviation of the TBRs for all four relative positions within the base layer is provided in Table 17,

Table 18 and Table 19 for the three base layer thicknesses.

Table 17. Summary of parametric study results for 300-mm-thick-base.

AC Thickness (mm)	Elastic Modulus (MPa)					
	Subgrade	Base	AC	N _f /1000 for unreinforced section	Ave. TBR	Std. Dev. TBR
100	35	100	2720	278	1.21	0.108
			4480	620	1.29	0.159
		300	2720	629	1.12	0.074
			4480	1330	1.17	0.097
	70	100	2720	779	1.23	0.120
			4480	2089	1.35	0.190
		300	2720	1742	1.15	0.077
			4480	4535	1.21	0.112
150	35	100	2720	1022	1.34	0.190
			4480	3918	1.58	0.359
		300	2720	1533	1.16	0.092
			4480	5701	1.26	0.158
	70	100	2720	2489	1.32	0.177
			4480	11929	1.55	0.323
		300	2720	3566	1.17	0.096
			4480	16590	1.27	0.152
200	35	100	2720	2679	1.44	0.256
			4480	15233	1.78	0.501
		300	2720	3242	1.19	0.114
			4480	18322	1.31	0.193
	70	100	2720	5053	1.35	0.195
			4480	33469	1.59	0.345
		300	2720	5929	1.17	0.096
			4480	38764	1.27	0.153

Table 18. Summary of parametric study results for 450-mm-thick-base.

AC Thickness (mm)	Elastic Modulus (MPa)			Nf/1000 for unreinforced section	Ave. TBR	Std. Dev. TBR
	Subgrade	Base	AC			
100	35	100	2720	840	1.26	0.142
			4480	2177	1.38	0.221
		300	2720	3926	1.18	0.114
			4480	11410	1.25	0.166
	70	100	2720	1802	1.26	0.138
			4480	5796	1.40	0.220
		300	2720	8409	1.17	0.099
			4480	31743	1.26	0.147
150	35	100	2720	2574	1.35	0.204
			4480	12095	1.59	0.369
		300	2720	6031	1.17	0.109
			4480	29923	1.27	0.175
	70	100	2720	4703	1.31	0.164
			4480	26872	1.51	0.289
		300	2720	10443	1.16	0.087
			4480	62625	1.24	0.140
200	35	100	2720	5346	1.39	0.225
			4480	35681	1.63	0.385
		300	2720	8348	1.16	0.099
			4480	56702	1.25	0.158
	70	100	2720	7740	1.30	0.164
			4480	56975	1.47	0.263
		300	2720	11833	1.14	0.077
			4480	88335	1.20	0.118

Table 19. Summary of parametric study results for 600-mm-thick base.

AC Thickness (mm)	Elastic Modulus (MPa)					
	Subgrade	Base	AC	N/1000 for unreinforced section	Ave. TBR	Std. Dev. TBR
100	35	100	2720	2329	1.31	0.177
			4480	8048	1.49	0.293
		300	2720	18474	1.19	0.122
			4480	90565	1.28	0.187
	70	100	2720	3417	1.28	0.142
			4480	13871	1.44	0.238
		300	2720	26939	1.17	0.094
			4480	155427	1.24	0.138
150	35	100	2720	6071	1.36	0.199
			4480	38087	1.57	0.341
		300	2720	18266	1.16	0.096
			4480	128558	1.22	0.140
	70	100	2720	7625	1.29	0.147
			4480	52462	1.45	0.241
		300	2720	22593	1.13	0.074
			4480	172116	1.19	0.101
200	35	100	2720	9988	1.33	0.181
			4480	79921	1.49	0.278
		300	2720	17894	1.13	0.074
			4480	147531	1.18	0.105
	70	100	2720	10680	1.27	0.129
			4480	87521	1.38	0.195
		300	2720	19634	1.11	0.060
			4480	166425	1.15	0.077

The modeling results are consistent with our understanding of pavement performance in that more passes are required to fail the pavement system as the asphalt concrete thickness, the base thickness and all of the layer modulus values increase. The relative benefit of adding Geogrid to the pavement system, however, produces some counter-intuitive results. For example, the maximum and minimum average TBR values for each base thickness is listed in Table 20, and indicate that relatively more benefit is obtained for the AC with the higher modulus value in all cases. Further, the intermediate AC thickness of 150 mm, receives relatively more benefit than 100 mm AC for the 600 mm base layer thickness.

Table 20. Summary of pavement properties for which the average maximum and minimum benefit that Geogrid provided relative to the unreinforced test section. Average refers to the average benefit provided by the Geogrid at all four relative distances above the bottom of the base layer.

Base layer thickness (mm)	TBR		AC Thickness (mm)	AC Modulus (MPa)	Base Modulus (MPa)	Subgrade Modulus (MPa)
300	Max	1.78	200	4480	100	35
	Min	1.12	100	2720	300	70
450	Max	1.63	200	4480	100	35
	Min	1.14	100	2720	300	70
600	Max	1.57	150	4480	100	35
	Min	1.11	200	2720	300	70

One interesting modeling result was that the maximum number of cycles to failure in unreinforced sections was predicted to occur for a section with the stiffest layer moduli and thickest base layer, as expected; but, with the intermediate thickness (150 mm) asphalt layer. The unreinforced section with $E_{AC} = 4,480$ MPa, $E_{sub} = 70$ MPa, $t_{base} = 600$ mm was predicted to carry about 3.6% more cycles before failing than the otherwise equivalent section with $t_{AC} = 200$ mm. Since the layer moduli and base thickness were maximized in these sections, the deformations in the asphalt layer were responsible for a majority of the total rutting in these sections. Increasing the asphalt thickness reduced all of the vertical design strains, but the net effect was still increased overall rutting due to additional rutting in the asphalt layer as a result of the increased thickness. This prediction suggests that it is possible to have “too much” asphalt concrete in some scenarios where the layer moduli are relatively high and the asphalt is supported by a thick base layer.

Based on the TBR values generated, the relative effectiveness of the geogrid, EG , as a function of one parameter, was quantified by comparing changes in TBR values, as shown in Equation 14, where TBR_1 is the TBR value corresponding to the initial parameter value and TBR_2 is the TBR value corresponding to a different value of the same parameter.

$$EG = \frac{TBR_2 - TBR_1}{TBR_1} \quad (14)$$

For example, to study the effectiveness of Geogrid (using EG values) for increasing E_{AC} from 2720 MPa to 4480 MPa, 144 EG values could be calculated since there are 288 total reinforced models with two different values of E_{AC} .

An example of how to interpret EG values follows: Say that we want to consider the effect of changing E_{base} = from 100 MPa to 300 MPa in a reinforced section with $LG = 0$ where $E_{AC} = 2720$ MPa, $E_{sub} = 35$ MPa, $t_{AC} = 100$ mm, $t_{base} = 300$ mm. The modeling results indicate that for $E_{base} = 100$ MPa, $TBR_1 = 1.33$, and for $E_{base} = 300$ MPa, $TBR_2 = 1.21$, implying $EG = (1.21-1.33)/1.33*100 = -9.3\%$. However, N_f corresponding to $E_{base} = 100$ MPa was only 370000 cycles, while N_f corresponding to $E_{base} = 300$ MPa was more than twice as large at 759000 cycles. The negative value of EG signifies that the relative improvement provided by the Geogrid decreased as E_{base} increased from 100 MPa to 300 MPa. Hence, negative values of EG do not necessarily imply that N_f for the parameter corresponding to TBR_2 is less than N_f for the parameter corresponding to TBR_1 .

Figure 78 through Figure 80 are example PS results expressed in terms of EG values. Figure 78, for example, indicates that for a grid at the bottom of the base ($LG = 0$, or the y-axis) and E_{base} of 100 MPa, $E_{subgrade}$ of 35 MPa, a 200 mm thick asphalt layer, a 300 mm thick base layer, increasing E_{AC} from 2720 to 4480 MPa results in an increased effectiveness of the Geogrid of about 38 percent.

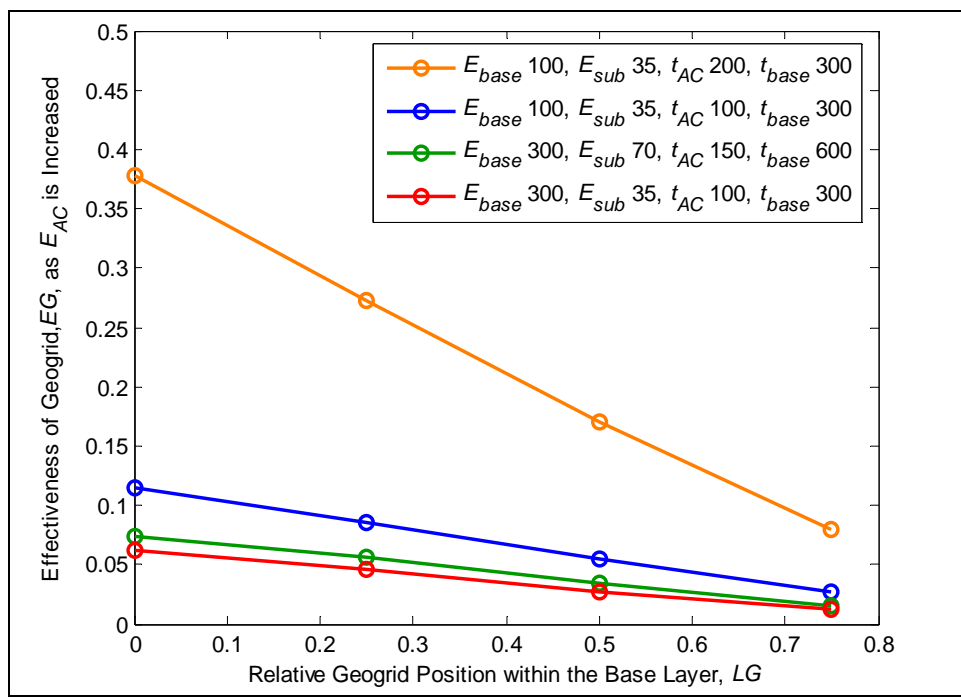


Figure 78. Effect of increasing the asphalt layer modulus from 2,720 MPa to 4,480 MPa on the EG (Effectiveness of Geogrid). Modulus units are in MPa, and thicknesses are given in mm.

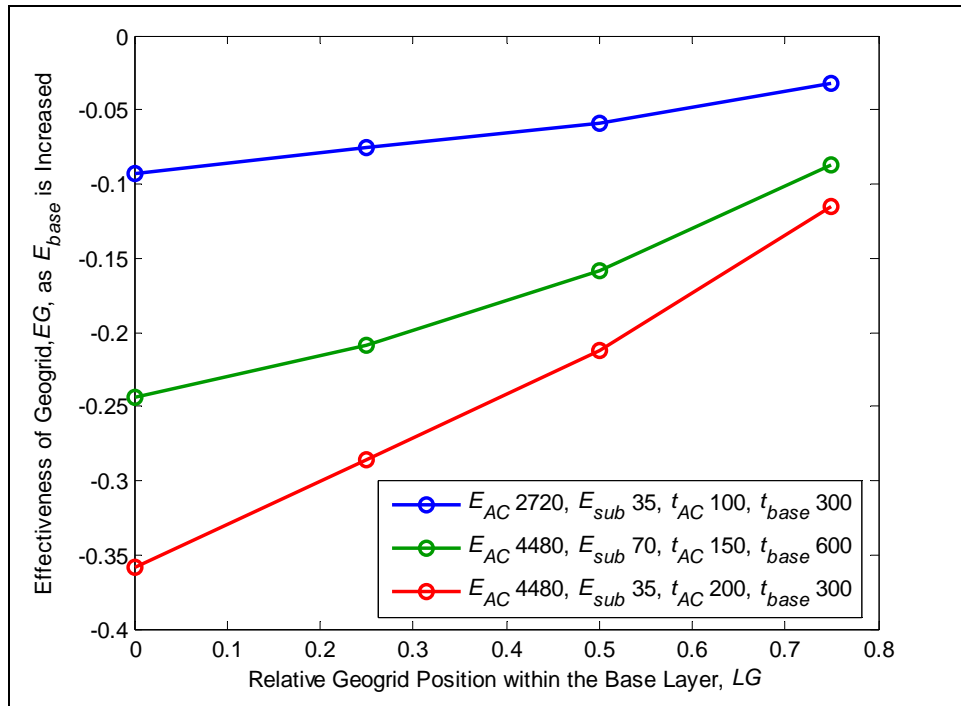


Figure 79. Effect of increasing the base layer modulus from 100 MPa to 300 MPa on the EG (Effectiveness of Geogrid). Modulus units are in MPa, and thicknesses are given in mm.

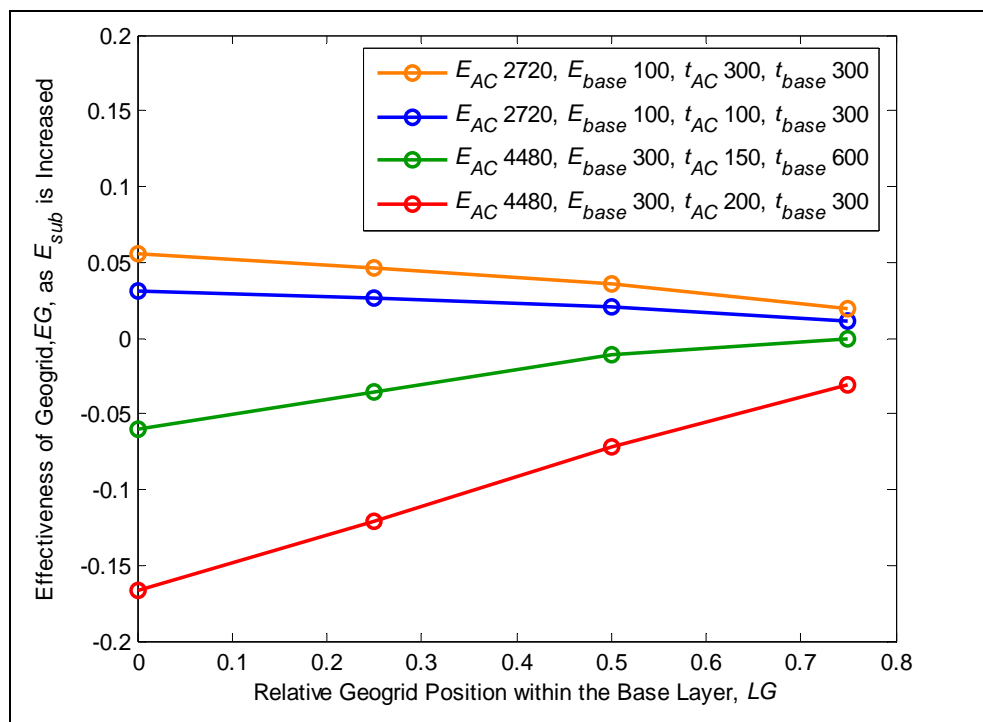


Figure 80. Effect of increasing the subgrade layer modulus from 35 MPa to 70 MPa on the EG (Effectiveness of Geogrid). Modulus units are in MPa, and thicknesses are given in mm.

Effect of Geogrid location within base layer – model constraint

For all PS configurations, the *TBR* was largest when it was located at the bottom of the base layer, and decreased as the Geogrid location moved higher into the base layer (Figures 78, 79 and 80). This represents a constraint of the model in that the pre-strain was decreased as a function of distance above the bottom of the base layer. When the model was run with equal pre-strain for all Geogrid locations, results indicated that each of the four Geogrid locations was sometimes the optimal location, depending on the rest of the pavement configuration.

Effect of asphalt modulus on Geogrid performance

Increasing E_{AC} always resulted in positive EG values (Figure 78). The range of EG values was from 1% to 24% and the average EG value was 8.5%. The largest EG value occurred for the configuration with, $E_{base} = 100$ MPa, $E_{sub} = 35$ MPa, $t_{AC} = 200$ mm, $t_{base} = 300$ mm, and $LG = 0$. The smallest EG value occurred for a section with $E_{AC} = 4,480$ MPa, $E_{base} = 300$ MPa, $E_{sub} = 35$ MPa, $t_{AC} = 100$ mm, $t_{base} = 300$ mm to 600 mm, and $LG = 0.75$. Once again, these results generally disagreed with expectations and may indicate that there are deficiencies in the modeling approach that

was used. The deficiency would stem from the fact that increasing the asphalt modulus tends to have a much larger relative effect on the strains in unreinforced models than on the strains in reinforced models (see “Effect of AC Layer Thickness on Geogrid Performance” for more information).

Effect of base layer modulus on Geogrid performance

Increasing E_{base} always resulted in negative EG values (Figure 79). This resulted in reduced vertical strains in unreinforced models, but greater reductions in the beneficial horizontal compressive strains due to reinforcement. The EG values for increasing E_{base} from 100 MPa to 300 MPa ranged from -36% to -3.2%. The largest EG value occurred for the configuration with $E_{AC} = 2,720$ MPa, $E_{sub} = 35$ MPa, $t_{AC} = 100$ mm, $t_{base} = 300$ mm, and $LG = 0.75$. The smallest EG value occurred for the configuration with $E_{AC} = 4,480$ MPa, $E_{sub} = 35$ MPa, $t_{AC} = 200$ mm, $t_{base} = 300$ mm, and $LG = 0$. These results agree with prior studies that have concluded that Geogrid was more beneficial in pavement sections with relatively soft soil layers, although the focus has generally been directed towards subgrade material, since higher quality base layer aggregate is typically chosen if possible. Subgrade material is site-specific, so soft subgrade materials must be dealt with, whereas soft base layer material can typically be avoided.

Effect of subgrade layer modulus on Geogrid performance

About 68% of the configurations indicated negative EG values as E_{sub} was increased from 35 MPa to 70 MPa, and the maximum EG value was only 5.6% (e.g., Figure 80). This small improvement occurred in a section with $E_{AC} = 4,480$ MPa, $E_{base} = 100$ MPa, $t_{AC} = 100$ mm, $t_{base} = 300$ mm, and $LG = 0$. The smallest EG value of -17% occurred in a section with $E_{AC} = 4480$ MPa, $E_{base} = 100$ MPa, $t_{AC} = 200$ mm, $t_{base} = 300$ mm, and $LG = 0$. The average EG value was -2.1%, which indicated that Geogrid was generally more effective in pavement sections with softer subgrade material. This was generally consistent with the conclusions from many prior studies.

Effect of base layer thickness on Geogrid performance

About 63% of the configurations indicated negative EG values as t_{base} was increased from 300 mm to 450 mm or from 450 mm to 600 mm. Of the

configurations that indicated positive EG values, 56 had $t_{AC} = 100$ mm, 15 had $t_{AC} = 150$ mm, and 0 had $t_{AC} = 200$ mm. This implies that Geogrid is generally predicted to be more effective when the base layer is increased in sections with thicker asphalt layers. The range of EG values was from -13% to 13% and the average EG value was -0.9%. The largest EG value occurred for the configuration with $E_{AC} = 4480$ MPa, $E_{base} = 300$ MPa, $E_{sub} = 35$ MPa, $t_{AC} = 100$ mm, t_{base} increased from 300 mm to 450 mm, and $LG = 0$. The smallest EG value occurred for a section with $E_{AC} = 4480$ MPa, $E_{base} = 100$ MPa, $E_{sub} = 35$ MPa, $t_{AC} = 200$ mm, t_{base} increased from 450 mm to 600 mm, and $LG = 0$.

Effect of AC layer thickness on Geogrid performance

Only 44% of the configurations indicated negative EG values as t_{AC} was increased from 100 mm to 150 mm or from 150 mm to 200 mm. All 64 of the configurations with $t_{base} = 300$ mm indicated positive EG values, whereas only 28 and 16 sections with $t_{base} = 450$ mm and 600 mm, respectively, indicated positive EG values. The range of EG values is from -8% to 35.9% and the average EG value was 2.1%. The largest EG value occurred for the configuration with $E_{AC} = 4480$ MPa, $E_{base} = 100$ MPa, $E_{sub} = 35$ MPa, t_{AC} increased from 100 mm to 150mm, $t_{base} = 300$ mm, and $LG = 0$. The smallest EG value occurred for the section with $E_{AC} = 4480$ MPa, $E_{base} = 100$ MPa, $E_{sub} = 35$ MPa, t_{AC} increased from 150 mm to 200 mm, $t_{base} = 600$ mm, and $LG = 0$. These results generally disagreed with expectations and may indicate that there are deficiencies in the modeling approach that was used. Specifically, increasing the asphalt thickness had a much larger relative effect on the strains in unreinforced models than on the strains in reinforced models. Thus, the Geogrid was predicted to provide more benefit in a relative sense. This may be physically realistic if a majority of the Geogrid strain is developed during compaction and is thus practically independent of asphalt thickness. On the other hand, if a majority of the Geogrid strain is developed through trafficking, the model-predicted benefit from reinforcement is likely overpredicted as the asphalt thickness is increased.

Parametric study conclusions

A summary of the effects of each of the parameters is shown in Table 21. The relative benefit of the grid was always greater for the lower base modulus values, i.e., increasing E_{base} resulted in negative EG values for all configurations. Beyond this observation; however, the interaction of all

input variables affected predicted pavement performance; and, therefore the relative benefit of adding geogrid. For example, increasing the subgrade modulus decreased the benefit of the grid most of the time (68%), as expected based on previous work with soft subgrades; but 32% of the sections showed that increasing the subgrade modulus improved the relative benefit of the grid.

Table 21. Summary of parameters on EG.

Parameter	Change		EG (%)		
	From	To	Max.	Min.	Mean
E_{AC} (MPa)	2720	4480	37.7	1.2	9.7
E_{base} (MPa)	100	300	-3.2	-35.8	-13.7
E_{sub} (MPa)	35	70	5.6	-16.7	-2.1
t_{AC} (mm)	100 or 150	150 or 200	35.9	-8.1	2.1
t_{base} (mm)	300 or 450	450 or 600	13.2	-13.3	-0.9

Increasing asphalt thickness, t_{AC} , or modulus, E_{AC} , generally resulted in positive EG values, contrary to expectations. This stemmed from the fact that increasing the asphalt thickness had a larger relative effect on the strains developed in unreinforced models than on the strains in reinforced models. This may be physically realistic if a majority of the Geogrid strain is developed during compaction and is thus practically independent of asphalt thickness or modulus. On the other hand, if a majority of the Geogrid strain is developed through trafficking, the EG values are likely overpredicted as the asphalt thickness or modulus is increased.

While TBR values greater than 50 have been reported in previous model studies—e.g., Perkins (1999a and 1999b), the maximum TBR value computed in this PS was 2.40 for a pavement with $E_{AC} = 4480$ MPa, $E_{base} = 100$ MPa, $E_{sub} = 35$ MPa, $t_{AC} = 200$ mm, $t_{base} = 300$ mm, and $LG = 0$. This translates to 21 million additional cycles that this section could carry, with a 48.9 kN wheel load, before developing a 12.5 mm rut depth. Based on all the configurations used in the PS where $LG = 0$, it was predicted that an average of 13 million additional cycles with a 48.9 kN wheel load could be carried before developing a 12.5 mm rut depth.

The average TBR value for sections with Geogrid located at the bottom of the base layer was 1.50 and the minimum was 1.18. According to the cost analysis presented by Maine DOT (2006), Geogrid increased the roadway

cost for reinforced sections in their project by about 17 percent. These results suggest that it is worthwhile to use Geogrid if the *TBR* values observed in practice are, in fact, close to the average prediction of 1.50, since this would imply that the roadway would be able to carry 50% more 48.9 kN wheel loads before a rut depth of 12.5 mm was reached. However, these results must be considered with caution since data from only eight test sections were used to calibrate the rutting models and only half of the test sections were trafficked to failure. Further, other failure modes not significantly affected by the presence of Geogrid reinforcement, such as asphalt fatigue cracking, become more likely as rutting life increases.

7 Discussion

This study utilized full-scale pavement sections that are typical of AASHTO. In addition, reasonably “good” subgrade conditions were utilized. For these conditions—with a subgrade modulus of approximately 50 MPa, the experimental measurements and modeling results suggest that reinforcement provides benefit in all pavement layer thicknesses, except for 150 mm asphalt and 600 mm base where modeling indicates benefit, but measured results did not (Table 10 and Table 15). Other than the exception in the experimental phase, measured and modeling results indicate Traffic Benefit Ratios ranging (TBRs) from 1.3 to 1.4 by adding geogrid. This project also examined the influence of AC pavement and base course layer thickness as well, and results suggest that a much larger benefit than adding Geogrid is gained from increasing asphalt layer thickness by 50 mm when the base course layer is 300 mm (TBR of about 3). Further, doubling the base course layer from 300 to 600 mm provided over 7 times the benefit of adding Geogrid reinforcement.

The TBRs that were calculated for the subgrade and base conditions of this full-scale experimental study were based on the number of load cycles to failure of a pavement, defined as a 12.5 mm-deep surface rut. A TBR of 1.3 to 1.4 thus represents a very small difference in total rut depth—less than 2 mm. This difference in rut depth would be difficult to measure in a highway section; hence, it suggests only a marginal benefit of Geogrid reinforcement.

This work extends previous work and indicates that specific subgrade conditions as well as pavement systems properties should be carefully weighed against benefit provided by Geogrid reinforcement. Compared to previous studies, the test sections constructed for this study were designed according to AASHTO procedures for a life of 3×10^6 ESALS, whereas previous studies were designed to study Geogrid benefits under conditions of extremely soft subgrades. Hence, the results generated in this project do not necessarily contradict those of previous studies that utilized thinner pavement sections and softer subgrade conditions where a greater Geogrid benefit would be expected than those dealt with here (e.g., Perkins et al. 1999a and 1999b and Kinney et al., 1998 a and b).

A limited modeling study of the effects of Geogrid creep and stiffness was conducted that simulated the thinnest test sections (100 mm of asphalt and 300 mm of base), indicating (as expected) that both influence pavement system performance. Constraining the Geogrid to zero creep caused the predicted *TBR* value to increase from 1.29 to 1.42-- implying that Geogrid creep affects the rutting response, although the greatest relative improvement possible by completely eliminating creep was only about 45% (42% more cycles to failure vs. 29% more cycles to failure). The influence of Geogrid stiffness on the same test section was that halving the stiffness resulted in a 48% loss in the number of cycles to failure and doubling it, resulted in a 25% increase in the number of cycles to failure.

A comprehensive parametric study (PS), conducted with the FE model developed in this project, for conditions quite similar to those tested, indicated a range of *TBR* due to the additions of Geogrid from 1.04 to 2.40. The *TBR* value of 1.04 was for a pavement section of 100 mm thick AC with a modulus value of 2720 MPa overlying 300 mm of base with a modulus 300 MPa, and the grid was located 225 mm above the bottom of the base. The *TBR* value of 2.40 was for a pavement section of 200 mm thick AC with a modulus of 4480 MPa overlying 300 mm of base (geogrid located at the bottom) with a modulus of 100 MPa and a subgrade with a modulus of 35 MPa.

The PS results indicated that the modulus value of the base layer is extremely important in determining the potential benefit of adding geogrid. The grid always provided more benefit when the lower-modulus base was used (i.e., 100 MPa vs. 300 MPa).

Surprisingly, the model also predicted that the Geogrid would provide more benefit for stiffer asphalt modulus values. Similar to increasing the asphalt modulus, increasing asphalt thickness, generally (but not always) resulted in more effective grid performance. This stemmed from the fact that increasing the asphalt modulus and thickness had a larger relative effect on the strains developed in the unreinforced model than in the reinforced model. This may be physically realistic if a majority of the Geogrid strain is developed during compaction and is thus practically independent of asphalt thickness or modulus. This may be particularly true in the case of increasing asphalt thickness, as there is more asphalt available for rutting. On the other hand, if a majority of the Geogrid strain

is developed through trafficking, the effectiveness of the Geogrid is likely over-predicted as the asphalt thickness and/or modulus is increased.

One specific limitation of the FE model used in this study is that the location of the Geogrid within the base layer was treated by assigning pre-strain to the grid as a function of relative distance above the bottom of the base. This forced the grid to be more effective at the bottom than within the base layer. This was done based on field observations and worked well in matching the performance of the field-scale study of this project to modeling results. Despite this limitation, the model shows potential as a planning tool to help optimize combinations of asphalt and base course thicknesses and to answer whether Geogrid inclusion will provide cost-effective benefit—i.e., a potential design tool.

More long-term studies would help clarify the role of Geogrid reinforcement of the base layer over time. Recall that the field study conducted by Helstrom et al. (2006) indicated that strains increased in Geogrid reinforcement after paving in sections with a 300 mm thick base layer, but did not in sections with a 600 mm thick base layer. However, Geogrid located at the bottom of base layers developed as much or more strain over the four years that they were monitored (post construction) than when located in the middle of base layers. And not surprisingly, Geogrid with the thinner base layers developed more strain over time than with the thicker base layers.

Future investigations of pavements designed according to AASHTO guidance over soft to very soft subgrades would help define the benefit of geogrid-reinforcement of base course layers. Properly documented, full-scale testing with control sections (i.e., grid and no-grid) would provide the necessary calibration data for numerical models used in the future to describe the performance of the pavement systems with and without grid-reinforcement of the base. In addition, a range of Geogrid stiffness should be included in future investigations.

8 Conclusions and Recommendations

Based on direct experimental observations, the following conclusions are made for full-scale pavement test sections with a subgrade with modulus values of approximately 55 MPa:

1. Grid-reinforced test sections took longer to develop surface rut depths than their matching unreinforced control sections for the following conditions: 300 mm base with 100 and 150 mm asphalt thicknesses. All of these test sections were trafficked to failure of at least 12.5 mm rut-depth. In one case, the base-reinforced test section appeared to perform less successfully than the unreinforced control section, but the subgrade was significantly softer for the grid-reinforced test section (38 MPa modulus vs. 70 MPa modulus), and later modeling showed improved performance of the grid-reinforced test section. These results suggest only a small benefit by adding a Geogrid since the benefit noted, TBRs of 1.3 to 1.4, represents a very small difference in total rut depth—less than 2 mm--a difference that would be difficult to detect or measure in the field.
2. The test sections with 600 mm thick base did not fail when trafficked to 6.5 million ESALs. For these 600 mm thick base test sections, benefit was noted for the thinner test section with 100 mm thick asphalt, but not for the test sections with 150 mm thick asphalt.
3. Under the traffic loads applied, 3–5 mm total permanent deformation of the asphalt was observed in all test sections.
4. Adjusted permanent deformation data indicates that for the test sections with 300 mm thick bases, the reinforced test sections experienced somewhat less base compression. No trend was noted for the thicker, 600 mm base test sections.
5. There was no decrease in vertical elastic strains of any layers due to grid presence. In fact, three of the four reinforced sections indicated increased vertical elastic strains in the base and subgrade layers. The other reinforced section indicated decreased vertical elastic strains in the subgrade layer. Comparisons in the base layer were not possible due to failed instrumentation.

6. Subgrade modulus values estimated with falling-weight-deflectometer (FWD) tests were highly correlated to moisture content of the subgrade.
7. FWD testing also indicated that the subgrade and base moduli of each test section decreased from immediately before testing to immediately after testing, then subsequently recovered. This suggests time-dependent behavior of the subgrade, and possibly the base as well. However, it is also possible that the base modulus values recorded immediately after trafficking were influenced by the decreased subgrade modulus values and were not due to trafficking. This indicates that traffic loading directly affects the subgrade modulus, and accelerated loading may prevent normal recovery.
8. Static load tests indicated that elastic Geogrid strains were generally larger in sections with a 300 mm base layer than in those with a 600 mm base layer.
9. The permanent strains in the Geogrid were correlated to the surface rut depth. Due to loss of instrumentation, it was not possible to draw definitive conclusions about the differences in permanent Geogrid strain as a function of pavement layer thicknesses

A finite element model was developed and calibrated with the experimental results that were generated. Currently accepted mechanistic-empirical permanent deformation models recommended by NCHRP (2004b) were extended and implemented in this model to predict rutting. The conclusions made with respect to the model development are:

1. Layer moduli obtained from FWD analyses, when implemented in the FE models, were shown to result in reasonable agreement between the measured and predicted elastic strains in the pavement system as measured during the static load tests. This has significant practical implications, since FWD testing is a widely used and relatively simple method for obtaining material properties necessary for FE models.
2. FE models with a de-bonded asphalt/base interface condition showed better agreement with measured strains than FE models with a fully bonded asphalt/base interface condition. This indicates that the de-bonded interface may be better representative of the in-situ conditions of the test sections in this study, which were designed to be representative

of typical field conditions. This is important because complete asphalt/base layer bonding is a typical assumption and may not be realistic.

3. The mechanistic-empirical rutting models published by the NCHRP (2004b) were extended to rationally account for accepted performance improvement mechanisms associated with Geogrid reinforcement. The models were calibrated using the deformation data collected in this study. The models and measured rut depths were in reasonable agreement, even when only a sub-set of the measured deformations was used to calibrate the model.
4. Based on equal layer moduli for all sections and the assumptions previously described, the calibrated rutting models predict that Geogrid reinforcement will improve the rutting life by 29-43% for the pavement thickness configurations of this study. However, it is also important to consider that only two of the four Geogrid sections in this study indicated an improvement over their corresponding control sections.
5. Better agreement between the measured and predicted rut depths may be possible if the relationship between Geogrid strain and pavement layer thickness is established and incorporated in the FE models.
6. Parametric studies conducted with the model indicate that base layer stiffness is very important in determining how much benefit the grid will provide. Significantly less benefit was provided by the grid when a relatively stiff base layer was modeled.

Future experimental efforts for pavements designed similarly to those used in this study should be conducted with a softer subgrade that is also of interest to state transportation agencies. The relatively stiff subgrade used in this study necessitated the addition of water to the test sections in order to maintain reasonably constant layer moduli. This resulted in time delays; and, the test sections with a 600 mm thick base layer could not be trafficked to the failure rut depth. Geogrid strain gages should be monitored throughout the construction and trafficking period. If possible, more accurate or redundant instrumentation should be used to quantify the deformations within the pavement layers.

The FE and rutting models developed and used in this study are an initial step in the development of methods for analyzing geogrid-reinforced pavement base layers. Further validation of and improvements to the FE and rutting models of this study are strongly recommended. Additional data are needed that include accurate measurements of layer moduli through FWD testing, surface rut depths, and deformations within pavement layers. Additional studies relating the strain developed in reinforcement to the surface rut depth in a variety of pavement configurations are required in order to more accurately model the effect of reinforcement in various pavement configurations.

References

- AASHTO. 1993. *Guide for Design of Pavement Structures*. Washington, DC: American Association of State Highway and Transportation Officials.
- ASTM International (2001). "Test method for determining tensile properties of geogrids by the single or multi-rib tensile method." ASTM D6637, ASTM Book of Standards Volume 04.13, Philadelphia.
- Barksdale, R. D., S. F. Brown, and F. Chan (1989). "Potential Benefits of Geosynthetics in Flexible Pavement Systems.", National Cooperative Highway Research Program Report No. 315, Transportation Research Board, National Research Council, Washington, DC, 56 p.
- Clapp, J.D. (2007). "Analysis of Rutting Development in Flexible Pavements with Geogrid-Reinforced Base Layers Using 3D Finite Element Analysis." M.S. Thesis, University of Maine, Orono, ME.
- Collin J.G., T.C. Kinney, and X. Fu (1996) "Full Scale Highway Load Test of Flexible Pavement Systems With Geogrid Reinforced Base Courses," *Geosynthetics International*, Vol. 3, No. 4, pp. 537-549.
- Davids, W.G. and J. Mahoney (1999). "Experimental Verification of Rigid Pavement Joint Load Transfer Modeling with EverFE." Transportation Research Record 1684: Journal of the Transportation Research Board, TRB, National Research Council, Washington, D.C., pp. 81-89.
- Davids, W.G., Z.M. Wang, G. Turkiyyah, J. Mahoney, and D. Bush, (2003). "3D Finite Element Analysis of Jointed Plain Concrete Pavement with EverFE2.2." Transportation Research Record 1853, TRB, Washington, D.C., p 92-99.
- Dondi, G. (1994). "Three-Dimensional Finite Element Analysis of a Reinforced Paved Road." Proceedings of the Fifth International Conference on Geotextiles, Geomembranes and Related Products 1: 95-100.
- Dynatest (2005). "Elmod 5." Dynatest International A/S, Glostrup, Denmark (http://www.dynatest.com/software/elmod_5.htm, accessed 5/07).
- Giroud, J.P. and J. Han (2004). "Design method for geogrid-reinforced unpaved roads. I. Development of Design Method." ASCE Journal of Geotechnical and Geoenvironmental Engineering, Vol. 130, No. 8, pp. 775-786.
- Goldberg, D.E. (1989). "Genetic Algorithms in Search, Optimization, and Machine Learning." Addison Wesley, New York.
- Goldberg, D.E. and K. Deb (1991). "A comparison of selection schemes used in genetic algorithms", Foundations of Genetic Algorithms 1 (FOGA-1), p. 69-93.

Haas, R., J. Walls, and R.G. Carroll (1988) "Geogrid Reinforcement of Granular Bases in Flexible Pavements," *Transportation Research Record 1188: Journal of the Transportation Research Board*, TRB, National Research Council, Washington D.C., pp. 19-27.

Helstrom, C.L., D.N. Humphrey, and J.M. Labbe (2006). "Performance and Effectiveness of a Thin Pavement Section Using Geogrids and Drainage Geocomposites in a Cold Region (Draft)." New England Transportation Consortium Project No. 00-8, 235 p.

Henry, Karen S., Edel R. Cortez, Lawrence S. Danyluk, Gregory Bretnrup, Nathan Lamie, and Troy W. Arnold (April 2008) Construction and Instrumentation of Full-Scale Geogrid Reinforced Pavement Test Sections, ERDC/CRREL TR-08-6, U.S. Army Corps of Engineers, Engineer Research and Development Center, Cold Regions Research and Engineering Laboratory, Hanover, New Hampshire. Available at: <http://www.crrel.usace.army.mil/library/technicalreports/ERDC-CRREL-TR-08-6.pdf>

HKS Inc. (2004). Hibbit, Kalsson & Sorensen, Inc. "ABAQUS Standard User's Manual Vol. 6.5-1.", Pawtucket, R.I.

Holland, J.H. (1975). *Adaption in natural and artificial systems*. University of Michigan Press, Ann Arbor, Mich.

Hossain, M., J. Zaniewski, and S. Rajan (1994) "Estimation of Pavement-Layer Moduli using Nonlinear Optimization Technique" *Journal of Transportation Engineering* 120(3): 378.

Huang, Y. H. (1993). "Pavement Analysis and Design." Prentice Hall, Upper Saddle River, NJ.

Janoo, Vincent, Lynne Irwin, and Robert Haehnel (2003) Pavement Subgrade Performance Study, ERDC/CRREL TR 03-5, U.S. Army Engineer Research and Development Center, Cold Regions Research and Engineering Laboratory, Hanover, New Hampshire. Available at: <http://www.crrel.usace.army.mil/library/technicalreports/TR03-5.pdf>.

Kang, Y.V. (1998). "Multifrequency Back-Calculation of Pavement-Layer Moduli" *Journal of Transportation Engineering* 124(1): 75.

Kinney, T., J. Abbott, and J. Schuler (1998a). "Benefits of Using Geogrids for Base Reinforcement with Regard to Rutting," *Transportation Research Record 1611*, Transportation Research Board, Washington, D. C., p. 86-96.

Kinney, T., J. Abbott, and J. Schuler (1998b). "Using Geogrids for Base Reinforcement as Measured by Falling Weight Deflectometer in Full-Scale Laboratory Study," *Transportation Research Record 1611*, Transportation Research Board, Washington, D. C., p. 70-77.

Ling, H.I. and Z. Liu (2003). "Finite Element Studies of Asphalt Concrete Pavement Reinforced with Geogrid." *Journal of Engineering Mechanics, ASCE* 129(7): 801-811.

- Maine DOT (2006), "Technical Report 99-8: Experimental Use of Geogrids as an Alternative to Gravel Placement, Final Report", Maine Department of Transportation, Augusta, ME.
- MathWorks (2005). *Programming, MATLAB Version 7.1 (R14SP3)* The MathWorks, Inc., Natick, MA.
- Michalewicz, Z. (1992). "Genetic Algorithms + Data Structures = Evolution Program." Springer-Verlag, Berlin.
- Miura, N., A. Sakai, Y. Taesiri, T. Yamanouchi, and K. Yasuhara (1990). "Polymer Grid Reinforced Pavement on Soft Clay Grounds.", Geotextiles and Geomembranes 9(1): 99-123.
- NCHRP (2004a). "NCHRP Synthesis 325, Significant Findings from Full-Scale Accelerated Pavement Testing.", (http://onlinepubs.trb.org/onlinepubs/nchrp/nchrp_syn_325.pdf, accessed 5/07).
- NCHRP (2004b). "NCHRP Project 1-37A Design Guide, Mechanistic-Empirical Design of New and Rehabilitated Pavement Structures.", <http://www.trb.org/mepdg/>.
- Park, S. and R.L. Lytton (2004). "Effect of Stress-Dependent Modulus and Poisson's Ratio on Structural Responses in Thin Asphalt Pavements." Journal of Transportation Engineering, ASCE 130(3): 387-394.
- Perkins, S.W. (1999a) "Mechanical Response of Geosynthetic-Reinforced Flexible Pavements," Geosynthetics International, Vol. 6, No. 5, pp. 347-382.
- Perkins, S.W. (1999b). "Geosynthetic Reinforcement of Flexible Pavements: Laboratory Based Pavement Test Sections." (Montana Department of Transportation, Helena, MT), Report No. FHWA/MT-99/8106-1.
- Perkins, S.W. (2001). "Numerical Modeling of Geosynthetic Reinforced Flexible Pavements." (Montana Department of Transportation, Helena, MT), Report No. FHWA/MT-01-003/99160-2.
- Perkins, S.W. and M.Q. Edens (2003) "Finite Element and Distress Models for Geosynthetic-Reinforced Pavements", International Journal of Pavement Engineering, 3(4): 239-250.
- Perkins, S.W., B.R. Christopher, E.L. Cuelho, G.R. Eiksund, I. Hoff, C.W. Schwartz, G. Svanø, and A. Watn (2004). "Development of Design Methods for Geosynthetic Reinforced Flexible Pavements." U.S. Department of Transportation, Federal Highway Administration, Washington, DC, FHWA Report Reference Number DTFH61-01-X-00068, 263 p.
- Perkins, S.W., B.R. Christopher, G.R. Eiksund, C.S. Schwartz, and G. Svanø (2005) "Modeling Effects of Reinforcement on Lateral Confinement of Roadway Aggregate." Proceedings of the Sessions of the Geo-Frontiers 2005 Congress, Advances in Pavement Engineering, January 24-26, 2005, Austin, Texas, 14 p.
- Perkins, S.W. and E.R. Cortez (2005) Evaluation of base-reinforced pavements using a heavy vehicle simulator. Geosynthetics International 12(2): 86-98.

- Perkins, S.W., and Ismeik, M. (1997), "A Synthesis and Evaluation of Geosynthetic-Reinforced Base Layers in Flexible Pavements: Part I," *Geosynthetics International*, Vol. 4, No. 6, pp. 549-604.
- Roberts, Freddy L., Prithvi S. Kandhal, E. Ray Brown, Dah-Yinn Lee, and Thomas W. Kennedy (1996) Hot Mix Asphalt Materials, Mixture Design and Construction, 2nd Edition, NAPA Research and Education Foundation, Lanham, Maryland 20706-4413.
- Romanoschi, S.A., J.B. Metcalf (2002). "The Errors in Pavement Layer Moduli Backcalculation due to Improper Modeling of Layer Interface Condition." Presented at 2002 TRB Annual Meeting, Washington D.C., 2002.
- Sugimoto, M. and Alagiyawanna, A.M.N. (2003) "Pullout Behavior of Geogrid by Test and Numerical Analysis", Journal of Geotechnical and Geoenvironmental Engineering, ASCE, 129(4), pp. 361-371.
- Tensar Earth Technologies, Inc. (2005) "Product Specification – Biaxial Geogrid BX1200", Retrieved September 6, 2005, from http://www.tensarcorp.com/uploadedFiles/SPECTRA_MPDS_BX_8.05.pdf.
- Uzan, J., Scullion, T., Michalek, C.H., Panedes, M., and Lytton, R.L. (1988). "A microcomputer based procedure of backcalculating layer moduli from FWD data." *Res. Rep. No. 1123*, Texas Transportation Institute, Texas A&M University, College Station, Tex.
- Vischer, W. (2003) Low-Volume Road Flexible Pavement Design with Geogrid-Reinforced Base. *Transportation Research Record* 1819. Washington D.C: Transportation Research Board.
- Wathugala, G.W., B. Huang, and, S. Pal (1996). "Numerical Simulation of Geosynthetic Reinforced Flexible Pavement." *Transportation Research Record* 1534, p. 58-65.

Appendix A – Test Protocol

The following preliminary test procedure was developed between ERDC-CRREL (Dr. Karen Henry) and the University of Maine prior to trafficking any of the test sections. This protocol was modified extensively based on instrumentation survivability, the measured rutting response as traffic cycles were applied, and other factors. The preliminary test procedure for conducting the test section trafficking was as follows:

Overview

The original test design was based on a design life of 3×10^6 equivalent single axle loads (ESAL) of 80 kN (18 Kips), a subgrade soil of CBR 4 and a resilient modulus value, M_r of 41.4 MPa (6,000 psi). According to the 1993 AASHTO Design Guide, this produces a required structural number of 4.3, and in order to achieve this with 90 percent reliability, a standard deviation of 0.45 and a serviceability index of 2 psi, a 610 mm (24 in) subbase and 127 mm (5 in) of asphalt is required. This configuration produces a structural number of 4.5.

However, the subgrade as constructed yielded measured CBR values (based on DCP tests) ranging from 9 to 44—i.e., about 2 to 10 times that initially desired. The laboratory-determined resilient modulus value of the soil as placed ranged from 69.0 to 137.9 MPa (10,000 to 20,000 psi), and that back-calculated based on FWD testing ranged from 107.6 to 122.7 MPa (15600 to 17800 psi)—about three times the desired value.

We have ‘softened’ the subgrade and base layers via adding water from December 2005 through April 2006. Using a modulus of subgrade reaction of 68.9 MPa (10000 psi), with asphalt moduli of 2660 MPa (386000 psi) for the 100 mm (4 in) asphalt (the 150 mm (6 in) thick asphalt has an estimated modulus of 2830 MPa (410,000 psi), and assuming a base layer modulus of 331 MPa (48000 psi) (in line with that measured by lab tests and back-calculated), the thinnest test section with the thinnest base layer and no Geogrid has a structural number of 4.04. For the 68.9 MPa (10000 psi) subgrade, we will need approximately 5×10^6 ESALS to fail this test section. For the same section with 600 mm

(24 in) of base, I estimate that we will need in excess of 50×10^6 ESALS to fail the test section.

It is not desirable to fail the test section with loads in excess of maximum single axle loads allowed by states—i.e., 89 kN (20000 lb).

Explanation of Measurements

The finite element (FE) model being developed computes displacements (strains) throughout the pavement section under a static loading condition. The displacements are used to calculate stresses based on material properties. The FE model is also capable of including the effects of the construction sequence.

Finite Element Model Input Parameters from CRREL

All facility geometry is necessary and has been provided. All pavement layer properties have been provided except those for the asphalt concrete (AC) layer. The density can be estimated with reasonable confidence; however, the resilient modulus can only be obtained accurately by testing core samples of the existing asphalt concrete layer. The magnitude of the wheel load and tire pressure must also be provided once it has been determined.

Construction Measurements

The finite element model includes the effect of staged construction, specifically the effect of compaction and asphalt concrete placement on the initial pre-strain of the geogrid. Measured displacements, stress, and strain in the pavement system after gage installation, compaction of the base layer, and placement of the AC layer, will be useful in calibrating the model for construction effects, if available.

First Measurements

Before any traffic loading occurs, record all gage readings throughout the pavement system and surface rut depth (ideally zero). Then, for all eight sections (i.e. windows 1-8), place the full wheel load at the following relative local coordinates [x (mm or in), y (mm or in)], which are defined in Henry, et al. (2008):

1. (-18289, 0) mm [-72, 0] in – Directly over a pair of transversely mounted strain gages on the geogrid.
2. (-1525, 0) mm [-60, 0] in – Directly over a pair of longitudinally mounted strain gages on the geogrid.
3. (-1219, 0) mm [-48, 0] in – Directly over a pair of transversely mounted strain gages on the geogrid.
4. (-1067, 0) mm [-42, 0] in – Directly over longitudinally oriented stress cells.
5. (-457, 0) mm [-18, 0] in – Directly over vertically oriented stress cells.
6. [0, 0] mm, in – Directly over Z-direction soil/AC strain gage.
7. (457, 0) mm [18, 0] in – Directly over Z-direction soil/AC strain gage stack.
8. (610, 0) mm [24, 0] in – Directly over X-direction soil/AC strain gage stack.

Record all gages with the wheel load at each location. The locations are also shown in Figures A1 to A3. Take readings approximately 10 sec. after final positioning of wheel in each case. Locations (1) – (3) are only necessary in sections with strain gages attached to the geogrid. The location of this static load test should be held constant for each test section throughout the trafficking period.

Measurements after trafficking

Repeat the process described above for the static load test every n/20 ESALs, where n is the total number of ESALs to be applied.

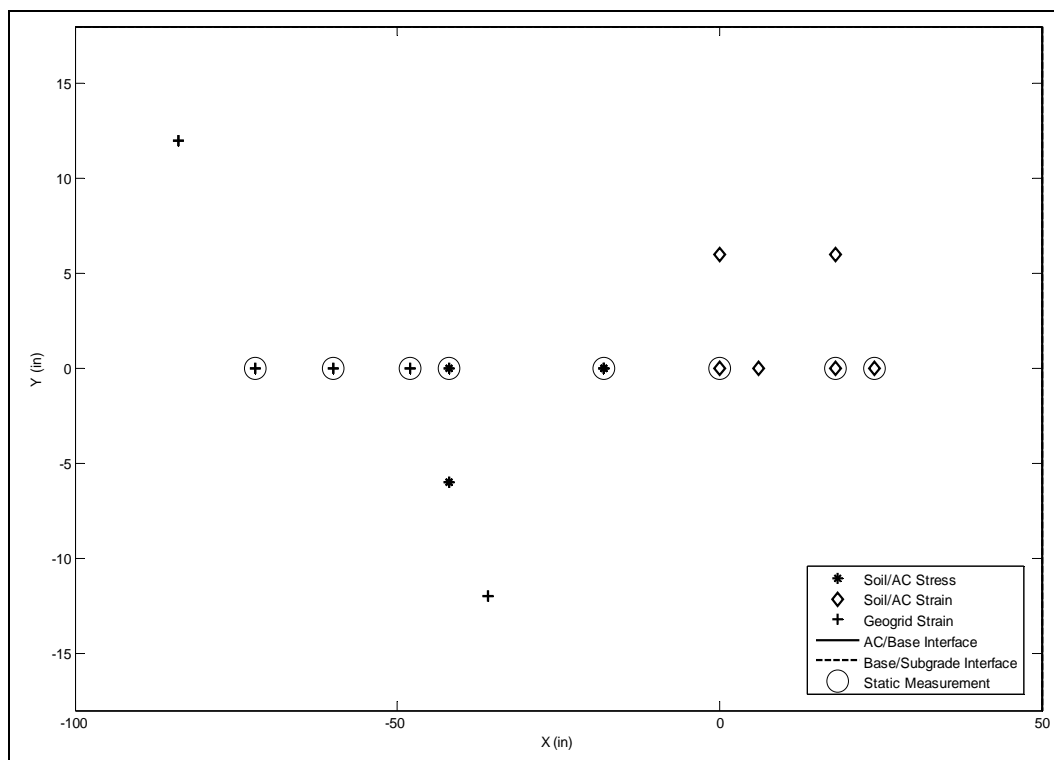


Figure A1. Plan view of stress/strain gages in Test Section 3.

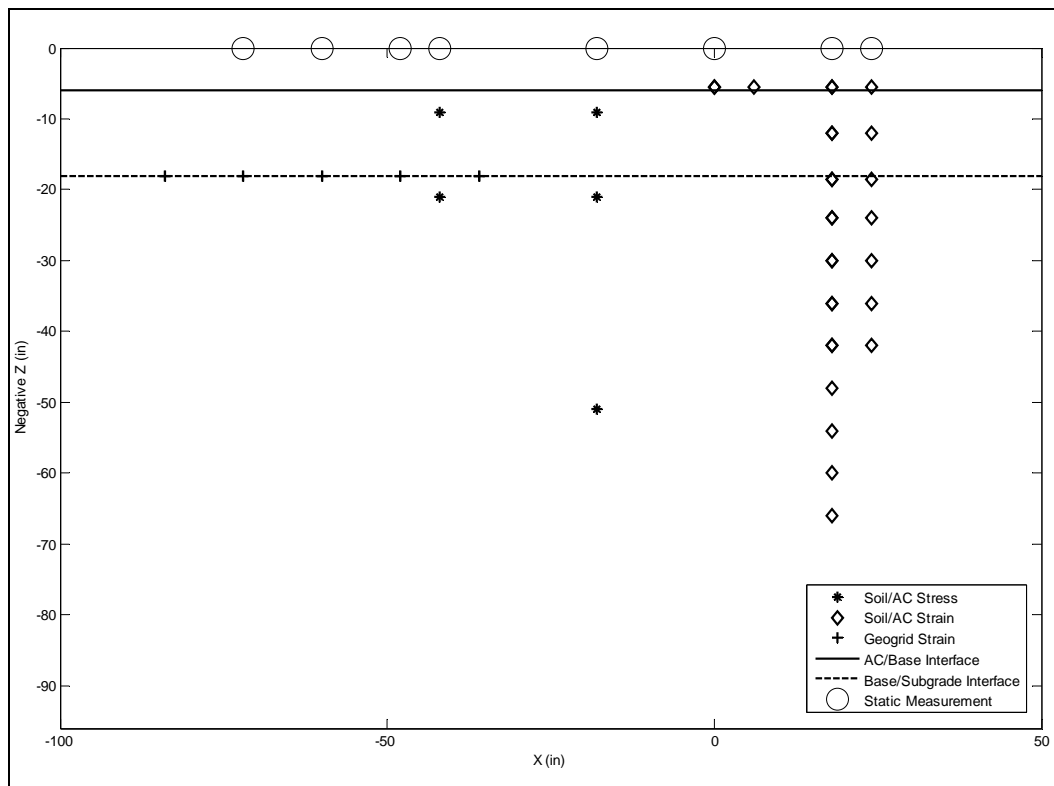


Figure A2. Plan view of stress/strain gages in Test Section 3.

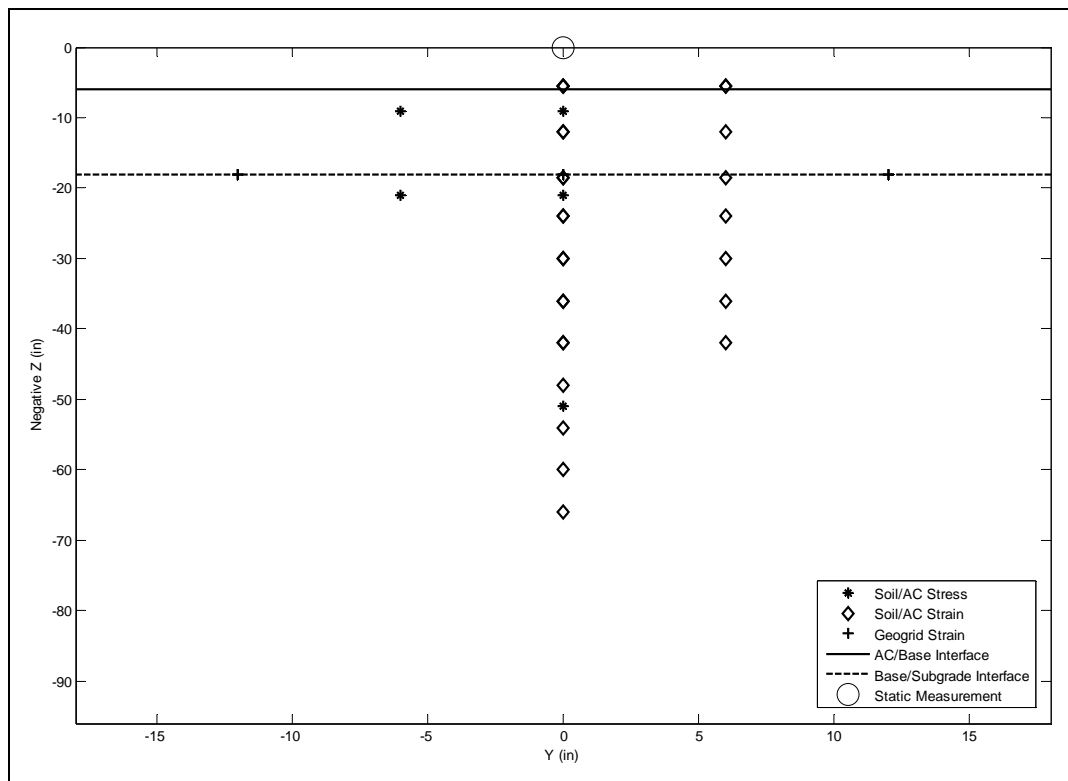


Figure A3. Cross section of stress/strain gages in transverse direction, Test Section 3.

Appendix B – Forensics

Test section characterization

Prior to excavation activities, the surface of each of the eight test sections was visually inspected and photographed to document distresses that developed during testing, as shown in Figure B1. Photographs were taken every few feet along the measuring tape stretched along the center of the test section. The surface condition of all eight test sections consistently showed the rutting due to the trafficking, but no other major distresses (cracking, etc.). The dark color of the test section surface is rubber build up from the test tire. A straight edge was placed across the traffic lane, in the vicinity of the emu strain gages, to show the rut depth (Figure B2). Photographs from test sections 1 and 7 are included here as representatives of all test sections (Figures B1 to B6).

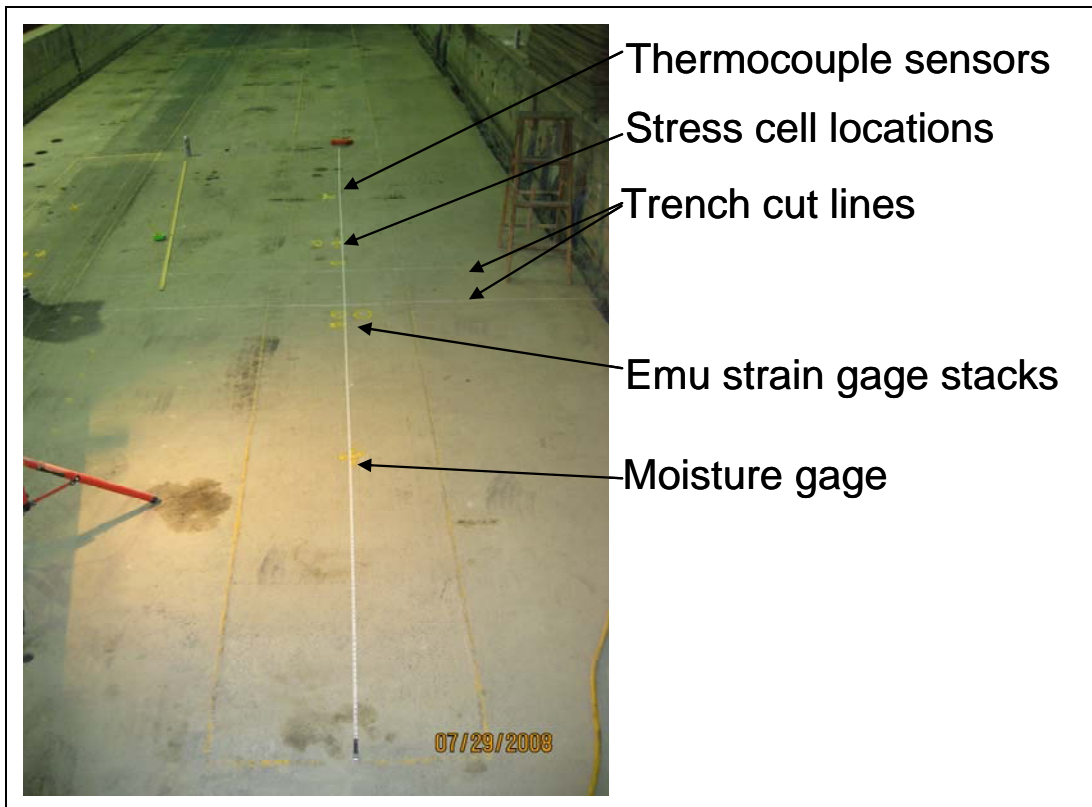


Figure B1. Test Section 1 surface condition.

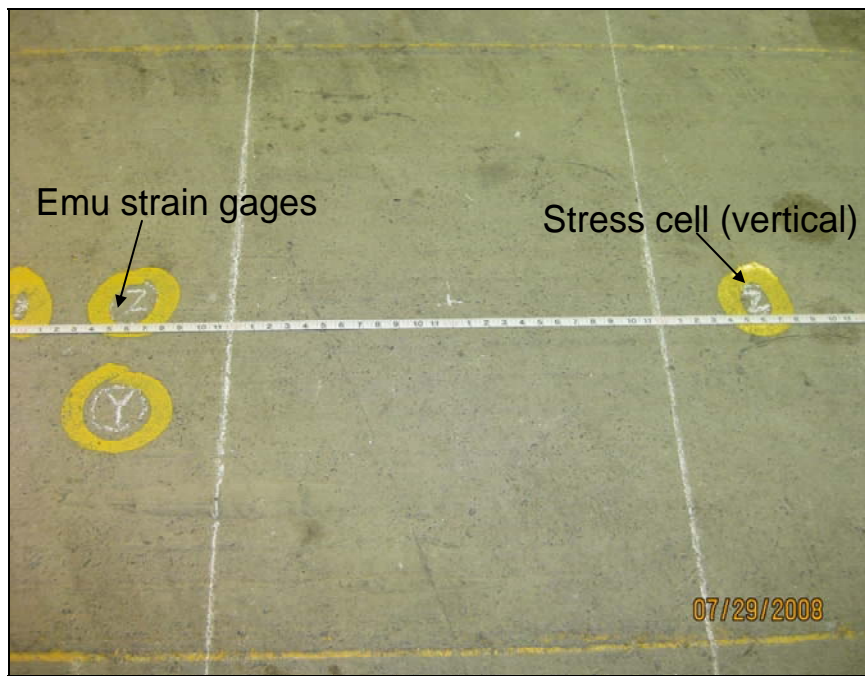


Figure B2. Test Section 1 surface condition showing trafficked surface near strain and stress instrumentation.



Figure B3. Rut depth near emu strain gage stacks.

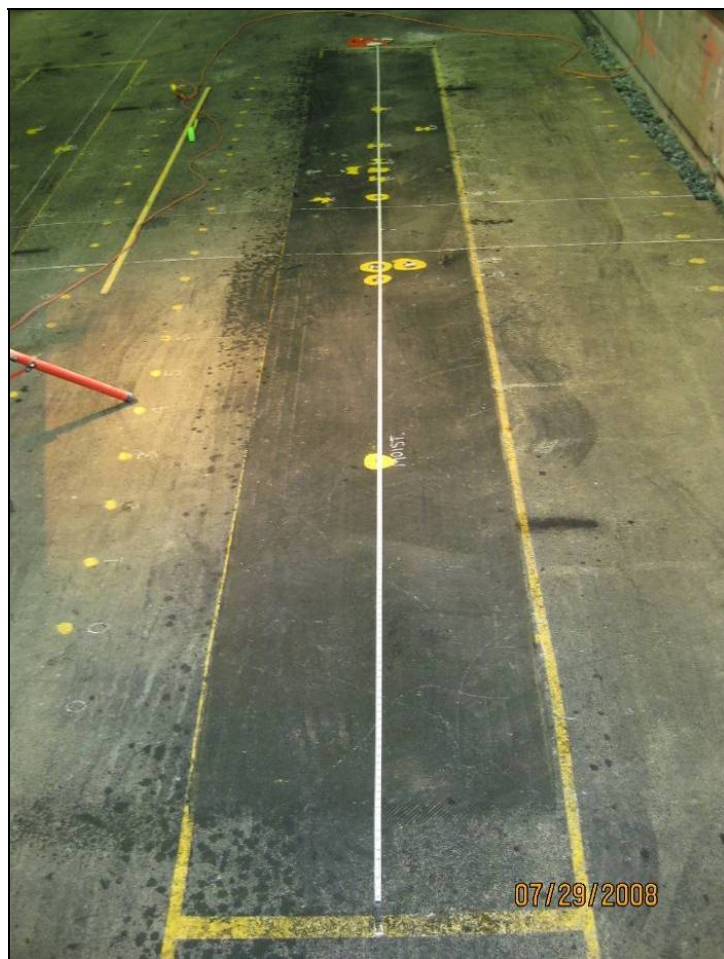


Figure B4. Test Section 7 surface condition.

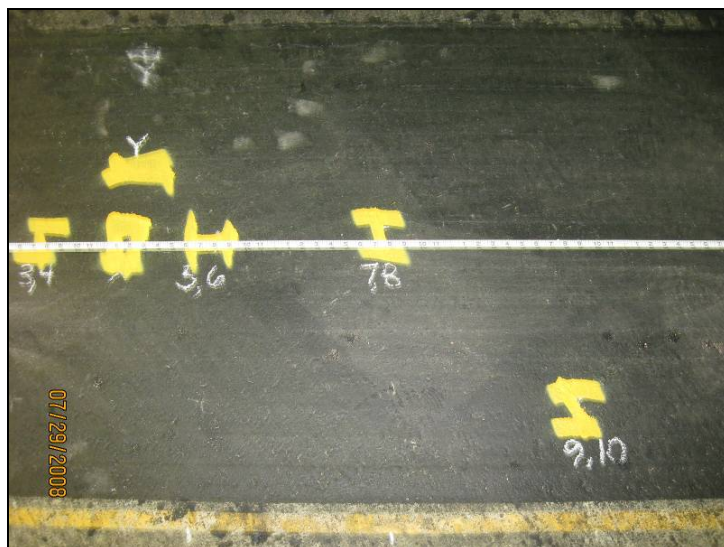


Figure B5. Test Section 7 surface condition near Geogrid strain gage locations.



Figure B6. Rut depth near Geogrid strain gage locations in Test Section 7.

A plan was established and followed during the forensics investigation. Upon removal of the HVS from the test area, final unloaded readings of the ε mu sensors were collected. Surviving Geogrid strain gages were located in Test Sections 7 and 8; therefore, measurements and excavation were conducted there, while Test Sections 1 and 2 were excavated near the ε mu sensors.

The asphalt surface was cut using a walk-behind pavement saw. The trench was cut just to the north side of the stacks of ε mu gages. This area was designed to be completely clear of interference with any instrumentation. Once the asphalt was removed, the surface of the base course was smoothed out using a shovel.

Soil strength

Soil strength measurements were taken with the dynamic cone penetrometer (DCP). The DCP consists of a 16 mm diameter steel rod with a sliding 8 kg hammer weight. The end of the rod is tipped with a 60° cone. The rod was driven into the soil, at least 25 mm, by raising the hammer to a height of 575 mm and dropping it. The depth of penetration was measured with a measurement scale. Readings were taken along the full length of the rod (900 mm) beginning at the top of the base course layer through into upper 600 mm of the subgrade layer. Using the

penetration data, the California bearing ratio (CBR) of the soil is determined using the relationship in Equation B1 (U.S. Air Force 2002). Soil strength profiles for the center of each test section are shown in Figures B7 to B10.

$$CBR = \frac{292}{DCP^{1.12}} \quad (B1)$$

Soil strength measurements were also made with the Clegg Hammer at the top of the base, and following excavation, at the top of the subgrade (Figure B11). The Clegg Impact Value (CIV) is used to estimate the soil CBR. At each test point, the hammer within the guide tube was dropped four times. As the hammer strikes the soil surface, the readout device records the deceleration value, or CIV (Clegg impact value). Within the four drops, the CIV value should be increasing. The 4th drop, or the peak CIV, is used to calculate the soil CBR using the following relationship (Equation B2, Clegg 1986). Table B1 lists the peak deceleration value and CBR for the base and subgrade soil layers:

$$CBR(\%) = [0.24(CIV) + 1]^2 \quad (B2)$$

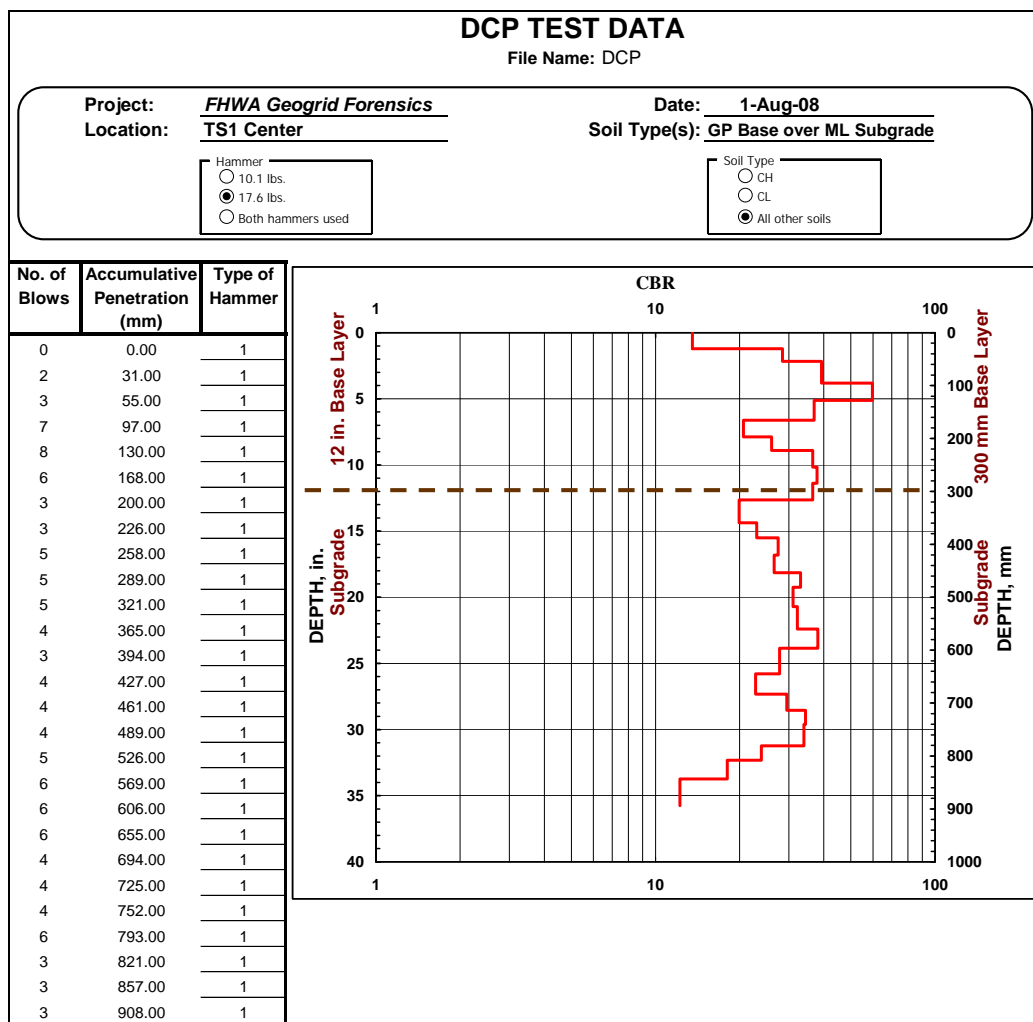


Figure B7. DCP soil strength profile for center of Test Section 1.

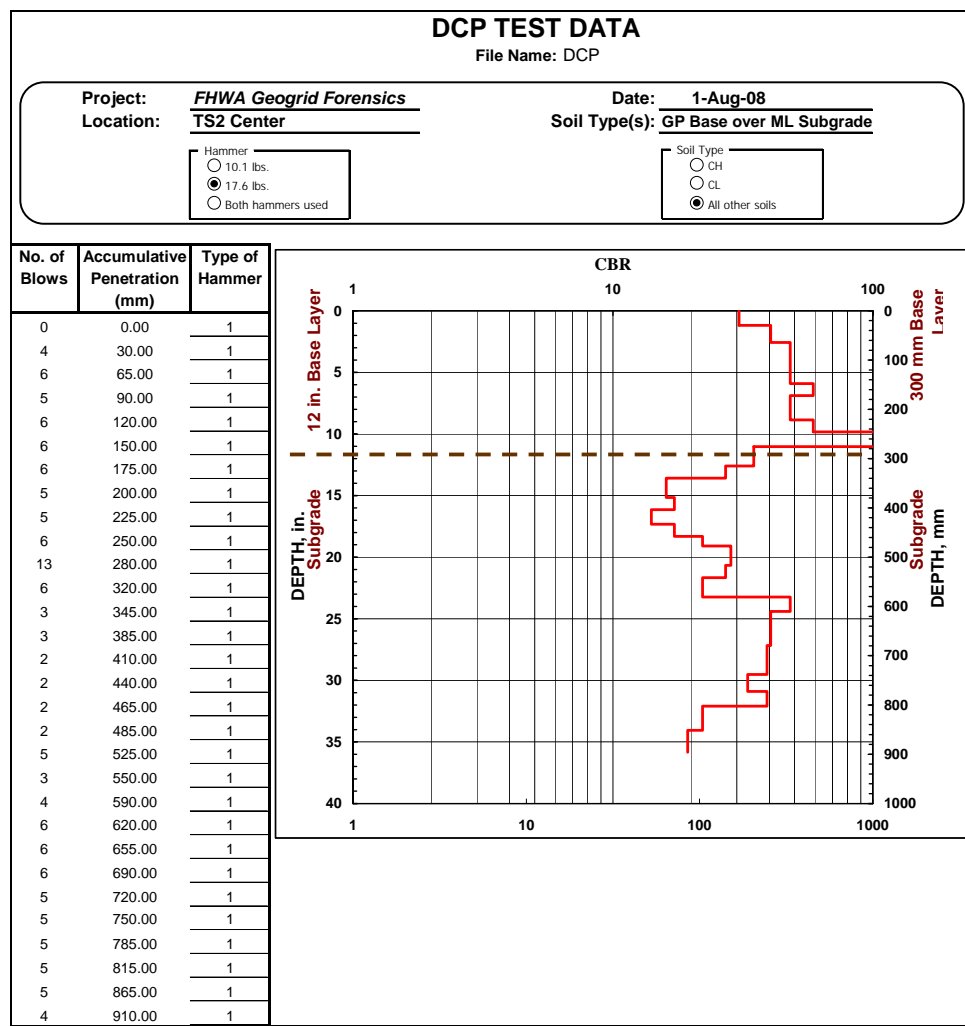


Figure B8. DCP soil strength profile for center of Test Section 2.

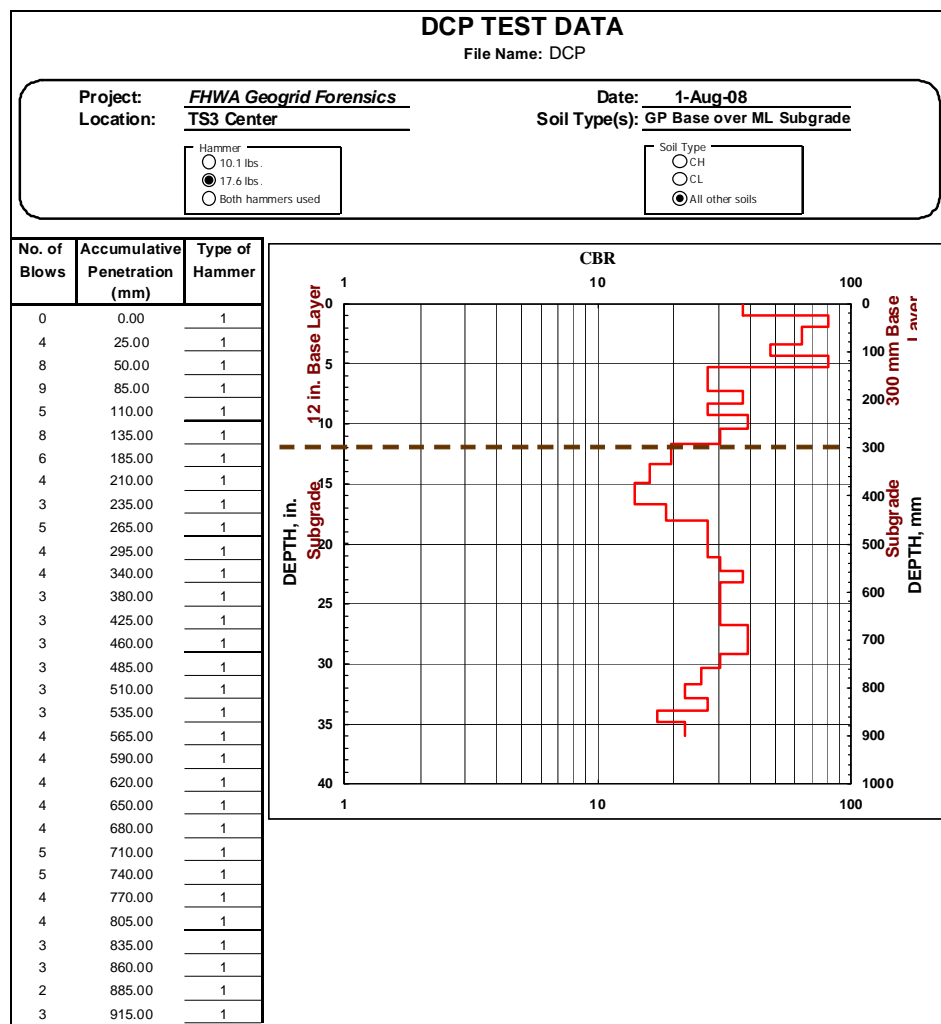


Figure B9. DCP soil strength profile for center of Test Section 3.

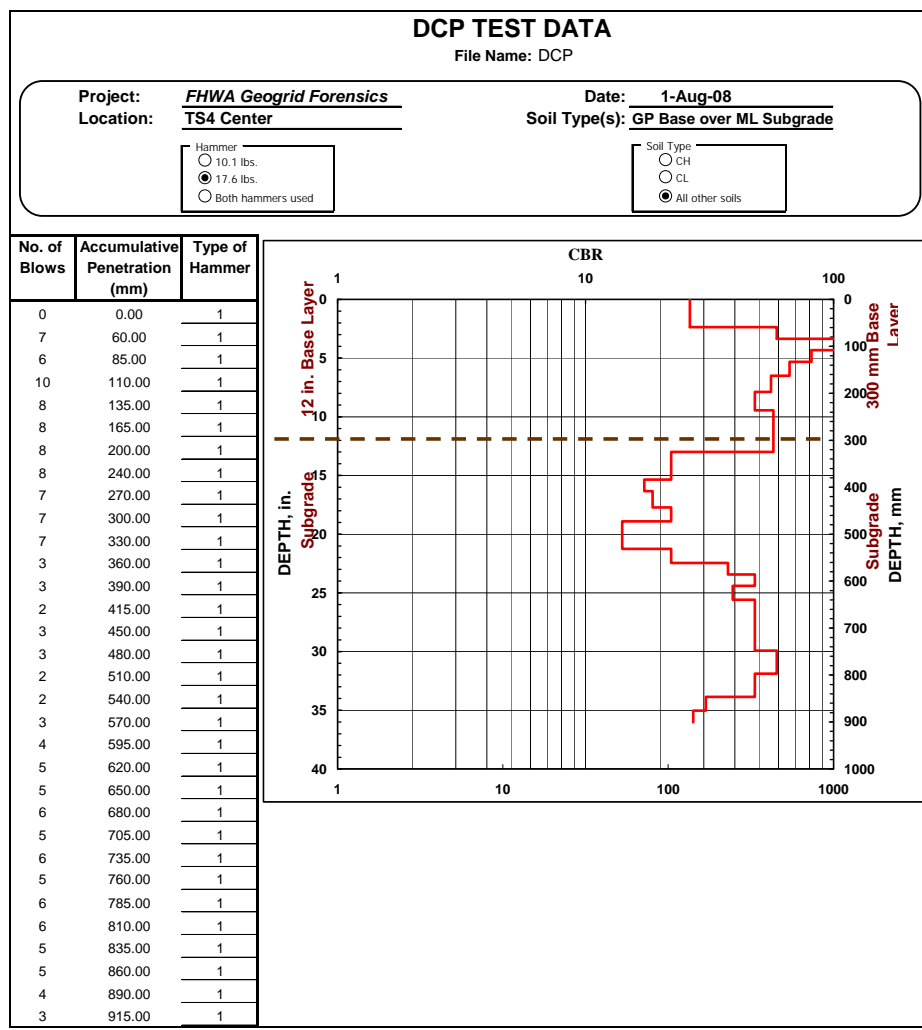


Figure B10. DCP soil strength profile for center of Test Section 4.



Figure B11. Clegg Hammer used to measure soil strength on test sections.

Table B1. Clegg Impact Value (CIV) and calculated soil CBR for base and subgrade layers in Test Sections 1 through 4.

Test Sections 1 and 2				
	CIV (g)		Calculated CBR (%)	
Location	Base	Subgrade	Base	Subgrade
West of TS 1	-----	9	-----	10
Center TS 1	17	9	26	10
Between TS 1 and TS 2	17	8	26	9
Center TS 2	22	9	39	10
East of TS 2	22	7	39	7
Test Sections 3 and 4				
	CIV (g)		Calculated CBR (%)	
Location	Base	Subgrade	Base	Subgrade
West of TS 3		7		7
Center TS 3		8		8
East of TS 3		7		7
West of TS 4		5		5
Center TS 4		9		10
East of TS 4		7		7

Soil moisture and density

The Troxler (Model 3440) nuclear gage was used to collect moisture and density readings through the base course layer and the upper 300 mm of the top of the subgrade (Figure B12). Readings were collected at 3 locations: one at the center of each test section and one in the un-trafficked section between the test sections. The radioactive sources used in the gage are Americium 241; Beryllium and Cesium-137. The gage has two modes of operation: direct transmission mode is used to measure the soil density; and backscatter mode is used to measure the soil moisture content (Troxler Electronic Laboratories, Inc. 2003). Soil density and moisture readings for each test section are listed in Table B2.



Figure B12. Soil moisture and density measurements taken with the Troxler nuclear gage.

Table B2. Troxler nuclear gage readings.

Middle of TS 1 Top of Base					
Depth from base surface (mm)	Dry Density (kg/m ³)	Wet Density (kg/m ³)	M	%M	Comments
0	2,012	2,073	3.7	3.0	Backscatter
50	2,190	2,262	4.5	3.3	
150	2,356	2,427	4.3	2.9	Mid-base
Middle of TS 1 Top of Subgrade					
0	1,647	1,937	18.1	17.7	
150	1,873	2,162	18.1	15.5	
300	1,881	2,182	18.9	16.1	
Middle of TS 2 Top of Base					
Depth from base surface (mm)	Dry Density (kg/m ³)	Wet Density (kg/m ³)	M	%M	Comments
0	1,949	2,009	3.7	3.0	
50	1,977	2,039	3.8	3.1	
100	2,145	2,201	3.5	2.6	
150	2,203	2,265	3.8	2.8	
250	2,171	2,235	4.0	3.0	
300	2,177	2,249	4.5	3.3	
Middle of TS 2 Top of Subgrade					
0	1,751	2,041	18.1	16.6	
50	1,874	2,171	18.2	15.6	
300	1,893	2,187	18.3	15.3	
Middle of TS 3 Top of Base					
Depth from base surface (mm)	Dry Density (kg/m ³)	Wet Density (kg/m ³)	M	%M	Comments
0	2,094	2,166	4.4	3.4	
50	2,183	2,246	4.0	2.9	
100	2,377	2,438	3.9	2.6	
150	2,299	2,366	4.5	3.2	
200	2,236	2,308	4.5	3.2	
250	2,243	2,308	4.2	3.0	
300	2,331	2,302	4.4	3.2	
Middle of TS 3 Top of Subgrade					
0	1,627	1,900	17.0	16.7	
50	1,616	1,890	17.1	16.9	
150	1,781	2,047	16.6	14.9	
250	1,836	2,106	16.9	14.7	
300	1,881	2,159	17.4	14.9	
Middle of TS 4 Top of Base					
Depth from base surface (mm)	Dry Density (kg/m ³)	Wet Density (kg/m ³)	M	%M	Comments
0	2,206	2,268	4.0	2.9	
2	2,171	2,244	4.5	3.3	
4	2,263	2,331	4.2	2.9	
6	2,278	2,344	4.2	2.9	

Depth from base surface (mm)	Dry Density (kg/m ³)	Wet Density (kg/m ³)	M	%M	Comments
8	2,270	2,344	4.6	3.3	
10	2,246	2,313	4.2	3.0	
12	2,223	2,292	4.3	3.1	
Middle of TS 4 Top of Subgrade					
0	2,154	2,448	18.3	13.6	
2	1,772	2,066	18.4	16.6	
6	1,823	2,108	17.8	15.7	
10	1,804	2,105	18.8	16.7	
12	1,813	2,108	18.5	16.3	

At the top of the subgrade, volumetric soil moisture readings were collected using a Dynamax ML2 probe (Figure B13). Soil moisture and density readings were collected within the upper inches of the top of the subgrade using small drive cylinders (Figure B14). The moisture contents, by weight, for the samples collected are given in Table B3. The items labeled 'Cylinders' describe the moisture contents, by weight, from the drive cylinders taken on the top of the subgrade. The calculated drive cylinder density values are listed in Table B3. The volumetric moisture contents are given in Table B4.

Soil samples were also collected and oven dried to obtain the gravimetric moisture content. These moisture contents are also listed in Table B3.



Figure B13. Dynamax ML2 probe used to take volumetric moisture content readings on the subgrade.



Figure B14. Drive cylinder used on surface of subgrade to determine moisture and density.

Table B3. Moisture contents, by weight, and drive cylinder density values.

FERF: GEOGRID REINFORCED PAVEMENT FORENSIC STUDY

LOCATION	Base	Base	Base	Base	Base	Base
TEST	TS 1 W	TS 1 C	TS 1 E	TS 2 W	TS 2 C	TS 2 E
DEPTH, mm	300	300	300	250	275	275
TIME	14:30	14:31	14:31	14:33	14:19	14:18
DATE	7/30/2008	7/30/2008	7/30/2008	7/30/2008	7/30/2008	7/30/2008
WATER CONTENT, w%	1.42	1.78	2.24	2.41	1.83	2.05
LOCATION	Cylinders	Cylinders	Cylinders	Cylinders	Cylinders	
TEST	TS 1 & 2 C	TS 1 C	TS 1 W	TS 2 E	TS 2 C	
DEPTH, mm	412.5	475	512.5	450	406.25	
TIME						
DATE	7/30/2008	7/30/2008	7/30/2008	7/30/2008	7/30/2008	
TARE NUMBER	108	101	102	99	100	
WATER CONTENT, w%	18.57	16.87	18.33	18.90	17.51	
WET DENSITY (kg/m ³)	2,403	2,519	2,482	2,549	2,532	
DRY DENSITY (kg/m ³)	2,026	2,156	2,098	2,143	2,155	
LOCATION	Subgrade	Subgrade	Subgrade	Subgrade	Subgrade	Subgrade
TEST	TS 1 W	TS 1 C	TS 1 E	TS 2 W	TS 2 C	TS 2 E
DEPTH, mm	762.5	762.5	762.5	725	700	700
TIME	13:58	13:59	14:00	14:01	14:02	14:03
DATE	7/31/2008	7/31/2008	7/31/2008	7/31/2008	7/31/2008	7/31/2008
TARE NUMBER	5	7	8	9	13A	15A
WATER CONTENT, w%	13.67	16.12	14.64	14.84	16.20	17.02
LOCATION	Base	Base	Base	Base	Base	Base
TEST	TS 3 W	TS 3 C	TS 3 E	TS 4 W	TS 4 C	TS 4 E
DEPTH, mm	300	300	300	250	250	250
TIME	8:39	8:39	8:39	8:40	8:40	8:40
DATE	7/31/2008	7/31/2008	7/31/2008	7/31/2008	7/31/2008	7/31/2008
TARE NUMBER	15	13	12	11	10	14A
WATER CONTENT, w%	1.12	1.09	1.52	1.49	1.39	1.66
LOCATION	Cylinders	Cylinders	Cylinders	Cylinders	Cylinders	
TEST	TS 3 W	TS 3 C	TS 3 & 4 C	TS 4 C	TS 4 E	
DEPTH, mm	487.5	500	431.25	400	400	
TIME						
DATE	8/1/2008	8/1/2008	8/1/2008	8/1/2008	8/1/2008	
TARE NUMBER	98	103	97	106	107	
WATER CONTENT, w%	18.18	17.13	19.39	17.68	17.88	
WET DENSITY (kg/m ³)	2,582	2,553	2,541	2,560	2,560	
DRY DENSITY (kg/m ³)	2,185	2,180	2,128	2,175	2,172	
LOCATION	Subgrade	Subgrade	Subgrade	Subgrade	Subgrade	Subgrade
TEST	TS 3 W	TS 3 C	TS 3 E	TS 4 W	TS 4 C	TS 4 E
DEPTH, mm	787.5	775	700	725	725	725
TIME	11:04	11:04	11:04	11:04	10:54	10:54
DATE	8/1/2008	8/1/2008	8/1/2008	8/1/2008	8/1/2008	8/1/2008
TARE NUMBER	16	17	18	19	20	21
WATER CONTENT, w%	16.18	16.41	16.71	15.66	14.46	16.29
LOCATION	Moist. Sensor	Moist. Sensor	Moist. Sensor	Moist. Sensor		
TEST	TS 1	TS 1	TS 2	TS 2		
DEPTH, mm	300	150	437.5	300		
TIME						
DATE	8/1/2008	8/1/2008	8/1/2008	8/1/2008		
TARE NUMBER	22	23	24	25		
WATER CONTENT, w%	16.01	2.17	17.49	3.02		

Table B4. Volumetric moisture content readings from the ML2 probe.

3 ft west of TS1

Can #102

Top of Cylinder from surface = 521 mm

Reading	Volumetric mc (%)	mv
1	30.0	716
2	32.7	765
3	33.2	773
Average	32.0	751

Center of TS 1

Can #101

Top of Cylinder from surface = 483 mm

Reading	Volumetric mc (%)	mv
1	30.7	728
2	30.8	730
3	31.7	748
Average	31.1	735

Center of TS 1 and TS 2

Can #108

Top of Cylinder from surface = 419 mm

Reading	Volumetric mc (%)	mv
1	35.3	808
2	31.6	745
3	32.7	765
Average	33.2	773

Center of TS 2

Can #100

Top of Cylinder from surface = 413 mm

Reading	Volumetric mc (%)	mv
1	29.6	710
2	32.9	767
3	31.2	738
Average	31.2	738

3 ft east of TS2

Can #99

Top of Cylinder from surface = 457 mm

Reading	Volumetric mc (%)	mv
1	35.4	810
2	36.1	821
3	34.5	795
Average	35.3	809

Using the moisture-density collected by the Troxler, the volumetric moisture content was calculated and compared to the moisture sensor data installed in the test sections. The oven dry moisture content is used with the wet density readings from the nuclear gage at the 150 mm and 300 mm depths to calculate the dry density (Equation B3). At these

depths, there tends to be fewer air gaps and surface effects, making the readings more reliable.

$$\rho_d = \frac{\rho}{(1 + \omega)} \quad (B3)$$

The volumetric moisture content may be determined using the dry density (as calculated above) and the oven dry moisture content in Equation B4:

$$\theta = \frac{oven_{mc} \times dry density}{62.4} \quad (B4)$$

The back-calculated volumetric moisture contents, compared with surviving moisture sensors, are given in Table B5.

Table B5. Calculated volumetric moisture contents and corresponding moisture sensor readings.

		Moisture Sensor %Vol	Depth (mm)	Depth Calc %Vol	Depth (in)	Dry Density As Built (kg/m ³)	Depth (mm)	Troxler (kg/m ³)
Test Section 1 150 mm AC / 300 mm Base no grid	Mid-base	BAD	300	4.2	250	2,193	300	2,385
	Top Subgrade	28	600	31.7	400-500	1,826	600	1,850
	Deep Subgrade	30	750	30.3	625-750	1,873	750	1,879
Test Section 2 100 mm AC / 300 mm Base no grid	Mid-base	17	300	4	250	2,143	300	2,220
	Top Subgrade	BAD	600	32.8	400-500	1,833	600	1,844
	Deep Subgrade	46	750	30.7	625-750	1,906	750	1,882
Test Section 3 150 mm AC / 300 mm Base Grid	Mid-base	BAD	300	2.5	250	2,150	300	2,340
	Top Subgrade	28	600	30.5	400-500	1,834	600	1,748
	Deep Subgrade	35	750	28	625-750	1,911	750	1,855
Test Section 4 100 mm AC / 300 mm Base Grid	Mid-base	7	300	3.2	250	2,271	300	2,311
	Top Subgrade	BAD	600	32.2	400-500	1,829	600	1,791
	Deep Subgrade	BAD	750	28.4	625-750	1,895	750	1,823

Soil temperature

The properties of asphalt concrete are susceptible to temperature changes (Roberts et al. 1996), and one goal was to keep the temperatures relatively constant in order to minimize distresses that may result from significant temperature changes. Temperature readings were recorded from 14 December 2005 to 1 August 2008.

The temperature sensors consisted of Type T, copper-constantan thermocouples. The temperature readings were collected by a datalogger every four hours, for a total of six readings per day.. At the completion of construction, 34 of the 40 total temperature sensors were operating, and continued to operate throughout the testing period.

The average daily temperature readings throughout the testing period are plotted for each test section in Figures B15 to B22. The trafficking period for each test window is indicated. In general, the asphalt and soil temperatures remained reasonably stable, between 20 to 23 °C within about ± 3 °C, during the testing. Temperature changes reflect normal diurnal and seasonal fluctuations. An exception to this occurred with a temperature drop between 15 February and 20 March 2007 while trafficking Test Section 1. This temperature decrease was associated with a temporary loss of building heat. Except for the temperature decreases in the winter of 2007, the temperatures remained reasonably constant throughout the trafficking of the test sections and any changes in temperature that occurred had minimal impact on the testing. While trafficking an individual test section, the mid-asphalt temperatures increased by as much as 6 °C. Elevated temperature readings during trafficking were recorded at the mid-base locations. The deep subgrade temperature readings were steady.

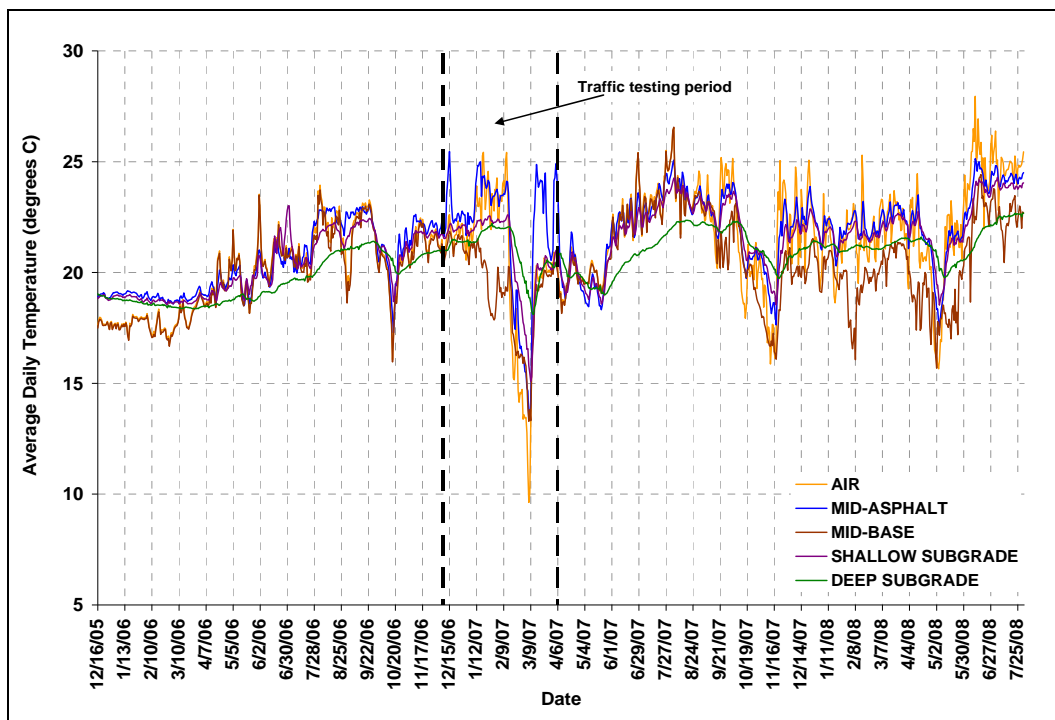


Figure B15. Average daily temperatures for Test Section 1.

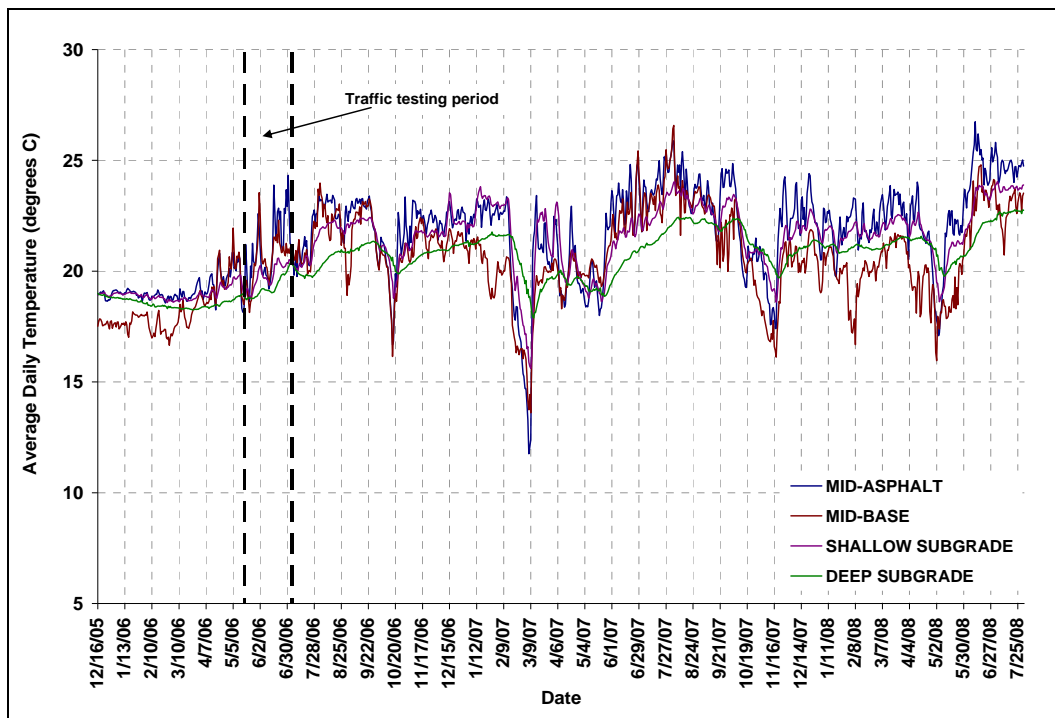


Figure B16. Average daily temperatures for Test Section 2.

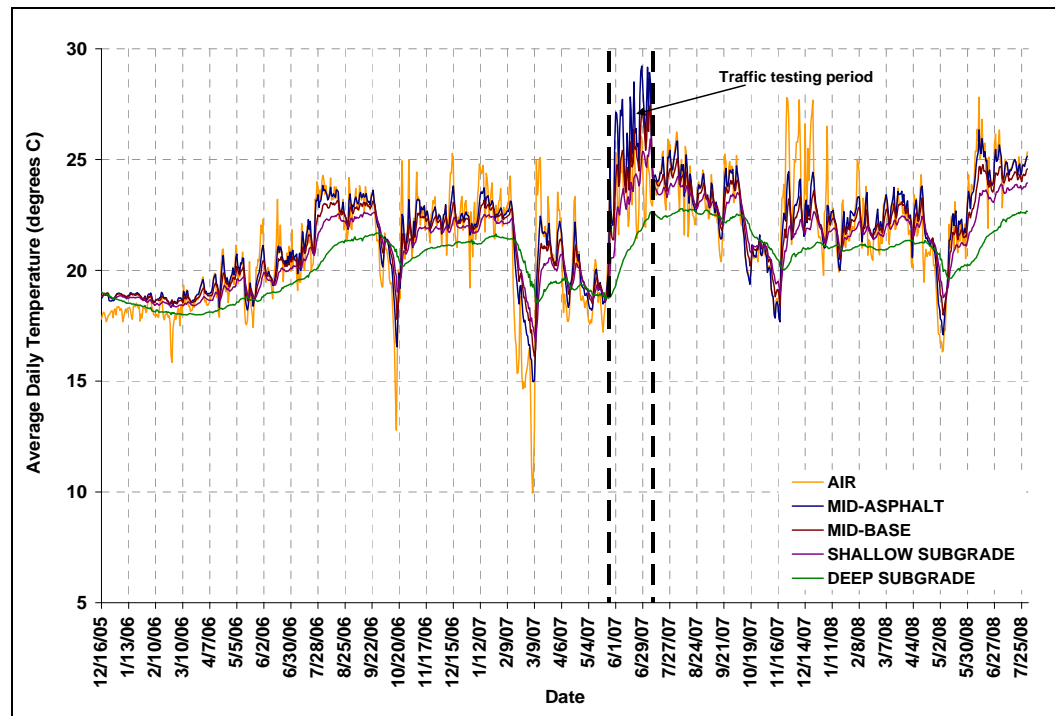


Figure B17. Average daily temperatures for Test Section 3.

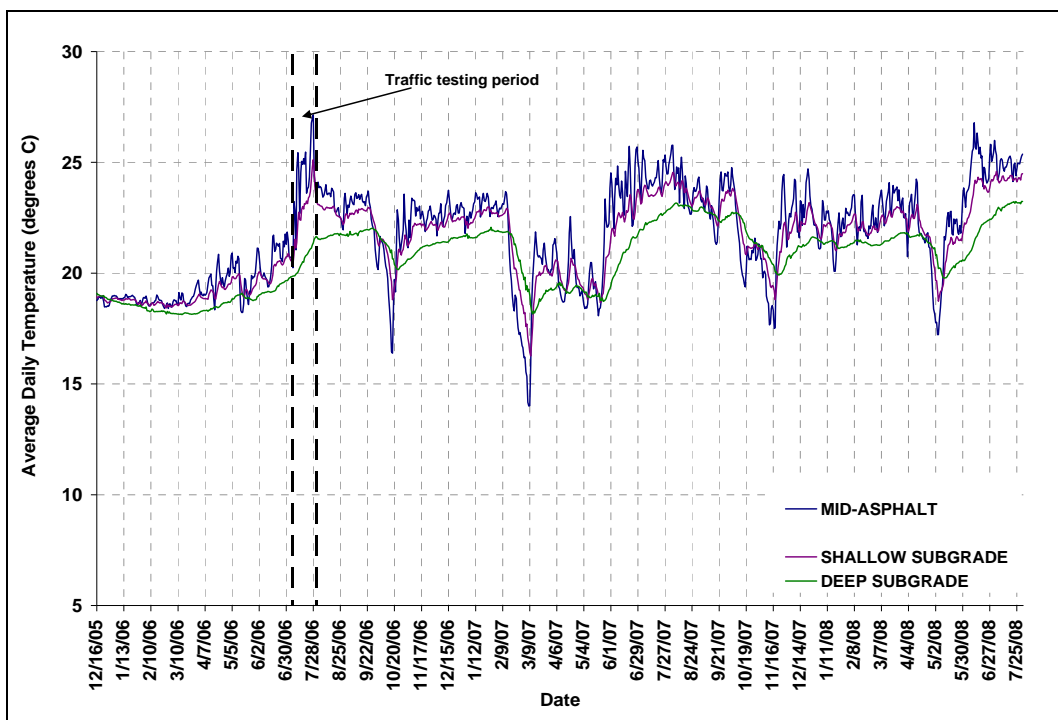


Figure B18. Average daily temperatures for Test Section 4.

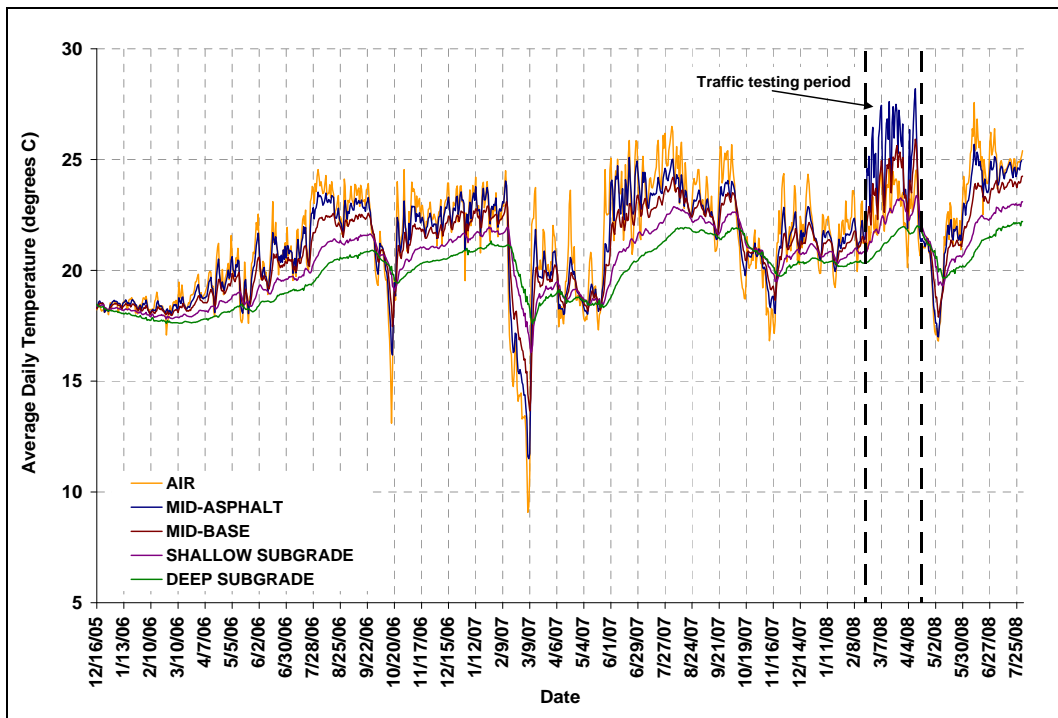


Figure B19. Average daily temperatures for Test Section 5.

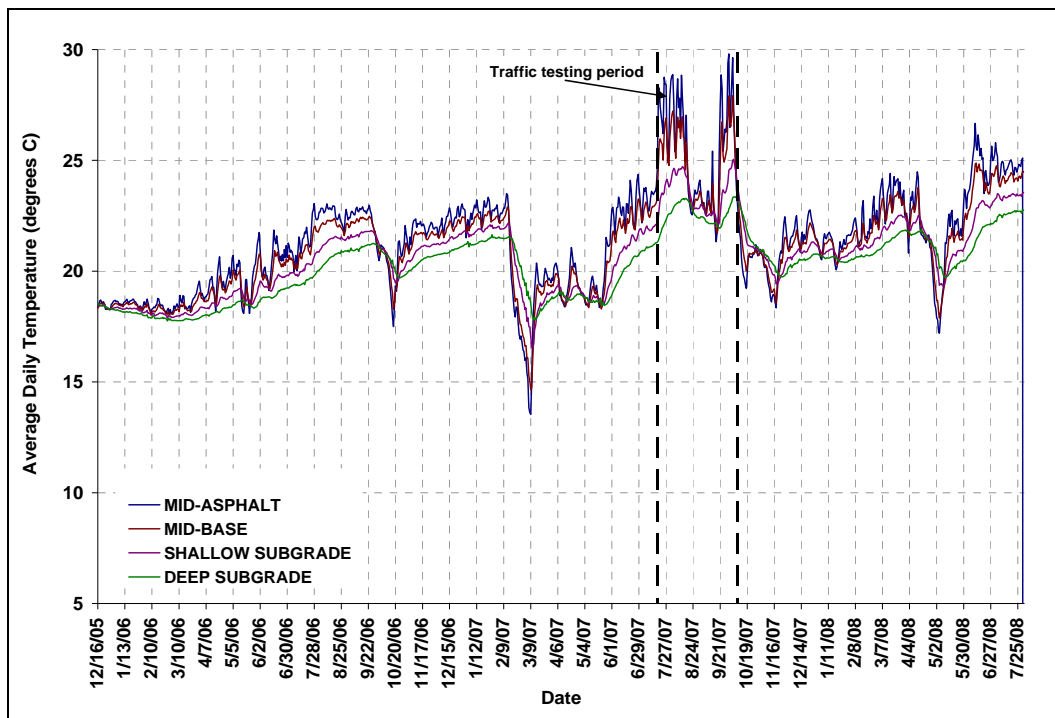


Figure B20. Average daily temperatures for Test Section 6.

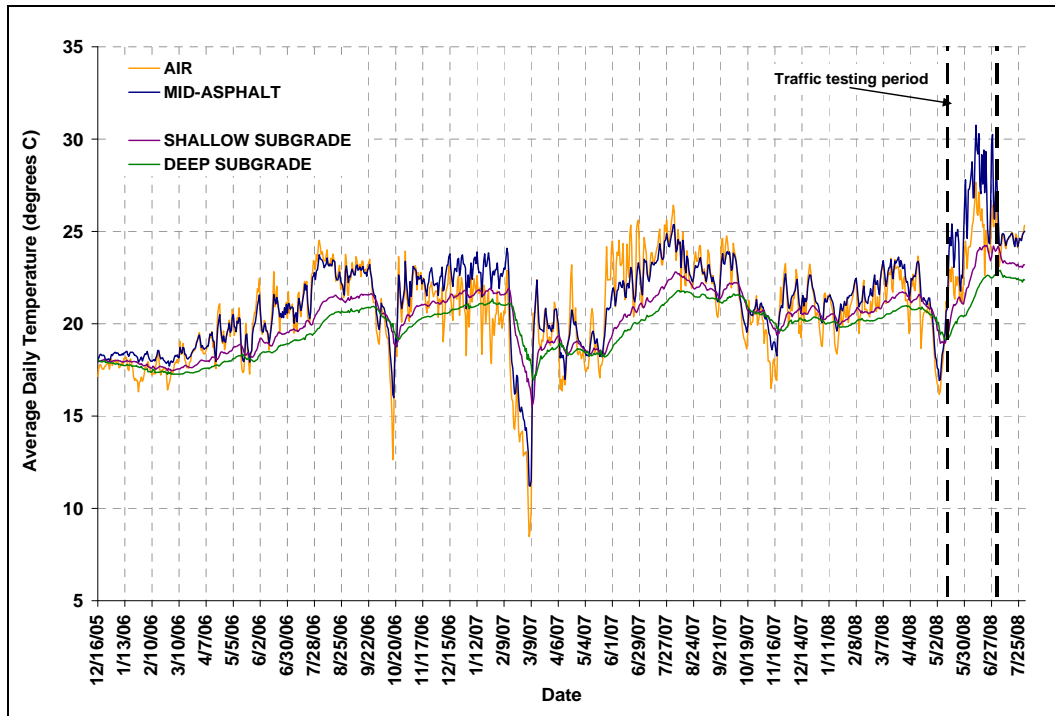


Figure B21. Average daily temperatures for Test Section 7.

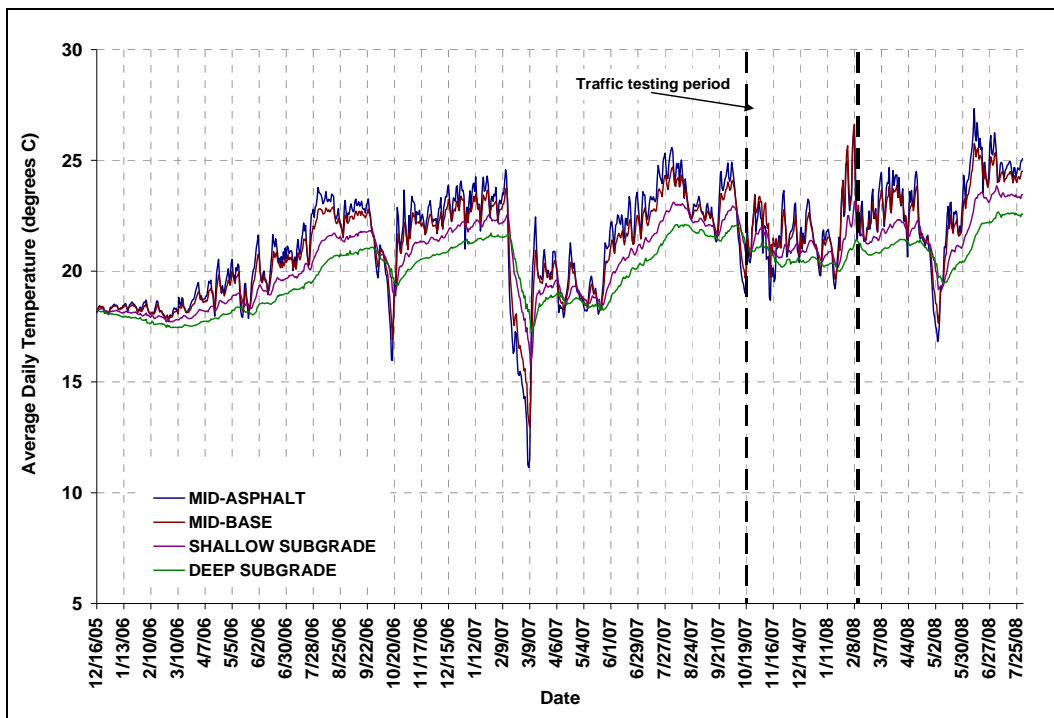


Figure B22. Average daily temperatures for Test Section 8.

Geogrid strain gages

During test section forensics, TS 7 and TS 8 were the only sections with functioning Geogrid strain gages. In these sections, the goal was to carefully excavate down to the Geogrid strain gages, cut the Geogrid around the gages, and record the response. The first step in the forensics process was to record all of the Geogrid strain gages to establish the initial strain readings. Then, the AC layer was cut with a concrete wet saw and then removed with a mini-excavator. While the concrete saw was in operation, the waste water was constantly vacuumed to minimize water seepage into the soil layers. The surface of TS 7 is shown in Figure B23 after cutting the AC layer and the location of instrumentation is noted.

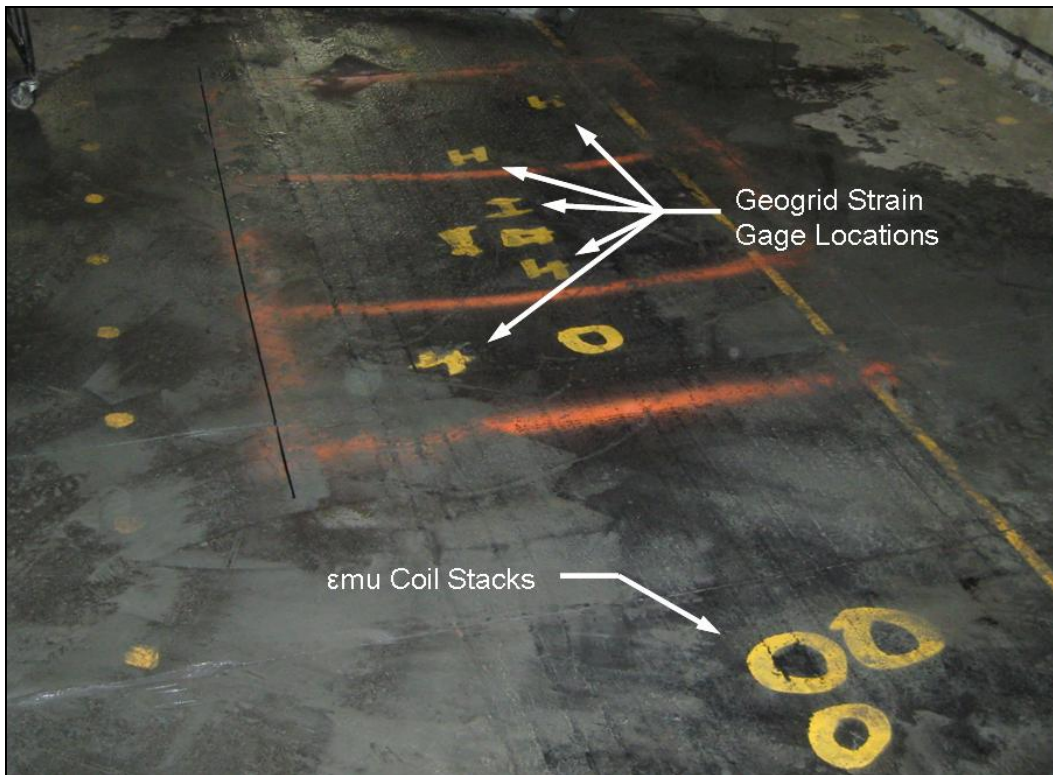


Figure B23. Surface of TS 7 showing instrumentation locations after cutting the AC layer.

The next step was to remove sections of the AC layer to make the Geogrid strain gages accessible. First, a strip of asphalt about 600 mm wide was removed across both TS 7 and TS 8 (left-to-right in Figure B24). Next, sections of asphalt approximately centered over the Geogrid strain gages were removed from TS 7 and TS 8, as shown for TS 7 in Figure B24. These sections had dimensions of about 1500 mm in the x direction and 900 mm in the y-direction.



Figure B24. Mini excavator removing a section of the AC layer in TS 7.

The forensics plan called for most of the base layer to be removed with the mini-excavator. Nonetheless, attempts were made to remove some of the base course by using hand tools, which proved to be very difficult and time consuming, as expected. Thus, the mini-excavator was used to remove a majority of the base course over the Geogrid strain gages, as shown in Figure B25 for TS 7. This was done first on TS 7. Periodic measurements were taken to ensure that the excavator was not digging too deep, but a small piece of Geogrid was accidentally ripped out in TS 7, as shown in Figure B26. This section of Geogrid happened to be where two of the surviving strain gages in TS 7 were located and this caused the gages to fail. No problems were encountered in TS 8.



Figure B25. Mini excavator removing base course in TS 7.



Figure B26. Close-up of Geogrid strain gages removed from TS 7 by the excavator.

The remainder of the base course in each section was carefully removed by hand to fully expose the surviving Geogrid strain gages, as shown in Figure B27 for TS 7. It was necessary to clear the base course around the gages enough to facilitate cutting the Geogrid while minimizing the disturbance to the gages. The strain gages were read immediately before and after cutting the Geogrid around the gages. A close-up view of one of the strain gage pairs attached to Geogrid cut out of TS 8 is shown in Figure B28. Additional readings of the stress-free Geogrid strain gages were also recorded in an effort to quantify the viscoelastic response (creep recovery) of the gages.

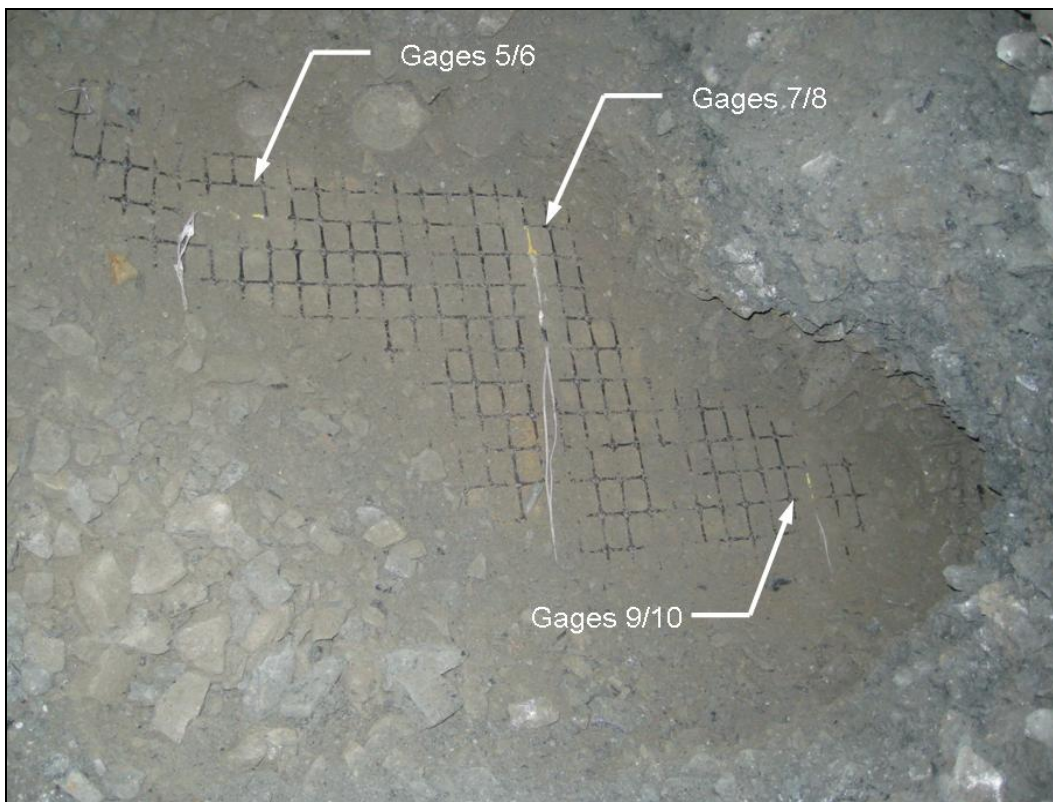


Figure B27. Geogrid strain gages exposed in TS 7.

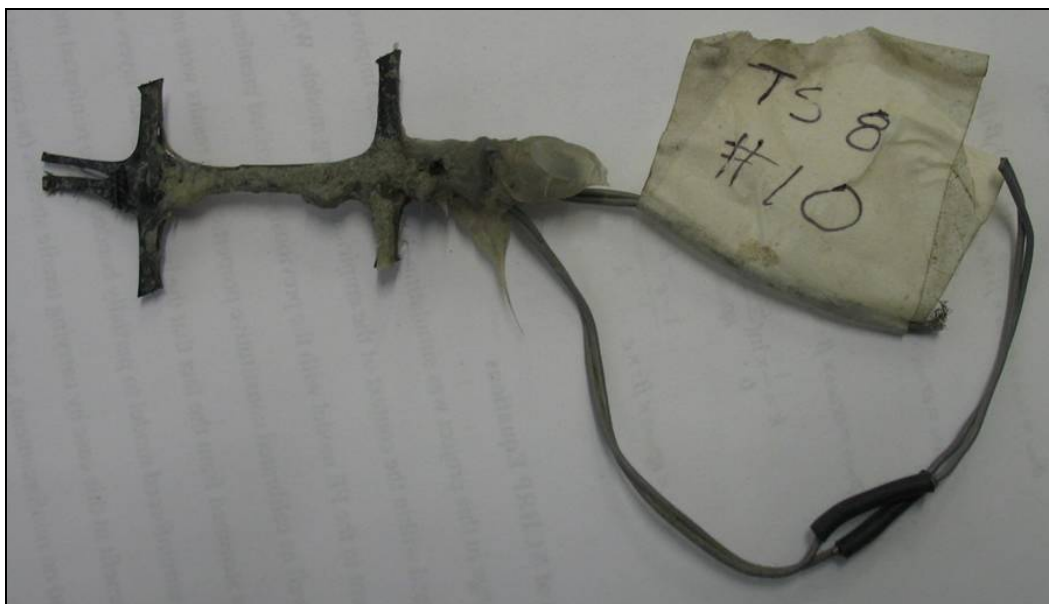


Figure B28. Close-up of Geogrid strain gages hand-cut from TS 8.

The relative recorded strains for all surviving Geogrid strain gages are presented in Figure B29. Gages 3 and 4 in TS 7 produced nearly identical responses for the readings that were obtained prior to gage failure. The removal of the AC layer in TS 7 appeared to have very little effect on these gages, which was also the case for the other gages in TS 7. The removal of the AC layer in TS 8 appeared to cause a significant decrease in strain in one of the two operating gages, while the other was not affected. Removal of the base layer had very little effect on the gages in TS 7 immediately after the base was removed, but significant strain decreases were observed as the gages were read just prior to cutting the Geogrid away. In TS 8, the gages were only read once between removal of the base course and cutting the Geogrid strain gages. For these readings, large decreases in strain were observed in both gages.

Cutting the Geogrid around the gages caused decrease in strain for the three surviving gages in TS 7 with gage 8 indicating the largest decrease and gage 9 indicating the smallest decrease. One of the gages in TS 8 indicated a decrease in strain, while the other indicated an increase in strain of comparable magnitude. The observed increase in strain as the gages were cut free may have been caused by unbending of the geogrid. All of the gage readings that were collected after the gages were cut free represent viscoelastic response (creep recover) of the Geogrid since the Geogrid was in a stress-free state. The viscoelastic response was monitored for less than one day. It is important to note that the viscoelastic

deformations may have accumulated over a period of years. The total relative strains that were observed over the forensics period ranged from about 600 to 2200 microstrains for the five gages that survived to the end.

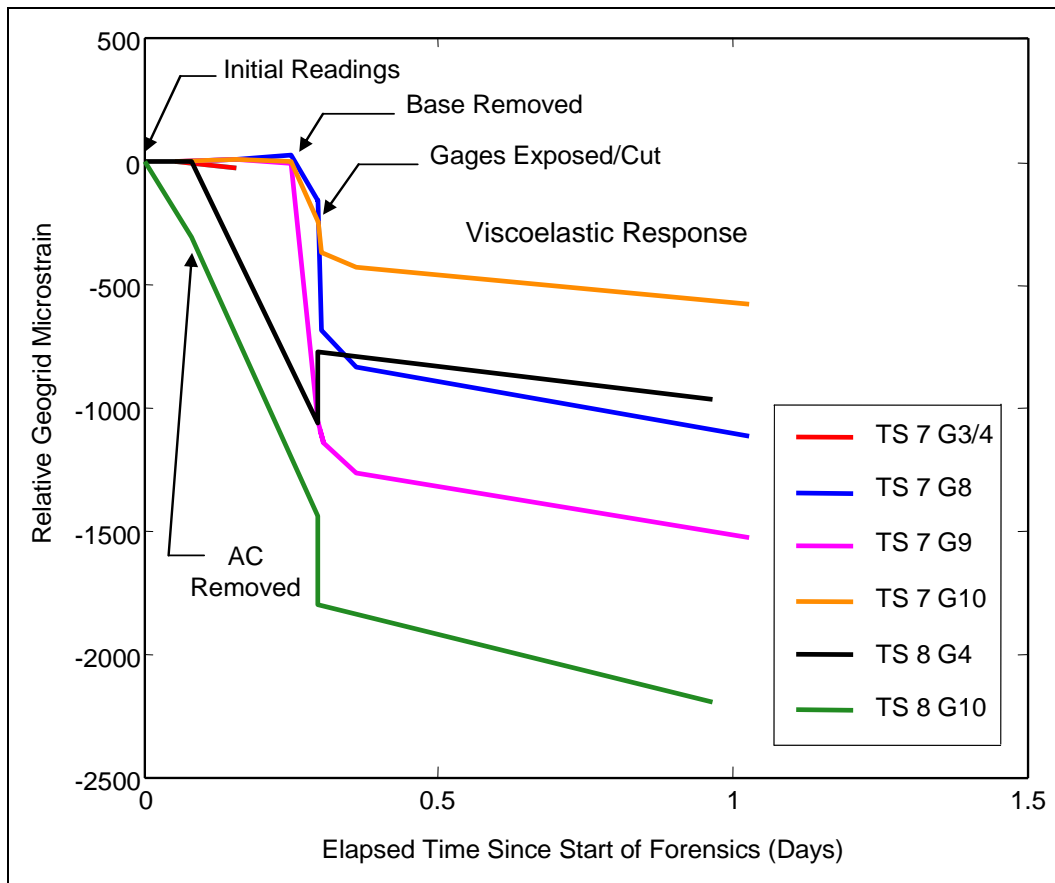


Figure B29. Relative Geogrid forensics strains as a function of elapsed time since the start of the forensics work.

emu coil distances

Another goal for the forensics work was to carefully excavate around the emu coils and physically measure the distance between them. The main reason for doing this was that the sum of the deformations measured by emu coils did not agree well with the measured surface deformations. It was suspected that this discrepancy may have been due to errors in emu coil distance measurements obtained throughout the trafficking period since the surface deformations were accurately measured with a laser profilometer and level surveys. Thus, the physical measurements served as a check on the accuracy of the in-situ emu coil measurements.

The first step in the forensics process was to record all of the unloaded emu coil readings to establish the in-situ measured distances for comparison. First, the asphalt was cut and removed with the mini-excavator to establish a trench measuring about 600 mm wide across Test Sections 1 and 2 and also across Test Sections 3 and 4, as shown in Figure B30.



Figure B30. Trench for measuring emu coil distances and soils properties after removing the AC layer.

After the density, moisture, and other tests detailed previously in this appendix were conducted on the base layer to quantify physical properties, the base layer was removed with the excavator. In-situ soil tests were repeated at the top of the subgrade; about 300 mm deep into the subgrade layer, and a final set of tests were conducted at a total trench depth of 900 mm. After these tests were conducted, the emu coils were carefully exposed by using hand tools, as shown in Figures B31 and B32 for TS 2.



Figure B31. Starting to expose the emu coils in TS 2 using hand tools figure.



Figure B32. Exposed emu coils in TS 2.

After the emu coils were exposed, a caliper was used to measure the vertical distance between the coils in the main stack. It was not possible to measure the horizontal distance between the coils in the main stack and the transverse stack with a caliper due to space limitations. Thus, a pencil was used to place marks on pieces of wood, which were then removed and measured with the calipers. One end of the piece of wood was aligned with the center of an emu coil and a mark was placed at the distance corresponding to the center of the adjacent emu coil, as shown in Figure B33.

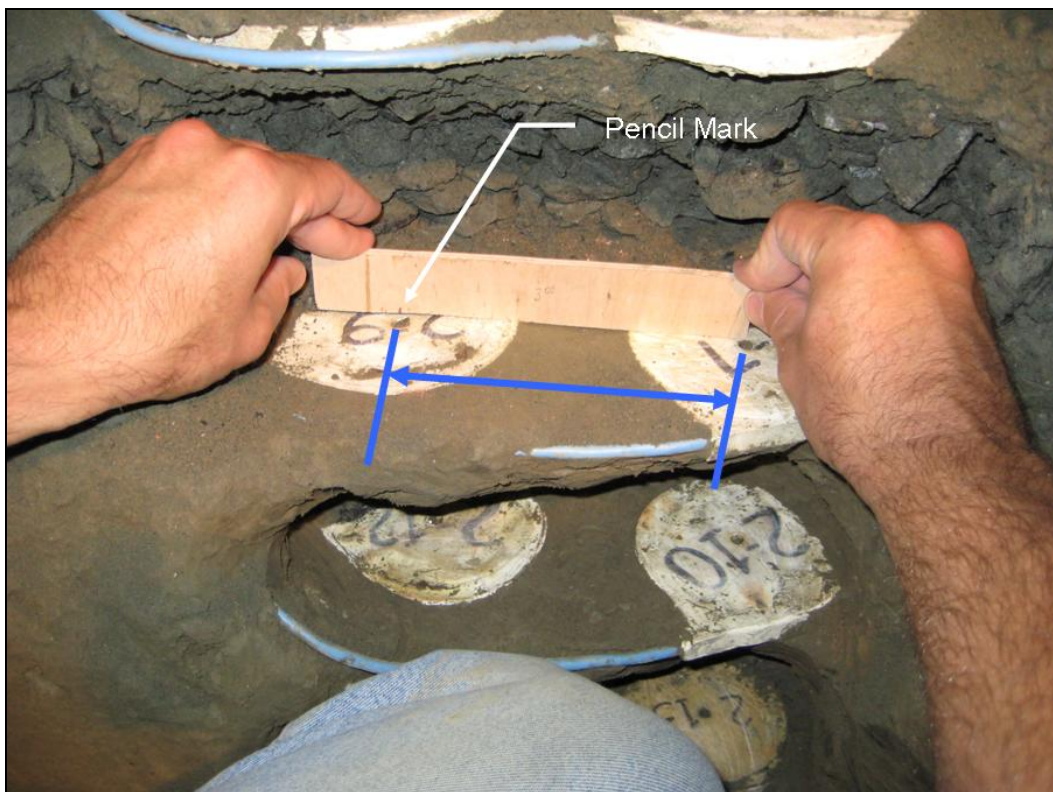


Figure B33. Method of measuring transverse emu coil distances figure.

The distances measured by the in-situ emu coils and those physically measured during the forensics work are presented in Tables B6 to B9. The differences between these measurements are also presented. The difference in vertical distance measurement ranged from 0 to 10 mm, whereas the difference in horizontal distance measurement ranged from 0 to 4 mm, so the horizontal measurements were generally more consistent. The largest difference in vertical measurement for the four sections always occurred in emu layer 2, which corresponded to the lower half of the base layer for these four sections.

The rutting models presented in Chapter 7 were calibrated from relative deformations measured with the emu coils. The differences in measured distances presented in Tables B6 to B9 do not necessarily mean that the relative distances (permanent deformations) were inaccurately measured. However, the data supports the suspicion that the deformations measured by the emu coils contained some error. This could have a large impact on the rutting models if the error was concentrated in a particular material layer since the deformations are broken down by material and the error was equally distributed through the depth of the pavement system in the adjustment process.

Table B6. Summary of emu layer measurements and errors for TS 1.

Emu Layer	Vertical Measurement (mm)			Transverse Measurement (mm)		
	In-situ	Physical	Difference	In-situ	Physical	Difference
0	180	177	3	--	--	--
1	143	143	0	--	155	--
2	177	170	7	159	156	2
3	123	125	-2	159	158	1
4	142	143	-1	157	161	-4
5	160	164	-4	160	158	2
6	--	--	--	153	151	2

Table B7. Summary of emu layer measurements and errors for TS 2.

Emu Layer	Vertical Measurement (mm)			Transverse Measurement (mm)		
	In-situ	Physical	Difference	In-situ	Physical	Difference
0	121	120	1	--	--	--
1	148	149	-1	--	155	--
2	149	159	-10	158	155	3
3	124	122	2	161	163	-2
4	149	148	1	164	162	2
5	156	163	-7	160	158	2
6	--	--	--	153	152	1

Table B8. Summary of emu layer measurements and errors for TS 3.

Emu Layer	Vertical Measurement (mm)			Transverse Measurement (mm)		
	In-situ	Physical	Difference	In-situ	Physical	Difference
0	217	215	2	--	--	--
1	130	132	-2	--	148	--
2	165	157	8	157	153	4
3	123	124	-1	155	152	3
4	142	147	-5	153	150	3
5	157	156	1	160	160	0
6	--	--	--	157	153	4

Table B9. Summary of emu layer measurements and errors for TS 4.

Emu Layer	Vertical Measurement (mm)			Transverse Measurement (mm)		
	In-situ	Physical	Difference	In-situ	Physical	Difference
0	137	136	1	--	--	--
1	141	137	4	--	159	--
2	145	151	-6	158	158	0
3	133	133	0	158	156	2
4	144	146	-2	159	156	3
5	151	156	-4	157	154	3
6	--	--	--	155	154	1

Asphalt layer thickness

The asphalt layer is generally the stiffest layer in a pavement system, as was the case for the test sections of this study when subjected to traffic cycles. It is also the section that is subjected to the largest stresses due to the applied wheel loads. The thickness of the AC layer was taken as the nominal thickness for all FWD, FE, and rutting model analyses in this study, which was either 100 or 150 mm, depending on the test section. Relatively small variations from the nominal thickness due to construction tolerances can affect the asphalt layer more than other layers because it represents a larger percentage of the total layer thickness. Thus, another goal of the forensics work was to investigate the validity of the assumption of nominal layer thickness by physically measuring the thickness of the asphalt layer where possible.

The results of this work are presented in Figure B34 for TS 1, 2, 7, and 8. The vertical dashed lines represent the boundaries of the testing windows

where wheel loads were applied and SLTs were conducted. The profiles in the figure were taken across adjacent test sections. The nominal thicknesses are also indicated by horizontal dashed lines for comparison. It is apparent that the measured asphalt thicknesses were generally much larger than the nominal thicknesses, sometimes by up to 25 mm (25% of the nominal 100 mm thickness). Thus, the assumption of nominal AC layer thicknesses in the models of this study may not have been accurate. It is important to consider that these profiles were only taken from one point along the length of each test section, so they may not represent the average AC layer thickness along the length of the sections. Ultimately, there is not enough justification to warrant the consideration of thicknesses other than the nominal values in the models of this study, although this should be considered when examining the results.

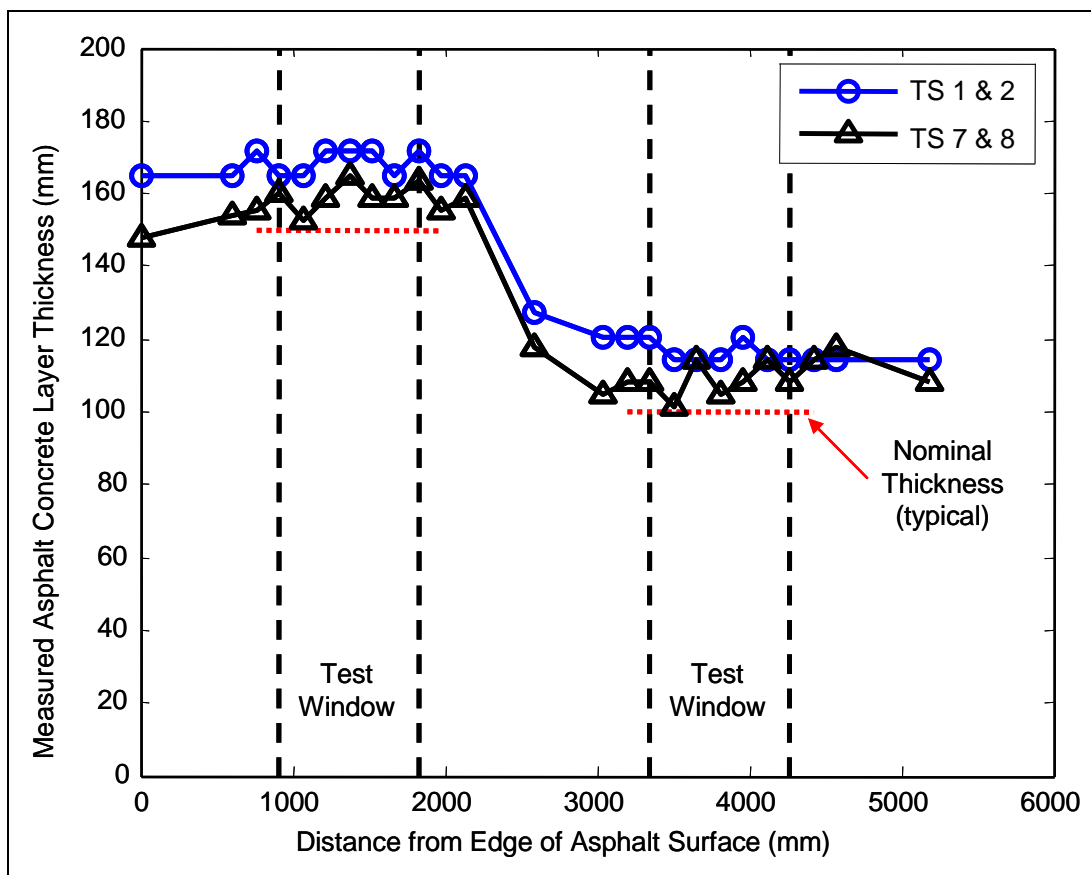


Figure B34. Measured and nominal AC layer thickness profiles for TS 1, 2, 7, and 8.

References, Appendix B

Troxler Electronic Laboratories, Inc. (2003) Model 3440 Surface Moisture-Density Gauge, Manual of Operation and Instruction. 3008 Cornwallis Road, Research Triangle Park, NC 27709. Available at: www.troxlerlabs.com

U.S. Air Force (2002) Airfield Pavement Evaluation Standards and Procedures, Engineering Technical Letter 02-19, Department of the Air Force, Headquarters Air Force Civil Engineer Support Agency.

Appendix C – Geogrid and Asphalt Viscoelasticity

Geogrid viscoelasticity and unit stiffness

The Geogrid in this study was made of polypropylene, which is highly viscoelastic, so it was important to establish the role that creep and relaxation played in overall pavement response. Although the finite element models conducted in this study are based on short-term static wheel loads and do not include viscoelastic effects, quantifying the creep and relaxation response of the Geogrid provides valuable information for future work that considers long-term Geogrid stresses and strains. Creep and relaxation of the grid can result in deformations (strains) that are not associated with increasing loads, so it is important to quantify this effect. Helstrom et al. (2006) concluded that creep deformations may have been responsible for the apparent increase in force per unit width over time observed in their study. They performed one laboratory creep test with a constant load magnitude representative of about 100-150% of the maximum load observed in their field test sections. To expand upon this work, and examine stress-dependency, two more creep tests were performed at approximately 50% and 150% of the load used by Helstrom et al. (2006).

Laboratory Geogrid creep testing

A creep testing frame was constructed out of stud-grade lumber in order to utilize the steel grips previously used for Geogrid creep testing by Helstrom et al. (2006), of which each consisted of two back-to-back 50x25x4.8 mm channel sections. The steel grips were 1500 mm long and were connected by bolts spaced at 150 mm on center. The creep testing frame and steel grips are shown in Figure C1.



Figure C1. Photo of Geogrid creep test setup.

Tests were conducted at the Advanced Manufacturing Center (AMC) laboratory at the University of Maine. This site was chosen because the climate was controlled. A piece of Tensar BX1200 geogrid, measuring 1220 mm in length, was bolted into the channel section grips spaced at 568 mm. It was positioned so that the load was applied in the cross-machine direction. A new piece of Geogrid that had never been previously loaded was used for each test. A thick layer of epoxy, manufactured by West System Inc. of Bay City, Michigan, was spread on both of the channel sections to thoroughly encase the geogrid. The grips were then immediately bolted together, which was completed before the epoxy pot-life had expired. Number 105 epoxy resin was combined with Number 206 hardener in a 5:1 ratio, respectively, and then Number 404 high-density filler was added until the epoxy had a consistency thick enough to fill the gaps between the channel sections and remain there until the epoxy cured. The epoxy was allowed to cure for at least 24 hours at a temperature of approximately 22°C prior to any load being applied. This was sufficient to restrain the Geogrid such that it did not slip out of the grips during testing.

Steel weights were suspended from the center of the bottom grip, subjecting the specimens to a constant tensile load for a total of 9 weeks. Deflections were measured using a pair of dial gages, accurate to 0.0025 mm, which were linked to the top grips using threaded steel rods. The average of the pair of dial gages was used to cancel the effect of rotation of

the bottom grip that occurs when loading. An aluminum plate square was attached to each bottom grip to contact the tip of the dial gage. A small hole just large enough to cradle the tip was drilled into each plate, which prevented lateral movement during the test. One of the two gages can be seen in Figure C2.



Figure C2. Close-up of dial gage used in creep test.

The lower load level test was conducted during the winter of 2005-2006 with an average tensile load per unit width of 0.887 kN/m. The upper load level test was conducted during the summer of 2006 with an average tensile load per unit width of 2.49 kN/m. Temperatures were recorded during the test period, since the Geogrid creep response is temperature-sensitive.

Both dial gages were read manually throughout testing. The first set of readings was taken just before loading, and then immediately after all the weights were applied, a process which took about 2 minutes and 4 minutes to complete for the lower load and upper load, respectively. The difference between the dial gage readings over this time span was considered to be the instantaneous deflection, while all remaining deflections were considered to be the result of creep. Gages were read more frequently at the beginning of the test in an effort to accurately capture the initial rapid creep response. The results are shown in Figure C3.

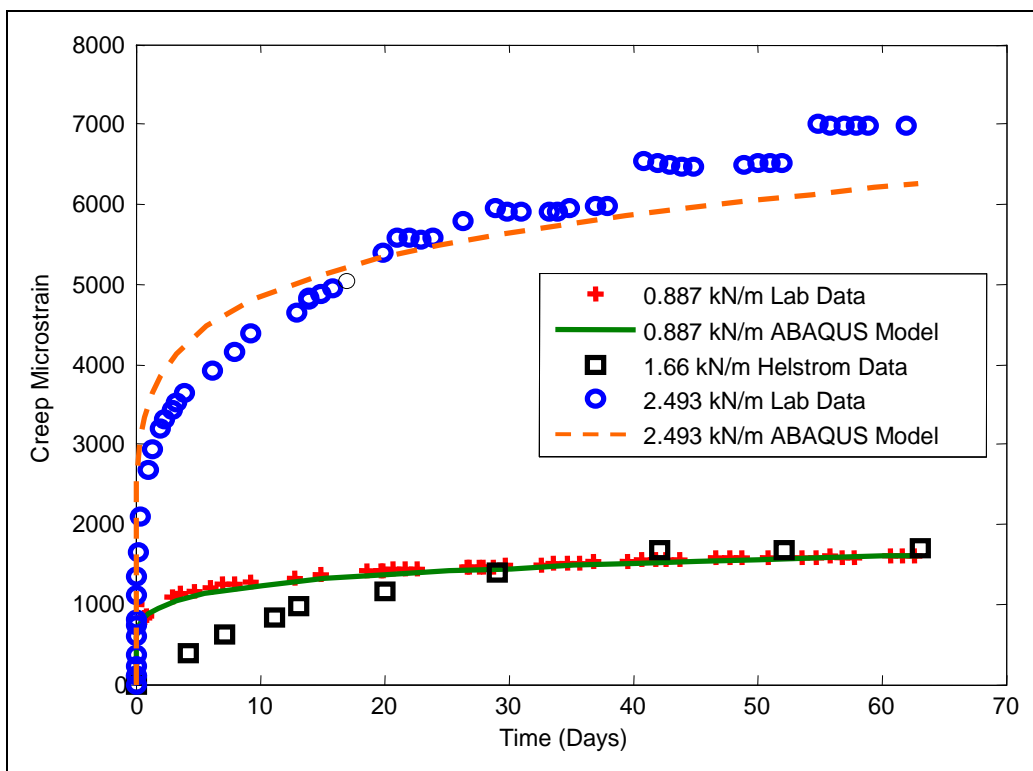


Figure C3. Geogrid creep microstrain over time.

It is apparent that there is a discrepancy between the results in this study and the results reported by Helstrom et al. (2006). One possible cause of the discrepancy is that Helstrom et al. had previously used their Geogrid creep specimen for calibrating strain gages at loads over three times larger than that used in the creep test, which may have affected the creep response.

The strain data from the upper load level test exhibited some obvious “jumps,” which was lacking in the lower load data. Each of these corresponded to times where the temperatures were up to about 8°C above average. The creep strain and temperature data for the lower load and upper load are shown in Figures C4 and C5, respectively, where the temperature axes are equal in both plots. It was apparent that the temperatures were much more erratic during the upper load test, and had a significant effect on the data.

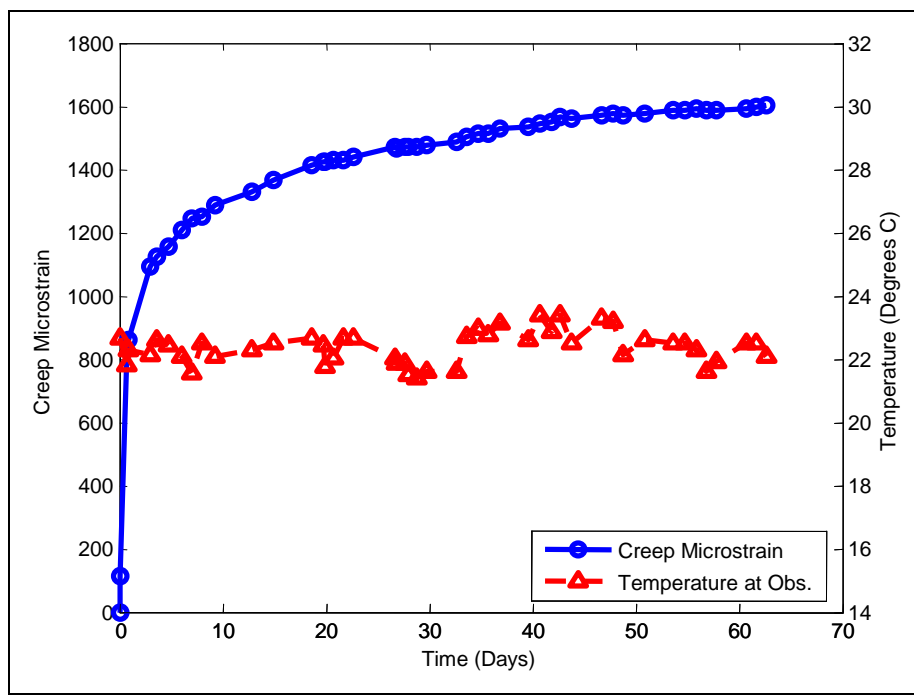


Figure C4. Lower load creep strains and temperatures.

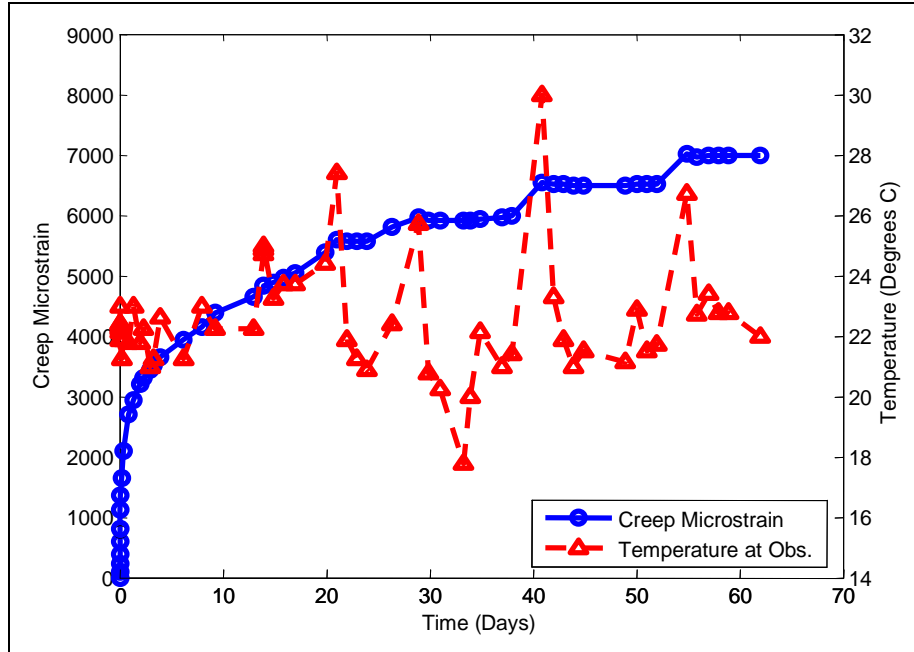


Figure C5. Upper load creep strains and temperatures.

The instantaneous Geogrid deflection, discussed previously, was further broken down into two components. The first component was considered to be slack in the specimen, which may have resulted from the specimen being rolled up prior to testing or other factors. The second component of

the instantaneous deflection was considered to be the true elastic deformation due to the applied load.

ASTM D6637 allows the slack to be removed for the calculation of elastic unit stiffness if desired. According to ASTM D6637, the slack displacement can be identified by examining the behavior of the load-displacement curve, assuming a sufficient number of data points exist. Since the primary purpose of the testing conducted in this project was to examine creep behavior and not to establish the elastic modulus, no data points were collected between zero load and full load, so another approach was used to estimate the slack displacement. The applied weights remained on the Geogrid for about nine weeks, so the Geogrid was considered to be in a slack-free state at the end of this time. When the weights were removed, the Geogrid rebound was thus considered to be entirely elastic. The difference between the relative deformation due to the application of the weights and the relative deformation due to the removal of the weights was considered to be slack. The Geogrid elastic modulus in the cross-machine direction was estimated with and without slack, as shown in Table C1. Clearly, as the load magnitude was increased, the effect of the initial slack was decreased, but the unit stiffness calculated at both load levels was affected. The fact that the moduli computed during unloading with the slack removed were within a few percent of each other at both load levels provided confidence that these were reasonable values.

Table C1. Effect of slack on Geogrid cross-machine direction unit stiffness calculations.

	Unit Stiffness, kN/m	
	Lower Load	Upper Load
Slack Included	483	712
Slack Removed	910	934

The stress-strain curve for polypropylene Geogrid is nonlinear. The effective modulus of elasticity is highest at low strain levels, and progressively drops as the strains increase. The modulus of elasticity of the Geogrid in the machine direction was specified as 450 kN/m at 2% strain (Tensar 2005), but dropped to 392 kN/m at 5% strain (Tensar 2005). It is important to note that Tensar did not subtract the initial slack from their strain measurements, so their reported elastic modulus values were consequently lower than those allowed by ASTM D6637 (2001). Further,

the strains in the Geogrid in this study were smaller than 2%, so it was not surprising that the measured modulus of elasticity (slack removed) was higher than that reported by Tensar.

This was an important consideration for choosing the elastic modulus of the Geogrid in the finite element model. The modulus with slack removed, as measured by UMaine, was appropriate for this study since the slack is assumed to be removed with the placement and compaction of the base and asphalt concrete (AC) layers. Therefore, the response of the Geogrid due to traffic loads would be unaffected by the initial slack. For simplicity, the unit stiffness values were taken as 900 kN/m in the XMD and 600 kN/m in the MD for the remainder of this study, which are both double the values reported by Tensar (2005), but less than the cyclic moduli values of 1114 kN/m and 835 kN/m, respectively, reported by Perkins et al. (2004). The MD modulus was not measured, so the ratio between XMD and MD moduli reported by Tensar (2005) was retained.

Finite element creep model

The goal of the creep test was to subject the Geogrid specimen to a constant tensile load (kN/m) over the duration of testing and measure permanent deformation. The steel grips were relatively stiff, but bending deformations still occurred that rendered the stress state in the Geogrid non-uniform. Further, as the Geogrid experienced creep, the stress distribution constantly changed during the test. The ‘stress’ (load per unit width) contours were generated within a simulation of the creep test using the commercially available FE package ABAQUS (HKS, Inc. 2004), which has several available creep models. The units for the contour shading have been manually entered for ease of visualization. The development of the ABAQUS model used to generate the results in Figures C6 and C7 is now discussed in greater detail.

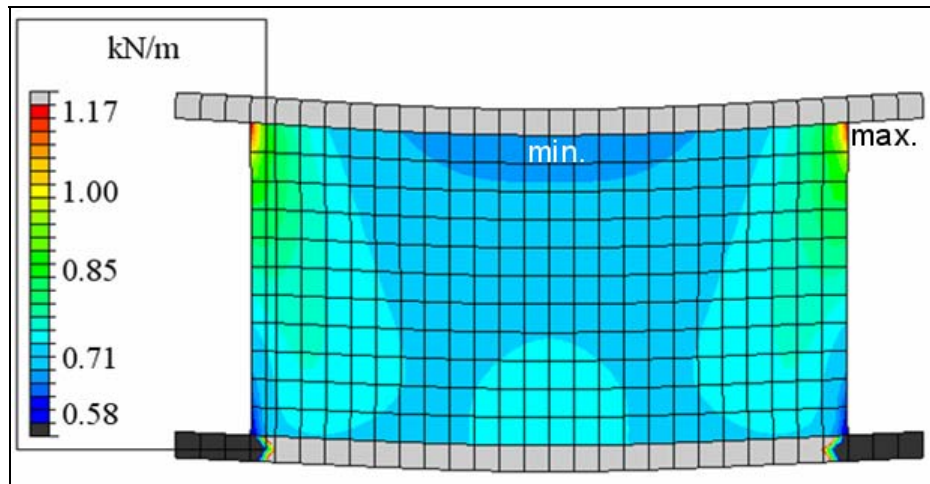


Figure C6. Von Mises 'stress' contours in Geogrid at start of creep test.

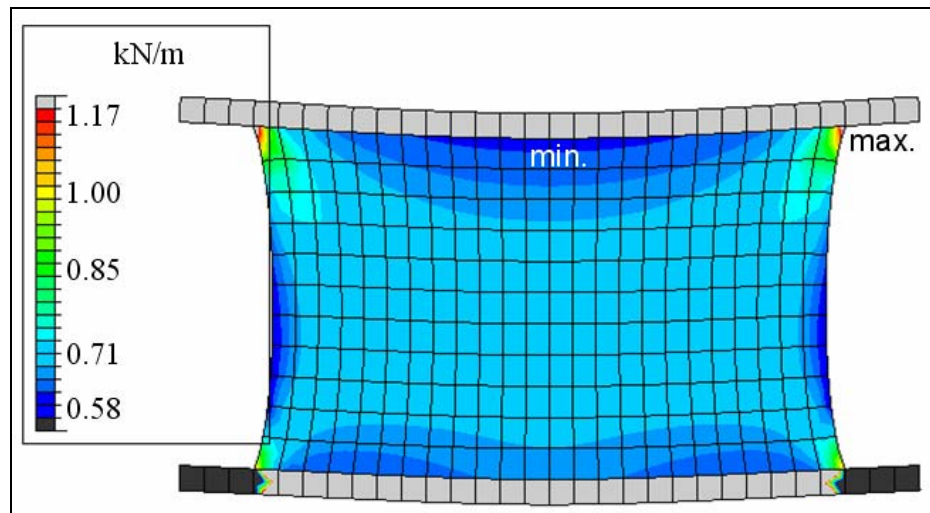


Figure C7. Von Mises 'stress' contours in Geogrid at end of creep test.

The first step was to choose a creep model that was applicable to the problem at hand. ABAQUS had several available creep models that are based on metal creep behavior. Of these, the power law model was chosen for this study for its relative simplicity. This creep law is used to model secondary or steady-state creep. The power law model is further divided into two forms: the time-hardening version and the strain-hardening version. The time-hardening version is more suitable when stresses remain relatively constant over the analysis period, whereas the strain-hardening version is more suitable when stresses vary. For either model, the stresses should be relatively low, particularly with respect to stress concentrations. Since the laboratory test consisted of a constant load over the analysis duration, and other requirements are satisfied, the time-hardening version of the power law model was chosen. It has the form

shown below in Equation C1, where ε_c is the uniaxial equivalent creep strain, q is the uniaxial equivalent deviatoric stress, t is time (taken as days), and A , n , and m are calibration constants. The uniaxial equivalent deviatoric stress, q , was simply taken as von Mises equivalent stress within ABAQUS since isotropic creep behavior was assumed.

$$\frac{d}{dt} \varepsilon_c = A \cdot q^n \cdot t^m \quad (\text{C1})$$

A two dimensional finite element model was selected to replicate the creep test setup. A zero vertical displacement boundary condition was applied to each bottom corner of the top grip, as well as one zero horizontal displacement to prevent rigid body motion. The steel grips were modeled with 8-noded quadratic shell elements, where the thickness was specified such that the internally calculated moment of inertia was equivalent to the actual moment of inertia for the pair of channel sections bending about the strong axis. The Geogrid was modeled with 8-noded membrane elements that were given lamina (plane stress version of orthotropic) material properties and a unit thickness. The respective loads used in the laboratory tests were applied to the bottom center of the bottom steel grip as point loads.

The three unknown calibration constants for the Geogrid creep model, shown in Equation C1, were determined by comparing the relative displacements between the bottom of the top grip and the top of the bottom grip over the testing period. The least squares error, φ , was minimized using the nonlinear objective function shown in Equation C2 below, where num_pts is the number of time points selected by ABAQUS to solve the problem, t_i is the time (days) corresponding to the i th point, δ_{lab_i} is the laboratory measured relative displacement linearly interpolated at t_i , Δ_{fe_i} is the FE-predicted relative displacement at t_i , and the other terms were previously defined.

$$\varphi(A, n, M) = \sqrt{\sum_{i=1}^{\text{num_pts}} (\delta_{\text{lab}_i} - \Delta_{\text{fe}_i}(A, n, m, t_i))^2} \quad (\text{C2})$$

The creep model was initially calibrated to the lower load only, and then used to predict the response of the upper load test, which resulted in reasonable agreement. However, the best fit was achieved by calibrating to the upper and lower data simultaneously. The final calibrated model is

shown in Equation C3 below, where all terms were previously defined and units were added such that the strain is unit-less, and it is presented in terms of strain rather than strain rate.

$$\varepsilon_{cr}(t, q) = 0.0013705 \left(\frac{t}{\text{day}} \right)^{0.13} \cdot \left[\frac{q}{\left(\frac{kN}{m} \right)} \right]^{1.3} \quad (\text{C3})$$

The creep model results shown in Figure C6 are based on Equation C3. The strains were calculated from the displacements that were output from the FE model. It was clear that the model was able to match the laboratory data reasonably well, which includes the stress-dependency of creep. The laboratory data for the upper load test at large time values were underpredicted, but this was believed to be due to the short periods of above-normal temperatures.

Asphalt concrete viscoelastic effects

The properties of the asphalt concrete (AC) material used in this study were time-dependent. Since the FE models in this study were calibrated from data obtained in static load tests, the effective elastic modulus of the asphalt was quantified through laboratory testing at UMaine, which is described in this section.

Details of specimens and test protocol

Four asphalt cores were taken from Test Sections 2 and 4 after trafficking was completed and were used to determine the effective asphalt modulus representative of the SLTs. The cores were taken away from the trafficked area to represent the initial undisturbed conditions. The properties of the asphalt cores are shown in Table C2, where the values represent the average of three measurements.

Table C2. Properties of asphalt core specimens.

Specimen	Thickness (mm)	Diameter (mm)	Gage Length 1 (mm)	Gage Length 2 (mm)
1	106.1	145.2	58.0	58.3
2	110.4	145.8	59.0	59.5
3	112.8	145.0	56.4	59.1
4	117.7	145.7	57.4	58.0

The cores were tested in compression at approximately the same load rate used in the SLTs. The applied compressive stress was taken as the tire pressure 0.69 MPa. The cross-sectional areas of the asphalt cores were smaller than the contact area of the actual dual tire, so the total load required to produce this stress was about 11.5 kN, as compared to 48.9 kN with the full contact area. The rate of loading was fixed at 11.5 kN per minute, such that it took 60 seconds to ramp up the load. The load was then held at 11.5 kN for two minutes to examine the change in asphalt modulus that occurred over the approximate time required to read all the emu gages.

Naturally, the tops of the asphalt cores were smooth and bottoms were rough. Two of the four specimens had relatively even bottoms, while the other two had distinct peaks, such that they rocked back and forth on a table with a gentle force. A saw was not available to remove the rough area, so 12.5 mm thick neoprene pads were placed on both ends of the specimens during testing in an effort to create a uniform stress distribution.

Testing was performed on an Instron Model 8874 Axial Torsion Fatigue Machine, which has a maximum capacity of 25 kN. Both load and extension data were collected by a data acquisition system at a frequency of 5 Hz. The displacements recorded by the Instron included the displacements in the neoprene pads, the displacements due to end roughness, and the desired displacements due to a uniform stress, so these were not useful values. Linear variable displacement transducers (LVDT) were used to measure the compressive deflections only in the uniform portion of the asphalt samples. Two LVDTs were attached to each sample on opposite sides of the specimen. The measured deflections were averaged to reduce the effect of non-uniform compression. The LVDTs were capable of measuring deflections in increments as small as 1.5×10^{-4} mm and 4.1×10^{-4} mm, respectively, which implied an accuracy of about plus or minus 0.03% or 0.08%, for the maximum measured deflection, which was acceptable for the purpose of this test. Figure C8 shows an instrumented asphalt core in the test machine.



Figure C8. Asphalt core testing setup.

The LVDTs were attached by fixed gage clamps to bolts that were bonded to the upper portion of the specimen with epoxy. Heavy duty plastic L-brackets were attached to the bottom portion of the specimen to contact the ball-point end of the LVDT. The position of the LVDT was manually adjusted such that it was within its working range.

Effective AC modulus results

The temperature was held constant at 21°C for all tests. The first test produced lower modulus values than the remaining tests. This may have been because the specimens were not given enough time to fully rebound before subsequent loads were applied. The tests were performed back-to-back for each specimen, with the rest period being just long enough to reset the Instron and setup a new file for the data.

The specimens were tested until failure. Failure was defined as the presence of a crack or cracks, primarily in the vertical direction, indicating that the stiffness of the specimen had degraded. An example of specimen failure due to cracking is shown in Figure C9. This was verified by analyzing trends in the data, and removing excessively low values from the average modulus calculations.



Figure C9. Typical asphalt core specimen failure.

With the exception of specimen number 4, which failed before the full load could be reached, all the specimens performed consistently, as shown in Table C3 for the secant modulus after 60 seconds. Specimens 1 and 3 failed during the last test listed in the table, although the secant modulus values were consistent with previously recorded values. The epoxy bond between the bolts and the asphalt core, described above, failed on Specimen 2 after five load tests, so this specimen was re-tested the next day after a new layer of epoxy had cured. This data is indicated with an asterisk in Table C3. It failed after six tests on the second day. The first and last values for all tests were excluded from calculations, which are reflected in the averages shown in Table C3. The average AC secant modulus over time for all thirteen valid tests is shown in Table C3. The two moduli that represent the range of times corresponding to the SLTs are also shown in Figure C10.

Table C3. Summary of asphalt secant modulus results after 60 seconds.

	Specimen Number				
	1	2	2*	3	4
Test Number	Secant Modulus after 60 Seconds (MPa)				
1	162	101	194	131	79
2	231	217	275	236	98
3	219	266	258	240	--
4	177	231	236	218	--
5	184	247	193	--	--
6	169	--	209	--	--
Average	203	238	241	238	--

* These tests were conducted one day after the others.

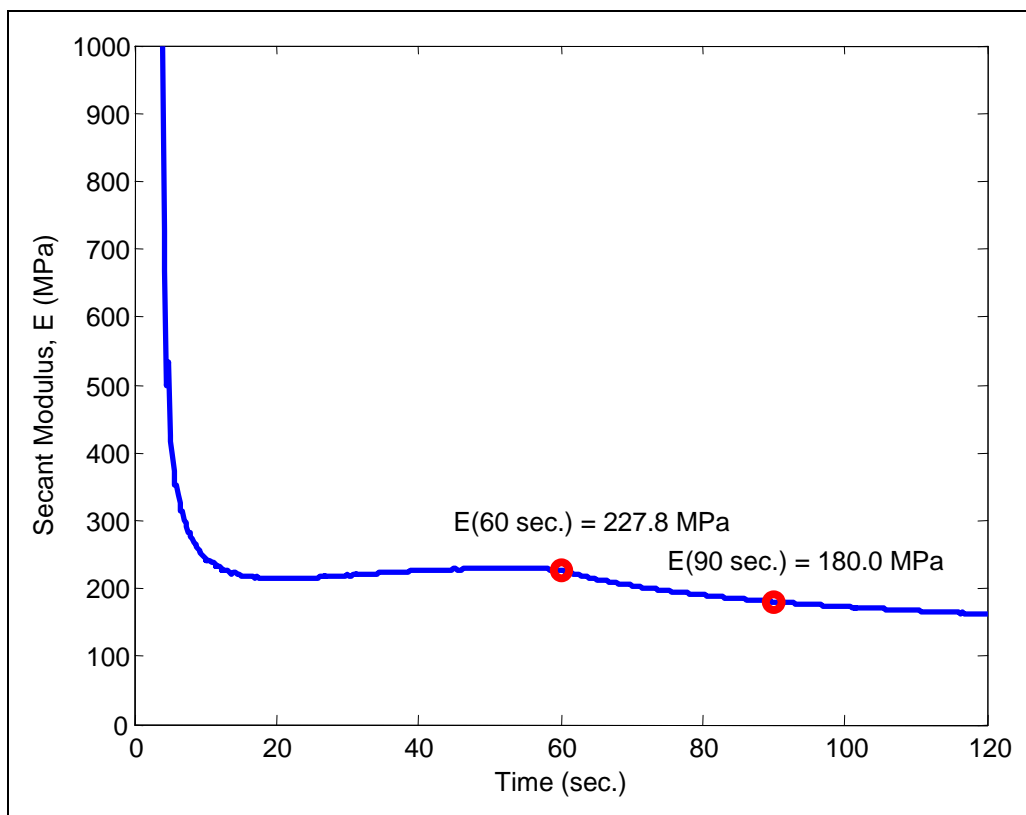


Figure C10. Example of measured asphalt core average secant modulus over time.

Since this test was based on the load being ramped over 60 seconds, the value of 228 MPa for effective secant modulus after 60 seconds was considered to be the effective SLT modulus measured by UMaine. It is important to note that these tests were performed with zero confining stress on the asphalt specimens, so the in-situ modulus may have been larger. However, it is worth noting that both the standard resilient modulus test and dynamic modulus laboratory tests are also conducted on unconfined specimens, but the effect of confinement may be more pronounced at slower load rates due to viscoelastic effects.

References, Appendix C

- Helstrom, C.L., D.N. Humphrey, and J.M. Labbe (2006). "Performance and Effectiveness of a Thin Pavement Section Using Geogrids and Drainage Geocomposites in a Cold Region (Draft)." New England Transportation Consortium Project No. 00-8, 235 p.
- HKS Inc. (2004). Hibbit, Kalsson & Sorensen, Inc. "ABAQUS Standard User's Manual Vol. 6.5-1.", Pawtucket, R.I.
- Perkins, S.W., B.R. Christopher, E.L. Cuelho, G.R. Eiksund, I. Hoff, C.W. Schwartz, G. Svanø, and A. Watn (2004). "Development of Design Methods for Geosynthetic Reinforced Flexible Pavements." U.S. Department of Transportation, Federal Highway Administration, Washington, DC, FHWA Report Reference Number DTFH61-01-X-00068, 263 p.
- Tensar Earth Technologies, Inc. (2005) "Product Specification – Biaxial Geogrid BX1200", Retrieved September 6, 2005, from http://www.tensarcorp.com/uploadedFiles/SPECTRA_MPDS_BX_8.05.pdf.

Appendix D – Parametric Study Results

Table D1. Results for $t_{AC} = 100$ mm, $t_{base} = 300$ mm.

Num.	Elastic Modulus (MPa)			Thickness (mm)		LG	$N_f/1000$	TBR
	AC	Base	Subgrade	AC	Base			
1	2720	100	35	100	300	None	278	--
2	2720	100	35	100	300	0	370	1.33
3	2720	100	35	100	300	0.25	347	1.25
4	2720	100	35	100	300	0.5	323	1.16
5	2720	100	35	100	300	0.75	300	1.08
6	4480	100	35	100	300	None	620	--
7	4480	100	35	100	300	0	919	1.48
8	4480	100	35	100	300	0.25	839	1.35
9	4480	100	35	100	300	0.5	760	1.23
10	4480	100	35	100	300	0.75	687	1.11
11	2720	300	35	100	300	None	629	--
12	2720	300	35	100	300	0	759	1.21
13	2720	300	35	100	300	0.25	726	1.15
14	2720	300	35	100	300	0.5	688	1.09
15	2720	300	35	100	300	0.75	657	1.04
16	4480	300	35	100	300	None	1330	--
17	4480	300	35	100	300	0	1704	1.28
18	4480	300	35	100	300	0.25	1605	1.21
19	4480	300	35	100	300	0.5	1495	1.12
20	4480	300	35	100	300	0.75	1407	1.06
21	2720	100	70	100	300	None	779	--
22	2720	100	70	100	300	0	1069	1.37
23	2720	100	70	100	300	0.25	998	1.28
24	2720	100	70	100	300	0.5	924	1.19
25	2720	100	70	100	300	0.75	851	1.09
26	4480	100	70	100	300	None	2089	--
27	4480	100	70	100	300	0	3271	1.57
28	4480	100	70	100	300	0.25	2959	1.42
29	4480	100	70	100	300	0.5	2652	1.27
30	4480	100	70	100	300	0.75	2361	1.13
31	2720	300	70	100	300	None	1742	--
32	2720	300	70	100	300	0	2159	1.24
33	2720	300	70	100	300	0.25	2056	1.18
34	2720	300	70	100	300	0.5	1944	1.12
35	2720	300	70	100	300	0.75	1841	1.06
36	4480	300	70	100	300	None	4535	--
37	4480	300	70	100	300	0	6080	1.34
38	4480	300	70	100	300	0.25	5682	1.25
39	4480	300	70	100	300	0.5	5258	1.16
40	4480	300	70	100	300	0.75	4884	1.08

Table D2. Results for $t_{AC} = 150$ mm, $t_{base} = 300$ mm.

Num.	Elastic Modulus (MPa)			Thickness (mm)		LG	$N_f/1000$	TBR
	AC	Base	Subgrade	AC	Base			
41	2720	100	35	150	300	None	1022	--
42	2720	100	35	150	300	0	1599	1.56
43	2720	100	35	150	300	0.25	1439	1.41
44	2720	100	35	150	300	0.5	1285	1.26
45	2720	100	35	150	300	0.75	1146	1.12
46	4480	100	35	150	300	None	3918	--
47	4480	100	35	150	300	0	7898	2.02
48	4480	100	35	150	300	0.25	6661	1.70
49	4480	100	35	150	300	0.5	5557	1.42
50	4480	100	35	150	300	0.75	4655	1.19
51	2720	300	35	150	300	None	1533	--
52	2720	300	35	150	300	0	1954	1.27
53	2720	300	35	150	300	0.25	1843	1.20
54	2720	300	35	150	300	0.5	1718	1.12
55	2720	300	35	150	300	0.75	1618	1.06
56	4480	300	35	150	300	None	5701	--
57	4480	300	35	150	300	0	8226	1.44
58	4480	300	35	150	300	0.25	7517	1.32
59	4480	300	35	150	300	0.5	6746	1.18
60	4480	300	35	150	300	0.75	6167	1.08
61	2720	100	70	150	300	None	2489	--
62	2720	100	70	150	300	0	3808	1.53
63	2720	100	70	150	300	0.25	3461	1.39
64	2720	100	70	150	300	0.5	3119	1.25
65	2720	100	70	150	300	0.75	2794	1.12
66	4480	100	70	150	300	None	11929	--
67	4480	100	70	150	300	0	23095	1.94
68	4480	100	70	150	300	0.25	19844	1.66
69	4480	100	70	150	300	0.5	16853	1.41
70	4480	100	70	150	300	0.75	14213	1.19
71	2720	300	70	150	300	None	3566	--
72	2720	300	70	150	300	0	4546	1.28
73	2720	300	70	150	300	0.25	4300	1.21
74	2720	300	70	150	300	0.5	4032	1.13
75	2720	300	70	150	300	0.75	3792	1.06
76	4480	300	70	150	300	None	16590	--
77	4480	300	70	150	300	0	23950	1.44
78	4480	300	70	150	300	0.25	21985	1.33
79	4480	300	70	150	300	0.5	19922	1.20
80	4480	300	70	150	300	0.75	18163	1.09

Table D3. Results for $t_{AC} = 200$ mm, $t_{base} = 300$ mm.

Num.	Elastic Modulus (MPa)			Thickness (mm)		LG	$N_f/1000$	TBR
	AC	Base	Subgrade	AC	Base			
81	2720	100	35	200	300	None	2679	--
82	2720	100	35	200	300	0	4674	1.74
83	2720	100	35	200	300	0.25	4091	1.53
84	2720	100	35	200	300	0.5	3546	1.32
85	2720	100	35	200	300	0.75	3077	1.15
86	4480	100	35	200	300	None	15233	--
87	4480	100	35	200	300	0	36608	2.40
88	4480	100	35	200	300	0.25	29626	1.94
89	4480	100	35	200	300	0.5	23606	1.55
90	4480	100	35	200	300	0.75	18881	1.24
91	2720	300	35	200	300	None	3242	--
92	2720	300	35	200	300	0	4283	1.32
93	2720	300	35	200	300	0.25	4004	1.24
94	2720	300	35	200	300	0.5	3690	1.14
95	2720	300	35	200	300	0.75	3444	1.06
96	4480	300	35	200	300	None	18322	--
97	4480	300	35	200	300	0	28254	1.54
98	4480	300	35	200	300	0.25	25433	1.39
99	4480	300	35	200	300	0.5	22361	1.22
100	4480	300	35	200	300	0.75	20087	1.10
101	2720	100	70	200	300	None	5053	--
102	2720	100	70	200	300	0	7993	1.58
103	2720	100	70	200	300	0.25	7203	1.43
104	2720	100	70	200	300	0.5	6431	1.27
105	2720	100	70	200	300	0.75	5711	1.13
106	4480	100	70	200	300	None	33469	--
107	4480	100	70	200	300	0	66986	2.00
108	4480	100	70	200	300	0.25	57182	1.71
109	4480	100	70	200	300	0.5	48121	1.44
110	4480	100	70	200	300	0.75	40199	1.20
111	2720	300	70	200	300	None	5929	--
112	2720	300	70	200	300	0	7605	1.28
113	2720	300	70	200	300	0.25	7183	1.21
114	2720	300	70	200	300	0.5	6719	1.13
115	2720	300	70	200	300	0.75	6308	1.06
116	4480	300	70	200	300	None	38764	--
117	4480	300	70	200	300	0	56377	1.45
118	4480	300	70	200	300	0.25	51702	1.33
119	4480	300	70	200	300	0.5	46695	1.20
120	4480	300	70	200	300	0.75	42472	1.10

Table D4. Results for $t_{AC} = 100$ mm, $t_{base} = 450$ mm.

Num.	Elastic Modulus (MPa)			Thickness (mm)		LG	$N_f/1000$	TBR
	AC	Base	Subgrade	AC	Base			
121	2720	100	35	100	450	None	840	--
122	2720	100	35	100	450	0	1200	1.43
123	2720	100	35	100	450	0.25	1105	1.31
124	2720	100	35	100	450	0.5	1008	1.20
125	2720	100	35	100	450	0.75	920	1.10
126	4480	100	35	100	450	None	2177	--
127	4480	100	35	100	450	0	3577	1.64
128	4480	100	35	100	450	0.25	3177	1.46
129	4480	100	35	100	450	0.5	2792	1.28
130	4480	100	35	100	450	0.75	2461	1.13
131	2720	300	35	100	450	None	3926	--
132	2720	300	35	100	450	0	5145	1.31
133	2720	300	35	100	450	0.25	4773	1.22
134	2720	300	35	100	450	0.5	4403	1.12
135	2720	300	35	100	450	0.75	4133	1.05
136	4480	300	35	100	450	None	11410	--
137	4480	300	35	100	450	0	16542	1.45
138	4480	300	35	100	450	0.25	14901	1.31
139	4480	300	35	100	450	0.5	13318	1.17
140	4480	300	35	100	450	0.75	12220	1.07
141	2720	100	70	100	450	None	1802	--
142	2720	100	70	100	450	0	2560	1.42
143	2720	100	70	100	450	0.25	2376	1.32
144	2720	100	70	100	450	0.5	2182	1.21
145	2720	100	70	100	450	0.75	1988	1.10
146	4480	100	70	100	450	None	5796	--
147	4480	100	70	100	450	0	9611	1.66
148	4480	100	70	100	450	0.25	8606	1.48
149	4480	100	70	100	450	0.5	7602	1.31
150	4480	100	70	100	450	0.75	6656	1.15
151	2720	300	70	100	450	None	8409	--
152	2720	300	70	100	450	0	10844	1.29
153	2720	300	70	100	450	0.25	10189	1.21
154	2720	300	70	100	450	0.5	9508	1.13
155	2720	300	70	100	450	0.75	8926	1.06
156	4480	300	70	100	450	None	31743	--
157	4480	300	70	100	450	0	45445	1.43
158	4480	300	70	100	450	0.25	41570	1.31
159	4480	300	70	100	450	0.5	37659	1.19
160	4480	300	70	100	450	0.75	34469	1.09

Table D5. Results for $t_{AC} = 150$ mm, $t_{base} = 450$ mm.

Num.	Elastic Modulus (MPa)			Thickness (mm)		LG	$N_f/1000$	TBR
	AC	Base	Subgrade	AC	Base			
161	2720	100	35	150	450	None	2574	--
162	2720	100	35	150	450	0	4103	1.59
163	2720	100	35	150	450	0.25	3676	1.43
164	2720	100	35	150	450	0.5	3255	1.26
165	2720	100	35	150	450	0.75	2888	1.12
166	4480	100	35	150	450	None	12095	--
167	4480	100	35	150	450	0	24683	2.04
168	4480	100	35	150	450	0.25	20786	1.72
169	4480	100	35	150	450	0.5	17201	1.42
170	4480	100	35	150	450	0.75	14338	1.19
171	2720	300	35	150	450	None	6031	--
172	2720	300	35	150	450	0	7869	1.30
173	2720	300	35	150	450	0.25	7324	1.21
174	2720	300	35	150	450	0.5	6762	1.12
175	2720	300	35	150	450	0.75	6348	1.05
176	4480	300	35	150	450	None	29923	--
177	4480	300	35	150	450	0	44232	1.48
178	4480	300	35	150	450	0.25	39776	1.33
179	4480	300	35	150	450	0.5	35296	1.18
180	4480	300	35	150	450	0.75	32182	1.08
181	2720	100	70	150	450	None	4703	--
182	2720	100	70	150	450	0	7062	1.50
183	2720	100	70	150	450	0.25	6472	1.38
184	2720	100	70	150	450	0.5	5857	1.25
185	2720	100	70	150	450	0.75	5260	1.12
186	4480	100	70	150	450	None	26872	--
187	4480	100	70	150	450	0	49661	1.85
188	4480	100	70	150	450	0.25	43427	1.62
189	4480	100	70	150	450	0.5	37258	1.39
190	4480	100	70	150	450	0.75	31692	1.18
191	2720	300	70	150	450	None	10443	--
192	2720	300	70	150	450	0	13164	1.26
193	2720	300	70	150	450	0.25	12454	1.19
194	2720	300	70	150	450	0.5	11691	1.12
195	2720	300	70	150	450	0.75	11030	1.06
196	4480	300	70	150	450	None	62625	--
197	4480	300	70	150	450	0	87539	1.40
198	4480	300	70	150	450	0.25	80728	1.29
199	4480	300	70	150	450	0.5	73551	1.17
200	4480	300	70	150	450	0.75	67637	1.08

Table D6. Results for $t_{AC} = 200$ mm, $t_{base} = 450$ mm.

Num.	Elastic Modulus (MPa)			Thickness (mm)			$N_f/1000$	TBR
	AC	Base	Subgrade	AC	Base	LG		
201	2720	100	35	200	450	None	5346	--
202	2720	100	35	200	450	0	8800	1.65
203	2720	100	35	200	450	0.25	7835	1.47
204	2720	100	35	200	450	0.5	6873	1.29
205	2720	100	35	200	450	0.75	6042	1.13
206	4480	100	35	200	450	None	35681	--
207	4480	100	35	200	450	0	74641	2.09
208	4480	100	35	200	450	0.25	62833	1.76
209	4480	100	35	200	450	0.5	51692	1.45
210	4480	100	35	200	450	0.75	42701	1.20
211	2720	300	35	200	450	None	8348	--
212	2720	300	35	200	450	0	10713	1.28
213	2720	300	35	200	450	0.25	10040	1.20
214	2720	300	35	200	450	0.5	9317	1.12
215	2720	300	35	200	450	0.75	8769	1.05
216	4480	300	35	200	450	None	56702	--
217	4480	300	35	200	450	0	81345	1.43
218	4480	300	35	200	450	0.25	74035	1.31
219	4480	300	35	200	450	0.5	66337	1.17
220	4480	300	35	200	450	0.75	60787	1.07
221	2720	100	70	200	450	None	7740	--
222	2720	100	70	200	450	0	11533	1.49
223	2720	100	70	200	450	0.25	10592	1.37
224	2720	100	70	200	450	0.5	9594	1.24
225	2720	100	70	200	450	0.75	8627	1.11
226	4480	100	70	200	450	None	56975	--
227	4480	100	70	200	450	0	101298	1.78
228	4480	100	70	200	450	0.25	89540	1.57
229	4480	100	70	200	450	0.5	77526	1.36
230	4480	100	70	200	450	0.75	66508	1.17
231	2720	300	70	200	450	None	11833	--
232	2720	300	70	200	450	0	14562	1.23
233	2720	300	70	200	450	0.25	13877	1.17
234	2720	300	70	200	450	0.5	13107	1.11
235	2720	300	70	200	450	0.75	12432	1.05
236	4480	300	70	200	450	None	88335	--
237	4480	300	70	200	450	0	118447	1.34
238	4480	300	70	200	450	0.25	110579	1.25
239	4480	300	70	200	450	0.5	101873	1.15
240	4480	300	70	200	450	0.75	94536	1.07

Table D7. Results for $t_{AC} = 100$ mm, $t_{base} = 600$ mm.

Num.	Elastic Modulus (MPa)			Thickness (mm)		LG	$N_f/1000$	TBR
	AC	Base	Subgrade	AC	Base			
241	2720	100	35	100	600	None	2329	--
242	2720	100	35	100	600	0	3545	1.52
243	2720	100	35	100	600	0.25	3221	1.38
244	2720	100	35	100	600	0.5	2887	1.24
245	2720	100	35	100	600	0.75	2589	1.11
246	4480	100	35	100	600	None	8048	--
247	4480	100	35	100	600	0	14780	1.84
248	4480	100	35	100	600	0.25	12819	1.59
249	4480	100	35	100	600	0.5	10916	1.36
250	4480	100	35	100	600	0.75	9335	1.16
251	2720	300	35	100	600	None	18474	--
252	2720	300	35	100	600	0	24752	1.34
253	2720	300	35	100	600	0.25	22799	1.23
254	2720	300	35	100	600	0.5	20891	1.13
255	2720	300	35	100	600	0.75	19501	1.06
256	4480	300	35	100	600	None	90565	--
257	4480	300	35	100	600	0	136697	1.51
258	4480	300	35	100	600	0.25	121559	1.34
259	4480	300	35	100	600	0.5	107356	1.19
260	4480	300	35	100	600	0.75	97486	1.08
261	2720	100	70	100	600	None	3417	--
262	2720	100	70	100	600	0	4910	1.44
263	2720	100	70	100	600	0.25	4571	1.34
264	2720	100	70	100	600	0.5	4187	1.23
265	2720	100	70	100	600	0.75	3793	1.11
266	4480	100	70	100	600	None	13871	--
267	4480	100	70	100	600	0	23653	1.71
268	4480	100	70	100	600	0.25	21233	1.53
269	4480	100	70	100	600	0.5	18620	1.34
270	4480	100	70	100	600	0.75	16119	1.16
271	2720	300	70	100	600	None	26939	--
272	2720	300	70	100	600	0	34372	1.28
273	2720	300	70	100	600	0.25	32422	1.20
274	2720	300	70	100	600	0.5	30322	1.13
275	2720	300	70	100	600	0.75	28514	1.06
276	4480	300	70	100	600	None	155427	--
277	4480	300	70	100	600	0	218301	1.40
278	4480	300	70	100	600	0.25	200985	1.29
279	4480	300	70	100	600	0.5	182903	1.18
280	4480	300	70	100	600	0.75	167982	1.08

Table D8. Results for $t_{AC} = 150$ mm, $t_{base} = 600$ mm.

Num.	Elastic Modulus (MPa)			Thickness (mm)		LG	$N_f/1000$	TBR
	AC	Base	Subgrade	AC	Base			
281	2720	100	35	150	600	None	6071	--
282	2720	100	35	150	600	0	9626	1.59
283	2720	100	35	150	600	0.25	8692	1.43
284	2720	100	35	150	600	0.5	7710	1.27
285	2720	100	35	150	600	0.75	6830	1.13
286	4480	100	35	150	600	None	38087	--
287	4480	100	35	150	600	0	75171	1.97
288	4480	100	35	150	600	0.25	64549	1.69
289	4480	100	35	150	600	0.5	53950	1.42
290	4480	100	35	150	600	0.75	45125	1.18
291	2720	300	35	150	600	None	18266	--
292	2720	300	35	150	600	0	23150	1.27
293	2720	300	35	150	600	0.25	21753	1.19
294	2720	300	35	150	600	0.5	20297	1.11
295	2720	300	35	150	600	0.75	19160	1.05
296	4480	300	35	150	600	None	128558	--
297	4480	300	35	150	600	0	178538	1.39
298	4480	300	35	150	600	0.25	163647	1.27
299	4480	300	35	150	600	0.5	148430	1.15
300	4480	300	35	150	600	0.75	137092	1.07
301	2720	100	70	150	600	None	7625	--
302	2720	100	70	150	600	0	11080	1.45
303	2720	100	70	150	600	0.25	10313	1.35
304	2720	100	70	150	600	0.5	9415	1.23
305	2720	100	70	150	600	0.75	8496	1.11
306	4480	100	70	150	600	None	52462	--
307	4480	100	70	150	600	0	90516	1.73
308	4480	100	70	150	600	0.25	81388	1.55
309	4480	100	70	150	600	0.5	71144	1.36
310	4480	100	70	150	600	0.75	61227	1.17
311	2720	300	70	150	600	None	22593	--
312	2720	300	70	150	600	0	27460	1.22
313	2720	300	70	150	600	0.25	26284	1.16
314	2720	300	70	150	600	0.5	24933	1.10
315	2720	300	70	150	600	0.75	23704	1.05
316	4480	300	70	150	600	None	172116	--
317	4480	300	70	150	600	0	224581	1.30
318	4480	300	70	150	600	0.25	211391	1.23
319	4480	300	70	150	600	0.5	196468	1.14
320	4480	300	70	150	600	0.75	183462	1.07

Table D9. Results for $t_{AC} = 200$ mm, $t_{base} = 600$ mm.

Num.	Elastic Modulus (MPa)			Thickness (mm)		LG	$N_f/1000$	TBR
	AC	Base	Subgrade	AC	Base			
321	2720	100	35	200	600	None	9988	--
322	2720	100	35	200	600	0	15367	1.54
323	2720	100	35	200	600	0.25	14025	1.40
324	2720	100	35	200	600	0.5	12559	1.26
325	2720	100	35	200	600	0.75	11190	1.12
326	4480	100	35	200	600	None	79921	--
327	4480	100	35	200	600	0	144896	1.81
328	4480	100	35	200	600	0.25	127729	1.60
329	4480	100	35	200	600	0.5	109609	1.37
330	4480	100	35	200	600	0.75	93409	1.17
331	2720	300	35	200	600	None	17894	--
332	2720	300	35	200	600	0	21738	1.21
333	2720	300	35	200	600	0.25	20731	1.16
334	2720	300	35	200	600	0.5	19621	1.10
335	2720	300	35	200	600	0.75	18682	1.04
336	4480	300	35	200	600	None	147531	--
337	4480	300	35	200	600	0	191404	1.30
338	4480	300	35	200	600	0.25	179536	1.22
339	4480	300	35	200	600	0.5	166646	1.13
340	4480	300	35	200	600	0.75	156096	1.06
341	2720	100	70	200	600	None	10680	--
342	2720	100	70	200	600	0	15031	1.41
343	2720	100	70	200	600	0.25	14110	1.32
344	2720	100	70	200	600	0.5	12984	1.22
345	2720	100	70	200	600	0.75	11802	1.11
346	4480	100	70	200	600	None	87521	--
347	4480	100	70	200	600	0	140035	1.60
348	4480	100	70	200	600	0.25	128328	1.47
349	4480	100	70	200	600	0.5	114376	1.31
350	4480	100	70	200	600	0.75	100268	1.15
351	2720	300	70	200	600	None	19634	--
352	2720	300	70	200	600	0	23075	1.18
353	2720	300	70	200	600	0.25	22309	1.14
354	2720	300	70	200	600	0.5	21373	1.09
355	2720	300	70	200	600	0.75	20474	1.04
356	4480	300	70	200	600	None	166425	--
357	4480	300	70	200	600	0	206214	1.24
358	4480	300	70	200	600	0.25	197058	1.18
359	4480	300	70	200	600	0.5	185992	1.12
360	4480	300	70	200	600	0.75	175709	1.06

REPORT DOCUMENTATION PAGE

*Form Approved
OMB No. 0704-0188*

Public reporting burden for this collection of information is estimated to average 1 hour per response, including the time for reviewing instructions, searching existing data sources, gathering and maintaining the data needed, and completing and reviewing this collection of information. Send comments regarding this burden estimate or any other aspect of this collection of information, including suggestions for reducing this burden to Department of Defense, Washington Headquarters Services, Directorate for Information Operations and Reports (0704-0188), 1215 Jefferson Davis Highway, Suite 1204, Arlington, VA 22202-4302. Respondents should be aware that notwithstanding any other provision of law, no person shall be subject to any penalty for failing to comply with a collection of information if it does not display a currently valid OMB control number. **PLEASE DO NOT RETURN YOUR FORM TO THE ABOVE ADDRESS.**

1. REPORT DATE (DD-MM-YYYY) October 2009		2. REPORT TYPE Final report		3. DATES COVERED (From - To)	
4. TITLE AND SUBTITLE Structural Improvements of Flexible Pavements Using Geosynthetics for Base Course Reinforcement				5a. CONTRACT NUMBER	
				5b. GRANT NUMBER	
				5c. PROGRAM ELEMENT NUMBER	
6. AUTHOR(S) Karen S. Henry, Joshua Clapp, William Davids, Dana Humphrey, and Lynette Barna				5d. PROJECT NUMBER	
				5e. TASK NUMBER	
				5f. WORK UNIT NUMBER	
7. PERFORMING ORGANIZATION NAME(S) AND ADDRESS(ES) U.S. Army Engineer Research and Development Center Cold Regions Research & Engineering Laboratory 72 Lyme Road Hanover, NH 03755-1290				8. PERFORMING ORGANIZATION REPORT NUMBER ERDC/CRREL TR-09-11	
9. SPONSORING / MONITORING AGENCY NAME(S) AND ADDRESS(ES) Federal Highway Administration McLean, VA 22101				10. SPONSOR/MONITOR'S ACRONYM(S)	
				11. SPONSOR/MONITOR'S REPORT NUMBER(S)	
12. DISTRIBUTION / AVAILABILITY STATEMENT Approved for public release; distribution is unlimited. Available from NTIS, Springfield, Virginia 22161.					
13. SUPPLEMENTARY NOTES					
14. ABSTRACT A study was conducted on full-scale pavement test sections to assess geogrid/base reinforcement in flexible pavements representative of major highways. The experimental design, trafficking protocol, results and development of rutting models are reported herein. Accelerated trafficking was conducted with a heavy vehicle simulator on eight pavement test sections. Four test sections were reinforced with geogrid placed at the base/subgrade interface, the other four were matching unreinforced (control) sections. Rut depths in the pavement surface as a function of applied traffic cycles were compared. Except for the thickest base and asphalt combination tested, the grid reinforcement provided benefit compared to unreinforced control sections as indicated by surface rut depth. (Four test sections reached 'failure' and four did not—traffic ceased at a set number of load cycles in these cases.) Empirical rutting models presented in NCHRP 1-37A, Guide for Mechanistic-Empirical Design of New and Rehabilitated Pavement Structures (available from http://www.trb.org/mepdg/) were extended to account for the reinforcement. Mechanistic finite element models were calibrated using strains measured throughout the test sections. Predicted rut depths using this mechanistic-empirical approach were in reasonable agreement with measured values. For the pavement configurations of this study, geogrid was predicted to increase the pavement life by 29 to 43%.					
15. SUBJECT TERMS Accelerated pavement testing Finite element models		Flexible pavements Geogrid reinforcement Geosynthetics		Heavy vehicle simulator Pavement rutting	
16. SECURITY CLASSIFICATION OF:		17. LIMITATION OF ABSTRACT	18. NUMBER OF PAGES	19a. NAME OF RESPONSIBLE PERSON	
a. REPORT UNCLASSIFIED	b. ABSTRACT UNCLASSIFIED			c. THIS PAGE UNCLASSIFIED	192